

UNIVERSIDADE DE LISBOA
INSTITUTO SUPERIOR TÉCNICO

Structural behaviour of FRP pultruded beams and columns

Francisco Felício Nunes

Supervisor: Doctor João Pedro Ramôa Ribeiro Correia

Co-Supervisor: Doctor Nuno Miguel Rosa Pereira Silvestre

Thesis approved in public session to obtain the PhD Degree in Civil Engineering

Jury final classification: Pass with Distinction and Honor

Jury

Chairperson: Chairman of the IST Scientific Board

Members of the Committee:

Doctor Joaquim António Oliveira de Barros

Doctor Fernando António Baptista Branco

Doctor Nuno Miguel Rosa Pereira Silvestre

Doctor João Pedro Ramôa Ribeiro Correia

Doctor Ricardo José de Figueiredo Mendes Vieira

Doctor Till Herman Franz Vallée

2016

UNIVERSIDADE DE LISBOA
INSTITUTO SUPERIOR TÉCNICO

Structural behaviour of FRP pultruded beams and columns

Francisco Felício Nunes

Supervisor: Doctor João Pedro Ramôa Ribeiro Correia

Co-Supervisor: Doctor Nuno Miguel Rosa Pereira Silvestre

Thesis approved in public session to obtain the PhD Degree in Civil Engineering

Jury final classification: Pass with Distinction and Honor

Jury

Chairperson: Chairman of the IST Scientific Board

Members of the Committee:

Doctor Joaquim António Oliveira de Barros, Full Professor, Escola de Engenharia, Universidade do Minho

Doctor Fernando António Baptista Branco, Full Professor, Instituto Superior Técnico, Universidade de Lisboa

Doctor Nuno Miguel Rosa Pereira Silvestre, Associate Professor (with Habilitation), Instituto Superior Técnico, Universidade de Lisboa

Doctor João Pedro Ramôa Ribeiro Correia, Associate Professor (with Habilitation), Instituto Superior Técnico, Universidade de Lisboa

Doctor Ricardo José de Figueiredo Mendes Vieira, Assistant Professor, Instituto Superior Técnico, Universidade de Lisboa

Doctor Till Herman Franz Vallée, Researcher, Fraunhofer Institute for Manufacturing Technology and Advanced Materials, IFAM, Germany

2016

ABSTRACT

Pultruded fibre reinforced polymer (FRP) profiles are being increasingly used as structural members in civil engineering applications, offering a competitive alternative to traditional construction materials, such as steel and reinforced concrete (RC). Certain specific aspects of FRP materials, such as their lightness, high strength, significant chemical resistance even when subjected to aggressive environmental agents and electromagnetic transparency have promoted their structural use in civil engineering structures. However, these innovative materials, namely those comprising glass reinforcement (GFRP), also present some drawbacks, like the typical high deformability and susceptibility to buckling phenomena, the brittle failure modes, the poor behaviour under elevated temperatures and the lack of consensual design codes.

The lack of consensual design codes might be overcome by providing more comprehensive insights on the structural behaviour and failure mechanisms of FRP pultruded profiles. In this context, this thesis aims at studying particular aspects of the structural behaviour exhibited by FRP profiles, namely: (i) their response under eccentric compression, (ii) the effects of incorporating different types of fibres (hybridization) in the same pultruded part, (iii) the numerical analysis of material progressive failure (using adequate failure criteria), and (iv) the web-crippling phenomenon of members subjected to transverse concentrated loads.

To achieve these goals, experimental, numerical and analytical investigations were carried out and the results yielded from each one were thoroughly analysed, compared and discussed in order to provide reliable information towards the establishment of more consensual approaches and guidelines for the design of FRP members. Experimental tests were carried out at IST and comprised two different stages: (i) comprehensive mechanical characterisation tests in small scale coupons for the definition of the elastic and strength properties, and (ii) full-scale tests in beams and columns aiming at studying their structural behaviour for both serviceability and ultimate load levels. Numerical finite element (FE) models of those members were developed within the framework of the commercial software ABAQUS and used to perform (i) eigenvalue linear buckling analyses, and (ii) geometrically nonlinear analyses considering (or not) the progressive failure of the composite material. Whenever possible, the experimental and numerical data were compared to the results given by FRP design formulae, available in specific design standards and guidelines or proposed by other authors, thus assessing their accuracy.

The studies presented in this thesis highlight relevant aspects of the structural behaviour of pultruded FRP beams and columns. The results obtained confirmed the linear elastic behaviour up to failure of the FRP material, which generally takes place in global and/or local buckling modes and occurs in a sudden and brittle way, for both beams and columns. When comparing the ultimate loads of concentrically and eccentrically loaded columns, it was concluded that small eccentricities affect both their stiffness and ultimate load. Hybridization with glass and carbon fibres proved to be effective in stiffening pultruded profiles, thus improving their serviceability performance. However, the premature delamination of the carbon fibre reinforcement (namely in members subjected to high compressive strain levels) leads to a reduction of the effective cross-section and consequently it may not contribute to increase the ultimate load. The FE models developed provided a very good agreement to the experimental data both in terms of loading path and failure behaviour. The application of the ABAQUS built-in Hashin-based progressive damage analysis was successful in all the load configurations tested and highlighted the importance of providing accurate input data for the numerical models (strengths and fracture energies), namely for failure mechanisms that allow for a significant stress redistribution (*e.g.* the web-crippling phenomenon). The analytical design approaches assessed in this thesis were not always fully accurate. The reasons for such lack of accuracy are discussed, and possible improvements are suggested.

KEYWORDS | FRP pultruded profiles | Eccentrically loaded columns | C-GFRP hybridization | Hashin progressive damage | Web-crippling.

RESUMO

Os perfis pultrudidos de polímero reforçado com fibras (FRP¹) têm sido cada vez mais utilizados como elementos estruturais na engenharia civil, apresentando-se como uma alternativa competitiva relativamente aos materiais tradicionais (tais como o aço ou o betão armado). De entre as principais vantagens dos perfis de FRP, destaca-se o seu peso próprio reduzido, a elevada resistência mecânica, a significativa resistência química em ambientes agressivos e a transparência eletromagnética. No entanto, os perfis de FRP apresentam alguns inconvenientes, tais como a elevada deformabilidade e a suscetibilidade a fenómenos de encurvadura, os modos de rotura tipicamente frágeis, o deficiente comportamento a temperatura elevada e a ausência de manuais de dimensionamento consensuais.

O facto de existirem abordagens analíticas distintas para o dimensionamento deste tipo de estruturas (agravado pelo amplo leque de propriedades apresentadas pelos diversos fabricantes) requer que o seu comportamento mecânico seja analisado com maior detalhe, de modo a melhorar a compreensão sobre os diferentes mecanismos de rotura. Neste contexto, a presente tese tem como principal objetivo o estudo e a análise de um conjunto de fenómenos particulares do comportamento estrutural exibido pelos perfis de FRP, nomeadamente: (i) a sua resposta estrutural quando sujeitos a forças de compressão excêntricas, (ii) o efeito da hibridização em vigas e colunas, utilizando diferentes tipos de fibras no mesmo perfil pultrudido, (iii) a avaliação numérica da evolução do dano do material e (iv) o esmagamento de almas de perfis sujeitos a forças concentradas transversais.

Para alcançar estes objetivos, foram realizados diferentes estudos experimentais, numéricos e analíticos. Os resultados obtidos foram cuidadosamente analisados e discutidos de modo a produzir um conjunto de informação útil sobre possíveis formas de melhorar os perfis de FRP e contribuir para uma melhor definição do domínio de validade das metodologias de dimensionamento existentes. Os estudos experimentais foram desenvolvidos no Laboratório de Estruturas e Resistência dos Materiais do Instituto Superior Técnico (IST) e dividiram-se em duas fases distintas: (i) caracterização mecânica do material para determinação das constantes elásticas e resistências e (ii) testes à escala real em vigas e colunas pultrudidas, estudando o seu comportamento em serviço e à rotura. Os modelos numéricos para a simulação desses ensaios foram desenvolvidos utilizando o *software* ABAQUS e incluem (i) análises lineares para a determinação de cargas críticas e modos de encurvadura e (ii) análises geometricamente não lineares considerando (ou não) o dano progressivo do material. Sempre que possível, os resultados experimentais e numéricos foram comparados com estimativas analíticas

¹ *Fibre Reinforced Polymer* (designação anglo-saxónica)

propostas pelos principais manuais de dimensionamento para perfis de FRP ou abordagens de outros autores, de modo a verificar a sua adequabilidade e precisão.

Os estudos apresentados nesta tese destacam aspectos relevantes sobre o comportamento estrutural de colunas e vigas de FRP. Os resultados obtidos confirmaram o comportamento elástico linear do material até à rotura, que ocorre geralmente de um modo frágil, tanto para membros à compressão (colunas) como à flexão (vigas). Comparando os resultados obtidos para colunas concêntricas e excêntricas, conclui-se que pequenas excentricidades no ponto de aplicação da carga afetam tanto a rigidez axial como a carga última. A hibridização com fibras de vidro e de carbono mostrou-se eficiente em aumentar a rigidez inicial dos perfis pultrudidos. Por outro lado, a delaminação prematura do reforço em fibras de carbono (nomeadamente para membros sujeitos a níveis de extensão elevados) fez com que, em grande parte dos provetes testados, não houvesse um aumento da carga última, mas sim uma redução da mesma, tanto à compressão como à flexão. Os modelos numéricos em elementos finitos demonstraram boa concordância com os resultados experimentais, tanto em termos de rigidez como de comportamento à rotura. A implementação de análises com dano progressivo baseadas no critério de Hashin foi bem sucedida para todas as configurações de carga testadas, tendo evidenciado a necessidade de definir parâmetros de *input* adequados (resistências e energias de fratura), sobretudo para mecanismos de rotura que permitam a redistribuição de esforços (por exemplo, o esmagamento da alma). Os resultados das metodologias de dimensionamento existentes e abordadas nesta tese, nem sempre foram coerentes com os resultados experimentais e numéricos obtidos. As razões para essa falta de concordância são discutidas, sendo propostas possíveis alterações a essas formulações.

PALAVRAS-CHAVE | Perfis pultrudidos de FRP | Colunas excêntricas | Hibridização C-GFRP | Dano progressivo de Hashin | Esmagamento da alma.

ACKNOWLEDGEMENTS

These next paragraphs are addressed to all those people who directly or indirectly helped me achieving my goals and to whom I would like dedicate this work and to express my sincere gratitude.

First of all, I would like to thank my scientific supervisors, Prof. João Ramôa Correia and Prof. Nuno Silvestre for their amazing support, knowledge, constant availability, friendship, guidance, encouragement and dedication in the last four years. There is no doubt that they are the main reason why I decided to do this PhD research and it surely would not be completed without their major contribution.

I would also like to thank my research colleagues (and friends) at IST, namely Tiago Morgado, Luís Valarinho, João Firmo, João Sousa, José Gonilha, Mário Garrido, Mário Arruda, David Martins, Mário Sá, José Sampaio, Cristina López, André Castelo and Lourenço Fernandes. Without their valuable help, suggestions and constant discussion it would be far more difficult to develop relevant research.

To the IST personnel at DECivil, LERM and LC, particularly Maria Helena Salvado, Fernando Alves, Fernando Costa, Leonel Silva and João Lopes, I would like to thank for their dedication and assistance in both administrative and laboratory work.

I would like to sincerely thank my girlfriend, Carolina Cesaroni, for all her love, patience, understanding, complicity, support and also for all the happy moments we have been living together and for being always present when I mostly needed her.

I am very grateful to all my family but most of all to my parents, António and Isabel Nunes, and to my sister, Rita Nunes, for always supporting me and believing in me, for their sacrifices, for their affection, their love and for making me who I am today.

I would absolutely like to thank my best friends, Manuel Correia, Vasco Raio, Roberto Feijóo, Liliana Páscoa, Catarina Lopes, José Lourenço, Pedro Garez, João Rocha and Gonçalo Pereira for all the good moments outside work, for their support, for the laughs and for the well enjoyed evenings and weekends.

I am grateful to my English tutor, Grant Brown, for the funny and relaxed moments at his classes and for drastically contributing to the improvement of my English speaking and writing skills.

Finally I would also like to thank to my colleagues and directors at Tetraplano Engenharia, namely Sofia Casanova, Ana Quintela and José Manuel Cruz, for the opportunity and tutoring in the development of large scale structural projects that highly contributed to the improvement of my professional skills as a structural engineer.

TABLE OF CONTENTS

Abstract	i
Resumo	iii
Acknowledgements	v
Table of contents	vii
List of figures	xi
List of tables	xix
Notation	xxi
 CHAPTER 1	
INTRODUCTION	1
1.1 OVERVIEW	1
1.2 MOTIVATION	2
1.3 OBJECTIVES AND METHODOLOGY	4
1.4 MAIN SCIENTIFIC CONTRIBUTIONS	5
1.5 DOCUMENT OUTLINE	7
 CHAPTER 2	
FRP PULTRUDED PROFILES: AN OVERVIEW	9
2.1 PRELIMINARY CONSIDERATIONS	9
2.2 CONSTITUENT MATERIALS	10
2.3 MANUFACTURING PROCESS.....	12
2.4 STRUCTURAL SHAPES	13
2.5 PHYSICAL AND MECHANICAL PROPERTIES	14
2.6 TYPES OF ANALYSES.....	16
2.7 HYBRIDIZATION.....	17
2.8 PULTRUDED CONNECTIONS	18
2.9 CIVIL ENGINEERING APPLICATIONS	19

2.10	MAIN RESEARCH NEEDS	21
2.11	CONCLUDING REMARKS	22

CHAPTER 3

STRUCTURAL BEHAVIOUR OF ECCENTRICALLY LOADED GFRP COLUMNS..... 23

3.1	PRELIMINARY CONSIDERATIONS	23
3.2	TEST PROGRAMME.....	25
3.2.1	Materials.....	25
3.2.2	Experimental series	25
3.2.3	Test setup, instrumentation and procedure.....	27
3.3	RESULTS AND DISCUSSION	30
3.3.1	Load vs. axial shortening behaviour.....	30
3.3.2	Stress vs. strain behaviour and elastic modulus estimation	32
3.3.3	Failure modes	34
3.3.4	Buckling loads (series NBC and BC).....	35
3.4	NUMERICAL STUDY	38
3.4.1	Objectives.....	38
3.4.2	Numerical models.....	38
3.4.3	Elastic buckling analysis	40
3.4.4	Nonlinear analysis	41
3.5	CONCLUDING REMARKS	44

CHAPTER 4

STRUCTURAL BEHAVIOUR OF HYBRID FRP COLUMNS..... 47

4.1	PRELIMINARY CONSIDERATIONS	47
4.2	EXPERIMENTAL STUDY.....	50
4.2.1	Objectives.....	50
4.2.2	Experimental series	51
4.2.3	Material characterisation tests	53
4.2.4	Test setup and instrumentation.....	54
4.3	EXPERIMENTAL RESULTS	56
4.3.1	Load vs. axial displacement behaviour.....	56
4.3.2	Axial stress vs. strain behaviour	61
4.3.3	Buckling behaviour	64
4.3.4	Failure modes	68
4.4	DESCRIPTION OF THE NUMERICAL MODELS.....	70

4.4.1	Finite element models	71
4.4.2	Failure criteria	74
4.4.3	Damage model.....	75
4.5	NUMERICAL RESULTS, ASSESSMENT AND DISCUSSION	78
4.5.1	Linear buckling behaviour.....	78
4.5.2	Damaged vs. undamaged column behaviour	81
4.5.3	Progressive failure behaviour of columns	84
4.6	ASSESSMENT OF DESIGN STANDARDS	92
4.7	CONCLUDING REMARKS	99
 CHAPTER 5		
STRUCTURAL BEHAVIOUR OF LATERALLY BRACED HYBRID FRP BEAMS.....		101
5.1	PRELIMINARY CONSIDERATIONS	101
5.2	EXPERIMENTAL STUDY	103
5.2.1	Objectives and experimental program.....	103
5.2.2	Experimental series and mechanical characterisation tests	103
5.2.3	Flexural tests - setup, instrumentation and procedure	104
5.3	EXPERIMENTAL RESULTS	106
5.3.1	Load vs. deflection behaviour.....	106
5.3.2	Load vs. strain behaviour.....	108
5.3.3	Failure modes	110
5.4	DESCRIPTION OF THE NUMERICAL MODELS.....	110
5.5	NUMERICAL RESULTS, VALIDATION AND DISCUSSION	113
5.5.1	Linear buckling behaviour.....	114
5.5.2	Progressive failure behaviour	115
5.6	ASSESSMENT OF DESIGN STANDARDS	121
5.7	CONCLUDING REMARKS	125
 CHAPTER 6		
PROGRESSIVE FAILURE OF THE WEB-CRIPPLING PHENOMENON.....		127
6.1	PRELIMINARY CONSIDERATIONS	127
6.2	SUMMARY OF PREVIOUS EXPERIMENTS.....	129
6.3	FINITE ELEMENT MODEL.....	131
6.4	PRELIMINARY ANALYSES AND REFERENCE MODEL.....	133
6.5	MODEL ASSESSMENT	135
6.6	MODEL SENSITIVITY	139

6.6.1	Strength parameters: transverse compression and in-plane shear	139
6.6.2	Fracture energy	142
6.6.3	Web-flange rounded corner	144
6.7	CONCLUDING REMARKS	145
 CHAPTER 7		
CONCLUSIONS AND FUTURE DEVELOPMENTS		
147		
7.1	CONCLUSIONS.....	147
7.1.1	Small eccentricity effects in columns.....	148
7.1.2	Hybridization effects in columns and beams.....	149
7.1.3	Web-crippling effects in beams	150
7.2	FUTURE DEVELOPMENTS	150
 References		
153		

LIST OF FIGURES

Figure 2.1: Types of fibre mats: (a) randomly disposed, (b) 0/90 bidirectional weaves, (c) bidirectional weaves and randomly disposed fibres and (d) 0/90/±45 aligned and randomly disposed fibres.....	11
Figure 2.2: Typical fibre architecture of GFRP pultruded profiles.	11
Figure 2.3: Pultrusion process schematic illustration.....	13
Figure 2.4: Conventional structural shapes of FRP pultruded profiles.	13
Figure 2.5: Lerida pedestrian bridge.	14
Figure 2.6: Examples of pultruded multicellular deck panels: (a) EZSpan (Atlantic Research), (b) Superdeck (Creative Pultrusions), (c) DuraSpan (Martin Marietta Materials) and (d) square tube and plate deck (Strongwell).	14
Figure 2.7: Scheme of a bridge deck system.....	15
Figure 2.8: Different types of analyses according to the structure level.	16
Figure 2.9: RVE examples using a square or hexagonal array.....	17
Figure 2.10: Transverse section of Route 601 bridge.....	18
Figure 2.11: Eyecatcher bulding in Switzerland.	19
Figure 2.12: Pontresina pedestrian bridge in Switzerland.....	20
Figure 2.13: GFRP pultruded profiles used in the rehabilitation of a timber floor.	20
Figure 3.1: I-section kern and definition of concentric and eccentric levels I and II of applied load. ..	26
Figure 3.2: Test setup for (a) series NBC, (b) series BC, and (c) series EBCI and EBCII (units in mm).	27
Figure 3.3: (a) Spherical hinge with a Teflon sheet and (b) steel plates for axial shortening measurement.....	29

Figure 3.4: (a) Steel bars used to prevent lateral deflections and (b) bottom end with cylindrical hinge.	29
Figure 3.5: Load vs. axial shortening curves: (a) series NBC, (b) series BC, (c) series EBCI and (d) EBCII.	30
Figure 3.6: Load vs. axial shortening curves of representative specimens from series BC, EBCI and EBCII (comparison)	31
Figure 3.7: Load vs. eccentricity – ultimate load (experimental, average \pm standard deviation) and initial failure and critical loads (numerical).	31
Figure 3.8: Experimental (representative) and numerical axial stress vs. strain curves of series: (a) BC (specimen BC_3), (b) EBCI (EBCI_1) and (c) EBCII (EBCII_1).	33
Figure 3.9: Global buckling in series NBC.	34
Figure 3.10: Failure mode in series BC: (a) buckled shape of the I-section profile tested; (b) failure mode with web–flange separation and material crushing.	35
Figure 3.11: Failure mode in specimens of series EBCI and EBCII.	35
Figure 3.12: Shapes of the most relevant GBT deformation modes.	40
Figure 3.13: Buckled shape of the first buckling mode: (a) series NBC, (b) series BC, (c) series EBCI and (d) series EBCII (ABAQUS)	41
Figure 3.14: Buckled shape of the first buckling mode: (a) series NBC, (b) series BC, (c) series EBCI and (d) series EBCII (GBTUL).	41
Figure 3.15: Tsai–Hill failure index vs. relative longitudinal and shear stresses curves: (a) series NBC, (b) series BC, (c) series EBCI and (d) series ECBII.	44
Figure 4.1: Reference GFRP (S0) and hybrid C-GFRP (S1 to S5) pultruded experimental series.	53
Figure 4.2: Test setup and instrumentation for (a) short, (b) intermediate and (c) long columns; (d) end support system; (e) bonded angle piece and transducer; (f) position of strain gauges.	55
Figure 4.3: Short columns representative (a) load vs. displacement curves for series S0 (specimen 60_S0_2) and (b) load vs. axial shortening curves for all series.	57

Figure 4.4: Intermediate columns representative (a) load vs. displacement curves for series S0 (specimen 100_S0_2) and (b) load vs. axial shortening curves for all series..... 57

Figure 4.5: Long columns representative (a) load vs. displacement curves of series S0 (specimen 200_S0_2) and (b) load vs. axial shortening curves for all series. 58

Figure 4.6: Percentage variation of ultimate load of the hybrid series compared to the reference profile for short and intermediate columns. 60

Figure 4.7: Axial stress vs. strain curves of short column specimens (a) 60_S1_1, (b) 60_S3_2, and (c) 60_S4_1..... 61

Figure 4.8: Axial stress vs. strain curves of intermediate column specimens (a) 100_S0_2, and (b) 100_S3_2..... 62

Figure 4.9: Axial stress vs. strain curves of long column specimens (a) 200_S0_2, and (b) 200_S4_1. 63

Figure 4.10: Percentage variation of the full section longitudinal elastic modulus under compression of the hybrid series compared to the reference profile (stress-strain data). 63

Figure 4.11: Application of the Southwell plot method for long column specimen 200_S0_2: (a) load vs. mid height deflection curve, and (b) δ_L/P vs. δ_L curve. 65

Figure 4.12: Illustration of the procedure to determine the data range to be used in the critical buckling load calculation (specimen 60_S1_3)..... 67

Figure 4.13: Application of the modified Southwell method to short column specimen 60_S1_3: (a) trend line of the P vs. s^2 curve in the selected range, and (b) lateral deflection δ_{L2} and corresponding quadratic fit. 67

Figure 4.14: Percentage variation of buckling load of the hybrid series compared to the reference profile for short, intermediate and long columns. 68

Figure 4.15: Comparison of average experimental critical loads for all series and column lengths. 68

Figure 4.16: Typical failure mode of short columns: (a) undeformed shape, (b) buckled shape, and (c) failure mode..... 69

Figure 4.17: Typical failure mode of intermediate columns: (a) undeformed shape, (b) buckled shape, and (c) failure mode. 70

Figure 4.18: Typical limit state of long columns: (a) undeformed shape, and (b) deformed shape.	70
Figure 4.19: Finite element model and mesh (short columns).	72
Figure 4.20: Damage variable as a function of equivalent displacement.	77
Figure 4.21: Equivalent stress vs. equivalent displacement.	77
Figure 4.22: First mode linear critical buckling load comparison for each series and column length. .	79
Figure 4.23: Deformed shape of the lowest buckling modes for (a) short, (b) intermediate, and (c) long columns.	80
Figure 4.24: Load vs. lateral deflection curves obtained from the undamaged and damaged column analyses: (a) short columns and (b) intermediate columns (series S0).....	83
Figure 4.25: Percentage difference between the ultimate experimental loads and failure loads for short and intermediate columns using different failure criteria (series S0).....	83
Figure 4.26: Load vs. axial shortening curves (numerical and experimental) of series S0 for (a) short, (b) intermediate and (c) long columns.....	85
Figure 4.27: Load vs. axial shortening curves (numerical and experimental) of series S3 for (a) short, (b) intermediate and (c) long columns.....	85
Figure 4.28: Percentage variation of critical loads (relative to reference S0) with column series and lengths (numerical analysis).....	87
Figure 4.29: Percentage variation of ultimate loads (relative to reference S0) with column series and lengths (numerical analysis).....	87
Figure 4.30: Stress vs. axial strain curves (numerical and experimental) of series S0 for (a) short, (b) intermediate and (c) long columns.	90
Figure 4.31: Stress vs. axial strain curves (numerical and experimental) of series S3 for (a) short, (b) intermediate and (c) long columns.	90
Figure 4.32: Pattern of delamination onset for (a) short, (b) intermediate and (c) long columns (series S3).	91
Figure 4.33: Delamination state in the onset of failure for (a) short and (b) intermediate columns (series S3).....	91

Figure 4.34: Pattern of damaged zones at the onset of failure of (a) short columns ($\Delta L = 2.91$ mm) and (b) intermediate columns ($\Delta L = 4.28$ mm) – reference series S0.....	91
Figure 4.35: Pattern of damaged zones in failure mode of (a) short columns ($\Delta L = 5.0$ mm) and (b) intermediate columns ($\Delta L = 5.23$ mm) – reference series S0.	92
Figure 4.36: Experimental post-failure shape of (a) short and (b) intermediate columns.	92
Figure 4.37: Column design curves from Italian guidelines, ASCE pre-standard and Bank’s approach, and comparison with experimental and numerical results (series S0).....	98
Figure 5.1: Reference GFRP (S0) and hybrid C-GFRP (S1 to S5) pultruded experimental series.	104
Figure 5.2: Setup used in four-point bending tests.....	105
Figure 5.3: Lateral bracing system: (a) RHS bars attached to the framework and (b) SHS bars welded to the supports.	106
Figure 5.4: Load vs. mid-span deflection curves for representative specimens of all series.	107
Figure 5.5: Relative difference between the average ultimate loads of the different hybrid series compared to reference series S0.	108
Figure 5.6: Load vs. strain curve of (a) specimen S0_1 and (b) specimen S3_1 (the circumferences (○) indicate the instant when strains stopped being measured).....	108
Figure 5.7: Load vs. squared strain gradient of specimen S0_1: application of modified Southwell plot method.....	109
Figure 5.8: Failure modes: (a) at one section of the loaded span (specimen S0_1) and (b) at one loaded section (specimen S0_2).....	110
Figure 5.9: Finite element model and mesh.	112
Figure 5.10: Deformed shapes of the main numerical buckling modes.	114
Figure 5.11: Numerical and experimental load vs. mid-span deflection curve for series S0.	115
Figure 5.12: Numerical and experimental load vs. mid-span deflection curve for series S3.	115
Figure 5.13: Numerical load vs. mid-span deflection curves comparison.	116

Figure 5.14: Numerical and experimental load vs. strain curves of series S0 (the circumferences (○) indicate the instant when strains stopped being measured).....	117
Figure 5.15: Numerical and experimental load vs. strain curves of series S3 (the circumferences (○) indicate the instant when strains stopped being measured).....	117
Figure 5.16: Shear stresses for series S0 (a) in the brink of failure and (b) after collapse (in MPa, according to colour scale).....	118
Figure 5.17: Hashin matrix compression index for series S0 (a) in the brink of failure and (b) after collapse.....	118
Figure 5.18: Matrix compression damage for series S0 (a) in the brink of failure and (b) after collapse.	119
Figure 5.19: Numerical failure mode of series S4*: (a) longitudinal delamination of the CF mats (F = 48.5 kN); (b) transverse delamination of the CF mats (F = 79.7 kN); (c) web-flange junction failure at the GFRP layer (F = 83.7 kN); and (d) matrix compressive damage and shear envelope in the brink of failure (colour scale of the damage variable for all figures: blue – 0.0 – to red – 1.0).	120
Figure 6.1: EOF, IOF, ETF and ITF load configurations for the study of the web-crippling phenomenon.	127
Figure 6.2: Experimental (E) and numerical (N) load-displacement curves for GFRP pultruded sections under ETF loading: (a) I100, (b) I120, (c) I200 and (d) I400.....	130
Figure 6.3: Experimental (E) and numerical (N) load-displacement curves for GFRP pultruded sections under ITF loading: (a) I100, (b) I120, (c) I200 and (d) I400.....	130
Figure 6.4: Whole meshed model.....	132
Figure 6.5: Load vs. displacement curves of the three tested meshes with different viscous regularization coefficients: (a) $\eta = 1 \times 10^{-7}$, (b) $\eta = 1 \times 10^{-5}$, (c) $\eta = 1 \times 10^{-4}$ and (d) $\eta = 1 \times 10^{-3}$	134
Figure 6.6: Load vs. displacement curves for the ETF configuration.	136
Figure 6.7: Load vs. displacement curves for the ITF configuration.	136
Figure 6.8: Transverse compressive stress fields at the onset of failure: (a) ETF_15, (b) ETF_50, (c), ETF_100, (d) ITF_15, (e) ITF_50 and (f) ITF_100.	137

Figure 6.9: Shear stress fields at the onset of failure: (a) ETF_15, (b) ETF_50, (c), ETF_100, (d) ITF_15, (e) ITF_50 and (f) ITF_100..... 137

Figure 6.10: Matrix compression damaged areas at the onset of failure: (a) ETF_15, (b) ETF_50, (c), ETF_100, (d) ITF_15, (e) ITF_50 and (f) ITF_100..... 137

Figure 6.11: ITF_100 profile on the brink of collapsing: (a) compressive stress, (b) shear stress and (c) matrix compression damaged areas..... 138

Figure 6.12: ITF_100 profile on the after collapsing: (a) compressive stress, (b) shear stress and (c) matrix compression damaged areas..... 138

Figure 6.13: Influence of the variation of $S_{2,c}$ for series ETF_50: (a) load vs. displacement curves, and (b) initial failure load and ultimate load variation..... 140

Figure 6.14: Influence of the variation of $S_{2,c}$ for series ITF_50: (a) load vs. displacement curves, and (b) initial failure load and ultimate load variation..... 140

Figure 6.15: Influence of the variation of S_{12} for series ETF_50: (a) load vs. displacement curves, and (b) initial failure load and ultimate load variation..... 141

Figure 6.16: Influence of the variation of S_{12} for series ITF_50: (a) load vs. displacement curves, and (b) initial failure load and ultimate load variation..... 141

Figure 6.17: Influence of the variation of G_{mc} for series ETF_50: (a) load vs. displacement curves, and (b) ultimate load variation..... 143

Figure 6.18: Influence of the variation of G_{mc} for series ITF_50: (a) load vs. displacement curves, and (b) ultimate load variation..... 143

Figure 6.19: Matrix compression damaged zones for the ETF_50 using different G_{mc} values: (a) reference – 0.948 N/mm – (b) 10 times higher – 9.48 N/mm – and (c) 50 times higher – 47.4 N/mm. 143

Figure 6.20: Approximated geometry of web-flange rounded corner using continuum shell elements. 144

Figure 6.21: Load vs. displacement curves of the numerical models with (w/) and without (w/o) considering the web-flange junction radius (WFJR): (a) ETF_50 and (b) ITF_50..... 145

LIST OF TABLES

Table 2.1: Advantages of FRP pultruded profiles over conventional construction materials.	9
Table 2.2: Main fibre reinforcement mechanical and physical properties.	11
Table 2.3: Main mechanical properties reported by manufacturers.	15
Table 2.4: Main physical properties reported by manufacturers.	16
Table 3.1: Mechanical properties and input data for numerical models.	25
Table 3.2: Test series of eccentrically loaded columns.	26
Table 3.3: Boundary conditions adopted in the experimental campaign and numerical models (axes in Figure 3.2).	27
Table 3.4: Summary of experimental results, critical loads obtained in both numerical analyses and deformation mode (cf. Figure 3.12, page 40) participation obtained in the GBT analysis.	32
Table 3.5: Initial failure loads (P_1) and respective axial shortening obtained in the ABAQUS nonlinear analysis; comparison with the elastic buckling load.	42
Table 4.1: Elastic properties of GFRP and C-GFRP laminates.	54
Table 4.2: Strength properties of GFRP laminate and C-GFRP laminae.	54
Table 4.3: Summary of experimental results (average \pm standard deviation*).	59
Table 4.4: Total number of elements and nodes in the model of each column.	72
Table 4.5: Elastic properties of composite materials.	73
Table 4.6: Strength properties of composite materials.	73
Table 4.7: Fracture energy associated to each failure mode and material.	78
Table 4.8: Critical load values for short, intermediate and long columns of different series (Δ is the relative difference w.r.t. the S0 columns).	79

Table 4.9: Initial imperfection amplitudes for nonlinear analyses.	82
Table 4.10: Initial and ultimate failure loads of short and intermediate columns using different numerical analyses (failure criteria) and experimental tests (series S0).	82
Table 4.11: Critical loads and ultimate loads obtained from numerical analyses and experimental tests (for comparison) for all column series and lengths.....	86
Table 4.12: Critical (ultimate) loads obtained from three different design approaches.	98
Table 5.1: Elastic properties of GFRP and C-GFRP laminates.....	103
Table 5.2: Strength properties of GFRP laminate and C-GFRP laminae.....	103
Table 5.3: Average bending stiffness (K), ultimate load (P_u), ultimate bending moment (M_u), and ultimate shear stress ($\tau_{LT,u}$).	107
Table 5.4: Elastic properties of the different composite materials.	112
Table 5.5: Strength properties of the different composite materials.	113
Table 5.6: Global ($P_{bk,g}$) and local ($P_{bk,l}$) buckling loads obtained from numerical analyses.	114
Table 5.7: Numerical bending stiffness (K_{num}) and ultimate loads ($P_{u,num}$) and comparison with reference series (S0) and experimental data.....	116
Table 5.8: Analytical predictions, experimental and numerical ultimate load results.....	124
Table 6.1: Elastic and strength properties adopted in the numerical models.	132
Table 6.2: Adopted values for fracture energies.	132
Table 6.3: FE mesh convergence analysis.....	133
Table 6.4: Comparison between numerical and experimental ultimate loads.....	136

NOTATION

Roman

A	Cross-section area
$A-B-D$	Tensile, coupling and flexural rigidity matrix
A_g	Gross cross-section area
A_v	Shear area
A_{web}	Web area
A_z	Cross-section area
a	Half-wave length
b_f	Flange width
b_{sg}	Distance between two strain gauges positioned in the same flange
c	Coefficient accounting for the local-global buckling interaction
C_d	Damaged elasticity matrix
d	Damage variable
d_f	Fibre damage variable
D_i	Displacement transducer ($i = 1$ to 5)
$D_L; D_{11}$	Flexural plate rigidity in the longitudinal direction
$D_{LT}; D_{12}$	Coupling flexural plate rigidity
d_m	Matrix damage variable
d_s	Shear damage variable
$D_S; D_{66}$	Shear plate rigidity
$D_T; D_{22}$	Flexural plate rigidity in the transverse direction
d_w	Web depth
e	Eccentricity level
E	Young's modulus
$E_{fs,c}$	Full-section longitudinal elastic modulus
$E_{fs,c,sg}$	Full-section longitudinal elastic modulus under compression computed using data from the strain gauges
$E_{fs,c,transd}$	Full-section longitudinal elastic modulus under compression computed using data from the displacement transducers
e_i	Strain gauges ($i = 1$ to 4)
$E_{i,p}$	Elastic modulus in direction i and plate p
EI_{eq}	Equivalent flexural stiffness

E_L, E_1	Longitudinal elastic modulus
$E_{L,c}$	Longitudinal elastic modulus under compression
$E_{L,t}$	Longitudinal elastic modulus under tension
E_{sg}	Longitudinal elastic modulus measured in strain gauges
E_T, E_2	Transverse elastic modulus
$E_{T,c}$	Transverse elastic modulus under compression
E_{transd}	Longitudinal elastic modulus measured in displacement transducers
f_c	Longitudinal compressive strength
f_{cr}	Critical stress
F_{crf}	Flange local buckling stress
F_{crw}	Web local buckling stress
F_{crx}	Buckling stress about the weak x-axis
F_{cry}	Buckling stress about the strong y-axis
$F_{f,c}$	Fibre compression index
$F_{f,t}$	Fibre tension index
f_l	Local buckling stress
$F_{L,comp}$	Material compressive strength in the fibre direction
$F_{m,c}$	Matrix compression index
$F_{m,t}$	Matrix tension index
F^{sbs}	Short-beam strength
G, G_{LT}, G_{12}	Shear modulus
G_f	Fracture energy
G_{fc}	Fibre compression fracture energy
G_{ft}	Fibre tension fracture energy
G_{mc}	Matrix compression fracture energy
G_{mt}	Matrix tension fracture energy
h	Web height
I_F	Failure index
I_h	Homogeneized moment of inertia
I_{min}	Moment of inertia about the minor axis
I_x	Moment of inertia about the x axis
K	Axial stiffness
\tilde{k}	Torsional stiffness given by the web
K_c	Axial stiffness under compression
k_c	Coefficient accounting for the web boundary conditions
K_{exp}	Experimental stiffness
K_i	Effective buckling length factor in direction i

k_{I-web}	Spring constant
K_{num}	Numerical stiffness
k_r	Rotational stiffness
L	Column length
L_{bk}	Buckling length
L_c	Finite element characteristic length
M	Bending moment; damage operator
M_{Rd}	Design bending moment
M_{Rd1}	Design bending moment due to material failure
M_{Rd2}	Design bending moment due to local buckling of the compressed flange
M_{Sd}	Bending moment
M_u	Ultimate bending moment
n	Mesh number
$N_{c,Italia}$	Italian guidelines analytical ultimate load prediction
$N_{c,Rd}$	Ultimate load
$N_{c,Rd1}$	Compressive squash load (accounting for material strength)
$N_{c,Rd2}$	Critical load (accounting for instability effects)
N_E	Flexural (Euler) buckling load
$N_{l,Rd}$	Local buckling load
N_{pl}	Axial plastic load of the steel column
P	Applied load
$P^{(2)}$	Post-critical path curvature in the modified Southwell plot
P_I	Initial failure load
P_{bk}	Critical buckling load
$P_{bk,Global}; P_{bk,g}$	Global buckling critical load
$P_{bk,lin}$	Linear eigenvalue buckling load
$P_{bk,Local}; P_{bk,l}$	Local buckling critical load
$P_{bk,num}$	Numerical buckling load
P_{comp}	Compressive squash load
P_{cr}	Critical buckling load
$P_{cr,Bank}$	Bank's approach analytical ultimate load prediction
P_{Euler}	Euler buckling load
$P_{if,MS}$	Maximum stress initial failure load
$P_{if,TH}$	Tsai-Hill initial failure load
P_l	Local buckling critical load
P_{lim}	Limit load corresponding to bucklin plateau
P_{max}	Maximum (peak) load

P_{min}	Minimum load considered
P_u	Ultimate load
$P_{u,American}; P_{u,Am}$	American pre-standard analytical ultimate load prediction
$P_{u,exp}$	Experimental ultimate load
$P_{u,H}$	Hashin ultimate load
$P_{u,It}$	Italian guidelines analytical ultimate load prediction
$P_{u,num}$	Numerical ultimate load
$P-\delta$	Second-order bowing effects
R^2	Correlation factor
r_i	Cross-section radius of gyration in direction i
s	Perturbation parameter for the modified Southwell plot method
S_{12}	Longitudinal shear strength
S_{23}	Transverse shear strength
$S_{c,1}$	Longitudinal compressive strength
$S_{c,2}$	Transverse compressive strength
S_i	Strain gauges (i = 1 to 4); series (i = 0 to 5)
$S_{t,1}$	Longitudinal tensile strength
$S_{t,2}$	Transverse tensile strength
t	Thickness; time step
t_f	Flange thickness
T_g	Glass transition temperature
t_w	Web thickness
V	Fibre volume
V_{Rd}	Ultimate shear force
V_{Sd}	Maximum shear force
W	Section modulus
x, y, z	Reference axes
y	Distance from the neutral axis to the outermost fibre

Greek

α	Thermal expansion coefficient; parameter that accounts for the contribution of shear stress to the Hashin fibre tension index; imperfection factor
γ_f	Safety factor
δ	Deflection
Δ	Perturbation parameter for the Southwell plot method; variation
δ_0	Initial imperfection of the strut

$\delta_{0,eq}$	Initial damage equivalent displacement
$\delta_{f,eq}$	Full damage strain equivalent displacement
δ_i	Displacement transducer (i = 1 to 4)
Δ_I	Eccentricity level II
Δ_{II}	Eccentricity level II
ΔL	Axial shortening
δL_i	Lateral displacement transducer (i = 1 to 2); lateral section deflection (i = 1 to 2)
δ_{ms}	Midspan deflection
ε	Strain
ε^0	Initial damage strain
ε_{bend}	Bending strain
ε^f	Full damage strain
ε_i	Strain measured in each strain gauge (i=1 to 4)
η	Viscous regularization coefficient
λ	Column slenderness
ν, ν_{12}, ν_{LT}	Poisson ratio
ξ	Factor that accounts for the flanges' restriction
ρ	Mass density
σ	Stress/strength
$\hat{\sigma}$	Effective stress tensor
$\sigma_{cr,local,I-web}$	Local buckling critical stress considering the elastic restriction provided by the flanges to the web
σ_f	Flange buckling stress
σ_L, σ_1	Longitudinal stress
$\sigma_{L,c}$	Longitudinal compressive strength
$\sigma_{L,t}$	Longitudinal tensile strength
$\sigma_{ss,free}$	Critical buckling stress of a simply supported/free plate
$\sigma_{ss,ss}$	Critical buckling stress of a simply supported/simply supported plate
σ_T, σ_2	Transverse stress
$\sigma_{T,c}$	Transverse compressive strength
$\sigma_{T,t}$	Transverse tensile strength
$\sigma_{u,T}$	Transverse strength
$\sigma_{u,L}$	Longitudinal strength
σ_w	Web buckling stress
$\sigma_{w,eff}$	Effective web buckling stress
$\tau; \tau_{LT}; \tau_{12}$	Shear stress/strength
$\tau_{u,LT}; \tau_u$	Shear strength

χ	Local buckling reduction factor
Φ	Auxiliary coefficient

Acronyms

BC	Braced columns
CF	Carbon fibres
CFRP	Carbon fibre reinforced polymer
C-GFRP	Hybrid carbon and glass fibre reinforced polymer
CLT	Classical laminate theory
EBCI	Eccentrically loaded braced columns (Level I)
EBCII	Eccentrically loaded braced columns (Level II)
EOF	End one flange
ETF	End two flange
FE	Finite elements
FEM	Finite element method
FRP	Fibre reinforced polymer
GBT	Generalised beam theory
GF	Glass fibres
GFRP	Glass fibre reinforced polymer
IOF	Internal one flange
IST	Instituto Superior Técnico
ITF	Internal two flange
LRFD	Load and Resistance Factor Design
NBC	Non-braced columns
NF	Narrow flange (I-sections)
NLA	Nonlinear analysis
RC	Reinforced concrete
RHS	Rectangular hollow section
RIM	Resin infusion moulding
RTM	Resin transfer moulding
RVE	Representative volume element
SFE	Shell finite elements
SFRSCC	Steel fibre reinforced self-compacting concrete
SHS	Square hollow tubes
SM	Standard modulus

UHM	Ultra high modulus
UMAT	User-defined material
UV	Ultraviolet radiation
VARTM	Vacuum-assisted resin transfer moulding
WF	Wide flange (H-sections)
XFEM	Extended finite element method

CHAPTER 1

INTRODUCTION

1.1 OVERVIEW

A composite material is known to be a material that comprises two or more constituents, which when combined gather in it better properties than uncoupled. Reinforced concrete (RC) structures are one of the most wide used examples of a composite construction material as they merge the best properties of concrete – compressive strength, relatively low thermal conductivity, resistance to corrosion, low cost – with those of the steel rebars – tensile strength, ductile behaviour.

Fibre reinforced polymer (FRP) composites were first developed for aeronautic, aerospace and other mechanical engineering related applications. The main advantages of their use in these fields were the low self-weight, high strength and low fatigue. Regarding civil engineering, over the past few decades, the costs related to the maintenance and repair of traditional construction materials (such as RC and steel) have been raising considerably. Moreover, there is more and more demand for lighter, faster and more durable construction materials which require little maintenance or are fully maintenance-free. Hence, fibre reinforced polymer (FRP) structural members are showing to be a potential alternative to traditional construction materials for civil engineering applications [1].

FRP materials basically consist of a set of fibre filaments (generally glass, carbon or aramid) embedded in a polymeric resin (usually polyester, vinylester or epoxy). While the fibres provide the elastic and strength properties, the resin keeps the fibres in place, namely when the structural member is compressed, and spreads the stresses uniformly across the section [2,3]. There are several types of FRP composite materials for different civil engineering applications, namely laminates, sheets for confinement, rebars, pre-stress tendons, sandwich panels and pultruded profiles, the latter being the object of this thesis.

Pultruded sections were first developed based on the steel construction's know-how. Therefore, currently, the most common pultruded shapes being manufactured are still narrow-flange (I-) sections, wide-flange (WF) sections and square hollow section (SHS or simply tubes). Despite being adapted

from steel section's design, the pultruded shapes are usually thicker to account for the typical lower axial stiffness of FRP materials compared to steel.

Comparing with traditional construction materials, such as steel and RC structures, FRP pultruded profiles present several advantages that they share with other advanced composites, namely the low self-weight, high longitudinal strength, reduced maintenance requirements and electromagnetic transparency. However, the lack of consensual design codes, the low in-plane stiffness, the absence of ductility (quasi-brittle collapse) and the poor behaviour under elevated temperatures are some of the drawbacks that are still hindering the spread use of FRP pultruded structures in civil engineering applications [4–6].

Primarily, FRP pultruded profiles were mostly used as secondary (non-structural) members, such as stairs, benches, doors and gates. Currently, they are already being used as primary structures, namely in pedestrian bridge girders, old buildings' structural retrofitting and reinforcement and structures located in chemically aggressive environments (such as sewage treatment plants or offshore platforms) [7].

1.2 MOTIVATION

The work presented in this thesis pursued the author's M.Sc. dissertation [8], which addressed the short-term structural behaviour of FRP pultruded profiles [4,9]. Even though FRP pultruded profiles are offering a suitable alternative to steel profiles, especially when lightness and durability are important requirements, and despite their obvious potential as civil engineering structures, there are still several issues regarding FRP structures that remain less studied, present scarce information or lack validation (experimental, numerical and analytical). Even the main FRP design standards and guidelines [10–13], which are strongly based in steel construction, are either incomplete or not fully accurate in some of their formulations [14,15]. Being orthotropic, the stress-strain behaviour exhibited by FRP materials is much more complex than that of traditional isotropic materials and thus, in general, those formulations need to be duly adapted before being suitable for the design of FRP composites. Different materials require different types of analysis.

There are very few studies addressing the beam-column behaviour of FRP pultruded profiles, namely those related to small eccentricities that yield from member misalignment or other construction errors. In fact, the effect of small eccentricities applied to the axial loading of FRP pultruded columns is not yet comprehensively studied; the scientific community has rather focused on the behaviour of bending members with low compressive loads rather than on the response of compression members with small eccentricities [16,17].

Another of the most concerning aspects about the use of FRP pultruded profiles, particularly incorporating glass fibres (GFRP), is the low stiffness-to-strength ratio. Once again comparing to steel structures, GFRP pultruded members present roughly the same longitudinal strength and about six to seven times lower longitudinal elastic modulus. Moreover, and since the material is not isotropic, the shear-to-longitudinal modulus ratio is lower (roughly 10%). Hence, one ought to consider the profiles' shear deformability when performing serviceability limit states calculations. Therefore, the Timoshenko beam theory [18] should be used instead of the Euler-Bernoulli theory for profiles subjected to transverse loading configurations (beams and column-beams) as it accounts for the flexural and shear deformability to the overall deflection. The latter formulation neglects the effect of shear deformability, which is rather low for isotropic materials but can be quite significant in composites. The incorporation of carbon fibres (CF) in GFRP profiles has already proved to be effective, but besides being more expensive the delamination of those mats may present a relevant issue, leading to cross-section reduction and consequently to premature failure.

The low in-plane stiffness of pultruded profiles, particularly GFRP ones, makes them prone to buckling issues when compressed – both local and global buckling phenomena may arise depending on the cross-section and plate slenderness. Indeed, most often the structural design of pultruded members is governed by deformability or buckling issues, not allowing for the full exploitation of the material strength. Buckling phenomena in flexural and compressive members has already been studied by several authors, experimentally and numerically [17,19–26]. Despite that, the global buckling phenomenon of compression members is already fairly studied and there is a consensual approach to predict the corresponding ultimate limit states while the local buckling phenomenon is still difficult to evaluate for the practise oriented engineer. This is mostly due to the large amount of elastic data required to compute the critical load (often not reported by manufacturers) and also due to the differences in the approaches proposed by design guidelines, standards and different authors [10–13]. Moreover, the studies that have been carried so far by the FRP research community address mostly the structural behaviour of wide-flange (WF) sections (*e.g.* H-sections). When referring to other shapes, like narrow-flange (NF) sections (*e.g.* I-sections), the experimental data necessary to validate the analytical design formulas is still scarce.

The orthotropic behaviour that characterises pultruded composites leads to an additional issue related to the design of these structures. As the fibres are aligned mostly in the longitudinal direction of the structural member (rovings), the transverse direction is considerably less stiff [2]. Conventional GFRP pultruded profiles usually present a transverse Young's modulus of roughly a third of the corresponding modulus in the longitudinal direction. The same situation applies to the material strength, which is three to four times higher in the longitudinal direction. Such fact turns these profiles very prone to transverse concentrated loading in the web plane. This phenomenon is called web-

crippling. While some authors have already provided insights regarding the response of FRP structures [14,15,27–29], the information available still does not provide a comprehensive understanding of this complex phenomenon that may involve material crushing, web buckling or a combination thereof.

As already mentioned, the collapse of FRP pultruded profiles is usually brittle and involves high energy release. However, for some specific failure mechanisms, it may involve some energy dissipation, being often referred to as pseudo-ductile. Despite that fact has already been observed in experimental tests, there are very few studies that address the progressive failure of the FRP material by numerical means. In fact, the large amount of data required to perform a progressive damage analysis (generally not reported by manufacturers) prevents researchers and practitioners from obtaining further insights on this subject. Also, it should be noted that numerical models allowing for the simulation of brittle material failures are high demanding in terms of complexity and present many convergence issues, in opposition to ductile materials such as steel. The few numerical studies that addressed the progressive damage behaviour of FRP materials [24,30,31] still present very scarce information due to the complexity inherent to this type of numerical analysis and are mostly related to simpler planar structures subjected to uniform loading, such as tensile FRP plates. To the authors best knowledge, the analyses regarding the structural behaviour and collapse of more complex three-dimensional structures (like pultruded profiles) were not yet addressed.

There are also other research needs concerning the structural behaviour of FRP materials, such as the durability of these materials and of their bonded connections, the behaviour under elevated temperature and fire, the creep behaviour and others (discussed further in section 2.10).

1.3 OBJECTIVES AND METHODOLOGY

The main objective of the work presented in this thesis is to provide further insights on some of the matters discussed in section 1.2 namely: (i) the structural behaviour of GFRP pultruded columns subjected to eccentric compression within the section kern²; (ii) the hybridization of the GFRP profiles with CF mats and the evaluation of the structural behaviour presented by these hybrid C-GFRP pultruded prototypes under flexure (beams) or compression (columns); (iii) the progressive failure analysis of FRP structures using specific criteria in numerical models (the Hashin criterion and an appropriate damage progression model); and (iv) the analysis of the web-crippling phenomenon and the assessment of different failure criteria for this specific problem.

Regarding the methodology pursued, in all studies that are carried out in the framework of this thesis, one aims at obtaining comprehensive and significant experimental data allowing for the thorough

² The section kern is a geometrically limited zone in the plane of the cross-section of the profile. If a given force, either compressive or tensile, is applied in a point inside the kern, the longitudinal stresses acting on the entire cross-section are either compressive or tensile, *i.e.* the neutral axis does not intersect the cross-section.

evaluation of several behavioural aspects of FRP pultruded profiles: the load vs. deflection, the stress vs. strain, the buckling modes and the failure modes. The first step of the experimental analyses is always the determination of the material elastic and strength properties for given plane stress load configurations. Hence, several tests in small scale coupons were carried out according to the corresponding standard test methods to obtain these properties. Next, and before conducting any full scale tests, one defined an adequate test setup to measure the applied loads, displacements and strains at judiciously selected positions. Finally, the full scale tests were carried out, computing the loading path and the ultimate behaviour for the evaluation of the serviceability and failure responses.

Alongside the experimental campaign, numerical models were developed and later calibrated and validated using the experimental data obtained *a priori*. The commercial software ABAQUS by Simulia and the GBTUL generalised beam theory software were used for the development of the numerical models. Three different types of analyses were carried out depending on the study: (i) linear eigenvalue analysis, (ii) geometrically nonlinear and physically linear analysis, and (iii) progressive damage analysis, geometrically and physically nonlinear (using the Hashin progressive damage analysis available in ABAQUS). The former analysis allows for the determination of the critical buckling loads and corresponding mode shapes (which can be used as initial imperfection for the nonlinear analyses). Both nonlinear analyses aim at evaluating the ultimate behaviour exhibited by the FRP profiles with one difference: the physically linear analysis allows only for the determination of the initial failure load (when the adopted failure index reaches its limit – usually 1.0) while the progressive damage analysis allows for the determination of the effective ultimate failure load, as well as the evaluation of the collapsing path. The main drawbacks of using progressive failure analyses are the large amount of data required, namely the fracture energies (not always known and difficult to determine) and the viscous regularisation coefficients, and the fact that they are much more time and computational resource consuming.

The experimental and numerical results obtained from each analysis are compared whenever possible to analytical predictions available in the literature, hence allowing assessing the suitability of their use. This thesis thus underpins its scope of providing reliable data that will help developing more consensual design codes.

1.4 MAIN SCIENTIFIC CONTRIBUTIONS

The work presented in this thesis provided further insights on the structural behaviour of FRP pultruded columns and beams, regarding their serviceability and failure behaviours. The numerical analyses conducted using both ABAQUS and GBTUL presented a good fit to the experimental data. The results obtained are quite relevant, providing a deeper understanding regarding the structural

response of these profiles. In the following paragraphs the main scientific contributions of this thesis are summarised.

The study regarding the eccentric compressive loading of GFRP I-section columns (Chapter 3) showed that small eccentricities about the major axis and within the section kern are of major importance for the behaviour of GFRP pultruded members under compression, both in terms of stiffness and ultimate load. The ultimate load in particular showed to be highly dependent on geometrical imperfections, as the maximum tested eccentricity level (inside the kern) caused a very significant an ultimate load decrease. The numerical and analytical results on the buckling loads presented a good agreement with the experimental data.

With respect to the study on the structural behaviour of hybrid C-GFRP columns and beams (Chapter 4 and Chapter 5), several relevant aspects can be highlighted. Several hybrid series comprising carbon fibre (CF) reinforcement and different fibre architectures were designed, manufactured and tested. Columns with three different lengths and laterally beams were tested monotonically up to failure. The obtained results confirmed the hybridization effectiveness in improving the serviceability performance. However, the CF reinforcement did not seem to increase the overall load carrying capacity of the FRP members, with some hybrid specimens presenting ultimate loads lower than that exhibited by the reference profile. Although not visible to the naked eye, at some point delamination of the CF mats has most likely occurred as the stiffness was reduced for higher strain levels, both in hybrid beams and columns. Numerical finite element (FE) models carried out using ABAQUS accurately simulated the overall behaviour of both columns and beams. Despite its inherent complexity, the Hashin-based progressive failure analysis proved to be a very useful tool for the study of the delamination and failure behaviours of FRP pultruded profiles.

The web-crippling progressive damage study (Chapter 6) highlighted that the progressive damage analysis is suitable for the simulation of the structural behaviour of transversely compressed GFRP pultruded. The analysis of the stress fields and the parametric studies performed after the development of the preliminary models showed that the in-plane shear stresses govern the failure initiation, but the transverse compressive stresses govern the ultimate behaviour. The adopted fracture energy associated to the governing failure mode also has a major influence in the profiles' ultimate behaviour under transverse concentrated loads.

The work developed in the framework of this thesis yielded a total of eight papers, six already published in ISI-indexed journals and the other two submitted for publication:

- M.M. Correia, F. Nunes, J.R. Correia and N. Silvestre. Buckling behavior and failure of hybrid fiber-reinforced polymer pultruded short columns, *Journal of Composites for Construction*, 17 (2013) 463–475³;
- F. Nunes, M.M. Correia, J.R. Correia, N. Silvestre and A. Moreira, Experimental and numerical study on the structural behavior of eccentrically loaded GFRP columns, *Thin-Walled Structures*, 72 (2013) 175–187;
- L.A. Fernandes, J. Gonilha, J.R. Correia, N. Silvestre and F. Nunes, Web-crippling of GFRP pultruded profiles. Part 1: Experimental study, *Composite Structures*, 120 (2015) 565–577⁴;
- L.A. Fernandes, F. Nunes, N. Silvestre, J.R. Correia and J. Gonilha, Web-crippling of GFRP pultruded profiles. Part 2: Numerical analysis and design, *Composite Structures*, 120 (2015) 578–590⁴;
- F. Nunes, J.R. Correia and N. Silvestre, Structural behaviour of hybrid FRP pultruded columns. Part 1: Experimental study, *Composite Structures*, 139 (2016) 291–303;
- F. Nunes, N. Silvestre, J.R. Correia, Structural behaviour of hybrid FRP pultruded columns. Part 2: Numerical study, *Composite Structures*, 139 (2016) 304–319;
- F. Nunes, J.R. Correia, N. Silvestre, Structural behaviour of hybrid FRP pultruded beams: Experimental and numerical studies, *Thin-Walled Structures*, (accepted for publication);
- F. Nunes, N. Silvestre, J.R. Correia, Progressive damage analysis of web-crippling of GFRP pultruded I-sections, *Journal of Composites for Construction*, (submitted for publication).

1.5 DOCUMENT OUTLINE

This chapter presented an overview of the contents to be presented and discussed throughout this thesis, namely the general context, the motivation, the objectives and the methodology adopted for this research. The main scientific contributions are herein summarised and the document outline is presented.

Chapter 2 presents a brief overview concerning pultruded FRP members, addressing their constituent materials, manufacturing process, main properties and types of analysis. The effects of hybridization, the know-how regarding pultruded connections, the main civil engineering applications and research needs are also presented.

In Chapter 3, the structural behaviour of eccentrically loaded pultruded I-columns is addressed. Experimental tests up to failure were carried out in free and laterally braced simply supported GFRP columns subjected to different eccentric compression levels. The experimental data obtained in terms

³ Part of the analyses and results presented in this publication were performed in the framework of the M.Sc. dissertations of the author [8] and Correia [9].

⁴ These two publications were prepared in the frame of the M.Sc. dissertation of Fernandes [96], in which the author had a significant collaboration, both in the experiments [14] and in the numerical studies [15].

of (critical and ultimate) loads, displacements and strains is presented, discussed and compared with results from numerical models developed in both ABAQUS and using GBT. The numerical analyses' results using both approaches are also compared.

Chapter 4 and Chapter 5 present the work developed regarding the structural behaviour of hybrid C-GFRP columns and beams, respectively. An extensive experimental campaign was conducted aiming at determining the main advantages of introducing carbon fibres in GFRP profiles under four-point bending and under compression. The experimental data are supported by numerical analyses using the ABAQUS built-in progressive damage analysis and the results obtained are compared to the main design approaches available in the literature.

The web-crippling phenomenon is addressed in Chapter 6, in which numerical analyses using the ABAQUS progressive damage analysis were performed and the obtained results were compared with those reported by Fernandes *et al.* [14,15]. Parametric studies are also presented regarding the influence of the parameters that govern the failure behaviour, namely the material strengths and fracture energies.

Finally, Chapter 7 outlines the main conclusions and scientific achievements obtained from this thesis and provides recommendations for future developments.

CHAPTER 2

FRP PULTRUDED PROFILES: AN OVERVIEW

2.1 PRELIMINARY CONSIDERATIONS

Fibre reinforced polymer (FRP) pultruded profiles are finding increasing use in civil engineering structural applications. At first they were mainly used as secondary structures such as stairs, grids and handrails. Currently, due to their several advantages over traditional construction materials, pultruded profiles are being more and more used as primary structural members [2,7,32]. Table 2.1 highlights the main potential of FRP pultruded structures for various performance aspects, comparing them to other conventional structural materials that compete more directly with FRPs. Note that the stiffness of FRP profiles, not addressed in Table 2.1 but discussed ahead, is very much dependent on the type of fibre reinforcement.

Table 2.1: Advantages of FRP pultruded profiles over conventional construction materials [33].

Aspect	FRP	Steel	Aluminium	Wood
Corrosion resistance	High	Low	Moderate	Low
Strength	High	High	High	Low
Self-weight	Low	High	Low	Moderate
Electric conductivity	Low	High	High	Moderate
Thermal conductivity	Very low	High	High	Low
Electromagnetic transparency	Yes	No	No	Yes
Ease of processing	Easy	Easy	Difficult	Easy
Maintenance costs	Low	Moderate	Moderate	High
Environmental impact	Low	High	High	Low

Despite their multiple advantages and strong potential as structural members there are some drawbacks inherent to FRP pultruded profiles that are still hindering their spread use, namely the relatively high deformability and proneness to buckling when reinforced by glass fibres (the ones used more often), the poor behaviour under fire and at elevated temperature, the lack of consensual design codes and their brittle failure behaviour [2,7,32].

In the following sections, the main characteristics and general aspects of FRP pultruded members are briefly presented, namely: (i) the constituent materials, (ii) the manufacturing process, (iii) the available structural shapes, (iv) the physical and mechanical properties, (v) the types of analyses, (vi) hybridization, (vii) connections, and (viii) the main applications. Also the current main research needs for FRP pultruded members are briefly discussed.

2.2 CONSTITUENT MATERIALS

Composite FRP members comprise two main constituent materials: fibres and resin. While the fibres provide strength and stiffness along their direction, the polymeric resin provides support to the fibres maintaining them in the same position, distributing the stresses uniformly across the composite lamina and protecting them from the environmental agents. Other residual materials, such as fillers and additives may also be added to the resin matrix to improve the manufacturing process, to improve/change specific properties (*e.g.* colour requirements, fire reaction) or simply for cost reduction [2].

The fibre reinforcement most widely used in pultruded structures is made of glass (glass fibre reinforced polymer – GFRP). However, other types of fibre reinforcement (such as carbon fibres, CF) may also be used in some specific applications, mainly when higher stiffness is required.

E-glass (electric glass) fibres are the ones that are mostly used for the production of FRP pultruded profiles [2]. S-glass (structural glass) fibres are mainly limited to aerospace composites as they comprise high performance reinforcement, but they are also the most expensive glass fibres. All glass fibres present high electrical resistivity, namely when comparing to carbon fibres [2]. They are also the most economical reinforcement available in the market.

Carbon fibres are stiffer than glass fibres, but are also more expensive and electrically conductive [2]. There are several types of carbon fibres available in the market being the standard modulus (SM) ones the most commonly used. Ultra-high modulus (UHM) carbon fibres are considerably stiffer than the standard modulus [2].

The main properties presented by each type of fibre described above are shown in Table 2.2⁵. Fibres can be up to 70% in volume of the whole composite material [34]. When increasing the fibre volume, the elastic and strength properties will be higher (along their direction), but the composite self-weight and cost will increase accordingly.

⁵ In addition to the fibres listed in Table 2.2, aramid fibres have also been used in FRP composites, but they are relatively uncommon in civil engineering applications. More recently, basalt fibres are starting to be increasingly used [2,97,98].

Table 2.2: Main fibre reinforcement mechanical and physical properties [2].

Fibres	Mass volume (g/cm ³)	Young's modulus (GPa)	Strength (MPa)	Elongation at failure (-)
E-glass	2.57	72.5	3400	0.025
S-glass	2.47	88.0	4600	0.030
SM-carbon	1.70	250	3700	0.012
UHM-carbon	2.10	800	2400	0.020

Two different types of fibre reinforcement are used for manufacturing pultruded components: mats and rovings. Fibre mats can be oriented ($0^\circ/90^\circ$ and $\pm 45^\circ$) or randomly stranded (Figure 2.1). They provide the shear stiffness and strength to the composite lamina. Surfacing veils are a very thin randomly oriented mat used next to the surface of FRP pultruded profiles to create a superficial coating layer of resin. Rovings on the other hand consist of unidirectional continuous fibre filaments supplied in coils, which provide for almost all of the axial strength and stiffness of pultruded profiles. Figure 2.2 illustrates the typical fibre architecture (mats and rovings) exhibited by GFRP pultruded I-section profiles.

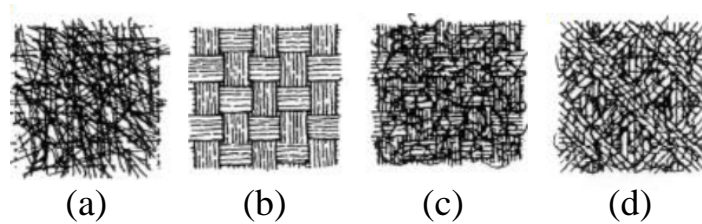


Figure 2.1: Types of fibre mats: (a) randomly disposed, (b) $0/90$ bidirectional weaves, (c) bidirectional weaves and randomly disposed fibres and (d) $0/90/\pm 45$ aligned and randomly disposed fibres [1].

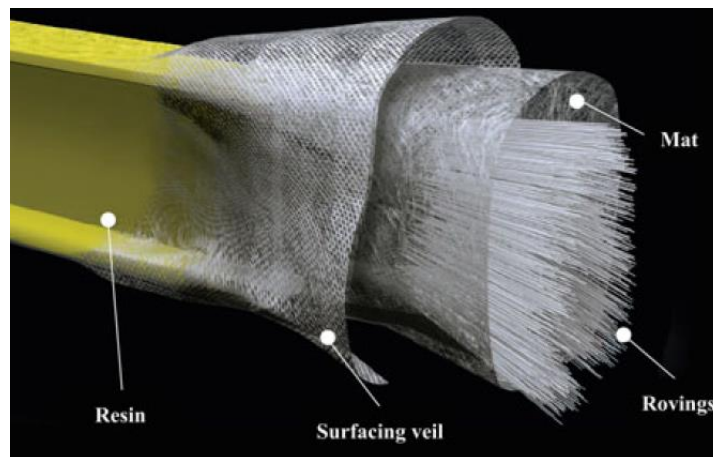


Figure 2.2: Typical fibre architecture of GFRP pultruded profiles [33].

The polymeric resins (or matrixes) more often used in the production of pultruded composites are polyester, vinylester and epoxy. Unsaturated polyester resins present a very cost-effective solution as they are the most economical, are easily processed and present reasonably good mechanical

properties [32]. Epoxy on the other hand is the most expensive polymeric matrix. It presents very high mechanical properties, durability and low shrinkage, namely when compared with polyester [2]. They are however more difficult to process due to their high viscosity and much more expensive, being mainly used in carbon fibre reinforced polymer (CFRP) composites. Vinylester is a hybrid resin made of polyester and epoxy and thus it combines the best properties of each of them [2]. It presents a reasonable balance between durability, mechanical properties, ease of processing and cost.

2.3 MANUFACTURING PROCESS

FRP composite materials can be produced by different manufacturing processes, which are selected depending on their configuration, geometry, fibre architecture and purpose. There are several processes for the production of single composite structural parts, such as hand layup, filament winding, resin transfer moulding (RTM), resin infusion moulding (RIM) and vacuum-assisted resin transfer moulding (VARTM).

Pultruded composite profiles with constant section are produced by a continuous process called pultrusion, in which the profiles are continuously manufactured and cut with the desired length (Figure 2.3). The pultrusion process and the first pultrusion machine (the Gladstruder) were developed in the early 1950s by Brandt Goldsworthy [2]. The machine comprises different stages described next:

- Resin impregnation – the fibres (rovings and mats) are pulled through the guide plates and are embedded in a resin tank.
- Shaping and curing die – the constituent materials (fibres and matrix) enter the shaping and curing die guided by more plates which shape the profile's cross-section. The resin is in a viscous state when entering the die and then it slowly cures due to the temperature gradient (90 to 180° depending on the type of resin).
- Pulling system – when outside the die, the profile is already solid and thus it can be pulled by the pulling system, which usually presents traction forces up to 200 kN. The profiles are produced at an average rate of 2 m/min (very much dependent on the shape and complexity of the cross-section).
- Cutting system – at the end of the manufacturing line, there is a moving cutting saw allowing for the production of profiles with any desired length.

Currently, there are already several tweaks being studied that can be added to the conventional pultrusion machine that allow manufacturing curved parts and also profiles with varying section, *i.e.* tapered members [2,35]. However, these are non-routine specifications that may significantly affect the cost of production.

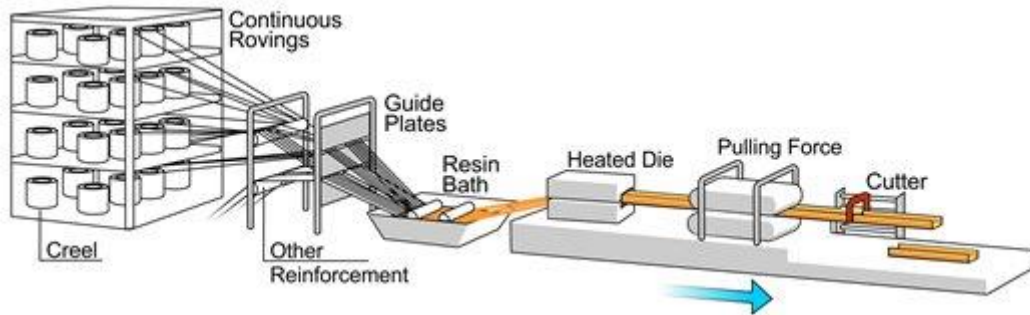


Figure 2.3: Pultrusion process schematic illustration [36].

2.4 STRUCTURAL SHAPES

The pultrusion process may yield several different types of structural members: rebars, pre-stress tendons, strips and structural profiles. Focusing on pultruded profiles, the so-called *first generation* shapes started being developed also in the 1950s (after the development of the pultrusion machine) and their structural sections initially mimicked those of steel profiles (thin-walled open sections) due to the vast know-how already available for those structures (Figure 2.4). Due to being very expensive at that time, from 1950s to 1970s pultruded profiles' niche market were buildings requiring electromagnetic transparency and chemical resistance. However, due to the fact that they can be produced with any length, they started being used as girders for pedestrian bridges (Figure 2.5).

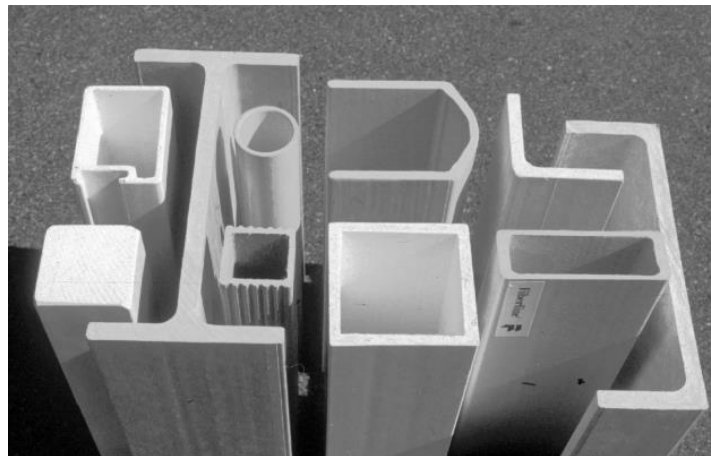


Figure 2.4: Conventional structural shapes of FRP pultruded profiles [37].

Due to their inherent sensitivity to buckling issues (both local and global phenomena may arise depending on their plate and global slenderness), the *second generation* of pultruded profiles were developed based on a simple structural principle: multicellular panels for floors and decks (Figure 2.6 and Figure 2.7). With multicellular (closed-form) panels both global and local buckling issues are mitigated. These FRP pultruded deck panels usually present lower depths than first generation profiles and thus they are more limited in terms of free span between supports. Transverse connections

between adjacent panels are generally performed by mechanical interlock and/or adhesive bonding [38].



Figure 2.5: Lerida pedestrian bridge [39].

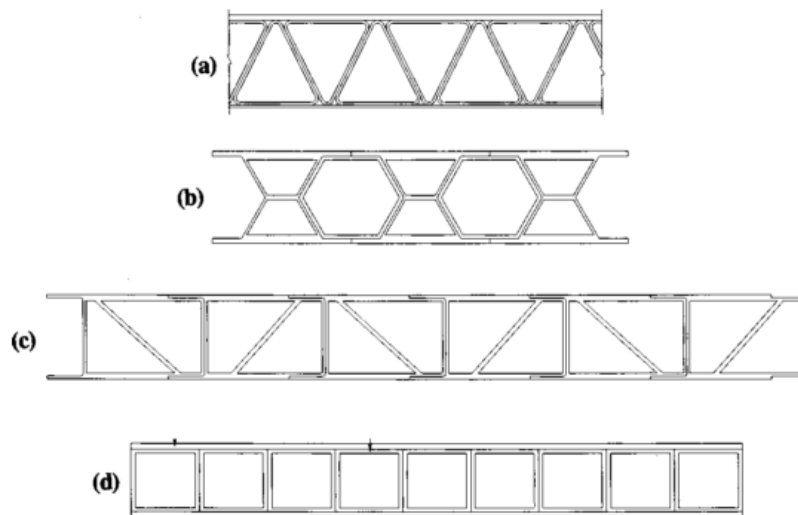


Figure 2.6: Examples of pultruded multicellular deck panels: (a) EZSpan (Atlantic Research), (b) Superdeck (Creative Pultrusions), (c) DuraSpan (Martin Marietta Materials) and (d) square tube and plate deck (Strongwell) [38].

2.5 PHYSICAL AND MECHANICAL PROPERTIES

The mechanical and physical properties of pultruded FRP members are very dependent on their constituent materials and fibre reinforcement volume. However, there are certain aspects that are common to all pultruded composites despite the type of fibres and resin used in their production. Since their fibres are aligned mostly in the direction in which they develop (one should remind that only the mats present fibres aligned in the transverse and shear directions), pultruded profiles are highly orthotropic. This is a major issue for practice oriented engineers as the structural design calculations

are far more complex and time-demanding when compared with an equivalent structure made of steel (which is isotropic). For instance, the transverse direction stiffness and strength are usually three to four times lower than in the longitudinal direction [14,15]. Such fact not only turns the profiles prone to transverse concentrated loads, but also affects the local buckling critical load (which is highly dependent on the transverse and shear stiffness).

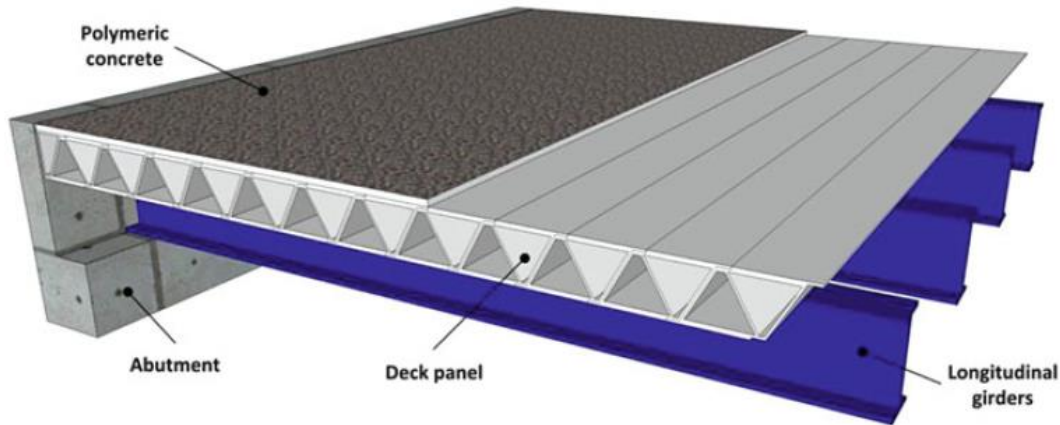


Figure 2.7: Scheme of a bridge deck system [3].

Other drawback concerning the use of FRP structures is their failure behaviour, which is characterised by being brittle and high energy releasing without any prior warning of failure. Table 2.3 and Table 2.4 present some of the properties reported by manufacturers for both GFRP pultruded profiles and CFRP strengthening strips. In these tables, E and G are the axial and shear moduli, ν is the Poisson ratio, σ and τ are the axial and shear stresses, ρ is the mass density, α is the thermal expansion coefficient and V is the fibre volume (subscripts L and T indicate longitudinal and transverse directions, respectively).

Table 2.3: Main mechanical properties reported by manufacturers [33,39–42].

Profile	E_L (GPa)	E_T (GPa)	G_{LT} (GPa)	ν	$\sigma_{u,L}$ (MPa)	$\sigma_{u,T}$ (MPa)	$\tau_{u,LT}$ (MPa)
ALTO – GFRP	20 – 28	n.a.	n.a.	n.a.	350 – 450	n.a.	n.a.
Fiberline – GFRP	23 – 28	8.5	3.0	0.23	240	50 – 100	25
Strongwell – GFRP	17 – 18	5.5	2.9	0.33	207	48 – 110	n.a.
S&P – CFRP strip	170 – 205	n.a.	n.a.	n.a.	2800	n.a.	n.a.
Zoltek – CFRP strip	130 – 140	n.a.	n.a.	n.a.	1400 – 2350	n.a.	n.a.

As seen in these tables, some of the properties required for the design of pultruded profiles are not always reported (*e.g.*, the shear modulus, G_{LT}). Such fact highlights why some practice oriented engineers struggle to accept pultruded profiles as a reliable alternative to other materials. The lack of information available, the differences from manufacturer to manufacturer and the wide range of design formulations made available by different authors and guidelines may be in fact hindering the widespread use of these structural members.

Table 2.4: Main physical properties reported by manufacturers [33,39–42].

Profile	ρ (g/cm ³)	α ($\times 10^{-6}$ K ⁻¹)	V (%)
ALTO – GFRP	1.8	11	60
Fiberline – GFRP	1.8	8-14	n.a.
Strongwell – GFRP	1.7 – 1.9	12	n.a.
S&P – CFRP strip	1.6	n.a.	68
Zoltek – CFRP strip	1.6	n.a.	65 – 75

2.6 TYPES OF ANALYSES

FRP structures might be analysed at four different scales (Figure 2.8): (i) micro – at the material (fibre and matrix) level and the interaction between both, (ii) lamina – considering a given fibre volume and orientation, (iii) laminate – considering a stack of laminae with different (or the same) orientations, thicknesses and reinforcement, and (iv) structure – considering the full section of the laminates and the full-section equivalent properties.

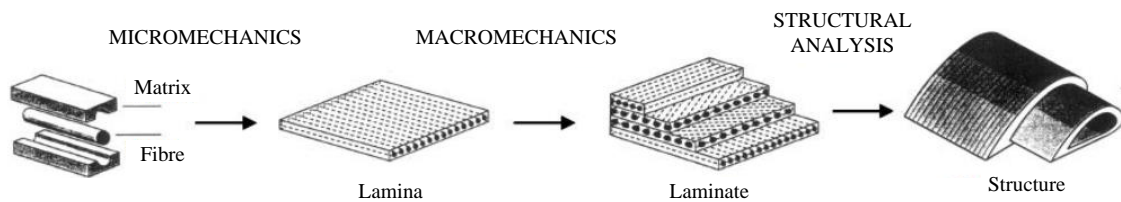


Figure 2.8: Different types of analyses according to the structure level [2].

At a micro level, one is often concerned with the properties of each material (fibre and resin) and mainly their interaction. At the lamina level, knowing the (isotropic) properties of the resin and the fibre reinforcement, one is able to define homogeneous equivalent properties for the whole lamina (often referred to as engineering constants, due to the orthotropic behaviour that characterizes FRP), such as the longitudinal elastic modulus (E_L), the transverse elastic modulus (E_T) and the shear modulus (G_{LT}). There is also other method called the Representative Volume Element (RVE) which allows for the definition of the lamina equivalent homogeneous properties [34]. This method makes use of the finite element method (FEM) and basically consists of defining a cubic part with two different materials (fibre filaments and embedding resin) with a fibre area over the total area ratio equal to the fibre volume of the corresponding lamina (Figure 2.9). Next, by applying specific imposed unit displacement fields and boundary conditions, and measuring the total reaction force one may determine the homogenised elastic constants. This method is much more accurate than the rule of mixtures, namely for the determination of the transverse elastic modulus.

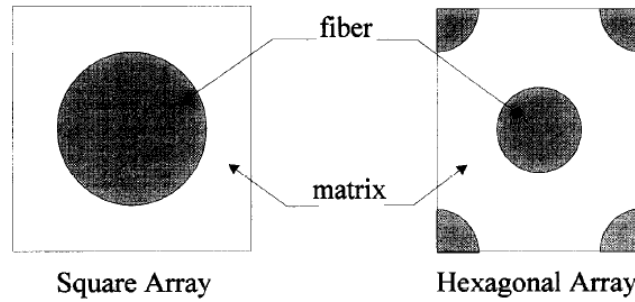


Figure 2.9: RVE examples using a square or hexagonal array [34].

With a given laminae stacking, the laminate's equivalent properties can be determined using the classical laminate theory (CLT). One should note that, due to the through-thickness heterogeneity, the axial and flexural stiffness may differ widely and thus, calculations often address the laminate stiffness rather than the engineering constants. The laminate stiffness matrix is usually defined as the A-B-D (6×6) matrix in which the A, B and D (sub-)matrices correspond respectively to the axial, coupling and flexural stiffness. For symmetric stacking sequences, the B matrix is null and the axial and flexural behaviours might be addressed separately.

At the structure level, the analyses are mostly related to the full-section effective properties and not so much to the laminate properties. These are mostly used for the structural design of civil engineering members, both for serviceability and ultimate limit states.

2.7 HYBRIDIZATION

Hybridization of FRP pultruded members generally consists of using different types of fibres (for instance glass and carbon) in the same laminate or profile [8,43–45]. Some hybrid members are pultruded separately and then adhesively bonded together, whilst others are pultruded alongside (and thus embedded in the same resin). Hybridization comprising glass and carbon fibres usually stems from the need of improving stiffness of a given member in a cost-effective solution [44]. In fact, one of the main issues of GFRP members is the high deformability (roughly seven to eight times higher than steel). On the other hand, although being considerably stiffer (see section 2.2), carbon fibres are much more expensive than glass fibres. Moreover, carbon fibre pultruded structures are more stable when embedded in an epoxy resin (also more expensive). In this regard, all-CFRP pultruded profiles do not offer a cost-competitive alternative to GFRP civil structures, and thus they are mostly limited to military and aerospace applications [46].

Hybrid FRP composites were first developed for aerospace and mechanical engineering applications. Bunsell and Harris [13] carried out one of the first studies regarding the response of hybrid laminates comprising different types of fibres. They have studied the behaviour of hybrid laminates comprising epoxy-based GF and CF alternate laminae, either bonded or non-bonded. Results have shown that the

laminates with bonded laminae presented a better ultimate behaviour, as the elongation at failure of the CFRP layers was higher than in the non-bonded specimens.

There are more recent studies that address the structural behaviour of hybrid FRP pultruded profiles comprising glass and carbon fibres both by experimental and numerical means [4,45,47]. These will be addressed and thoroughly discussed later, in Chapter 4 and Chapter 5. These so-called hybrid C-GFRP profiles allowed for the installation of the first road traffic bridge comprising FRP pultruded members in Route 601 (USA) [48]. A total of eight *Strongwell Extren DWB* multicellular double web beams were used in an 11.8 meter span to accomplish the target maximum deflection of $L/800$ (Figure 2.10).

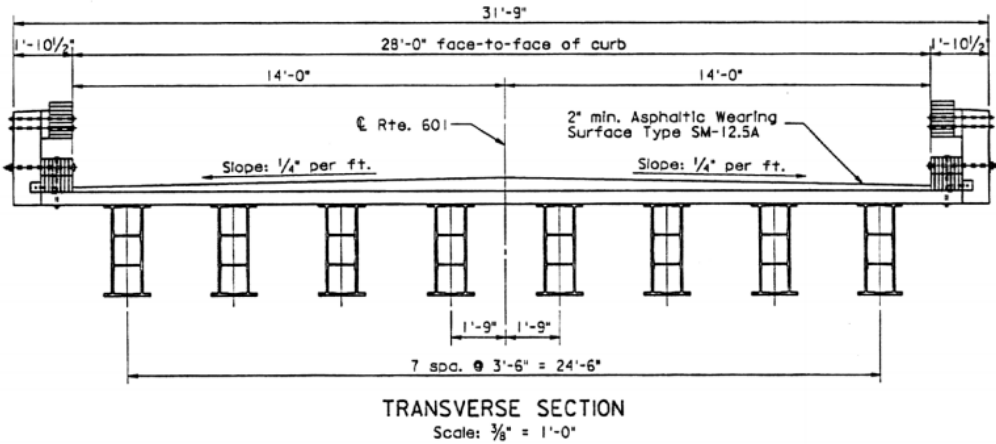


Figure 2.10: Transverse section of Route 601 bridge [48].

2.8 PULTRUDED CONNECTIONS

Similarly to the FRP structural shapes, pultruded connections were first developed by copying the metallic construction and thus using bolted connections. However, due to the distinct material behaviour, soon the scientific community realised that this was not the best solution for pultruded composites [32]. The linear elastic and brittle behaviour of these profiles make them prone to high stress concentrations in the bolt-plate contact surface. Such fact is aggravated due to the orthotropic behaviour of pultruded structures, since they are more sensitive to these stress concentration in their transverse direction (in which their strength is roughly three to four times lower than in the longitudinal direction).

Later, bonded connections started spreading as a solution that uniformly distributes contact stresses along the bonded surfaces, thereby avoiding the stress concentrations presented by bolted connections. Despite being much more adapted for the structural behaviour exhibited by FRP pultruded members, they are still being hindered due to uncertainties regarding their long-term behaviour and performance under elevated temperature [37].

To overcome the issues exhibited by either bolted or bonded connections, mixed connections started being developed using bolts and adhesives alongside, thus merging their inherent advantages. These solutions seem to comply with the requirements set by the scientific and technical communities, as they uniformly distribute contact stresses and are stiffer (bonded connection), while guaranteeing a certain redundancy (bolted) if/when the adhesive starts to deteriorate. Moreover, the surface-to-surface pressure applied by the bolted connection increases the bonding performance.

More recently, interlock connections (with or without bonding adhesives) started being used, mostly to transversely connect second generation pultruded decks (*cf.* Figure 2.6, page 14). The utmost advantage of this type of connection relies on the very fast and easy execution and the fact that it can also be adhesively bonded to maximise stiffness and stress transfer in panel-to-panel connections.

2.9 CIVIL ENGINEERING APPLICATIONS

As mentioned before, initially FRP pultruded profiles were only used as secondary structural members, such as stairs, grids, benches, gates or fences. They started being used as main civil engineering structural members mostly due to their electromagnetic transparency and chemical resistance. The *Apple Computers* building in the USA was one of the first examples of a large structure constructed with FRP pultruded profiles in 1985 [2]. In the early 2000s, Keller [37] has reviewed the main all-composite and hybrid structural applications available using FRP pultruded members. From these one should highlight the Eyecatcher building and the Pontresina pedestrian bridge, both built in Switzerland (Figure 2.11 and Figure 2.12, respectively).



Figure 2.11: Eyecatcher building in Switzerland [37].



Figure 2.12: Pontresina pedestrian bridge in Switzerland [37].

Recently, due to their low self-weight and resistance to corrosion, FRP pultruded profiles are being increasingly used as an alternative to timber, steel and reinforced concrete (RC) structures. Construction markets, such as the rehabilitation of timber building floors and steel structures subjected to chemically aggressive environments, are embracing the use of FRP composites due to their benefits over traditional materials (Figure 2.13).



Figure 2.13: GFRP pultruded profiles used in the rehabilitation of a timber floor [3].

As already mentioned, other examples in which FRP pultruded profiles are being increasingly used as structural members are pedestrian bridges. Recently, two different bridge prototypes incorporating pultruded profiles were developed and studied at IST. Gonilha [49] and Gonilha *et al.* [50–53] addressed the structural behaviour of a pedestrian bridge with GFRP pultruded girders and slabs made of steel fibre reinforced self-compacting concrete (SFRSCC). This footbridge was recently installed in the city of Ovar. Sá [54] and Sá *et al.* [55–57] studied the behaviour of a different pedestrian bridge concept comprising steel girders and second generation multicellular pultruded decks. This footbridge was built in the city of Viseu.

Both studies comprised the experimental, numerical and analytical investigations on the serviceability behaviour (short-term deformations, creep and vibrations) and failure behaviour (collapse) of the footbridges and their GFRP components. The connection between the slabs/decks and the girders were also addressed.

2.10 MAIN RESEARCH NEEDS

Despite their already relatively long history of use as structural applications, pultruded profiles are still one of the most relevant research areas in civil engineering, at both material and structural scales.

From a technological point of view, different types of manufacturing processes are still being developed, namely processes that allow for the production of curved pieces, tapered members (with non-constant cross-section). New types of fibres, resins and additives (*e.g.* flame retardants) are currently being studied as well.

The main research needs in this field include the behaviour under fire and at elevated temperature, the creep behaviour, the durability when subjected to different environmental agents, the connections' technology, the (environmental and economic) sustainability and, finally, the hybridization and geometrical optimization of cross-sections, the latter being one of the topics of this thesis.

Since FRP structures are made of thermoset polymeric resins, they are prone to elevated temperatures and fire. The glass transition temperature (T_g) of typical FRP materials is very low (roughly 100°C to 150°C) and thus, their elastic moduli are highly affected when subjected to fire, mostly when under compression or shear stresses. Fire protection systems are currently being developed and studied at IST aiming at delaying the loss of stiffness and strength of different types of FRP systems, including strengthening strips, reinforcing bars and structural profiles [5,58].

The creep behaviour, which is strongly affected by temperature and moisture, is also one of the main research areas. Some analytical models, including the empirical Findley's power law, have been developed and proved to be able to simulate the long-term viscoelastic behaviour of this type of structures. However, their calibration is a quite demanding process, as relatively long periods of testing are required under controlled temperature, relative humidity and loading [50,55,56,59].

Despite their high resistance to corrosion when compared to traditional construction materials even under chemically aggressive environments, FRP pultruded profiles are prone to degradation due to several phenomena that affect their chemical, physical, aesthetical, mechanical and structural performance, namely water and salt water, thermal cycles and UV radiation. These phenomena are currently being studied at IST [60,61].

The environmental and economical sustainability of these structures is also a matter of major concern, namely regarding the manufacturing process, the service life and the end of the service life [3]. For instance, the partial reuse of manufacturing waste material is a possible approach for the minimization of both the waste disposal and the raw materials' cost [62]. However, limited recycling options are available at the end of the service life. Thorough life cycle assessment of FRP constructions and its comparison with conventional materials is needed.

Finally, fibre hybridization and the optimisation of the cross-section/fibre architecture are also one of the most relevant FRP research fields. As already mentioned, the deformability issues presented by GFRP structures might be overcome by the introduction of stiffer fibres, for instance carbon, in judiciously chosen fractions and locations. However, since carbon fibres are much more expensive than glass ones, fibre architecture optimisation is required in order to maximize the hybridization effectiveness [4,45,47].

2.11 CONCLUDING REMARKS

In this chapter, the general aspects of FRP pultruded profiles were briefly summarised, from their constituent materials and their main properties to the present main research areas. One has also discussed their potential as primary structural members and why they are currently a fitting alternative to traditional construction materials, such as steel, timber and reinforced concrete.

One of the most concerning issues presented by FRP pultruded structures is the wide range of properties reported by manufacturers (not always consistent with the actual properties of FRP profiles) and the lack of consensual design codes [8]. Therefore, there is an actual need of (i) standardizing production methods, (ii) accurately defining the material properties using widely accepted international test standards (ISO or ASTM), (iii) developing calibrated and validated numerical and analytical models supported by extensive experimental data, and (iv) finding consensual design approaches.

This thesis aims at filling some of the above mentioned gaps concerning FRP pultruded profiles, namely in what concerns the short-term serviceability behaviour (deformations) and the ultimate behaviour of this type of structures. The following chapters aim at contributing for a better understanding of the structural behaviour exhibited by bare GFRP and hybrid C-GFRP I-section pultruded profiles. With that purpose an extensive experimental campaign was carried out and appropriate numerical models were developed to simulate those tests. Whenever possible, the experimental and numerical data obtained were compared to analytical predictions available in the literature to assess the accuracy of such modelling tools.

CHAPTER 3

STRUCTURAL BEHAVIOUR OF ECCENTRICALLY LOADED GFRP COLUMNS

3.1 PRELIMINARY CONSIDERATIONS

Conventional FRP pultruded profiles under compression are particularly susceptible to local buckling due to their low in-plane moduli and high wall width-to-thickness ratio. Such phenomenon has been studied by many researchers using experimental, numerical and analytical tools. For instance, Tomblin and Barbero [20] studied the local buckling phenomenon in GFRP compressed members. The analytical results obtained from the modified Southwell method fitted very well the experimental values. Turvey and Zhang [63] also performed experimental and numerical studies aiming at studying the initial failure of post-buckled GFRP short columns, with length-to-radius of gyration ratios (from now on referred to as slenderness) varying from 4.7 to 19.0. A phenomenological failure criterion was proposed (Tsai-Wu criterion) and incorporated in the FE models to simulate the web-flange junction initial failure, providing good correlation with the experimental results.

Regarding the global buckling phenomenon, several studies addressed the behaviour of both beams and columns made of GFRP. Correia *et al.* [25] and Silva *et al.* [26] studied the structural behaviour of GFRP cantilevers by both experimental and numerical means. Nguyen *et al.* [64] performed a numerical study about the influence of the load height as well as of the boundary conditions and geometric imperfections on the lateral-torsional buckling of FRP beams. Zureick and Scott [65] studied the short-term behaviour under axial compression of GFRP slender members, with slenderness ratios varying from 19.2 to 85.0. Several specimens with different slenderness were tested and their critical loads were then compared with analytical predictions obtained from (i) the Euler's buckling equation and (ii) the equation proposed by Engesser [66], which takes into account the shear deformation (often relevant in orthotropic materials with $E_L \gg G_{LT}$). Results showed good agreement between experimental data and analytical predictions (relative differences between 1% and 15%). The authors also provided a step-by-step design procedure and a sample calculation for GFRP slender members under compression.

The interaction between local and global buckling in GFRP columns was also studied by several authors. Hashem and Yuan [67] proposed a criterion to distinguish short from long GFRP columns, based on a critical slenderness ratio. A total of 24 full-scale specimens with different cross-sections and slenderness ratios ranging from 3.79 to 78.9 were tested. Experimental results were then compared to predictions provided by the Euler's buckling equation and the classical plate theory showing that such critical slenderness ratio is about 50. Barbero and Tomblin [21] proposed a design equation that takes into account the interaction between local and global buckling in FRP columns. The experimental verification of such equation was also performed by Barbero *et al.* [68]. While each isolated local or global buckling mode has a stable post-critical path, the coupled mode arising from interaction at similar buckling loads is unstable and highly sensitive to imperfections. Such equation was also used by Correia *et al.* [4] and it gave satisfactory predictions of buckling loads of FRP pultruded short columns.

The literature regarding the structural behaviour of GFRP members under eccentric compression is very scarce. Barbero and Turk [16] carried out an experimental study regarding the effect of eccentric loading about the minor (weak) axis of wide flange (WF) and I-section profiles. Results showed that the main factors controlling failure in beam-columns are the eccentricity, the member length and the specimen's mechanical and geometrical properties. The authors considered only one eccentricity ($e = 25.4$ mm, corresponding to an eccentricity/height ratio (e/h) between 0.125 and 0.25 for the different cross-sections tested), and unfortunately they did not perform any numerical simulations to study the effect of different eccentricities. Mottram *et al.* [17] carried out an experimental study regarding the effect of eccentric loading about the major (strong) axis and moment gradient in GFRP members with WF cross-section. They analysed different levels of high eccentricity, with e/h ranging from 0.5 to 2.0, aiming at studying the influence of combined compression and bending when joints in braced frames are simple (hinged) to semi-rigid. In this investigation, numerical simulations were not performed.

According to the author's best knowledge, no studies were reported up to present on the effect of small eccentricities⁶ about the major (strong) axis in GFRP compressed members. Although in structural design the axial loading in columns may be assumed to be concentric, such eccentricities often exist both due to (i) geometrical imperfections of the members and (ii) construction errors (*e.g.*, member axis misalignment). Hence, this chapter presents results of experimental and numerical investigations on the structural behaviour exhibited by GFRP pultruded columns subjected to small eccentric loading. To accomplish such goal, three series of GFRP I-section pultruded columns were tested under compression, applied with the three following eccentricity/height ratios – $e/h = 0.00, 0.15$ and 0.30 .

⁶ The author considered that small eccentricities refer to situations in which the load application point is located inside the cross-section kern, *i.e.* only compressive stresses develop (at least for a first-order analysis). The kern of a cross-section is the area in which the (eccentric) compressive load is applied leading only to compressive or null stresses within the whole cross-section area.

Results obtained from the experimental campaign were compared to numerical simulations using (i) the finite element method (FEM) and (ii) the generalised beam theory (GBT).

3.2 TEST PROGRAMME

3.2.1 Materials

The GFRP pultruded material used in this experimental campaign was produced by the company Fiberline DK and consists of an I-section profile with $120 \times 60 \times 6$ mm (height \times width \times wall thickness). The profile was supplied in lengths of 6.0 m and is made of alternating layers of E-glass fibre rovings oriented in the longitudinal direction and continuous strand mats, all embedded in a resin matrix of polyester. Burn-off tests carried out in small specimens extracted from the web and flanges indicated a similar inorganic content of roughly 70% (in weight).

Table 3.1 summarises the main mechanical properties of the GFRP profile obtained from coupon-testing, indicating the test standard and the number of specimens used in each case. The values of the following material properties are listed: longitudinal (E_L) and transverse (E_T) elastic moduli, shear modulus (G_{LT}), Poisson ratio (ν), longitudinal tensile ($\sigma_{L,t}$) and compressive ($\sigma_{L,c}$) strengths, transverse tensile ($\sigma_{T,t}$) and compressive ($\sigma_{T,c}$) strengths and shear strength (τ_{LT}). All parameters with the exception of E_L , E_T and $\sigma_{T,t}$ were obtained by testing coupons cut from the profile. The value of E_L was obtained from strain gauge measurements in the test of a full-scale column (from series BC, cf. section 3.3.2), the value of E_T was provided by the manufacturer and the value of $\sigma_{T,t}$ (not relevant in the present analysis) was considered to be equal to the value of $\sigma_{T,c}$.

Table 3.1: Mechanical properties and input data for numerical models.

Property	E_L (GPa)	E_T (GPa)	G_{LT} (GPa)	ν	$\sigma_{L,t}$ (MPa)	$\sigma_{L,c}$ (MPa)	$\sigma_{T,t}$ (MPa)	$\sigma_{T,c}$ (MPa)	τ_{LT} (MPa)
Ave. \pm std. dev.	28.9 ± 0.1	8.5	3.89 ± 0.44	0.279 ± 0.031	308 ± 27	360 ± 65	121	121 ± 8	30.8 ± 1.2
Test method	series BC full-scale tests	(1)	ISO 527-5	ISO 527-4	ISO 527-4	ASTM D695	(2)	ASTM D695	ISO 527-5

(1) Reported by the manufacturer.

(2) Considered to be equal to the transverse compressive strength ($\sigma_{T,c}$).

3.2.2 Experimental series

To study the effect of eccentric loading in pultruded GFRP profiles, the following four different series were defined: (i) concentric loading in non-braced columns, series *NBC* (this series was tested mainly to calibrate and provide further validation to analytical and numerical models); (ii) concentric loading in braced columns, series *BC*; (iii) eccentric loading (level I) in braced columns, series *EBCI*; and

(iv) eccentric loading (level II) in braced columns, series *EBCII*. Table 3.2 specifies for each series the general loading, boundary and bracing conditions.

Table 3.2: Test series of eccentrically loaded columns.

Series	Loading	End supports	Lateral bracing
NBC	Concentric	Spherical hinges	None
BC	Concentric	Clamped	Parallel to the web
EBCI	Eccentric (I), $e/h = 0.15$	Cylindrical hinges	Parallel to the web
EBCII	Eccentric (II), $e/h = 0.30$	Cylindrical hinges	Parallel to the web

For each series, three replicate specimens were tested, with lengths of 1.5 m. The structural behaviour of each profile was studied in terms of load-displacement behaviour, axial stiffness, ultimate strength and failure mode.

In order to evaluate the effect of eccentric loading in compressed members, two different eccentricities were defined: (i) Eccentric level (I) was considered to be equivalent to half of the distance from the section’s stiffness centroid to the boundary of the section kern along the major axis; and (ii) Eccentric level (II) was considered to be equivalent to the distance from the section’s stiffness centroid to the boundary of the section kern along the major axis (double of the Eccentric level (I)). Figure 3.1 illustrates the section kern (with dashed boundaries) alongside the three load application points considered in this experimental campaign, concentric and two eccentric levels (Δ_I and Δ_{II}).

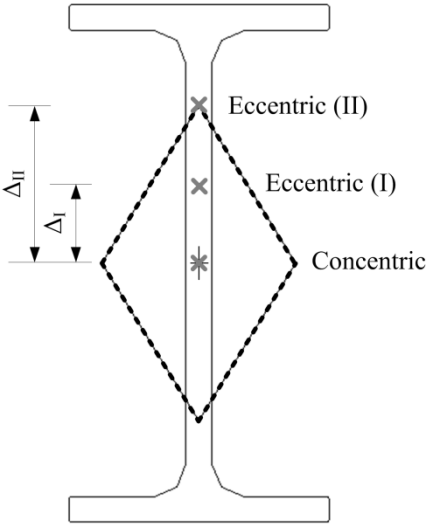


Figure 3.1: I-section kern and definition of concentric and eccentric levels I and II of applied load.

3.2.3 Test setup, instrumentation and procedure

The test setup for each series is illustrated in Figure 3.2. Table 3.3 provides a summary of the boundary conditions adopted in the experimental campaign and used later in the numerical study (section 3.4), in which y is the longitudinal axis, and x and z are the cross section's minor and major axes, respectively.

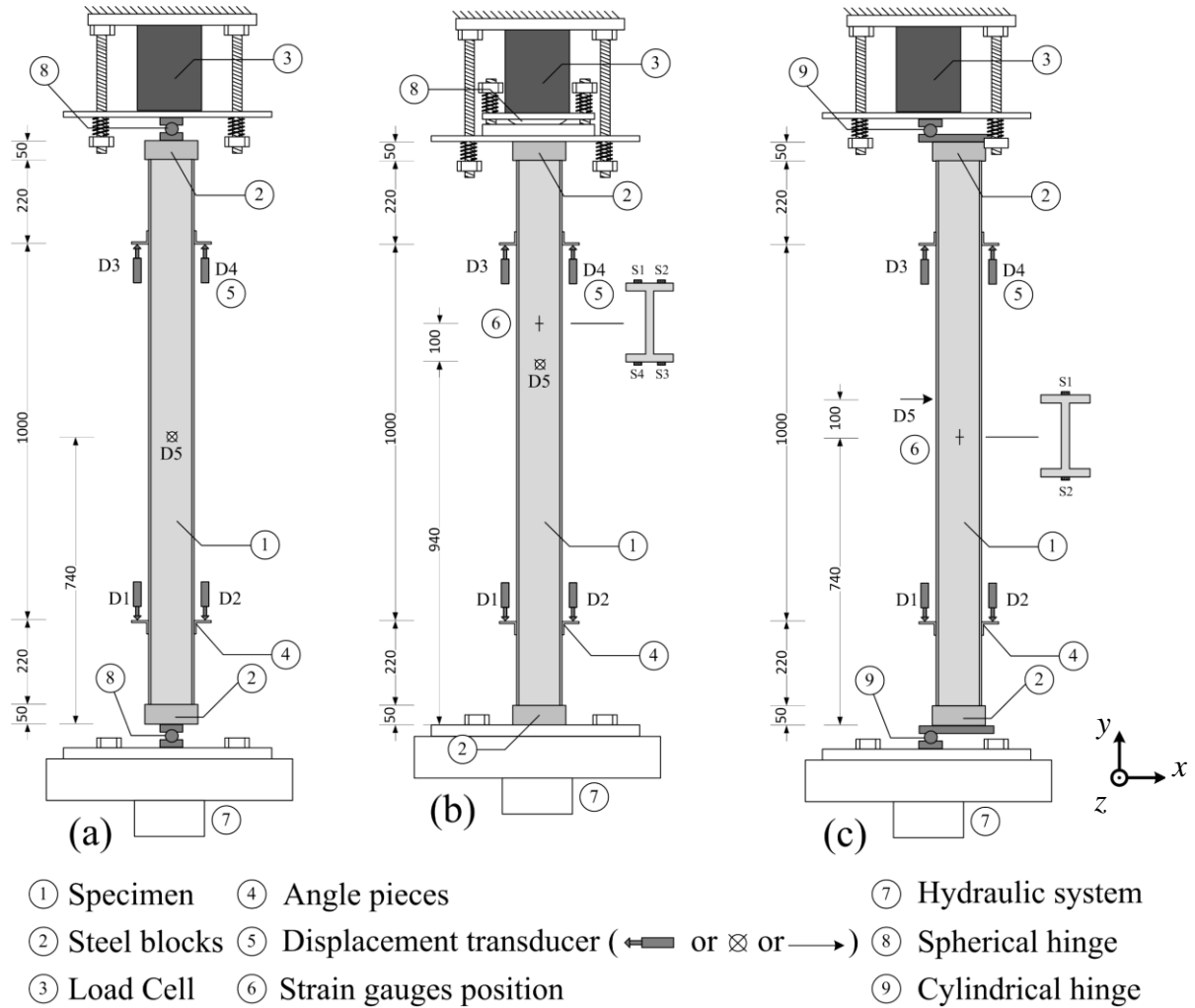


Figure 3.2: Test setup for (a) series NBC, (b) series BC, and (c) series EBCI and EBCII (units in mm).

Table 3.3: Boundary conditions adopted in the experimental campaign and numerical models (axes in Figure 3.2).

Series	Top end restriction						Bottom end restriction					
	Displacement			Rotation			Displacement			Rotation		
	x	y	z	x	y	z	x	y	z	x	y	z
NBC	0	1	0	1	1	1	0	0	0	1	1	1
BC	0	1	0	0	0	0	0	0	0	0	0	0
EBCI and EBCII	0	1	0	1	0	0	0	0	0	1	0	0

0 – Fixed (restrained) degree

1 – Free degree

Most of the adopted instrumentation was the same for all series. However, the boundary conditions were slightly different for each series. Also, the positions of the strain gauges and lateral displacement transducers varied among the different series.

In what concerns common instrumentation, four 20 mm deep steel angle pieces were bonded to each profile's flanges with cyanoacrylate glue, in order to measure the effective axial shortening. Two of them were bonded at 25 cm from the bottom end section, while the other two were bonded at 125 cm from that section. By measuring the displacements at the angle pieces instead of at the end sections, one avoided the influence of the end sections' bearing on the measurements, thereby obtaining more reliable axial shortening results [4]. Two machined steel blocks (with a diameter of 140 mm, a thickness of 50 mm and 30 mm deep grooves with the negatives of the section walls) were used in order to restrain any relative displacement or rotation of the end sections. The internal width of the grooves was slightly higher than that of the section walls in order to provide some geometrical tolerance and avoid crushing mechanisms during loading due to local misalignments.

The load was applied to the bottom end of the columns by an *Enerpac* hydraulic system with a capacity of 3000 kN and was measured by a *Microtest* load cell, also with 3000 kN capacity, placed on the top end. The axial shortening was measured between the bonded angle pieces with four *TML 25* displacement transducers (D1 to D4, with precision of 0.01 mm). An additional *TML 500* displacement transducer (D5, also with precision of 0.01 mm) was used to measure the lateral displacements of each tested specimen. Its position varied among each series in order to better monitor the expected failure mechanism. Load, displacement and strain data were acquired at a rate of 10 Hz using two *HBM*, model *Quantum X* data loggers. In the following sub-sections the detailed instrumentation for each series is described.

3.2.3.1 Concentric loading in non-braced columns (NBC)

Rotations about all axes at each end section were set free by the introduction of two spherical hinges with *Teflon* sheets in the contact interfaces (Figure 3.3(a)). Since in this series the lateral displacements were expected to be significant, 2 mm thick steel plates were welded to the steel angle pieces in order to measure the axial shortening throughout the whole test. Consequently, the initial distance between monitored sections (D1 to D4) was 996 mm instead of 1000 mm (Figure 3.3(b)). The lateral displacement transducer (D5) was positioned perpendicularly to the web at the mid-height section.

3.2.3.2 Concentric loading in braced columns (BC)

Since for long plates (length \gg width, which was the case), the end support conditions have very little (or no) influence in both critical and ultimate loads, a simpler test setup was adopted. In both ends the

negative steel blocks were directly bolted to the loading system. To prevent the introduction of additional stresses from end section imperfections, a spherical hinge was used in the top end. Four strain gauges were bonded to each specimen's flanges, at 102 cm from the bottom end with the objective of determining both the longitudinal elastic modulus and the bending strains (*cf.* Figure 3.2). The lateral displacement transducer was positioned perpendicularly to the web 10 cm above the strain gauges. The lateral bracing system was provided by three pairs of steel bars positioned at distances of 39, 75 and 111 cm from the bottom end (Figure 3.4(a)).

3.2.3.3 Eccentric loading in braced columns (EBCI and EBCII)

The rotations about the major axis at both end sections were set free by the introduction of two cylindrical hinges (Figure 3.4(b)). Two strain gauges were bonded to each specimen's flanges, at mid-height section, with the objective of determining both the longitudinal elastic modulus and the bending strains (*cf.* Figure 3.2). The lateral displacement transducer was positioned perpendicularly to the flanges 10 cm above the strain gauges. The lateral bracing system was the same as in the series BC.

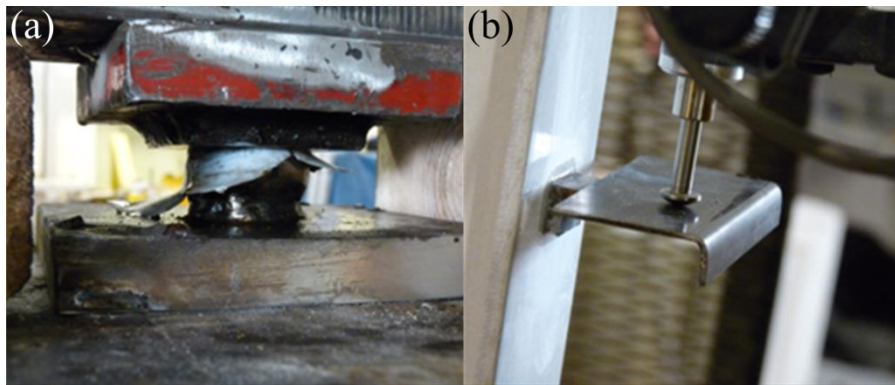


Figure 3.3: (a) Spherical hinge with a Teflon sheet and (b) steel plates for axial shortening measurement.

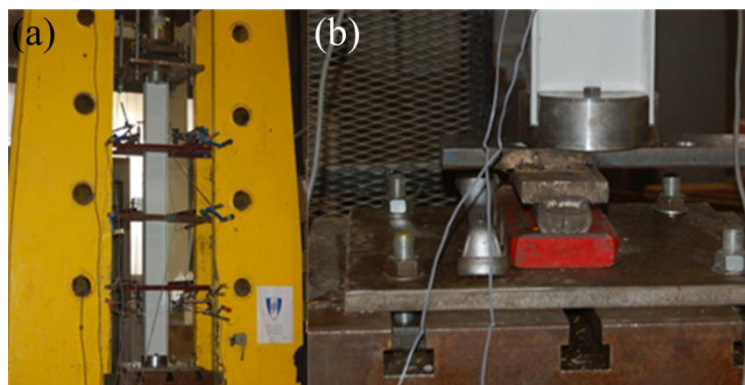


Figure 3.4: (a) Steel bars used to prevent lateral deflections and (b) bottom end with cylindrical hinge.

3.3 RESULTS AND DISCUSSION

3.3.1 Load vs. axial shortening behaviour

Figure 3.5 presents the load vs. axial shortening curves of all specimens from each one of the series. Table 3.4 presents a summary of the test results with reference to the following parameters: ultimate load (P_u); axial stiffness (K), longitudinal elastic modulus determined from either the displacement transducers D1 to D4 (E_{transd}) or the strain gauges (E_{sg}), the critical load obtained by the application of the Southwell method (P_{bk}) and the limit load (P_{lim} , only for series NBC). Figure 3.6 presents a comparison of the behaviour exhibited by series BC, EBCI and EBCII. Figure 3.7 presents the ultimate loads as a function of the eccentricity level.

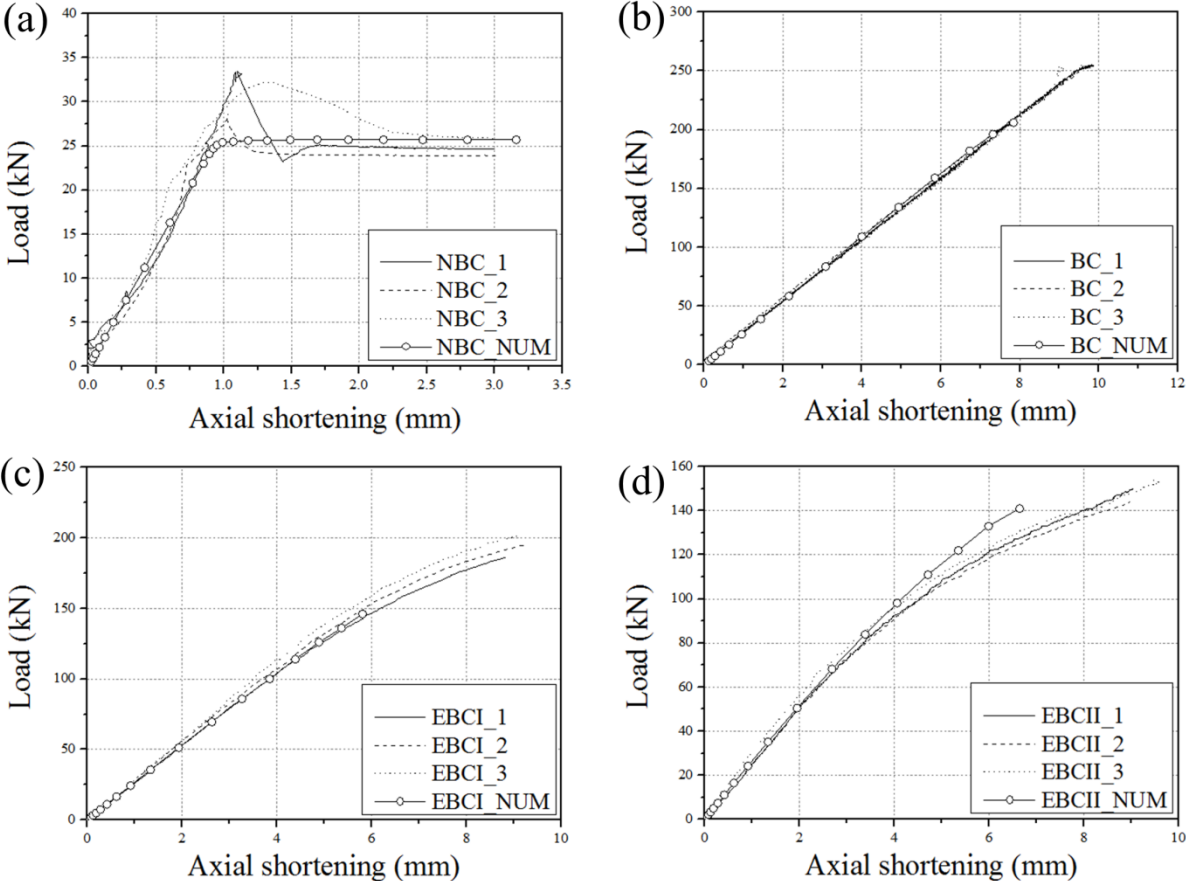


Figure 3.5: Load vs. axial shortening curves: (a) series NBC, (b) series BC, (c) series EBCI and (d) EBCII.

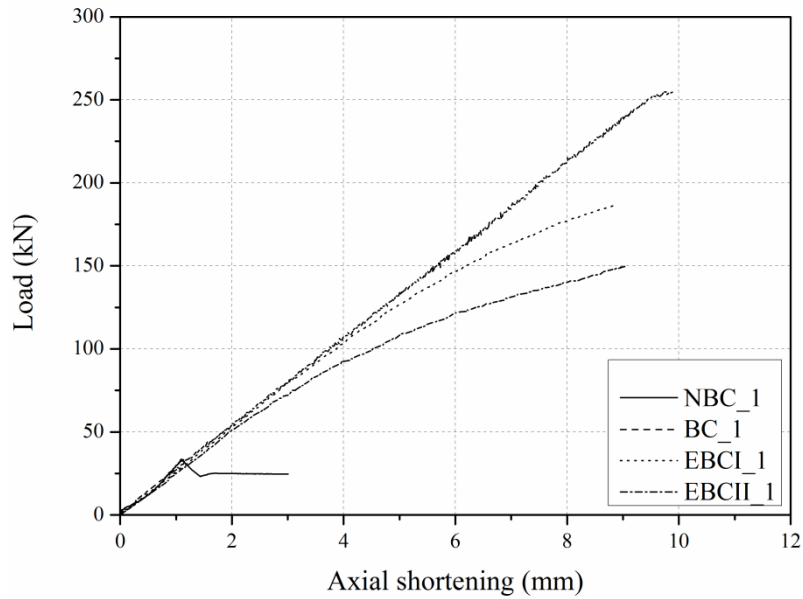


Figure 3.6: Load vs. axial shortening curves of representative specimens from series BC, EBCI and EBCII (comparison)

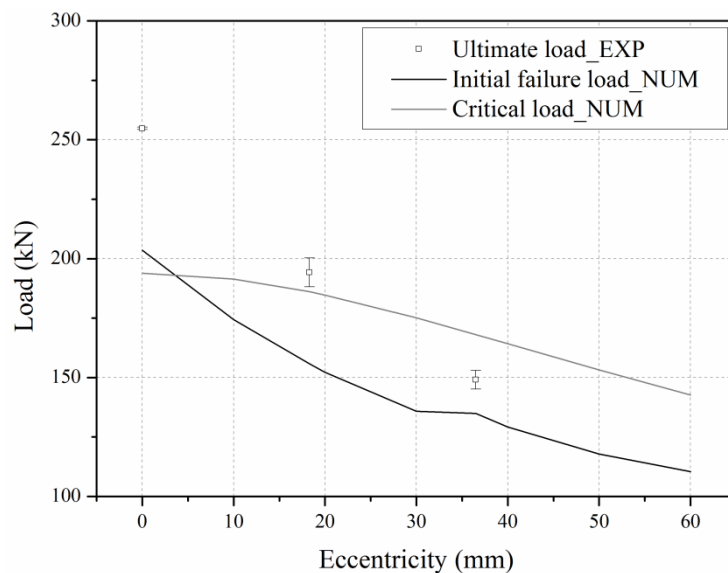


Figure 3.7: Load vs. eccentricity – ultimate load (experimental, average \pm standard deviation) and initial failure and critical loads (numerical).

The load vs. axial shortening curves of series NBC (Figure 3.5(a)) were more irregular than those of the other series. Since the same type of profile was used in all series, such irregularity most likely stemmed from the lower deflection magnitudes measured in this series. The average stiffness of series NBC was roughly the same as that of the other series. Regarding the global buckling phenomenon, after reaching the maximum load, all specimens presented a significant decrease of the applied load, which then remained roughly constant until the end of the test (columns were unloaded without reaching failure). Such fact suggests the existence of residual friction forces at the spherical hinges, which restrained rotations at both ends and slightly delayed the buckling phenomenon. Therefore two different critical loads were determined for series NBC with the following procedures: (i) using the

Southwell plot method (P_{bk} , which takes into account unavoidable residual friction forces) and (ii) considering the limit load of the stabilized plateau after the buckling was triggered (P_{lim}) as the critical load. Figure 3.5(b) (series BC) shows the typical behaviour of GFRP profiles: linear elastic until the brink of failure. In this series, instants prior to collapsing, a significant loss of axial stiffness occurred due to the local buckling phenomenon.

Table 3.4: Summary of experimental results, critical loads obtained in both numerical analyses and deformation mode (cf. Figure 3.12, page 40) participation obtained in the GBT analysis.

Series	Experimental results						$P_{bk,num}$ (kN)		GBT deformation mode participation (%)					
	P_u (kN)	K (kN/mm)	E_{transd} (GPa)	E_{sg} (GPa)	P_{bk} (kN)	P_{lim} (kN)	ABAQUS	GBT	3	5	6	7	11	other
NBC	31.5 ± 2.0	41.3 ± 3.6	29.2 ± 2.6	-	33.6 ± 2.3	24.8 ± 1.0	25.7	27.7	99.35	0.6	-	0.04	-	<0.01
BC	254.8 ± 0.5	39.3 ± 0.4	27.8 ± 0.1	28.9 ± 0.1	208.6 ± 21.5	-	193.9	188.7	-	85.01	-	14.7	0.50	0.42
EBCI	194.2 ± 6.1	40.7 ± 1.5	28.7 ± 1.1	3.4 ± 1.7	-	-	186.1	180.4	-	71.25	17.2	10.34	0.42	0.97
EBCII	149.1 ± 33.9	36.2 ± 0.7	25.5 ± 0.5	29.6 ± 0.2	-	-	168.1	161.8	-	62.29	28.53	7.21	0.45	1.52

For the eccentrically loaded profiles (Figure 3.5(c) and (d)), in the initial loading phase, the axial stiffness was roughly the same as in series BC and NBC (cf. Figure 3.6), and then it gradually decreased throughout the test. The slope decreased with increasing eccentricity because the bending component was higher and, consequently, the bowing effects caused the amplification of the column shortening for similar levels of applied load.

Figure 3.7 shows that the ultimate load decreases as the eccentricity level increases. The increase of eccentricity leads to the increase of longitudinal stresses in the most compressed flange and, consequently, causes failure for lower load levels. From Figure 3.7 one can notice that by applying the load with an eccentricity equivalent to the kern boundary (series EBCII) there is an ultimate load reduction of roughly 100 kN. This means a loss of more than 40% of load capacity when comparing to an identical profile subjected to concentric loading (BC). Such fact is of major importance in GFRP structural design. These results point out the importance of adequately simulating the geometry of the connections between GFRP members, as small eccentricities may cause considerable ultimate load reductions. Moreover, it should be emphasized that the ultimate load decreases with an approximately linear trend for small eccentricities (at least inside the cross-section kern).

3.3.2 Stress vs. strain behaviour and elastic modulus estimation

As previously mentioned series BC, EBCI and EBCII were monitored with strain gauges (S1 to S4 in series BC and S1 to S2 in series EBCI and EBCII) in order to measure axial strains, enabling the

determination of the longitudinal elastic modulus under compression as well as the bending strains. Also the strain gauges in specimens of series BC allowed determining the local buckling critical loads (*cf.* section 3.3.4). The axial stress vs. strain representative curves for each series are presented in Figure 3.8.

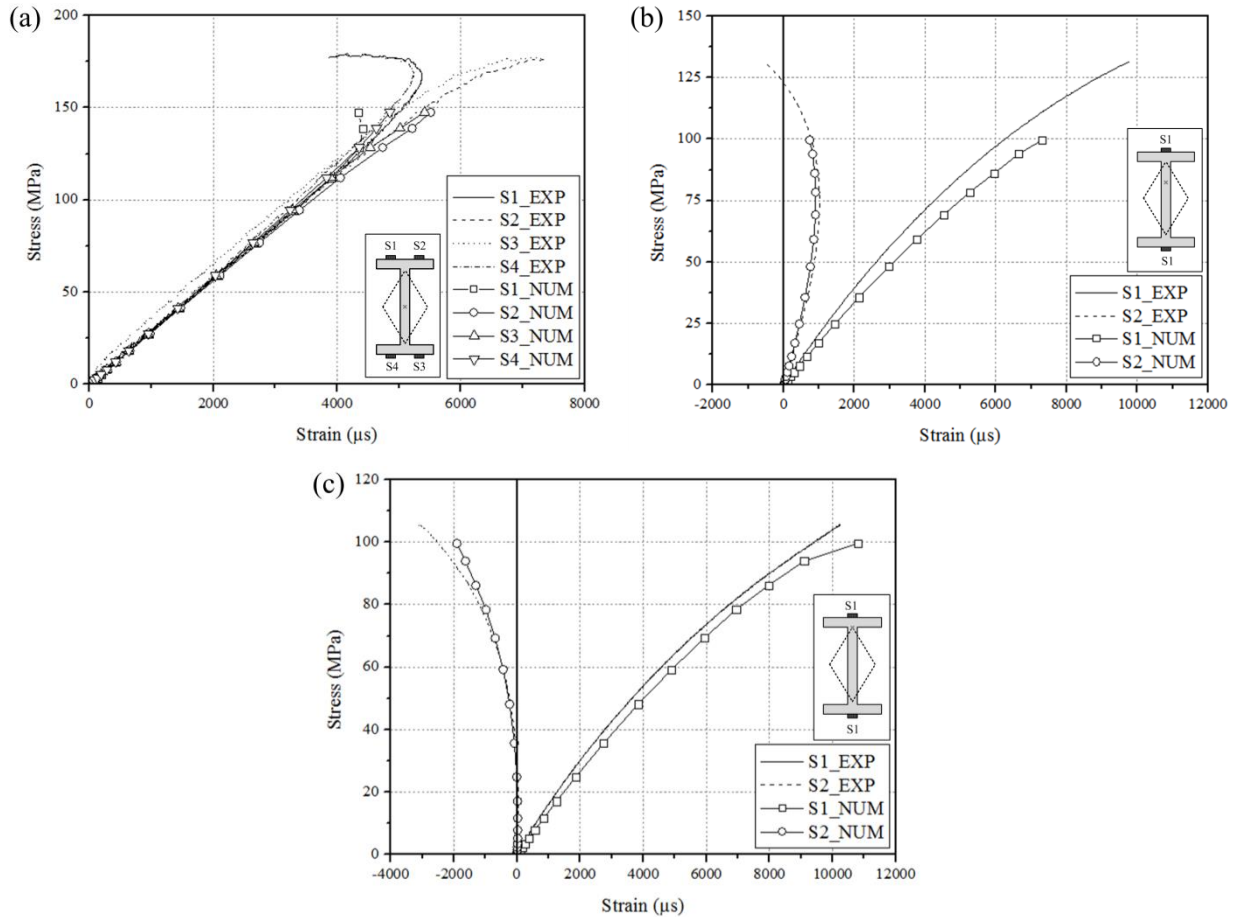


Figure 3.8: Experimental (representative) and numerical axial stress vs. strain curves of series: (a) BC (specimen BC_3), (b) EBCI (EBCI_1) and (c) EBCII (EBCII_1).

As expected, specimens of series BC developed uniform strains until the critical buckling load was reached. At the onset of local buckling, the I-section starts to deform in its own plane and the flanges' strains ($S1 \approx S4$ vs. $S2 \approx S3$) diverge from each other until the collapse occurs (Figure 3.8(a)). In specimens of the EBCII series (Figure 3.8(c)), in which the load is applied to the kern boundary, the strains at the outer surface of the uncompressed flange (S2) remain null up to an applied load of about 40 kN, *i.e.*, the neutral axis remains tangent to the cross-section boundary. Thus, it can be stated that linear theory of elasticity can be applied with confidence for $P < 0.27 P_u$ ($40/149.1 = 26.6\%$). For higher load levels, bowing and second order $P-\delta$ effects develop, the neutral axis approaches the cross-section centroid and tensile stresses emerge in the part of the profile opposed to the load application point. Regarding specimens of the EBCI series (Figure 3.8(b)), one can notice that until the above mentioned load level (about 40 kN) is reached, the stress-strain relation is almost linear. Beyond a load of 40 kN,

and similarly to the series EBCII, second order $P-\delta$ effects started being considerable and the stresses evolved nonlinearly with the strains.

From the stress *vs.* strain data, it was possible to obtain the full-section longitudinal elastic modulus under compression, namely by plotting the stress *vs.* average strain results and performing a linear regression in the initial linear branch of those curves. Results obtained based on such procedure are presented in Table 3.4. The consistency between the obtained average results together with the low standard deviation within each series allows concluding that the application of eccentric loading does not have a major effect on the profile's global initial stiffness, contrasting with its negative effect on the profile's ultimate load.

3.3.3 Failure modes

Failure modes differed widely among each tested series, but were roughly the same within each series. Specimens of series NBC buckled globally about the minor axis without visible material failure (Figure 3.9). Once global buckling occurred, the columns started to gradually lose their stiffness as the applied load remained roughly constant with increasing axial shortening. For these specimens, as the author did not spot any damage after the end of the tests, a second compressive test was conducted in each specimen. In average, columns buckled for lower loads (roughly 90% of those measured in the first tests) showing that although the global behaviour of the columns was not affected when re-loaded, some micro-scale damage might have occurred in the first loading tests.

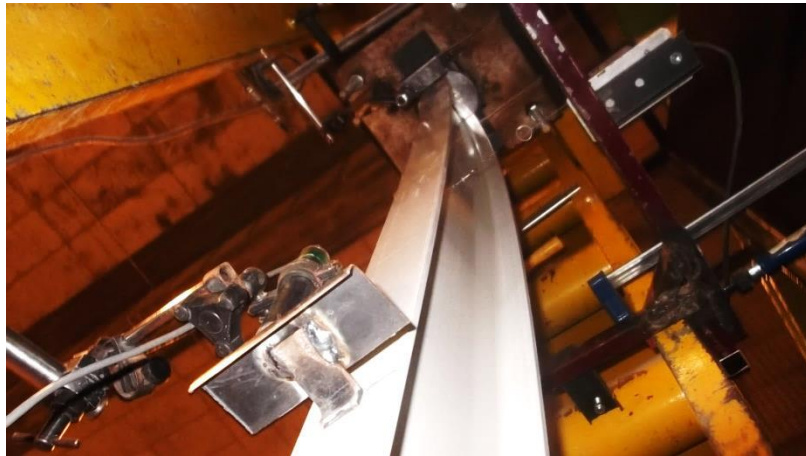


Figure 3.9: Global buckling in series NBC.

In specimens of series BC, failure occurred with local buckling. In such failure mode, the profiles buckled into several half-waves along their length. However, since the flanges of the studied profile are very narrow (and thus the amplitude of the buckled shape is rather low), they were not very visible (Figure 3.10(a)). Sequentially, the columns collapsed due to web-flange separation followed by material crushing (Figure 3.10(b)). Such failure mode has already been studied and it is known to be

mainly due to high shear stresses in the web-flange junction near inflection points of the buckled shape [4].

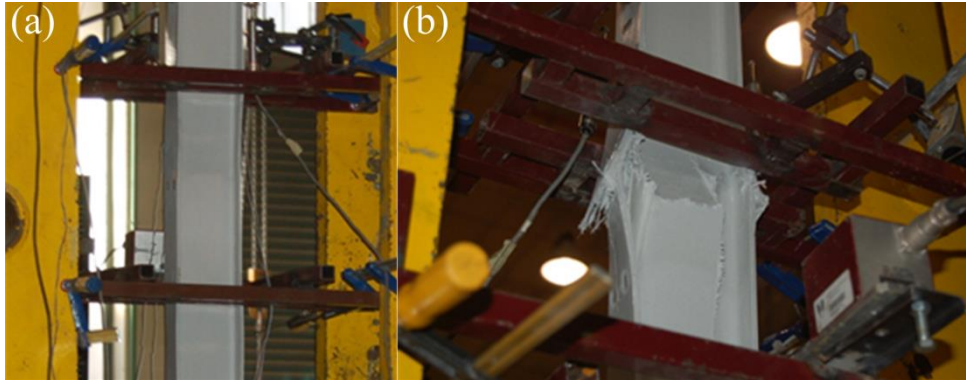


Figure 3.10: Failure mode in series BC: (a) buckled shape of the I-section profile tested; (b) failure mode with web-flange separation and material crushing.

The columns of EBCI and EBCII series failed due to crushing of the most compressed flange and web tearing. Local buckling at the most compressed flange was not visible at “human eye level” – any twist of the narrow compressed flange led to small displacement of its tip. Nevertheless, local buckling might have occurred and led to primary failure of the most compressed web-flange junction and that failure towards the less damaged zone occurred immediately after that. In Figure 3.11, both phenomena are visible: (i) the web-flange separation and local failure of the most compressed flange and (ii) the global failure of the column (notice the deformed longitudinal axis).

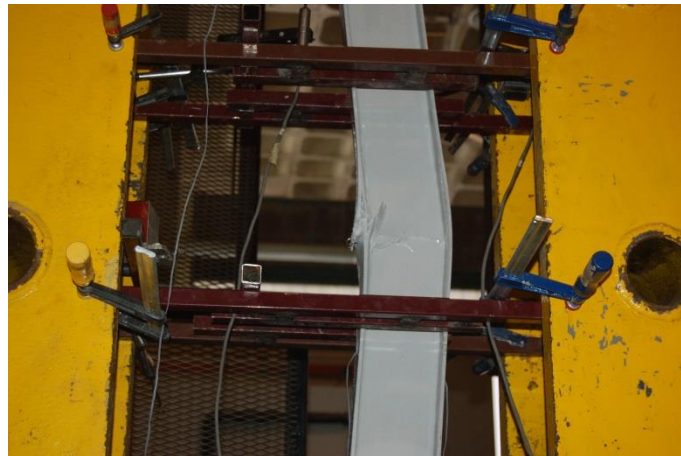


Figure 3.11: Failure mode in specimens of series EBCI and EBCII.

3.3.4 Buckling loads (series NBC and BC)

The global buckling critical load ($P_{bk,Global}$) for each specimen of series NBC was determined applying the Southwell method [69],

$$\Delta = \frac{\Delta}{P} P_{bk,Global} + C \quad (1)$$

where Δ is the perturbation parameter (in this case, the lateral deflection), P is the applied load and C is a dependent constant. In this method, a regression analysis is performed using Δ and P experimental data. The critical buckling load is then taken as the slope of the referred trend line. The average and the standard deviation values of the critical load P_{bk} are presented in Table 3.4. As already mentioned, results provided by the Southwell method take into account the residual friction forces at the spherical hinges. Therefore, the limit loads after the buckling was triggered (also listed in Table 3.4) were considered to be more representative of the critical load than the result provided by the Southwell method. Notice that the global flexural buckling has no post-buckling strength and load tends to the horizontal straight line at the critical load level.

The average experimental global buckling critical loads were compared with an analytical prediction (P_{Euler}), using the Euler's buckling formula given by,

$$P_{Euler} = \frac{\pi^2 E_L I_x}{(L_{bk})^2} = 27.7 \text{ kN} \quad (2)$$

where E_L is the longitudinal elastic modulus ($E_L = 28.9 \times 10^6 \text{ kPa}$), I_x is the cross-section inertia about the minor axis ($I_x = 2.187 \times 10^{-7} \text{ m}^4$) and L_{bk} is the buckling length ($L_{bk} = 1.50 \text{ m}$).

Zureick [65] proposes a reduction of the Euler's buckling load to take into account the effect of shear deformation, even though its influence in the overall global buckling load ($P_{bk,Global}$) in most cases is small,

$$P_{bk,Global} = \frac{P_{Euler}}{1 + P_{Euler}/A_{web}G_{LT}} = 27.4 \text{ kN} \quad (3)$$

where A_{web} is the web area ($A_{web} = 720 \text{ mm}^2$) and G_{LT} is the shear modulus ($G_{LT} = 3.89 \text{ GPa}$).

The analytical results are slightly higher than the experimental buckling loads after buckling was triggered (in average 25.8 kN, limit load) – the relative difference is about 6%. The higher difference between analytical predictions and the critical load provided by the Southwell method (roughly 18%) is explained by the existence of residual friction forces in the spherical hinges (even though efforts were carried out in

order to minimize them). This fact suggests that the structural design of compressed GFRP profiles considering free rotational end supports may lead to overly conservative solutions.

The local buckling critical load ($P_{bk,Local}$) for specimens of series BC was determined by applying the modified Southwell method proposed by Barbero and Trovillion [70],

$$P = P_{bk,Local} + \frac{1}{2}P^{(2)}s^2 \quad (4)$$

where P is the applied load, $P^{(2)}$ is the curvature of the post-critical path and s is the perturbation parameter. In this campaign, bending strains measured in the flanges' strain gauges were used as perturbation parameter. Results are presented in Table 3.4. The average experimental local buckling critical load (208.6 kN) was compared with an analytical prediction using Kollár's orthotropic plate theory [71]. The critical wall was first determined by calculating the critical stress of both the flanges and the web using respectively Equations (5) and (6),

$$(\sigma_{free}^{ss})_f = \frac{\pi^2}{t(b_f/2)^2} \left[D_L \left(\frac{b_f/2}{a} \right) + \frac{12}{\pi^2} D_s \right] = 194.5 \text{ MPa} \quad (5)$$

$$(\sigma_{ss})_w = \frac{2\pi^2}{t d_w^2} (\sqrt{D_L D_T} + D_{LT} + 2D_S) = 145.8 \text{ MPa} \quad (6)$$

where t is the wall thickness ($t = 6 \text{ mm}$), b_f is the flange width ($b_f = 60 \text{ mm}$), a is the half-wave length (one assumed $a = 2.5 \times b_f = 150 \text{ mm}$ [2]), d_w is the web depth ($d_w = 108 \text{ mm}$) and D_L , D_T , D_{LT} and D_S are the longitudinal, transverse, coupling and shear flexural rigidities ($D_L = 0.532 \text{ kN/m}$, $D_T = 0.157 \text{ kN/m}$, $D_{LT} = 0.044 \text{ kN/m}$ and $D_S = 0.070 \text{ kN/m}$).

The above mentioned analytical results show that the web is the critical wall. The following equation was then used to determine the local buckling critical stress taking into account the elastic restriction provided by the flanges to the web's longitudinal edges,

$$\sigma_{cr}^{local,l-web} = \frac{\pi^2}{t d_w^2} \left[2\sqrt{(D_L D_T)(1 + 4.139\xi)} + (D_{LT} + 2D_S)(2 + 0.62\xi^2) \right] = 156.3 \text{ MPa} \quad (7)$$

where ζ is the factor that accounts for the flanges' restriction ($\zeta = 0.153$). Considering the compressive stress as uniform in the whole cross-section, the local buckling critical load is given by the following equation,

$$P_{bk,Local} = \sigma_{cr}^{local,I-web} A = 213.8 \text{ kN} \quad (8)$$

where A is the cross-section area ($A = 1.416 \times 10^{-3} \text{ m}^2$). This local buckling load presents very good agreement with experimental results obtained in the present study (relative difference of only 2.5%).

3.4 NUMERICAL STUDY

3.4.1 Objectives

Numerical models using the finite element method (FEM) and the generalized beam theory (GBT) were developed aiming at comparing experimental and numerical data and validating numerical models. Linear buckling analyses were performed using ABAQUS software [72] and GBTUL software [73,74]. The main objective of both analyses was to determine the elastic critical loads of each series' columns as well as the corresponding buckling modes. GBT was used mainly because it allows identifying the buckling modes in a more intuitive way, *i.e.* with more physical meaning. Numerical results were then compared to experimental data to evaluate the accuracy of those simulation tools. In addition, simulations obtained from each numerical approach were also compared, highlighting the modal nature of GBT results. Finally, in order to determine the initial failure load, geometrically nonlinear analyses were carried out using ABAQUS software. One should be aware that the material progressive damage was not considered in the present study. Therefore, the initial failure load provides a conservative result of the effective ultimate load.

3.4.2 Numerical models

3.4.2.1 Geometrical and mechanical properties

Both models were defined with the same mechanical properties (*cf.* Table 3.1, page 25). The adopted geometrical properties were also the same for both numerical approaches. The web height was considered to be 114 mm (distance between both flanges' mid line) while the flange width was considered to be 60 mm. The wall thickness was considered to be 6 mm (constant in the whole cross section).

3.4.2.2 ABAQUS model

Shell finite element (SFE) models were developed, using the ABAQUS Standard software [72], in order to evaluate their applicability in predicting the ultimate load of eccentrically loaded columns. A 17-node cross-section discretization was used and isoparametric shell elements with four nodes, full integration (S4) and five integration points across the thickness were adopted. The flanges and web were meshed uniformly, with 4 elements across the width for each flange and 8 elements across the web height. The models were meshed with 50 elements along the length, therefore aspect ratios of 2:1 and 2.1:1 for the flanges and web, respectively, were obtained, which were considered to be small enough not to affect the accuracy of numerical calculations [63]. The total number of elements was 800 and the total number of nodes was 867. Four groups of rigid elements (R3D3) were meshed at each column end to transmit the load and the boundary conditions, as well as to simulate the influence of the steel blocks. The top and bottom elements converged into two auxiliary nodes with varying z -axis coordinate in order to simulate the eccentric loading, while the elements which simulate the steel blocks converged to the node located in the longitudinal axis. A compressive load was applied at the top node in the y -axis direction. Boundary conditions were different for each series, according to the experimental tests – Table 3.3 (page 27) presents the displacement and rotation restrictions at the top and bottom auxiliary nodes. Preliminary studies on the convergence of FE mesh were performed (not shown here).

3.4.2.3 GBT model

In the GBT buckling analysis, seven intermediate nodes across the web and one across each half-flange were defined, leading to a total of 17 nodes in the cross-section (according to the mesh geometry defined in ABAQUS). A linear buckling analysis was performed using GBT in which the most relevant section deformation modes are illustrated in Figure 3.12. The same analysis was performed using ABAQUS with the main objective of determining the numerical critical loads of each series' columns.

Regarding the model of series NBC, the participation of all deformation modes available was considered. For all other series' models (BC, EBCI and EBCII), the participation of the deformation modes **3** and **4** (minor-axis bending and torsion, respectively) was set to null due to the boundary restrictions imposed in the experiments, namely the lateral bracing system adopted. The end supports varied from model to model according to the experimental campaign. For series EBCI and EBCII, and since GBT is a “beam theory”, the eccentricity was simulated by applying a bending moment at both ends ($M = P \times e$) of 1.83 kN.cm and 3.65 kN.cm, respectively (corresponding to the application of a “unit”, 1.0 kN, compression load). Results obtained from GBT analysis are discussed next and compared with both experimental data and the numerical results provided by the ABAQUS analyses.

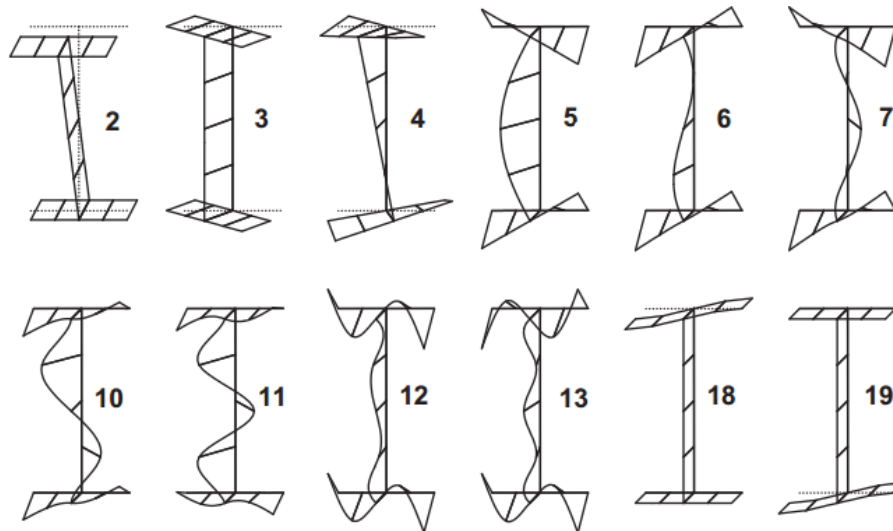


Figure 3.12: Shapes of the most relevant GBT deformation modes [26].

3.4.3 Elastic buckling analysis

The critical buckling loads of each series were predicted by performing a GBT linear buckling analysis. Such analysis also provided the participation of each section deformation mode in the overall buckling mode. For more details about GBT mode participation, the interested reader is referred to [73,75]. Results were then compared to the same analysis performed using ABAQUS. The GBT and FEM critical loads as well as the participation of GBT deformation modes in the critical buckling mode are presented in Table 3.4 (page 32).

It should be mentioned that the participation of deformation mode **6** (web in double curvature, *cf.* Figure 3.12) increases with the eccentricity, while the contribution of deformation mode **5** (web in single curvature, *cf.* Figure 3.12) drops. Note that the flanges twist in the same direction for mode **6**, while they rotate in opposite direction for mode **5**. The increasing contribution of mode **6** and decreasing contribution of mode **5** led to different twist of the flanges. For pure compression (BC), both flanges twist the same amount in opposite direction because mode **6** is absent. For increasing eccentricity, the less compressed flange twists less than the most compressed flange and this effect is given by the addition of mode **6** and its increasing participation. It is interesting to note that there is a linear (proportional trend) between the eccentricity level (e/h) and the participation of mode **6**: $e/h=0$ and 0% participation; $e/h=0.15$ and 17.0% participation; $e/h=0.30$ and 28.5% participation. However, it should be mentioned that the participation of mode **6** for pure bending ($e/h \rightarrow \infty$) is about 50%. Therefore, the variation of mode **6** participation with the ratio e/h should be highly nonlinear for $e/h > 0.3$.

The numerical results presented a difference of roughly 8% *w.r.t.* the experimental critical buckling loads of both series NBC (considering the limit load) and BC, which is very satisfactory.

Figure 3.13 illustrates the buckled shape of the first buckling mode of the four different series in ABAQUS. The same buckled shapes of the first buckling mode of the four different series obtained in GBTUL are presented in Figure 3.14.

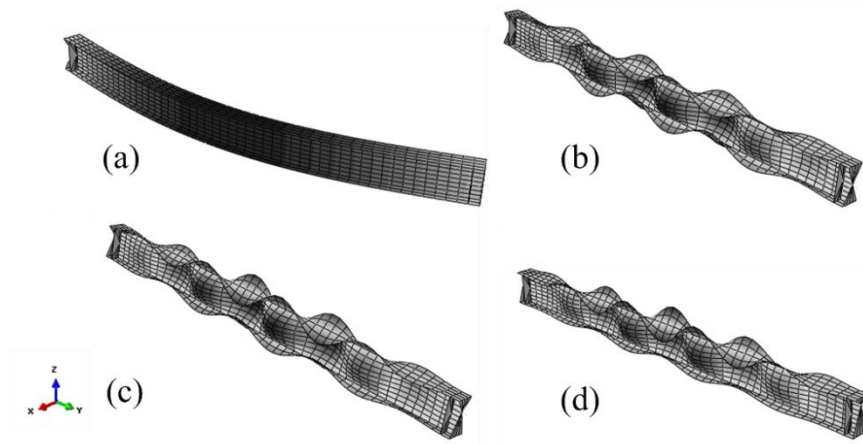


Figure 3.13: Buckled shape of the first buckling mode: (a) series NBC, (b) series BC, (c) series EBCI and (d) series EBCII (ABAQUS)

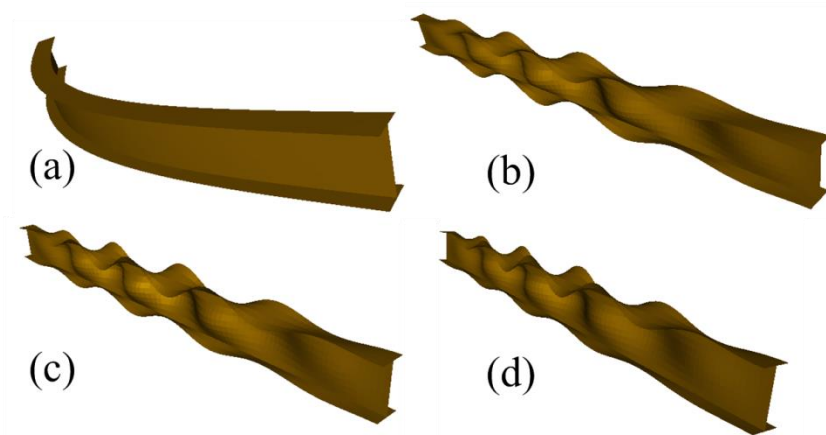


Figure 3.14: Buckled shape of the first buckling mode: (a) series NBC, (b) series BC, (c) series EBCI and (d) series EBCII (GBTUL).

As one may see in both analyses, from series BC (b) to series EBCII (d), the less compressed flange (lower flange in Figure 3.13 and Figure 3.14) exhibits waves with lower amplitudes while the compressed flange remains with the same amplitude.

3.4.4 Nonlinear analysis

A nonlinear analysis (NLA) was carried out using ABAQUS Standard software and considering an initial imperfection according to each series' first buckling modes. For the NLA, the modified Riks method with arc-length control was used to determine the incremental-iterative equilibrium configurations of the column. Initial geometrical imperfections had the shape of the first buckling mode obtained from the elastic buckling analysis with maximum amplitude of 0.1 mm. This value was

considered to be small enough not to influence the post-buckled shape, but sufficiently large to avoid numerical problems close to the bifurcation point [4]. The NLA does not include the material progressive failure; therefore, the initial failure load (P_I) was predicted through the Tsai-Hill failure criterion [76], whose failure index (I_F) is given by the following equation,

$$I_F = \frac{\sigma_L^2}{\sigma_{u,L}^2} - \frac{\sigma_L \sigma_T}{\sigma_{u,L}^2} + \frac{\sigma_T^2}{\sigma_{u,T}^2} + \frac{\tau_{LT}^2}{\tau_u^2} < 1.0 \quad (9)$$

where σ_L is the longitudinal stress, σ_T is the transverse stress and τ_{LT} is the shear stress; $\sigma_{u,L}$ is the longitudinal strength, $\sigma_{u,T}$ is the transverse strength and τ_u is the shear strength. The strength values are given in Table 3.1 (page 25). Results regarding the initial failure load as well as the corresponding axial shortening for each series' model are presented in Table 3.5. Also the post-critical strength is presented in Table 3.5 in the form of initial failure load/critical load ratio (P_I/P_{bk}).

Table 3.5: Initial failure loads (P_I) and respective axial shortening obtained in the ABAQUS nonlinear analysis; comparison with the elastic buckling load.

Series	P_I (kN)	Axial shortening (mm)	P_I/P_{bk}
NBC	25.9	18.3	1.01
BC	203.5	7.68	1.05
EBCI	155.8	6.45	0.83
EBCII	134.9	8.82	0.80

The load vs. axial shortening numerical curves for each series are plotted in Figure 3.5 (page 30), in which they are compared with their experimental counterparts. Numerical curves present a very satisfactory agreement with the experimental ones. Only initial failure loads present larger differences when compared to the experimental ultimate load (between 9.5% and 20.1%), being conservative in all series. However, as already mentioned, such difference was expected to occur since the comparison is being performed between different parameters (ultimate load vs. first failure load). In order to compare experimental and numerical ultimate loads directly, one should have performed more complex simulations including material progressive failure. These issues will be addressed and discussed in the following chapters in which the material progressive damage is addressed.

Longitudinal strains were monitored in the elements equivalent to the position of the strain gauges in the experimental campaign. Figure 3.8 (page 33) depicts the average longitudinal stress (load divided by the total cross-section area) vs. longitudinal strain numerical curves, comparing them with those obtained in the experimental programme. Again, a fairly close agreement was obtained.

Figure 3.15 depicts the variation of the ratios σ_L/σ_{Lu} and τ/τ_u with the Tsai-Hill index I_F (see Equation (9)), where σ_L , σ_{Lu} , τ , τ_u are the acting longitudinal stress, longitudinal strength, acting shear stress and shear strength, respectively. In the case of series NBC (Figure 3.15(a)), only longitudinal stresses come into play. In the case of series BC, EBCI and EBCII (Figure 3.15(b), (c), (d)), both longitudinal and shear stresses are meaningful. The critical load of BC series occurs for $I_F \approx 0.35$ (Figure 3.15(b)), that is previously to the first failure occurrence ($P_l/P_{bk} = 1.05$ – cf. Table 3.5). This value corresponds to a transition point between the uniform compression behaviour ($I_F < 0.35$, almost null τ/τ_u values and linear increase of ratio σ_L/σ_{Lu} with I_F) and local buckling behaviour ($I_F > 0.35$, linear increase of ratio τ/τ_u with I_F and roughly uniform σ_L/σ_{Lu} ratio). When I_F reaches 1.0 (column first failure), it is seen that the contribution of shear stress ratio ($\tau/\tau_u=0.88$) is almost twice that of longitudinal stress ratio ($\sigma_L/\sigma_{Lu} = 0.47$). Therefore, it can be concluded that the shear stress component at the web-flange junction and arising from local buckling (flange twisting) triggers the collapse of the column.

The critical load of EBCI and EBCII series takes place for $I_F > 1.0$ (note that $P_l/P_{bk} = 0.83$ and 0.80 – cf. Table 3.5), which means that first failure occurs prior to column local buckling. Thus, there are almost linear variations of the ratios σ_L/σ_{Lu} and τ/τ_u with the Tsai-Hill index I_F . In case of EBCI (Figure 3.15(c)), one has $\sigma_L/\sigma_{Lu} > \tau/\tau_u$ for $I_F < 0.81$. However, for $I_F > 0.81$, this trend reverses ($\tau/\tau_u > \sigma_L/\sigma_{Lu}$) and first failure of the EBCI takes place mainly due to shear stress component associated to local buckling of the most compressed flange (flange closer to the load application point). In case of EBCII (Figure 3.15(d)), one has always $\tau/\tau_u > \sigma_L/\sigma_{Lu}$, regardless of the I_F value. This evidence could be attributed to the amplification of initial imperfection (with local shape) right from the beginning of load application⁷. Similarly, the most relevant contribution to EBCII first failure ($I_F = 1.0$) stems from shear stress component.

Using the ABAQUS models, a parametric study was performed in which the critical and initial failure loads were computed for different eccentricities than those tested in the experimental campaign (Figure 3.7, page 31). It is clear that the initial failure load curve is roughly parallel to that of the experimental ultimate load.

⁷ This fact does not necessarily mean that acting shear stresses are higher than acting longitudinal stresses. Note that one used stress ratios (τ/τ_u and σ_L/σ_{Lu}) and the longitudinal strength ($\sigma_{Lu} = 360.3$ MPa) is more than eleven times the shear strength ($\tau_u = 30.8$ MPa) – see Table 3.1 (page 25).

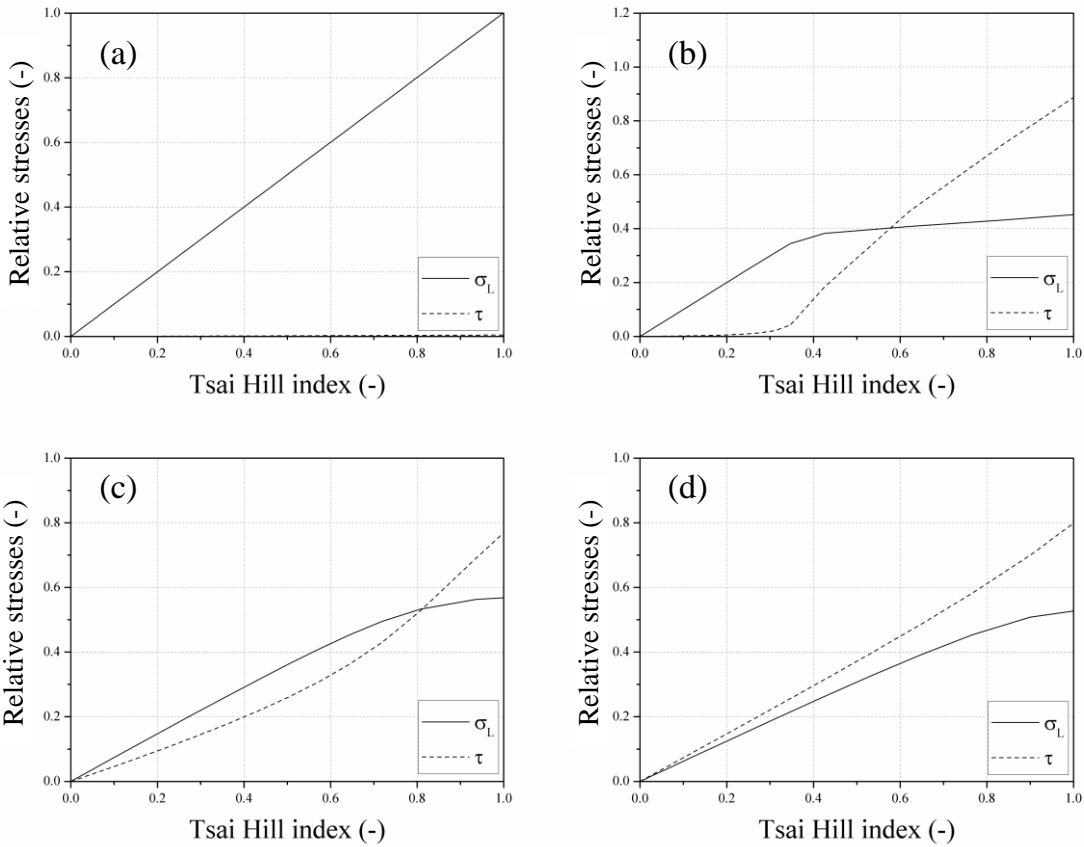


Figure 3.15: Tsai–Hill failure index vs. relative longitudinal and shear stresses curves: (a) series NBC, (b) series BC, (c) series EBCI and (d) series ECBII.

3.5 CONCLUDING REMARKS

This chapter presented an experimental and numerical study on the effect of small eccentric loading ($e/h = 0.00, 0.15$ and 0.30) about the major axis of GFRP pultruded I-section columns. The following main conclusions are drawn:

1. Results obtained for non-braced (series NBC) and braced (series BC) columns under concentric loading outlined the importance of designing lateral bracing systems in compressed GFRP members as the ultimate loads obtained for braced columns were roughly 8 times higher than in non-braced columns.
2. Results obtained for braced columns under concentric (BC) and eccentric (EBCI and EBCII) loading showed that small eccentricities that may arise from both geometrical imperfections of the members and construction errors are of major importance for the behaviour of GFRP pultruded members under compression.
3. Columns subjected to loads applied within the kern boundaries exhibited similar initial axial stiffness compared to concentrically loaded columns; however, for increasing load levels, their axial stiffness

decreased due to bowing and second-order $P-\delta$ effects. Eccentrically loaded columns proved to be highly sensitive to those small eccentricities with an approximately linear load capacity decrease up to 40%.

4. In non-braced columns global buckling about the minor axis occurred. In braced columns failure was caused by local buckling, which triggered web-flange separation followed by material crushing. This failure mode is due to high shear stresses in the web-flange junction near inflection points of the buckled shape. In eccentrically loaded columns, such material crushing developed in the most compressed flange and was followed by the global buckling of the columns about the major axis.
5. Estimates for the global and local buckling loads of series NBC and BC obtained using respectively Euler's and Kollar's equations provided very good agreement with experimental data (relative differences of 6% and 2.5%, respectively).
6. The linear elastic analyses performed using both GBT and ABAQUS provided good agreement with experimental results of series NBC and BC.
7. GBT results showed that the combination of local modes **5** (symmetric configuration) and **6** (anti-symmetric configuration) changes with the eccentricity. For increasing eccentricity level, the less compressed flange twists less than the most compressed flange and this effect is given by the increasing participation of mode **6** (anti-symmetric) and decreasing participation of mode **5** (symmetric). It was interesting to note that the variation of mode **6** participation with the eccentricity level (e/h) was nearly linear inside the cross-section kern. Noting that the participation of this mode is nearly 50% for pure bending ($e/h \rightarrow \infty$), this variation should be highly nonlinear for higher eccentricity levels (outside the cross-section kern).
8. Results obtained from the nonlinear analysis performed with ABAQUS, in terms of axial strains and axial shortening, were very consistent with experimental data. Using the Tsai-Hill criterion, it was found that longitudinal stresses have a prevalent contribution to the failure index in the linear elastic stages (for series NBC, BC and EBCI). However, as the load increases to levels closer to the local buckling load, the cross-section starts to deform and flange twisting emerges, thus leading to a key role of the shear stress components. At failure, their contribution to the index failure is always higher than the longitudinal stress counterpart, regardless of the eccentricity level.

CHAPTER 4

STRUCTURAL BEHAVIOUR OF HYBRID FRP COLUMNS

4.1 PRELIMINARY CONSIDERATIONS

The structural behaviour of GFRP pultruded members subjected to compression has been already widely investigated through experimental, analytical and numerical studies, which are summarised next. These studies have shown that the buckling behaviour of GFRP members is a major issue in their structural design, since they are usually slender thin-walled profiles (similar to commercial steel profiles) with relatively low longitudinal elastic modulus (about six to seven times lower than that of steel).

Barbero and Tomblin studied the global and local buckling phenomena in wide-flange GFRP pultruded columns [19–21]. Experimental global buckling critical loads, computed using the Southwell plot method, were compared to predictions provided by Euler's formula, which proved to be very accurate (relative differences below 6%) [19]. Regarding the local buckling phenomenon, experimental data were compared to theoretical predictions obtained using the Levy method. Experimental and analytical results presented a reasonable agreement for the shorter columns, while for the intermediate columns (which, albeit longer, also exhibited local buckling) the relative difference was up to 24%. The higher differences obtained for intermediate columns were associated to a possible interaction between global and local buckling modes [20]. Later, the same authors presented a further study about the interaction between global and local modes, and proposed a design equation for intermediate columns featuring an interaction constant calibrated with the experimental results [21].

Mottram [23] also studied the local buckling phenomenon in wide-flange pultruded GFRP profiles. Results from tests on short columns were compared to analytical predictions provided by nine different design equations included in manuals and publications related to pultruded columns. The author found the design equations often difficult to implement due to the lack of information provided by manufacturers regarding the elastic and strength material properties, namely the shear modulus, which plays a major role in local buckling phenomena.

Ragheb [45] performed a parametric numerical study about the behaviour of pultruded hybrid C-GFRP profiles using the commercial software ANSYS. Eight different fibre architectures (or patterns), with varying carbon fibre amount, were designed aiming at maximizing the critical buckling load of I-section beams under four-point bending. Results from the buckling analysis indicated that the critical buckling load is highly dependent on the CF reinforcement geometry and content. Some of the tested patterns presented a critical buckling load even lower than that of the all-GFRP reference section. The optimal CF geometry consisted of reinforcing the web-flange junction – it provided the maximum increase of critical load and, at the same time, it was the most economical hybrid solution. The hybrid pattern in which the cross-section was reinforced in the edges of the flanges caused a reduction in the critical load. Despite their relevance, the numerical results obtained in this study were only validated for the all-GFRP series – no experimental data were available for the hybrid cross-sections. Moreover, neither the delamination between the GFRP and the CFRP layers nor the failure behaviour of the FRP beams were addressed.

Preceding the research presented in this thesis (but partly developed in its framework), Correia *et al.* [4] studied the influence of introducing longitudinal CF mats in I-section pultruded GFRP short columns by experimental, analytical and numerical means. Such hybridization procedure proved to be effective, increasing both the axial stiffness and the ultimate load of the hybrid columns. Shell finite element (FE) models were developed in the commercial software ABAQUS and used to carry out geometrically nonlinear analyses, in which the failure initiation loads were predicted using the Tsai-Hill criterion. The numerical results compared well to the experimental data, with relative differences in terms of ultimate load below 5%. In this study, only the local buckling behaviour was addressed (short columns) and the delamination of the CF mats was not considered in the numerical models.

Due to their intrinsic orthotropic behaviour and brittleness, the complexity of computational models that describe the constitutive stress-strain laws of FRP materials is much higher than those of isotropic ductile materials (*e.g.*, steel). This complexity underpins the widespread absence of reliable numerical studies on the progressive failure of pultruded FRP members. Effectively, scarce information is still available regarding the progressive failure mechanisms of those members.

Several criteria (*e.g.*, Tsai-Hill, Tsai-Wu, Maximum Stress and Maximum Strain) have been implemented in numerical analyses to simulate the ultimate behaviour of FRP members [4,15,63]. Although these criteria enable the identification of failure initiation, they do not influence the subsequent incremental stiffness. Even though such criteria usually provide reasonable estimates of collapse loads of FRP columns [4], they have been found to largely underestimate the strength of FRP members under other types of loading [15]. Recently, Fernandes *et al.* [15] found that the aforementioned criteria led to inaccurate (too conservative) ultimate load estimates of FRP members under very localized forces.

The most recent versions of the commercial software ABAQUS [72] include a fibre composite specific progressive damage analysis, which combines the Hashin damage initiation criterion [77,78] with a damage evolution model based on the approach proposed by Camanho and Dávila [79]. Despite being a very powerful and useful tool for the modelling and simulation of composite structures, there is still a lack of scientific information available for the practice-oriented engineer to implement such damage analyses. Most likely, the spread use of the Hashin-based damage analysis has been hindered by the large amount of required material data, such as the strengths, fracture energies and viscous regularization parameters, as manufacturers often do not report these data.

Before having become a built-in ABAQUS feature, the progressive damage analysis comprising the Hashin criterion could only be implemented using User-Defined Material Models (UMAT). Knight [80] presents an overview of several laminated composites' failure initiation criteria (Maximum Stress/Strain, Tsai-Wu and Hashin) and damage progression models (ply-discounting and internal state variable) using ABAQUS/Standard, as well as the UMAT implementation and some numerical results.

To the best of the author's knowledge, there are very few studies that address the built-in Hashin-based damage progressive analysis within ABAQUS framework to analyse FRP laminates. Barbero *et al.* [31] proposed a methodology for the determination of material parameters to be used in the ABAQUS progressive damage analysis. Considering a given ply sequence, these authors performed several simulations using random transverse tensile strength and fracture energy values, within reasonable bounds and using an error minimization algorithm between the numerical and experimental results. Using the calibrated properties, they compared numerical and experimental results for other ply sequences and obtained good accuracy whenever failure was governed by transverse tensile damage. Coelho *et al.* [30] developed finite element (FE) guidelines for the simulation of notched composite laminated plates under in-plane tension using Hashin-based damage analysis within ABAQUS framework. Both carbon/epoxy composites used in aerospace engineering and pultruded glass fibre reinforced polymer (GFRP) laminates used in civil engineering were simulated and consistency between numerical and experimental results was obtained. These authors adopted material properties available in the literature and implemented a sequence of operations for an efficient and accurate simulation, having provided the following recommendations: (i) model simplifications for symmetric boundary conditions should not be employed; (ii) incremental displacements should be imposed rather than applied loads; and (iii) global stabilization and viscous regularization should be used to improve numerical convergence.

This chapter presents experimental, numerical and analytical studies about the structural behaviour of pultruded hybrid FRP columns, comprising both glass and carbon fibres. Due to the fact that the structural design of GFRP members is often governed by serviceability limit states (deformability and vibrations) and buckling phenomena, the partial replacement of the glass reinforcement by carbon fibres (stiffer yet more expensive material) is a possible approach to improve their performance [2]. Nonetheless, previous research shows that although providing stiffness increase, for relatively high strain levels the introduction of CF mats in GFRP pultruded profiles might lead to premature delamination at the interface between both reinforcing materials [8].

A reference I-section GFRP profile and a total of five hybrid C-GFRP prototypes, with incorporation of different types and architectures of CF reinforcement, were designed according to previous experience obtained by the author and information from the literature. The profiles were manufactured by *ALTO Perfis Pultrudidos, Lda*. Regarding the compressive behaviour, only four of these hybrid series were tested (*cf.* section 4.2.2); the remaining series was tested only in bending (*cf.* Chapter 5). Three different lengths were defined for the columns: short, intermediate and long. The main goal was to investigate the influence of introducing CF reinforcement in GFRP pultruded columns with different slenderness values, and hence exhibiting different governing failure modes, including those triggered by local and global buckling. Due to the scarce number of previous Hashin-based studies, namely in what concerns pultruded profiles, one of the objectives of the study described in this chapter is also to investigate the suitability of that failure criterion to predict the ultimate behaviour of hybrid FRP members under compression. Hence, sections 4.4 and 4.5 present a numerical study on the progressive failure of the studied I-section pultruded column. Three-dimensional FE models of those columns using the commercial software ABAQUS [72] and comprising the Hashin-based material damage analysis are presented. The FE models were validated through the comparison between numerical and experimental results. Additionally, design formulae existing in current standards are used to predict the ultimate strength of hybrid C-GFRP prototypes.

4.2 EXPERIMENTAL STUDY

4.2.1 Objectives

As already mentioned, the main objectives of the experimental study were to evaluate the main advantages and drawbacks of introducing CF mats in all-GFRP profiles subjected to compression, regarding their performance for both serviceability and ultimate limit states. Three different column heights were tested aiming at studying local and global buckling phenomena, namely the influence of introducing the CF reinforcement in those buckling modes. Several hybrid series were designed and manufactured comprising different types and architectures of CF mats (unidirectional and bidirectional).

This experimental study allowed determining, for the different series, the full-section longitudinal elastic modulus under compression ($E_{fs,c}$), the critical buckling load (P_{bk}), and the ultimate load (P_u). In addition, the different buckling modes were analysed.

4.2.2 Experimental series

As mentioned the five hybrid FRP pultruded series were designed based on previous research carried out by the author [4,8] and the literature review, namely the numerical study of Ragheb [45]. All pultruded profiles were manufactured and supplied by *ALTO Perfis Pultrudidos, Lda* with the same I-section geometry ($200 \times 100 \times 10$ mm, web height \times flange width \times wall thickness). In their design stage (performed by the author) the following options were taken to allow for a sound comparison between the different hybrid series: (i) whenever possible, the introduction of the CF mats was made by replacing the original GF mats and (ii) roughly similar CF volumes were used in each series.

Two different types of CF reinforcement were used in this experimental programme: (i) unidirectional (0°) 350 g/m^2 mats, and (ii) bidirectional ($0^\circ/90^\circ$) 400 g/m^2 mats. Despite the efforts made in using CF mats with the same fibre volume, this was the closest match made available by the manufacturer. Thus, the unidirectional and bidirectional mats present a difference of roughly 12.5% in terms of CF volume.

The introduction of unidirectional or bidirectional CF mats in GFRP pultruded profiles obviously presented different scopes. Unidirectional CF mats consist of a set of fibres aligned in the 0° direction, thus providing an increase in the longitudinal stiffness of axial and flexural members. In this case, the transverse and shear stiffness are nearly unaffected. On the other hand, bidirectional CF mats present fibre filaments oriented in the 0° and 90° directions roughly in the same proportion, which allows increasing the longitudinal, transverse and shear stiffness; this can be particularly advantageous for members subjected to local buckling phenomena and those compressed in the transverse direction [2].

In all hybrid series, despite slight differences in fibre volume (for the different series), a total of four CF mats with 100 mm of width and roughly 0.25 mm of thickness were used. The CF reinforcement configuration adopted in each series, illustrated in Figure 4.1, prompts the following comments:

- Series S0 – an all-GFRP profile, was defined as the reference series.
- Series S1 – presents a set of two unidirectional CF mats in one flange and another set of two bidirectional CF mats in the other flange. Both sets of mats were introduced in the midline of both flanges aiming at maximizing their saturation and minimizing delamination issues. This series was originally designed for flexural members (Chapter 5), but one decided to study the behaviour of this asymmetric cross-section also under compression.

- Series S2 – presents a configuration of CF mats similar to those used in series S1, but now using unidirectional mats in both flanges. This series (and the next, S3) were designed to compare the structural behaviour exhibited by profiles with unidirectional vs. bidirectional CF mats.
- Series S3 – is similar to series S1 and S2, but features two sets of bidirectional CF mats on both flanges. Initially, series S3 was supposed to present the same CF architecture as series S1 and S2, differing only in the type of reinforcement. However, due to difficulties reported by the manufacturer in fully saturating the coupled set of mats, one decided to separate them, placing one at the outer face of the flange and the other inside it.
- Series S4 – was designed to increase the shear stiffness and strength of the web-flange junction, presenting four CF bidirectional mats around that particular location. After local buckling is triggered, high shear stresses develop at the inflection points of the buckled shape near the web-flange junction [4]. Therefore, the mats were introduced in such a position to prevent premature failure due to stress concentrations in those zones. However, due to the manufacturer production procedure, it was not possible to replace the GF mats in this series; instead, the CF reinforcement was stitched to the superficial GF mats, and therefore series S4 presented a slightly higher fibre volume than the remaining series.
- Series S5 – since compressed walls are more prone to delamination issues and fibre buckling, this series comprised four mats of unidirectional CF fibres in the bottom (tensioned) flange aiming at mitigating delamination even further and thus providing a constant bending stiffness up to failure (this series was addressed only for flexural members – Chapter 5). However, this architecture presents a noticeable drawback: since the cross-section is no longer bisymmetric, the neutral axis offsets from the centroid in the direction of the bottom flange, thus increasing the stresses developed in the top flange. This series was designed aiming also at hybrid applications, e.g. GFRP-concrete cross-sections, such as those tested by Gonilha *et al.* [50–53,81].

For each series (reference and hybrid), three replicate specimens with the following three different lengths (L) were produced:

- $L = 60$ cm – short columns, with failure governed by local buckling modes;
- $L = 100$ cm – intermediate columns, with failure due to the interaction between global and local buckling modes;
- $L = 200$ cm – long columns, with failure governed by global buckling modes.

In this campaign, a total of 45 specimens were tested under concentric compression. To identify each specimen as unique, the following nomenclature was adopted: *height_series_specimen*. For instance, the second specimen of the long columns of series S0 is identified as *200_S0_2*.

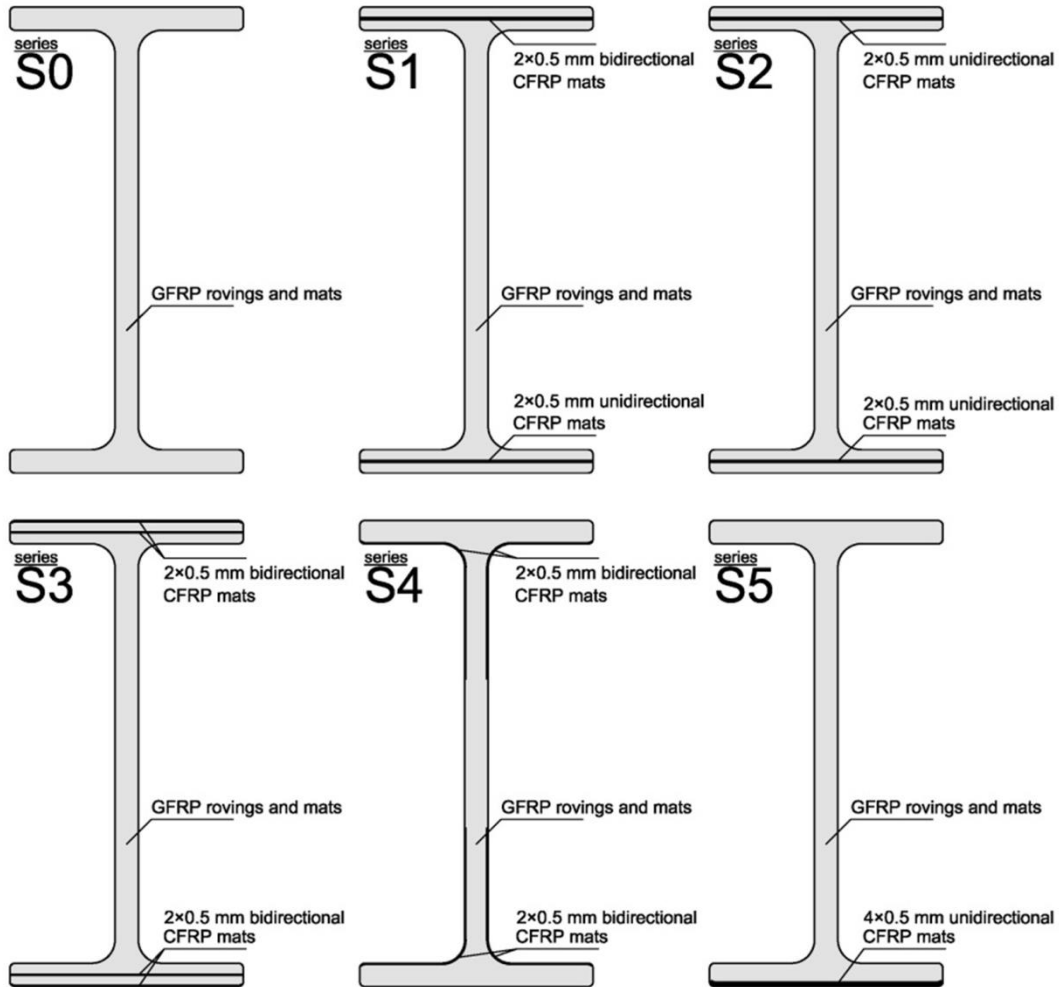


Figure 4.1: Reference GFRP (S0) and hybrid C-GFRP (S1 to S5) pultruded experimental series.

4.2.3 Material characterisation tests

The following material characterisation tests were performed on small-scale coupons extracted from the web of the reference profile (similar to that of the hybrid profiles) and the flanges of the different series: (i) tensile tests (according to ISO 527 [82,83]), (ii) compression tests (ASTM D695-02 [84]), (iii) in-plane shear tests (ISO 527-5 [85]), and (iv) interlaminar shear tests (ASTM D2344 [86]). The main stiffness and strength properties of the GFRP and C-GFRP laminates are listed in Table 4.1 and Table 4.2, where E is the Young's modulus, G is the shear modulus, ν is the Poisson ratio, σ is the axial strength, τ is the in-plane shear strength and F^{sbs} is the interlaminar shear strength; the subscripts L and T correspond to the longitudinal and transverse directions, while t and c correspond to tensile and compressive loading. The properties of the C-GFRP laminates were only determined for the architectures with two unidirectional or two bidirectional CFRP mats, and just for the longitudinal tensile load configuration. Note that the properties listed in Table 4.1 refer to the homogenized GFRP and C-GFRP hybrid laminates.

Table 4.1: Elastic properties of GFRP and C-GFRP laminates.

Type of laminate	$E_{L,t}$ (GPa)	$E_{L,c}$ (GPa)	$E_{T,c}$ (GPa)	G_{LT} (GPa)	ν
GFRP	32.7	33.4	10.8	3.65	0.266
Uni. C-GFRP	40.8 ⁽¹⁾	-	-	-	-
Bidir. C-GFRP	35.9 ⁽²⁾	-	-	-	-

⁽¹⁾ From the laminate geometry and fibre architecture, the unidirectional CFRP longitudinal elastic modulus was computed as 193 GPa based on the classical lamination theory (rule of mixtures).

⁽²⁾ Using the same procedure, the bidirectional CFRP longitudinal elastic modulus was computed as 95.9 GPa.

Table 4.2: Strength properties of GFRP laminate and C-GFRP laminae.

Type of laminate/laminae	$\sigma_{L,t}$ (MPa)	$\sigma_{L,c}$ (MPa)	$\sigma_{T,c}$ (MPa)	τ_{LT} (MPa)	F^{sbs} (MPa)
GFRP laminate	365	468	110	30.6	27.6
Uni. C-GFRP laminae	1389 ⁽¹⁾	-	-	-	-
Bidir. C-GFRP laminae	837 ⁽¹⁾	-	-	-	-

⁽¹⁾ The longitudinal strength corresponds to the CFRP layers only and was computed by multiplying the CFRP material longitudinal elastic modulus by the ply failure strain.

The properties obtained for the GFRP material were within typical bounds found in the literature [2]. The introduction of the CF mats allowed increasing the laminate (10 mm thick) longitudinal tensile stiffness by 24.7% and 9.8%, whether two layers of respectively unidirectional or bidirectional reinforcement were used. As expected, the unidirectional CF material provided a higher stiffness increase as its fibres are all aligned in the longitudinal direction.

4.2.4 Test setup and instrumentation

Figure 4.2 illustrates the test setup and instrumentation used in the experimental campaign, which presented slight differences for the various column heights tested. Contrary to the intermediate (Figure 4.2(b)) and long (Figure 4.2(c)) columns, in which the end sections were designed to rotate freely about the minor axis, the short columns' (Figure 4.2(a)) rotation at the end sections was fully restrained. This procedure aimed at the proper triggering of the local buckling phenomenon, since the behaviour of short columns is roughly equivalent to that of a long column laterally braced along its height; therefore, the (fixed) end supports of the short columns aimed at simulating two inflection sections of the long column's buckled shape, in which the section relative displacements and rotations are negligible.

Two machined steel blocks (with diameter of 250 mm, thickness of 60 mm and 30 mm deep grooves with the negatives of the I-section walls) were used in order to restrain any relative displacement or rotation of the end sections. To set free the rotation (for intermediate and long columns), a 7 mm deep chamfer was made in the back of the steel blocks, along the web, with an opening angle of 120°. The

negative piece consisted of a $30 \times 20 \text{ mm}^2$ rectangular solid bar machined into a sharpened wedge (with 90°) welded to a thick support plate. This procedure was made in an effort to mitigate the friction forces registered in Chapter 3 when using spherical hinges (even if using Teflon sheets in their interface). Figure 4.2(d) shows the end support system, namely the individual and assembled set of pieces.

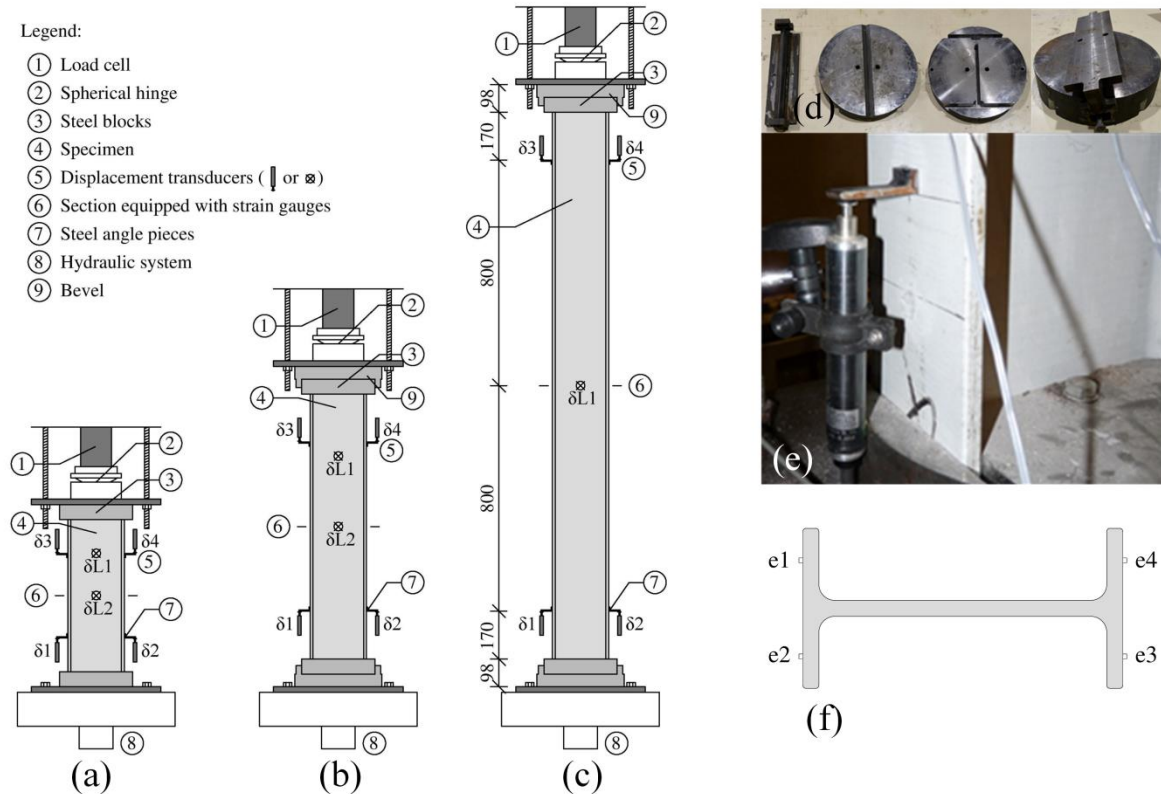


Figure 4.2: Test setup and instrumentation for (a) short, (b) intermediate and (c) long columns; (d) end support system; (e) bonded angle piece and transducer; (f) position of strain gauges.

The load was applied to the lower plate of the press by an *Enerpac* hydraulic system with capacity of 3000 kN and maximum stroke of 400 mm. The applied load was measured by means of a *Microtest* load cell with 3000 kN of capacity. All tests were conducted under load control, at an average speed of 1 kN/s. In order to measure the axial deformations, two (out of three) specimens within the same series and height were instrumented with strain gauges (*TML FLK-6-1-3L*) positioned at the mid height section, with an offset of 20 mm from the flange border (Figure 4.2(f)). Data were acquired at a rate of 5 Hz using *HBM Spider8* data loggers and registered in a PC.

The axial shortening was measured by four displacement transducers (*TML-10* and *TML-25*, with precision of 0.01 mm) applied in internal sections of the columns (Figure 4.2(e)), thus avoiding the effect of the local bearing at the end sections. The transducers were mounted on small steel angle pieces, which were bonded to the middle of each column's flanges with cyanoacrylate glue at

distances of 15 cm (short columns) or 20 cm (intermediate and long columns) from both end sections (Figure 4.2(e)).

Lateral deflections were measured in either one (long columns) or two (short and intermediate) cross-sections, using respectively one or two (according to the column's height) *TML-500* displacement transducers applied to the reference sections (Figure 4.2). Two different sections were monitored in the short and intermediate columns, because their critical local buckling loads associated to symmetric and anti-symmetric buckled shapes match (*cf.* section 4.5). That particularity does not apply to the global buckling phenomenon, in which the critical load of the first buckling mode is considerably lower than that of the second buckling mode; therefore, only one section was monitored, that presenting the highest deflection amplitude (the mid-height section).

4.3 EXPERIMENTAL RESULTS

4.3.1 Load vs. axial displacement behaviour

The axial load vs. displacement data enabled the determination of the axial stiffness under compression (K_c)⁸, which was used to compute the apparent full-section longitudinal elastic modulus ($E_{fs,c,transd}$), and the ultimate load (P_u). The axial shortening (ΔL) was calculated from the displacements measured by each displacement transducer. The apparent full-section longitudinal elastic modulus ($E_{fs,c,transd}$) was then determined using the following equation,

$$E_{fs,c,transd} = K_c \frac{L}{A} \quad (10)$$

in which L is the length of the column, and A is the cross-section area.

The ultimate load (P_u) corresponds to the maximum load attained by a given specimen before failure. Ultimate load results are only presented for short and intermediate columns, because the long column specimens were not loaded beyond failure.

Figure 4.3(a) presents a representative load vs. axial shortening (ΔL) curve of the short columns from series S0 (specimen 60_S0_2), as well as the corresponding displacements measured by each transducer ($\delta 1$ to $\delta 4$, position illustrated in Figure 4.2). Figure 4.3(b) depicts the comparison between the representative load vs. axial shortening curves of all series⁹.

⁸ To determine the compressive stiffness, a trend line was computed from the linear range of the load vs. axial shortening curves. For columns with the same height, a “preferred” load range was defined to compute the trend lines. If the limits of that range were somehow inadequate for a given specimen (due to setup adjustments or other perturbations in the measurements), a different range of values was chosen for that specimen only.

⁹ It is worth mentioning that specimen 60_S4_2 presented the lowest ultimate load among all specimens tested, but it has also presented a distinct failure mode. Contrary to all other specimens, in which several cracks were heard in the final stage of the test, this specimen collapsed due to flange wrinkling and web crushing with absolutely no prior warning of failure. This

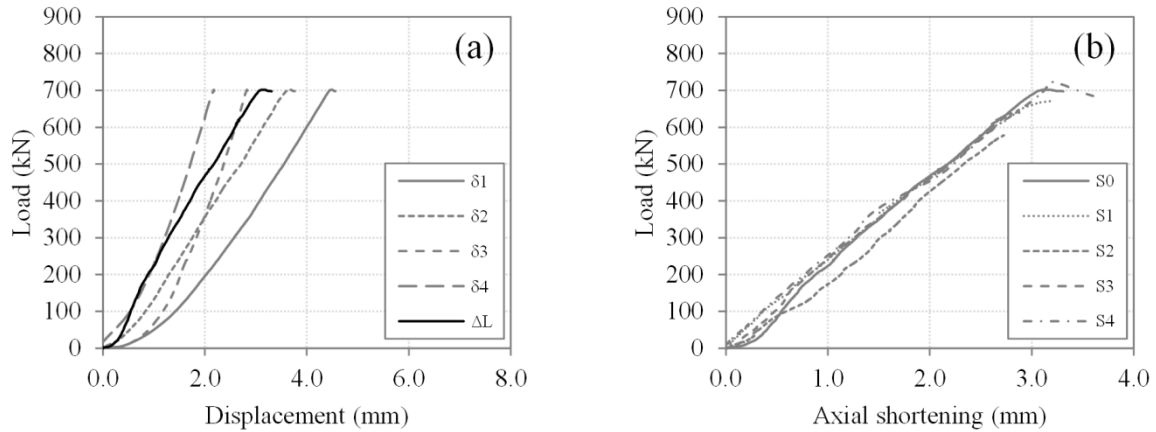


Figure 4.3: Short columns representative (a) load vs. displacement curves for series S0 (specimen 60_S0_2) and (b) load vs. axial shortening curves for all series.

That figure shows that the loading path was roughly linear, despite being sensitive to some setup adjustments throughout the test. Such fact highlights the elastic behaviour of all FRP series up to failure, despite some noise in the presented curves. From these results it is not possible to state if there was delamination of the CF mats. Furthermore, from Figure 4.3(b) the advantages of introducing CF mats are not so clear, since the ultimate load of the hybrid profiles did not show any improvement when compared to the reference profile.

Figure 4.4(a) illustrates the typical load vs. axial shortening curve for the intermediate columns, while Figure 4.4(b) presents the comparison between representative specimens of all series.

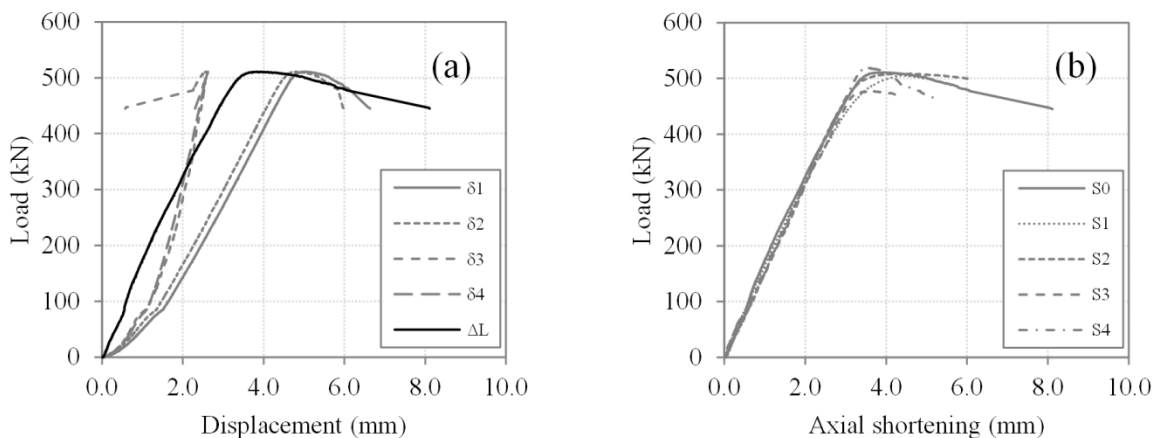


Figure 4.4: Intermediate columns representative (a) load vs. displacement curves for series S0 (specimen 100_S0_2) and (b) load vs. axial shortening curves for all series.

Figure 4.4 shows that the loading path of the intermediate columns was highly linear up to the onset of buckling. The displacements measured by each transducer showed a consistent difference in terms of

“premature collapse” suggests that specimen 60_S4_2 might have had some kind of imperfection, which has likely stemmed from the manufacturing process itself and thus it was not considered in this analysis.

slope before and after an axial load of around 80 kN, which most likely stemmed from small adjustments in the test setup. After buckling was triggered, all columns presented a progressive and significant load decrease, which may have been due to the interaction between global and local buckling modes and the material damage. From the experimental data, it is not possible to conclude about the cause of such decrease (one of those factors or a combination thereof)¹⁰.

Figure 4.5(a) presents the load vs. axial shortening curves of a representative reference long column specimen, whereas Figure 4.5(b) compares representative curves from all series. As mentioned, contrary to short and intermediate columns, none of the long columns collapsed; they were all unloaded after buckling without presenting any visible damage. The end of each curve corresponds to the instant when that column started being unloaded.

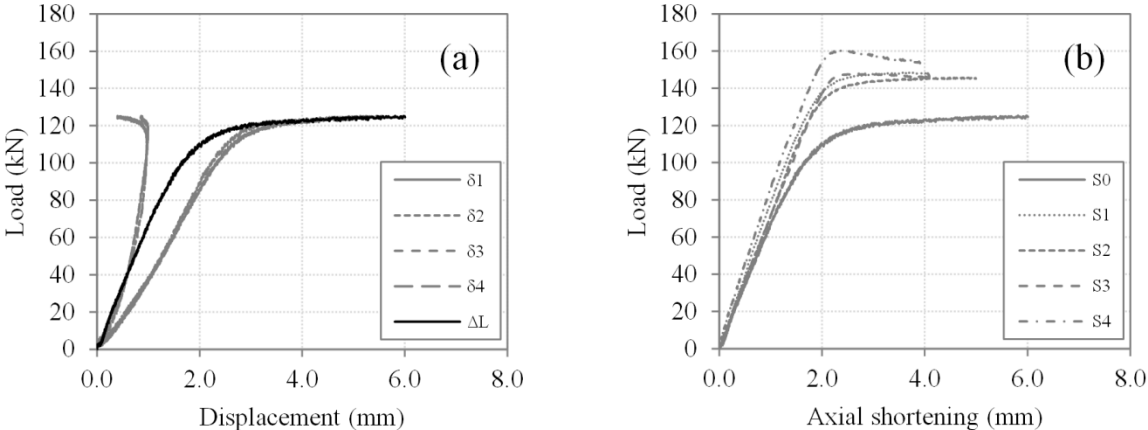


Figure 4.5: Long columns representative (a) load vs. displacement curves of series S0 (specimen 200_S0_2) and (b) load vs. axial shortening curves for all series.

Similarly to the intermediate columns, the load vs. axial shortening response of the long columns was also approximately linear prior to the triggering of (global) buckling. Subsequently, the columns maintained the applied load level for an increasing axial shortening. This (expected) behaviour was consistent with a stable post-buckling path. Some specimens, such as 200_S4_1 (Figure 4.5(b)), exhibited a (small) load peak that most likely stemmed from some residual friction forces at the end supports, despite the efforts in minimizing those forces (the usual behaviour of columns subjected to global buckling normally presents an asymptotic deflection path). Once the friction forces were overcome, the applied load decreased and tended to the critical load.

Table 4.3 presents a summary of the results obtained for each series and height, namely the compressive full-section longitudinal elastic modulus measured using the displacement transducers

¹⁰ Numerical models presented in sections 4.4 and 4.5, which allow accounting for the effect of material damage, provide further insights in this regard.

($E_{fs,c,transd}$), and the ultimate load (P_u); the elastic modulus measured with the strain gauges ($E_{fs,c,sg}$) and the buckling load (P_{bk}), discussed further ahead in this chapter, are also listed in Table 4.3.

Table 4.3: Summary of experimental results (average \pm standard deviation*).

Length	Series	$E_{fs,c,transd}$ (GPa)	$E_{fs,c,sg}$ (GPa)	$\Delta E_{fs,c,sg}$	P_{bk} (kN)	ΔP_{bk}	P_u (kN)	ΔP_u
Short (60 cm)	S0	-	37.4	-	689.9 \pm 22.1	-	733.7 \pm 32.9	-
	S1	-	38.1	1.9%	645.2	-6.5%	754.7 \pm 73.0	2.9%
	S2	-	38.5	2.9%	624.3	-9.5%	667.6 \pm 78.2	-9.0%
	S3	-	37.3	-0.3%	617.1	-10.6%	660.2 \pm 15.4	-10.0%
	S4	-	39.6	5.9%	682.8	-1.0%	689.9	-6.0%
Intermediate (100 cm)	S0	36.5 \pm 6.7	37.3	-	547.3 \pm 57.5	-	531.3 \pm 53.2	-
	S1	39.2 \pm 4.8	39.5	5.9%	529.6 \pm 4.8	-3.2%	511.4 \pm 18.1	-3.7%
	S2	39.1 \pm 5.4	38.7	3.8%	531.5 \pm 7.0	-2.9%	517.4 \pm 22.0	-2.6%
	S3	39.1 \pm 6.4	41.4	11.0%	476.6 \pm 10.4	-12.9%	457.9 \pm 18.4	-13.8%
	S4	38.6 \pm 3.8	41.5	11.3%	502.5 \pm 8.6	-8.2%	486.3 \pm 28.9	-8.5%
Long (200 cm)	S0	34.5 \pm 2.0	35.3	-	133.4 \pm 2.0	-	-	-
	S1	37.9 \pm 1.1	39.5	11.9%	153.0 \pm 1.9	14.7%	-	-
	S2	36.2 \pm 4.3	38.2	8.2%	149.6 \pm 2.6	12.1%	-	-
	S3	36.4 \pm 1.4	40.5	14.7%	146.4 \pm 3.6	9.7%	-	-
	S4	41.5 \pm 0.3	41.2	16.7%	155.4 \pm 1.9	16.5%	-	-

* For parameters/specimens with only one or two results available, only the average value is presented.

The apparent longitudinal elastic modulus is only presented for the intermediate and long columns, since in short columns (due to the lower gauge length or the “stiffer” test setup) the results were not considered to be precise enough. In this regard, results obtained for the longer columns are deemed to be the most accurate/representative. The ultimate load is only presented for the short and intermediate columns, as long columns were unloaded before collapse.

In intermediate columns, the apparent longitudinal elastic modulus exhibited a significant and consistent average increase in all hybrid series (up to 7.1% – series S2 and S3), while – in long columns it presented an even higher increase (20.4%), but only for series S4, which has overlapped CF and GF mats. These results indicate that, as expected, the axial stiffness of pultruded GFRP profiles increases with the introduction of CF mats.

Figure 4.6 shows the percentage variation of the ultimate load obtained in each series compared to the reference profiles (series S0).

Regarding the short columns, series 60_S2 was the only one that presented an increase in load carrying capacity (very slight, in average 2.9%) when comparing to the reference GFRP profile; however, this variation does not seem to be statistically significant, given the experimental scatter. The

remaining series presented a significant decrease in the average ultimate load (from 6.0% to 10.6%). Both the stiffness and the ultimate load results indicate that there might have been delamination of the CF mats throughout the test, causing a loss of cross-sectional area, and thus leading to a worse performance in terms of ultimate limit states.

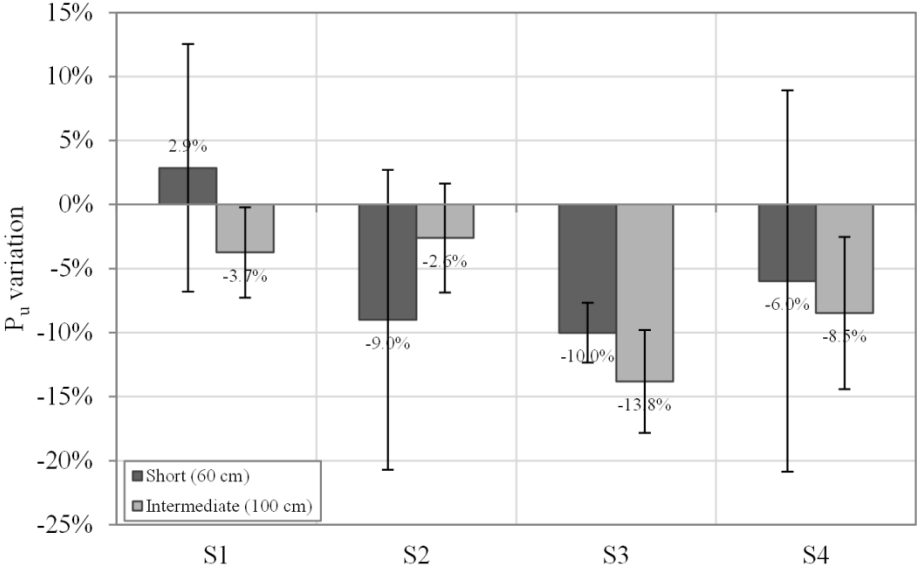


Figure 4.6: Percentage variation of ultimate load of the hybrid series compared to the reference profile for short and intermediate columns.

In the intermediate columns, all hybrid series presented lower load carrying capacity than that exhibited by the reference profile (531 kN). Among the hybrid columns, series 100_S1 and 100_S2 presented the highest average ultimate loads (511 kN and 517 kN, respectively), while series 100_S3 and 100_S4 presented the lowest average ultimate loads (458 kN and 486 kN, respectively). These results reflect the difficulty of pultruding bidirectional CF mats due to their reduced permeability, as already referred. If the CF mat is not fully saturated by the polymeric matrix, the interface between that mat and the GFRP bulk material may become a “weak point” of the structural member, and lead to premature delamination.

The average ultimate load of almost all hybrid series was lower than that of the reference profile. That is most likely due to the fact that, for higher axial strains, progressive delamination occurred at the interface between the CF mats and the GF rovings (more critical in hybrid columns containing bidirectional CF mats), leading to a cross-section reduction and subsequent premature failure. Such occurrence is consistent with the audible cracks registered in the tests of the hybrid columns.

4.3.2 Axial stress vs. strain behaviour

The analysis of the axial stress vs. strain data were performed in order to validate the axial stiffness results presented earlier and to assess the buckling behaviour through the analysis of the strain gradient in the section instrumented with strain gauges (section 4.3.3).

Figure 4.7 plots the axial stress vs. strain curves of three representative specimens of the short columns. The stresses and strains presented in this figure were measured up to failure.

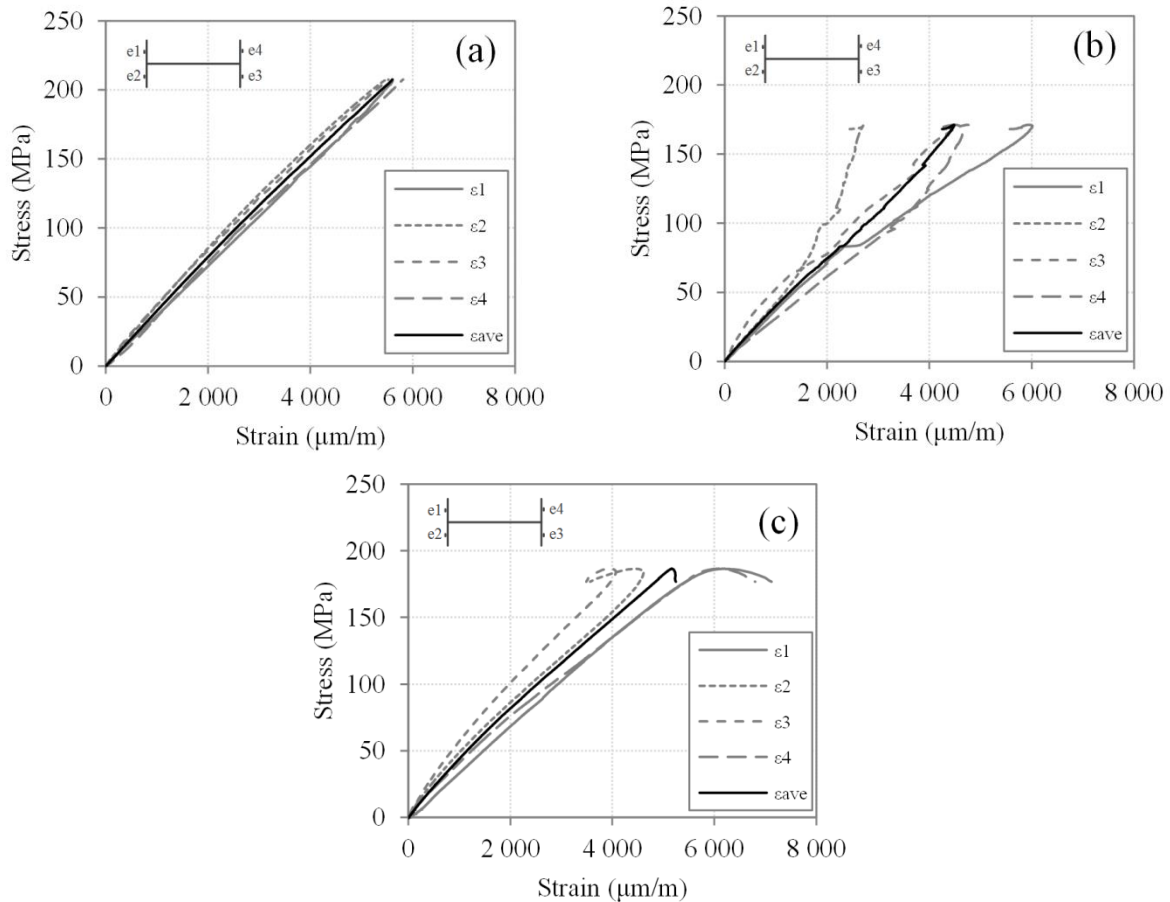


Figure 4.7: Axial stress vs. strain curves of short column specimens (a) 60_S1_1, (b) 60_S3_2, and (c) 60_S4_1.

The axial stress vs. strain behaviour exhibited by the curves of short columns was highly dissimilar, as illustrated by the distinct behaviour presented by the three specimens represented in Figure 4.7. Some specimens, such as 60_S4_1 (Figure 4.7(c)), showed evidence of local buckling prior to failure: in fact, in the final stage of the test, before collapsing they presented a noticeable nonlinearity in the strain gradient. In opposition, specimen 60_S1_1 (Figure 4.7(a)) presented a roughly uniform strain distribution (across the section width) up to failure, showing no evidence of local buckling; nevertheless, since the strain gauges were bonded to the mid-height section and that is the inflexion point of the anti-symmetrical buckled mode shape, the local buckling phenomenon might have been triggered but not detected by the strain gauges. Finally, specimen 60_S3_2 (Figure 4.7(b)) showed

signs of delamination in the CF external mats, since for stresses higher than 80 MPa the axial strain readings showed a noticeable perturbation, becoming highly nonlinear, and hence being deemed to be no longer representative of the behaviour of the whole section. In these cases, the longitudinal elastic modulus was computed considering only the data prior to delamination (Table 4.3).

Now regarding the intermediate columns, the axial (stress vs. strain) behaviour exhibited by the different series, illustrated in Figure 4.8, was much more homogeneous. Most specimens presented stress vs. strain curves similar to those exhibited by specimen 100_S0_2 (Figure 4.8(a)), in which it is possible to distinguish three different stages in the loading path: (i) elastic stage, (ii) buckling stage, and (iii) post-peak stage. Both specimens of series S3 that were monitored with strain gauges (e.g., 100_S3_2, presented in Figure 4.8(b)) presented some kind of delamination of the CF mats; as in the short column tests, such occurrence could be noticed for an average stress around 80 MPa.

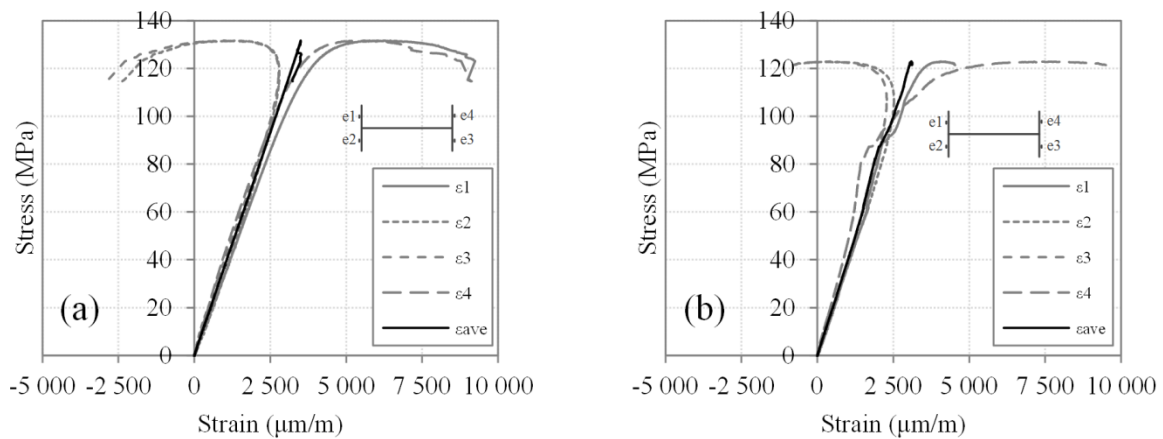


Figure 4.8: Axial stress vs. strain curves of intermediate column specimens (a) 100_S0_2, and (b) 100_S3_2.

In specimens from series S3, the strain gauges were directly bonded to the CF mats. Since the remaining mats were embedded inside the profile and not at the surface, the referred delamination might have occurred in other specimens and still remain unnoticed. This assumption is supported by the fact that all hybrid series presented lower ultimate loads than the reference series.

The typical stress vs. strain curves exhibited by long columns are plotted in Figure 4.9. The behaviour of most specimens was consistent with the load vs. axial shortening response presented earlier, typical of long columns subjected to axial compression: measured strains presented a roughly hyperbolic loading path, linear in the early stage of the test and then asymptotically tending to the critical load. Some specimens, such as 200_S4_1 (Figure 4.9(b)), showed a load peak that may have been due to some residual rotational friction at the end supports. In the long column tests, unlike the short and intermediate columns, there was no evidence of delamination in any specimen. This is explained by the much lower axial strains that developed in the longer columns, well below the 80 MPa threshold that was associated to the occurrence of delamination in the short and intermediate columns.

Figure 4.10 compares the average variation in the longitudinal elastic modulus presented by each hybrid series compared to the reference profiles for all column lengths tested. It is clear from this figure that for longer columns the increase in axial stiffness was more relevant than in short and intermediate columns. Such fact highlights the already referred assumption that delamination of the CF mats occurred throughout the compressive tests. One should note that for short and intermediate columns the range of data used to determine this parameter included values higher than 80 MPa, and thus the delamination of the CF mats might have been already triggered. One may then state that the results obtained for the long columns are more reliable since their range of data is lower to the triggering of the CF mats delamination.

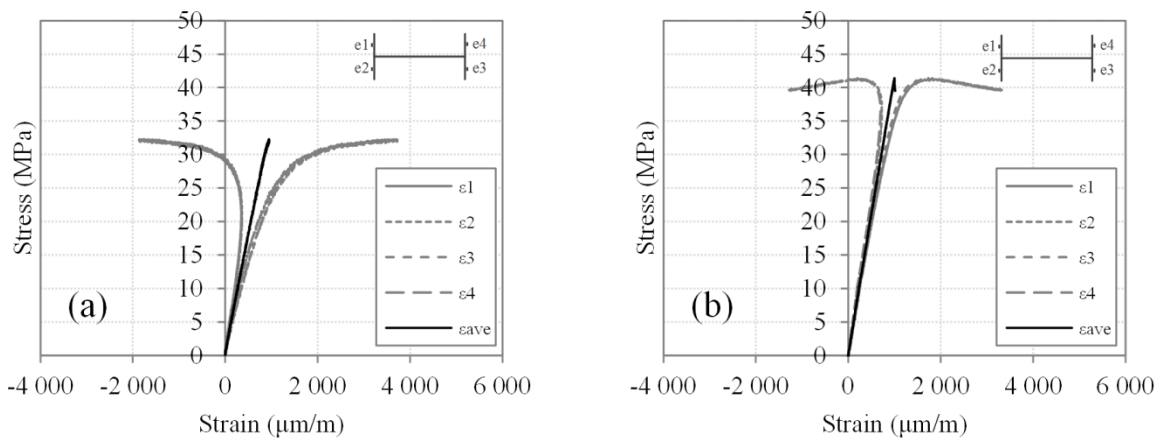


Figure 4.9: Axial stress vs. strain curves of long column specimens (a) 200_S0_2, and (b) 200_S4_1.

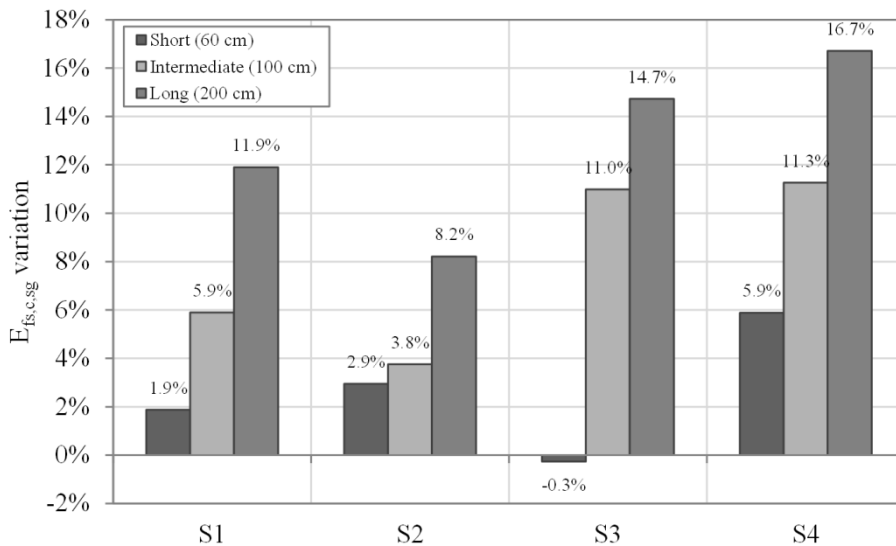


Figure 4.10: Percentage variation of the full section longitudinal elastic modulus under compression of the hybrid series compared to the reference profile (stress-strain data).

4.3.3 Buckling behaviour

The critical buckling load (P_{bk}) of each specimen, listed in Table 4.3 (page 59), was determined using both the original Southwell plot method [69] and the modified Southwell plot method [70]. The lateral deflection, measured in both transverse displacement transducers, and the bending strain were used as perturbation parameters for buckling calculations. The bending strain is defined as the strain gradient along the minor axis of the cross-section and it is computed according to the following equation,

$$\varepsilon_{bend} = \frac{\varepsilon_1 - \varepsilon_2 - \varepsilon_3 + \varepsilon_4}{2 b_{sg}} \quad (11)$$

in which ε_i is the strain measured in the strain gauge i and b_{sg} is the distance between two strain gauges positioned in the same flange ($b_{sg} = 0.06$ m).

The results obtained using the different perturbation parameters are fairly similar and thus for intermediate and long columns only the lateral deflection results are shown next (as they were obtained from three specimens, instead of two). In short columns, both the lateral deflection and the bending strain were used as perturbation parameter due to an increased difficulty in determining the critical buckling load of these columns. Several factors, such as (i) the limited sensitivity of the displacement transducers, (ii) the low amplitude of the buckled shapes in some specimens, and (iii) the interaction between buckling and material damage at the final stage of the test, may have hampered the measurement of the perturbation parameters. For instance, in series 60_S4, it was only possible to determine the critical load in one specimen, and therefore results for short columns have less statistical significance than those obtained for intermediate and long columns.

Southwell [69] demonstrated that provided that the load vs. deflection curve is roughly a rectangular hyperbola passing through the origin, then the ratio of deflection to load (δ/P) plotted against the deflection (δ) is a straight line whose inverse of the slope is the least critical load (P_{bk}), and the intersection with the vertical axis is the relation between the initial imperfection of the strut (δ_0) and the critical load:

$$\frac{\delta}{P} = \frac{\delta}{P_{bk}} + \frac{\delta_0}{P_{bk}} \quad (12)$$

Regarding the determination of the critical buckling load of long columns, Figure 4.11 illustrates (for specimen 200_S0_2) the application of the Southwell plot method using the referred coordinates' transformation.

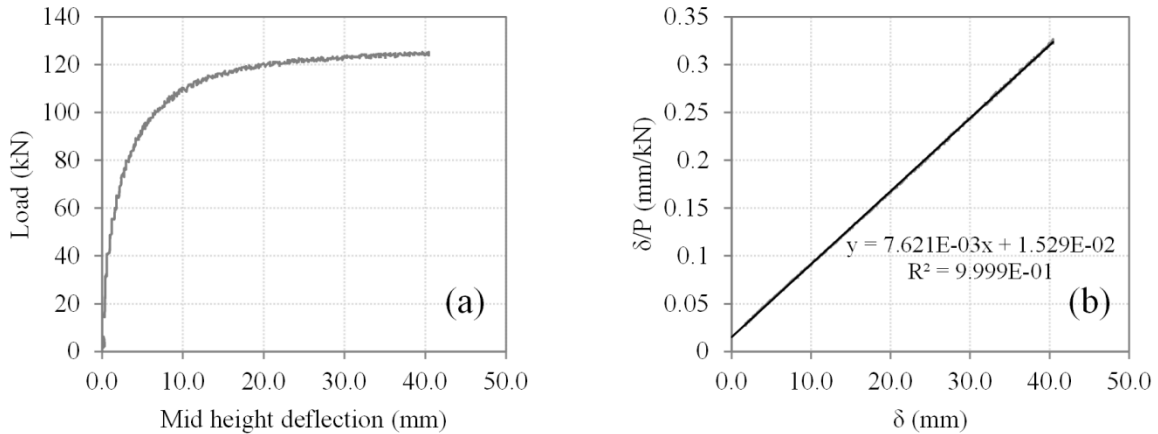


Figure 4.11: Application of the Southwell plot method for long column specimen 200_S0_2: (a) load vs. mid height deflection curve, and (b) δ_L/P vs. δ_L curve.

Figure 4.14 presents the variation of buckling load of the different hybrid long columns when compared to the reference profile (results obtained for the short and intermediate columns, discussed later in this section, are also plotted in this figure). The results obtained clearly show that all long columns reinforced with CF presented higher critical buckling loads than the reference profile (10 to 17% increase for the different series). Series S4 presented the highest increase in the global buckling load (17%) when comparing to the reference series; however, as already mentioned, the production of this series was only possible by overlapping the glass and carbon mats in the web-flange junction, and thus it presents a higher fibre volume than the remaining series.

Regarding the determination of the critical buckling load of intermediate columns, the load vs. deflection data cannot be depicted as a hyperbolic path due to the decrease of the load level when the buckling mode coupling is triggered. Therefore, the same procedure was adopted, but with a slight difference: the upper bound of the data range used in the linear regression was defined as the maximum load reached in the test (P_{max}). The comparison in terms of the critical buckling load between the hybrid series and the reference one is also shown in Figure 4.14. Critical buckling loads were very consistent within each series, presenting low scatter and a roughly similar average result using the transverse deflection and the bending strain data. None of the hybrid series presented better performance when compared to the reference series. As already mentioned, the onset of delamination for higher axial strains was most likely the cause for such decrease, since in long columns (with considerably lower strains) all hybrid series presented higher critical loads than those presented by the reference series. Series S3 presented the lowest average critical buckling load, once again confirming the already mentioned difficulties encountered in the saturation of the CF mats. It is worth mentioning that the application of the Southwell plot method was very effective in determining both the global buckling load and the coupled global-local buckling behaviour of respectively long and intermediate columns.

Contrary to long columns, short columns do not exhibit a hyperbolic buckling path, but rather an approximately quadratic post-critical path. Barbero and Trovillion [70] have proposed a formulation in which this post-critical stiffening is considered to follow a quadratic path, thus allowing to predict the local buckling critical load in a more accurate and reliable way. The following equation was applied to a defined range of data to predict the critical local buckling load,

$$P = P_{bk} + \frac{1}{2}P^{(2)}s^2 \quad (13)$$

in which P is the applied load, $P^{(2)}$ is the curvature of the post-buckling path, and s is the perturbation parameter.

Since the initial post-buckling path is assumed to be approximately quadratic, the range of data used to compute the trend line of the equation above is supposedly linear. However, there is still the issue of the mixed effects of buckling and material damage, which combined lead to a decrease in the column load carrying capacity in the brink of failure. Therefore, the upper bound of the data range was defined as the maximum load registered in the test (P_{max}) and the lower bound was assumed to be the lowest value of applied load (P_{min}) in which the trend line of the above equation had a correlation factor (R^2) higher than 0.90 (Figure 4.12)¹¹.

Figure 4.13 illustrates the application of the modified Southwell plot method to specimen 60_S1_3. The comparison in terms of local buckling critical load between the hybrid series and the reference one is presented in Figure 4.14. It is possible to state that, similarly to what was observed for the intermediate columns, the short columns made of the reference GFRP profile presented the highest average critical buckling load (Figure 4.14), and hence the introduction of CF mats did not provide any improvement regarding this parameter (confirming once more the occurrence of delamination). Series 60_S3 was the one that presented the lowest buckling load, due to the aforementioned manufacturing difficulties.

Figure 4.15 plots the critical buckling loads as a function of the specimens' length for each series. It should be mentioned that the results presented for the different heights (60, 100 and 200 cm) correspond to the average values (obtained from three measurements) connected with straight lines. The results presented in Figure 4.15 confirm the advantage of introducing CF mats in long columns (increasing the global buckling load compared to the reference profile), but also the detrimental effect of such hybridization in short and intermediate columns (leading to reductions of the critical loads). The explanation for this result is two-fold: (i) local buckling critical load is more dependent on the

¹¹ Barbero and Trovillion [70] have considered a different criterion for the range of data used for the application of the modified Southwell plot. They have used all the deflection data larger than $t/10$ (in which t is the wall thickness). However, they have studied wide-flange columns in which the deflection is much more noticeable than that of narrow-flange columns. In this study, since the deflection results were widely variable and in some specimens it was even impossible to apply the modified Southwell method, a different (less limitative) criterion was chosen for the data range.

shear modulus of the plates than on their elastic longitudinal modulus; and (ii) the delamination that most likely occurred during the tests of the short and intermediate hybrid columns caused a slight decrease in both inertia and stiffness for higher load levels (higher strains).

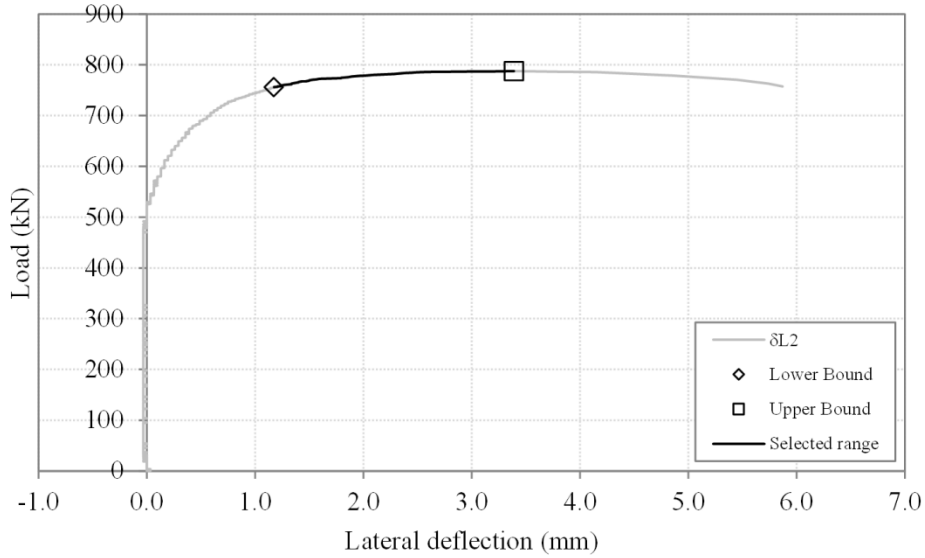


Figure 4.12: Illustration of the procedure to determine the data range to be used in the critical buckling load calculation (specimen 60_S1_3).

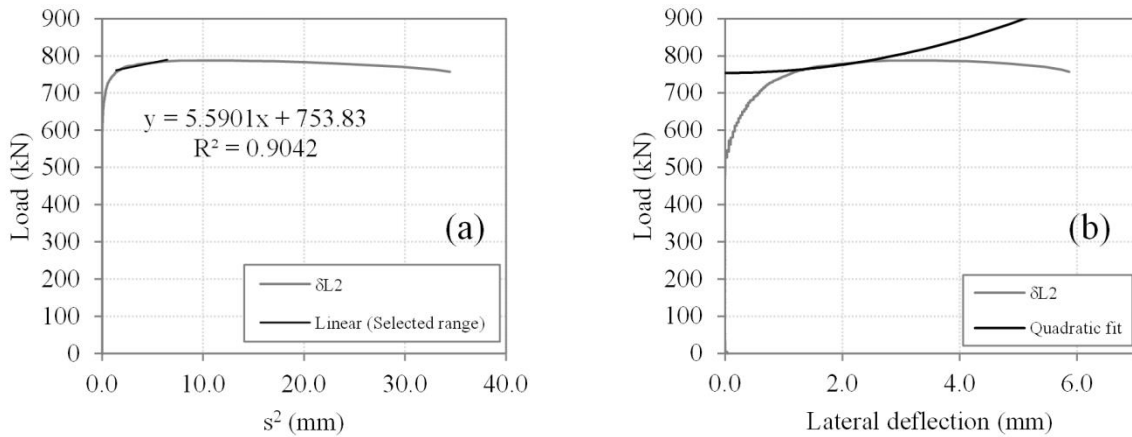


Figure 4.13: Application of the modified Southwell method to short column specimen 60_S1_3: (a) trend line of the P vs. s^2 curve in the selected range, and (b) lateral deflection δ_{L2} and corresponding quadratic fit.

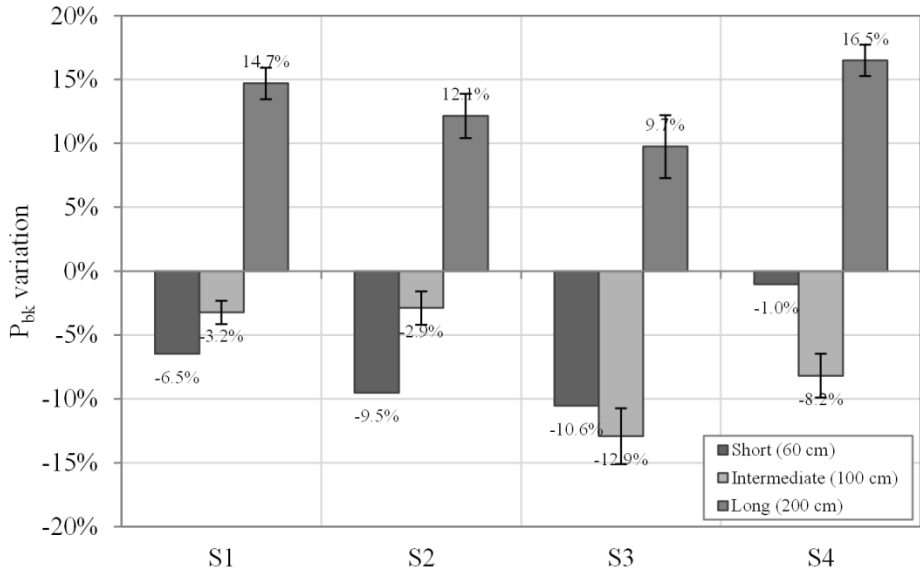


Figure 4.14: Percentage variation of buckling load of the hybrid series compared to the reference profile for short, intermediate and long columns.

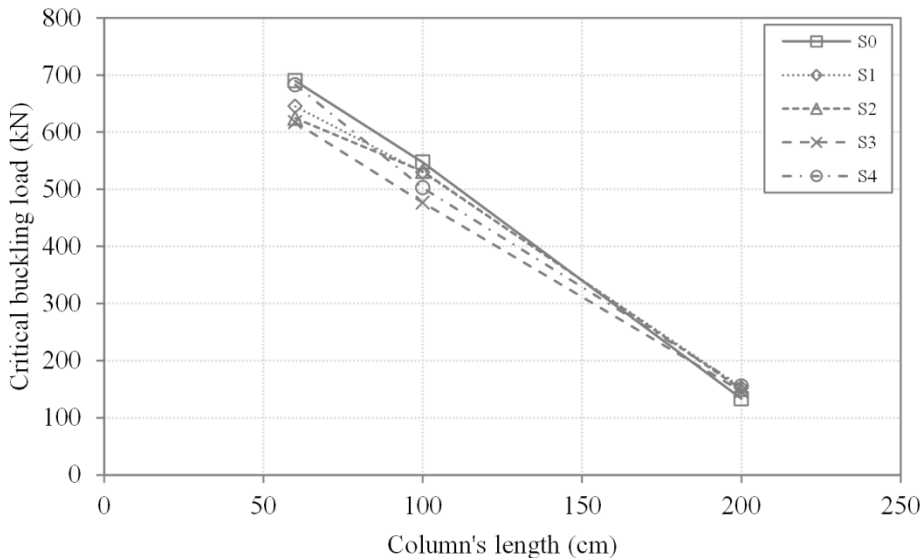


Figure 4.15: Comparison of average experimental critical loads for all series and column lengths.

4.3.4 Failure modes

For a given column height, the failure modes presented by the different series were similar and very consistent, with all specimens generally exhibiting a single failure mode, despite slight variations in ultimate and critical loads.

Short columns were the only ones in which some specimens presented more than one failure mode. The failure mode that was expected and that in fact occurred more frequently (10 out of 15 specimens) was local buckling with symmetrical or anti-symmetrical mode shapes, followed by partial or total

web-flange separation (Figure 4.16). As already mentioned, the literature review indicates that this failure mode occurs due to high shear stresses developed in the web-flange junction after the onset of buckling [4]. Also when buckling was triggered, several audible cracks were heard, indicating a possible interaction between the local buckling phenomenon and material progressive damage in the final stage of the test. This assumption is consistent with the load vs. perturbation parameter data showing almost no post-buckling stiffness, in opposition to the typical behaviour exhibited by wide-flange profiles, as presented by Barbero and Trovillion [70].

Some other specimens (four out of 15) also presented audible cracks in the final stage of the test, but the local buckling phenomenon was not clear, both to the naked eye and from the load vs. perturbation parameter curves. Despite that, the collapse occurred also with web-flange separation, thus indicating that the failure mode might have been the same, but with higher influence of material damage and very low (or null) amplitude of the mode shape (undetected by the transducers and strain gauges). As already mentioned, one specimen (60_S4_2) presented an apparently anomalous behaviour and hence was discarded from the analysis.

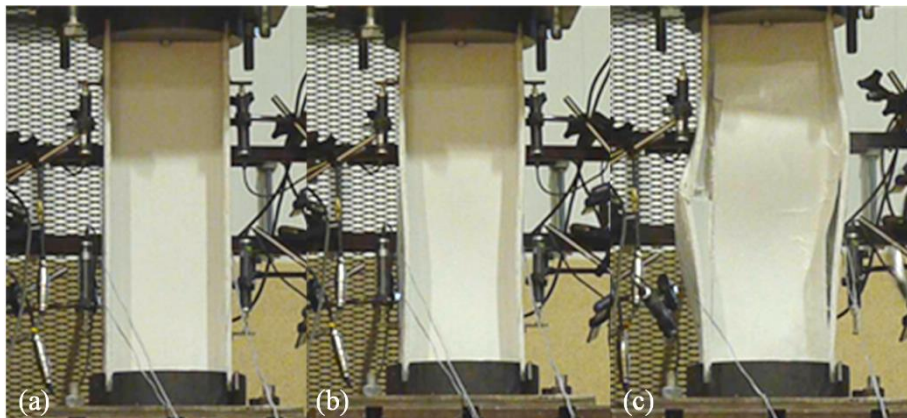


Figure 4.16: Typical failure mode of short columns: (a) undeformed shape, (b) buckled shape, and (c) failure mode.

Intermediate columns presented the very same failure mode in all 15 tests. The failure mode basically consisted of two different stages. In a first stage, columns buckled in a global mode shape up to a lateral deflection of 5.0 to 10.0 mm, and at the end of this stage the maximum load (P_{max}) was reached. In a second stage, the interaction between global and local modes and the progressive damage of the material were triggered and specimens started losing their load carrying capacity (unstable buckling path). Finally, the collapse of the specimen occurred due to partial web-flange separation and flange crushing (Figure 4.17).

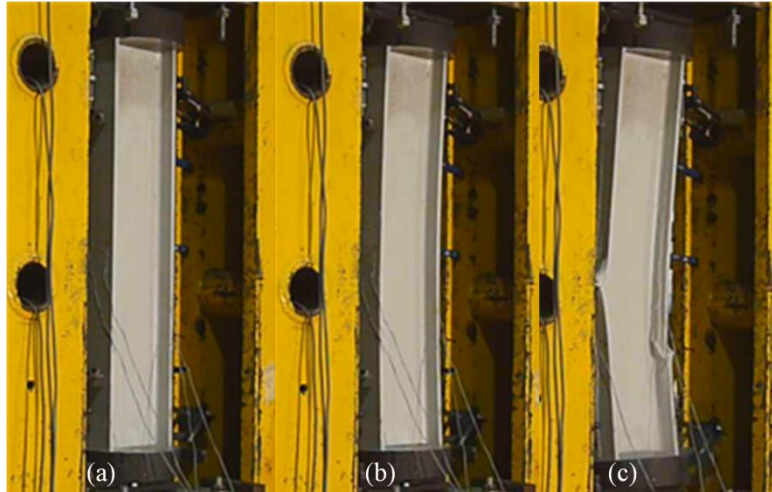


Figure 4.17: Typical failure mode of intermediate columns: (a) undeformed shape, (b) buckled shape, and (c) failure mode.

Long columns did not collapse and thus it is more accurate referring to their limit state rather than to their failure mode. As expected, the limit state presented by the long columns was global buckling about the minor axis (Figure 4.18). The buckling path roughly followed a hyperbola, asymptotically tending to the critical load, which confirms the stable post-buckling path of the global buckling phenomenon. At the end of the test, the columns were unloaded without any visible damage.



Figure 4.18: Typical limit state of long columns: (a) undeformed shape, and (b) deformed shape.

4.4 DESCRIPTION OF THE NUMERICAL MODELS

The main objective set for the numerical models proposed in the following sections was to accurately simulate the behaviour of the hybrid FRP pultruded columns exhibited in the experimental tests. In

order to achieve this goal, the FE models are first described, namely: the FE types and mesh, the columns' supports and loading, and the FRP material properties considered. Then, three failure criteria for composite materials (Maximum Stress, Tsai-Hill and Hashin) are presented and their differences discussed. Finally, the damage model implemented in ABAQUS within the framework of Hashin criterion is briefly described.

One should note that experimental series S4 was the only one in which the introduction of the CF mats was not made by direct replacement of the original GF mats. Thus, this series presented more reinforcing material than the remaining ones. For an accurate and fair numerical comparison between the different series, a similar fibre content (partially replacing glass fibres) was considered in this series and thus it was designated as S4* in this section.

4.4.1 Finite element models

In the development of the FE models in ABAQUS [72] two different parts were modelled: (i) the I-section FRP pultruded profile, and (ii) the load bearing plates. Bearing plates, with diameter of 250 mm and thickness of 27 mm, were meshed using eight-node solid elements with reduced integration (C3D8R) and assigned to rigid-body behaviour. The I-section FRP profiles (200×100×10 mm) were meshed using eight-node continuum shell elements with reduced integration and three integration points across the thickness of each layer's (SC8R). Continuum shell elements are assumed as three-dimensional bodies and are assigned to a composite layup with different layers corresponding to each experimental series. Contrary to conventional shell elements, in which the thickness is a section property, the thickness of continuum shell elements is defined by the distance between nodes in the element normal direction [72]. Therefore, it is recommended to have only one element across the shell thickness. Similarly to continuum solid elements, continuum shell elements present only displacement degrees-of-freedom but their kinematic and constitutive behaviour is similar to that of conventional shell elements. Element data, such as stress, strain and damage index, are calculated and presented at each integration point along the thickness and there is no through-thickness interpolation.

Apart from the web-flange junction, the FRP profiles were meshed uniformly along their length, flange width and web height, with an element length-to-width ratio of 10:5 (mm). In order to have a single element across the web thickness, the web-flange junction was meshed with an element length-to-width ratio of 10:10 (mm). Thus, the cross-section of FRP pultruded profiles comprised a total of 74 elements and 150 nodes. The total number of elements, which varied according to the length of each column, is presented in Table 4.4. Figure 4.19 shows the FE model and mesh for the short columns, as an illustrative example. Preliminary studies on the convergence of FE mesh were performed (not shown here).

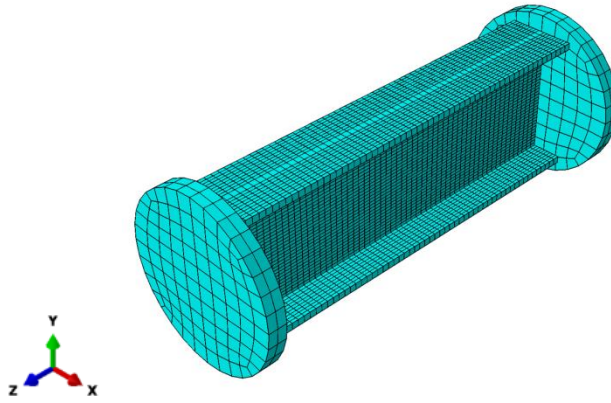


Figure 4.19: Finite element model and mesh (short columns).

The interface between different parts was modelled using a surface-to-surface tie interaction, which restrains all degrees-of-freedom of the slave surface according to those of the master surface. Loading and kinematic boundary conditions were applied directly to both bearing plates. Loading was applied to the bottom bearing plate in the positive way of the z axis by means of (i) a concentrated load in the linear buckling analyses¹² and (ii) an imposed displacement in the nonlinear failure analyses. The transverse displacements (along x -axis and y -axis) were restrained in both bearing plates. In the opposite (top) bearing plate, the displacement along z -axis was set to zero (fully fixed). Rotations about the x and z axes were restrained in all columns while the rotation about the y -axis was set free for intermediate and long columns but restrained for short columns (according to the experimental test setup – cf. Figure 4.2, page 55).

Table 4.4: Total number of elements and nodes in the model of each column.

Column	Length (cm)	# elements	# nodes
Short	60	4440	9000
Intermediate	100	7400	15000
Long	200	14800	30000

According to the experimental series, there are three different types of materials to be considered: (i) GFRP, (ii) unidirectional CFRP, and (iii) bidirectional CFRP. All three composite materials' elastic and strength properties are presented in Table 4.5 and Table 4.6, respectively. In these tables, E_i is the Young's modulus in the i direction, ν_{ij} is the Poisson ratio between directions i and j , G_{ij} is the shear modulus in the ij plane, $S_{t,i}$ is the tensile strength in the i direction, $S_{c,i}$ is the compressive strength in the i direction and S_{ij} is the shear strength in the ij plane. Note that the layer plane is 12, 1-axis is the fibre (pultrusion) direction, 2-axis transverse direction, and 3-axis is orthogonal to the layer plane, *i.e.* is thickness-oriented.

¹² Imposed displacements could have also been used instead of application of loads. However, this assignment provides explicitly the buckling loads as a result of the eigenvalue problem.

Table 4.5: Elastic properties of composite materials.

Material	E_1 (MPa)	E_2 (MPa)	ν_{12}	G_{12} (MPa)	G_{13} (MPa)	G_{23} (MPa)
GFRP laminate	36633	10754	0.266	3648	3648	1601
Unidir. CFRP laminae	192853	10754	0.266	3648	3648	1601
Bidir. CFRP laminae	95920	95920	0.266	3648	3648	3648

Table 4.6: Strength properties of composite materials.

Material	$S_{t,1}$ (MPa)	$S_{c,1}$ (MPa)	$S_{t,2}$ (MPa)	$S_{c,2}$ (MPa)	S_{12} (MPa)	S_{23} (MPa)
GFRP laminate	365	468	85.8	110	30.6	30.6
Unidir. CFRP laminae	1389	569	85.8	110	30.6	30.6
Bidir. CFRP laminae	837	201	837	201	30.6	30.6

As already mentioned, some of these properties were obtained through mechanical tests of small-scale specimens according to the standard test methods for pultruded composites (*cf.* section 4.2.3). Since it was readily impossible¹³ to determine all the properties needed for the numerical model input data, the following assumptions were made:

- The longitudinal elastic moduli of the CFRP materials were determined from series S2 (unidirectional) and S3 (bidirectional) small-scale specimen tests.
- Regarding the shear modulus, only the GFRP material's G_{12} was determined; G_{13} was assumed to be the equal to G_{12} and G_{23} was set as the resin shear modulus, calculated using the rule of mixtures (these assumptions are fairly accurate).
- The transverse properties of the unidirectional CFRP were assumed to be equal to those of the GFRP, as matrix controls the behaviour in the transverse direction; transverse properties of the bidirectional CFRP were considered to be equal to the longitudinal ones, as now carbon fibres govern the behaviour in the transverse direction.
- Shear moduli of both CFRP materials were assumed to be equal to the GFRP material. The exception was the shear modulus G_{23} of the bidirectional CFRP material, which was considered equal to G_{12} and G_{13} .
- The Poisson's ratio, determined from tensile tests of GFRP specimens, was assumed to be equal for all materials.
- The transverse compressive-to-tensile strength ratio was assumed equal to the longitudinal one ($S_{c,2}/S_{t,2}=S_{c,1}/S_{t,1}$), which was measured from tests. The transverse tensile strength ($S_{t,2}$) of GFRP was estimated under this assumption and using the measured transverse compressive strength ($S_{c,2}$) of GFRP.

¹³ Due to the specimen dimension requirements and the difficulty of testing the CFRP material separately.

- The CFRP material's longitudinal compressive strengths were defined as the delamination stresses determined (i) by Nunes [8] for unidirectional mats, and (ii) in the experimental campaign of this study (corresponding to a section average stress of 80 MPa) for bidirectional mats (*cf.* section 4.3.2, page 61);
- The shear strength (S_{12}), measured for GFRP laminates, was adopted for the CFRP; S_{23} was assumed equal to S_{12} .

4.4.2 Failure criteria

The experimental characterisation of composite materials is based on coupon tests with different loading configurations. However, in most cases, coupons are subjected to uniaxial stress states. When referring to an actual composite structure under serviceability or ultimate loading, the cases in which the material is subjected to uniaxial stress states is the exception rather than the rule. Therefore, the simplest procedure is to set the safety check of any point of the structure dependent on the strength of that point for individual stress states (separate uniaxial loadings) or even for combinations of these (interaction between uniaxial loadings). This procedure requires the definition of adequate failure envelopes based on the data of uniaxial stress states [76]. Based on different conditions, the following failure criteria will be presented: (i) the Maximum Stress criterion, (ii) the Tsai-Hill criterion and (iii) the Hashin damage initiation criterion.

The Maximum Stress criterion is the simplest criteria of all [76]. It basically consists of assuming that there is no stress interaction and that a given composite lamina will carry load up to the lowest of its strengths (longitudinal, transverse or shear). It is defined by the following set of equations,

$$-S_{c,1} < \sigma_1 < S_{t,1} \quad (14)$$

$$-S_{c,2} < \sigma_2 < S_{t,2} \quad (15)$$

$$|\tau_{12}| < S_{12} \quad (16)$$

where σ_1 is the stress in the longitudinal direction (I -axis), σ_2 is the stress in the transverse direction (2 -axis), both positive when tensioned and negative when compressed, and τ_{12} is the shear stress.

Unlike the Maximum Stress criterion, the Tsai-Hill criterion [76,87] considers the interaction between longitudinal, transverse and shear stresses of a composite layer subjected to in-plane loading (σ_1 , σ_2 , τ_{12}). To a certain point, it is the extension of von Mises criterion (isotropic materials) to orthotropic materials. It is given in the form of a failure index (I_F) according to the following equation,

$$I_F^{TH} = \frac{\sigma_1^2}{S_1^2} - \frac{\sigma_1\sigma_2}{S_1^2} + \frac{\sigma_2^2}{S_2^2} + \frac{\tau_{12}^2}{S_{12}^2} < 1.0 \quad (17)$$

where $S_i = S_{t,i}$ if $\sigma_i > 0$ (tensile stress) or, if $\sigma_i < 0$, $S_i = S_{c,i}$ (compressive stress). Note that the Tsai-Hill criterion not only recovers Maximum Stress criterion conditions, through (i) Eq. (14) for longitudinal uniaxial loading ($\sigma_2=\tau_{12}=0$), (ii) Eq. (15) for transverse uniaxial loading ($\sigma_1=\tau_{12}=0$) and (iii) Eq. (16) for shear loading ($\sigma_1=\sigma_2=0$), but it also considers the interaction between σ_1 and σ_2 for biaxial loading. ABAQUS code includes a built-in output function for the visualisation of Tsai-Hill index pattern in the whole structure, which enables a straightforward evaluation of critical zones where failure is initiated [72], *i.e.* $I_F > 1$. Despite considering the stress interaction, the Tsai-Hill criterion does not take into account the material stiffness degradation when $I_F > 1$. It may thus provide very conservative estimates of the composite structure ultimate load, depending on the loading nature [15].

Like the Maximum Stress and the Tsai-Hill criteria, the Hashin damage initiation criterion also allows the prediction of failure initiation in composite structures. Generally speaking, it comprises four different and independent failure indexes: (i) fibre tension index – F_f^t ; (ii) fibre compression index – F_f^c ; (iii) matrix tension index – F_m^t ; and (iv) matrix compression index – F_m^c . According to the Hashin criterion, a given point is safe if all the following conditions are satisfied [31],

$$F_f^t = \frac{\sigma_1^2}{S_{t,1}^2} + \alpha \frac{\sigma_{12}^2}{S_{12}^2} < 1.0 \quad (18)$$

$$F_f^c = \frac{\sigma_1^2}{S_{c,1}^2} < 1.0 \quad (19)$$

$$F_m^t = \frac{\sigma_2^2}{S_{t,2}^2} + \frac{\sigma_{12}^2}{S_{12}^2} < 1.0 \quad (20)$$

$$F_m^c = \frac{\sigma_2^2}{4 S_{23}^2} + \left(\frac{S_{c,2}^2}{4 S_{23}^2} - 1 \right) \frac{\sigma_2}{S_{c,2}} + \frac{\sigma_{12}^2}{S_{12}^2} < 1.0 \quad (21)$$

where S_{23} is the transverse shear strength and α is a parameter that accounts for the contribution of shear stress to the fibre tension index F_f^t . The criterion version proposed by Hashin and Rotem [77] is recovered if $\alpha=0.0$, while the version proposed by Hashin [78] is obtained if $\alpha=1.0$. Because the fibre tension condition does not govern the material damage in the present study, the value adopted for α is not relevant. Thus, the default value ($\alpha = 0.0$) provided in the ABAQUS built-in analysis was used [72].

4.4.3 Damage model

In ABAQUS, the Hashin damage initiation criterion is used alongside a progressive damage variable (d), which computes, for each failure mode, the damage state at each increment based on the stress state and the fracture energy. ABAQUS requires the definition of four different fracture energy parameters (G_f), one for each failure mode. It should be noted that in the Hashin progressive damage analysis, the damage variables (associated to each failure mode) are independent of each other, which

means that a given finite element may be damaged in one direction and still display stiffness in the other direction.

Once damage is achieved in a finite element, the effective stress tensor ($\hat{\sigma}$) is computed using the relation [72],

$$\hat{\sigma} = \mathbf{M} \sigma \Leftrightarrow \hat{\sigma} = \begin{bmatrix} \frac{1}{(1-d_f)} & 0 & 0 \\ 0 & \frac{1}{(1-d_m)} & 0 \\ 0 & 0 & \frac{1}{(1-d_s)} \end{bmatrix} \sigma \quad (22)$$

where \mathbf{M} denotes the damage operator and d_f , d_m and d_s are the damage variables corresponding to the fibre, matrix and shear failure modes, respectively, described earlier. These damage variables are given by,

$$d_f = \begin{cases} d_f^t & \text{if } \hat{\sigma}_1 > 0 \\ d_f^c & \text{if } \hat{\sigma}_1 < 0 \end{cases} \quad (23)$$

$$d_m = \begin{cases} d_m^t & \text{if } \hat{\sigma}_2 > 0 \\ d_m^c & \text{if } \hat{\sigma}_2 < 0 \end{cases} \quad (24)$$

$$d_s = 1 - (1 - d_f^t)(1 - d_m^t)(1 - d_f^c)(1 - d_m^c) \quad (25)$$

in which the superscripts t and c correspond to tensile and compressive modes, respectively.

Prior to damage initiation, the damage operator corresponds to the identity matrix. Once any of the failure indexes reaches the unit in a given material point, the stress state in that damaged point is computed by means of,

$$\begin{aligned} \sigma &= \mathbf{C}_d \varepsilon \Leftrightarrow \begin{Bmatrix} \sigma_1 \\ \sigma_2 \\ \sigma_{12} \end{Bmatrix} \\ &= \frac{1}{D} \begin{bmatrix} (1-d_f)E_1 & (1-d_f)(1-d_m)\nu_{21}E_1 & 0 \\ (1-d_f)(1-d_m)\nu_{12}E_2 & (1-d_m)E_2 & 0 \\ 0 & 0 & (1-d_s)GD \end{bmatrix} \begin{Bmatrix} \varepsilon_1 \\ \varepsilon_2 \\ \varepsilon_{12} \end{Bmatrix} \end{aligned} \quad (26)$$

in which \mathbf{C}_d is the damaged elasticity matrix and $D = 1 - (1 - d_f)(1 - d_m)\nu_{12}\nu_{21}$. The difference of stress states (before and after damage) in a material point should be responsible for a sudden drop of strength of the structure to which that point belongs and also a decrease of its post-damage stiffness (softening stage).

It is well known that crack and damage problems are dependent on the mesh and its refinement [88–90]. In order to reduce the mesh dependency of the softening stage, the constitutive law is expressed in

terms of stress vs. displacement, rather than strain. Accordingly, ABAQUS [72] introduces the element characteristic length into the formulation, L_c , which corresponds to the square root of the element surface area. Once the failure index is reached (for any of the failure modes), the damage variable tends to 1.0 as the equivalent displacement increases and stress tends to zero (see Figure 4.20 and Figure 4.21). After this stage, the damage variable remains constant (equal to 1.0) as the equivalent displacement increases. The bilinear constitutive law of the material is schematically shown in Figure 4.21, in which the area under the curve corresponds to the fracture energy, G_f .

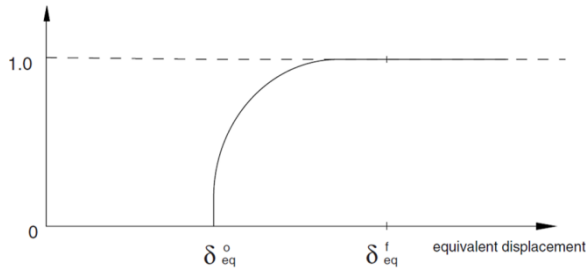


Figure 4.20: Damage variable as a function of equivalent displacement [72].

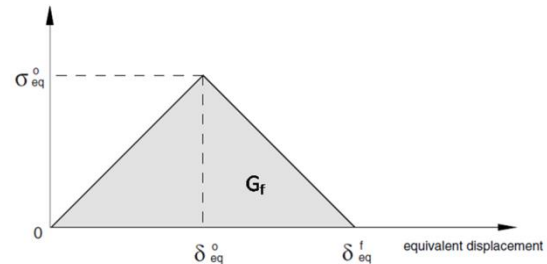


Figure 4.21: Equivalent stress vs. equivalent displacement [72].

According to the best of the author's knowledge, the estimation of the fracture energy G_f of FRP composites is not yet standardized, namely for pultruded unidirectional laminates. Thus, in the present study, the fracture energy was defined as the area under the stress vs. strain curves obtained from the mechanical characterisation tests¹⁴.

The extensive input data required by ABAQUS to perform a progressive failure analysis is often difficult to characterise. In this case, as already mentioned in 4.4.1, some assumptions had to be made. Moreover, the fracture energy associated to the transverse tensile failure mode (G_m) was defined by setting constant the ϵ^0/ϵ^f ratio ($\delta_{eq}^0/\delta_{eq}^f$ in Figure 4.21) for both tensile damage modes (longitudinal and transverse).

The delamination between the CF mats and the GFRP material was simulated also using the Hashin damage. As already mentioned in section 4.4.1., the webs and flanges were modelled using continuum shell elements and were assigned a composite layup. This means that the interface is not explicitly modelled. Thus, the delamination does not actually correspond to the physical separation between the GFRP and CFRP layers at their interface but it is assumed¹⁵ to correspond to the strength decrease in the layers of CF mats.

¹⁴ This approach has inherent limitations, namely because after failure the (small-scale) coupons presented damage only in a certain extension, not in the entire specimen. Future investigations should aim at obtaining more reliable fracture energy values to be used as input for FE models.

¹⁵ Note that CF mats display their own stiffness properties (*i.e.* carbon fibre), but their strength properties are those corresponding to the delamination (not their own carbon fibre strength).

Table 4.7 indicates all the fracture energies used as input in the numerical models. Due to the convergence difficulties associated with softening analyses, the use of the damage stabilization option is recommended [72]. In this study, the value of 1.0×10^{-5} was used for all materials' viscosity coefficients.

Table 4.7: Fracture energy associated to each failure mode and material.

Material	G_{ft} (N/mm)	G_{fc} (N/mm)	G_{mt} (N/mm)	G_{mc} (N/mm)
GFRP laminate	2.38	5.28	0.424	0.948
Unidirectional CFRP laminae	5.86	5.42	0.424	0.948
Bidirectional CFRP laminae	4.28	1.36	4.28	1.36

4.5 NUMERICAL RESULTS, ASSESSMENT AND DISCUSSION

This section provides the results of the numerical study. First, the elastic buckling behaviour of the columns is evaluated. The buckling loads and corresponding buckling modes for columns with different lengths (60, 100 and 200 cm) and series tested in the experimental campaign (S0 to S4) are presented. Next, in section 4.5.2, a comparison is made between the results of analyses using different failure criteria (Maximum Stress, Tsai-Hill and Hashin) and the behaviour between damaged and undamaged columns is presented. In order to simulate the nonlinear behaviour and failure of hybrid columns, the results of the progressive failure analyses (using Hashin criterion with damage model) are shown after in section 4.5.3. In particular, the results comprise load-displacement curves, buckling loads and ultimate loads, stress-strain curves and failure modes. The results are compared to the experimental data (presented in sections 4.2 and 4.3) to validate the numerical models.

4.5.1 Linear buckling behaviour

Linear buckling analyses were performed to determine the elastic critical loads and corresponding buckling modes for each column series' with different lengths. In these analyses, it was assumed that delamination of the CF mats is not allowed to occur. Table 4.8 comprises the results obtained for each column length and Figure 4.22 depicts the performance increase presented by each hybrid series with respect to the reference series S0.

Table 4.8: Critical load values for short, intermediate and long columns of different series (Δ is the relative difference w.r.t. the S0 columns).

Series	$P_{bk,lin}$ (kN)					
	Short	Δ	Intermediate	Δ	Long	Δ
S0	660.7	-	485.3	-	141.1	-
S1	685.8	3.8%	549.6	13.2%	161.2	14.2%
S2	696.4	5.4%	578.1	19.1%	170.2	20.6%
S3	685.3	3.7%	521.9	7.5%	152.3	7.9%
S4*	722.0	9.3%	508.9	4.9%	147.0	4.2%

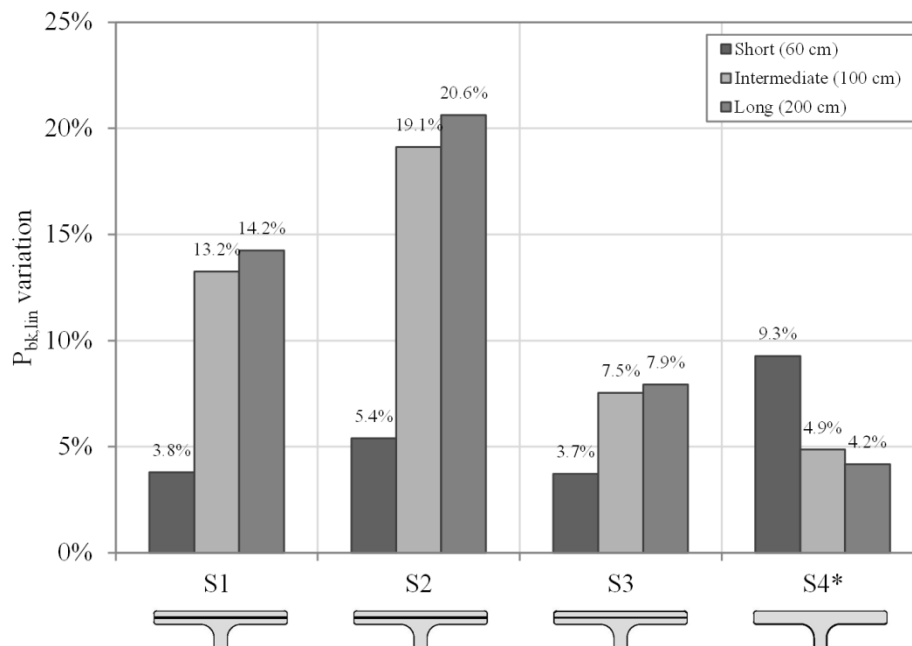


Figure 4.22: First mode linear critical buckling load comparison for each series and column length.

Figure 4.23 shows the critical mode deformed shapes of short, intermediate and long columns. Since they do not differ significantly from series to series, only the results of series S0 are presented. In the nonlinear analyses (sections 4.2 and 4.3), these buckling modes will be used as initial imperfection shapes of the columns.

As seen in Figure 4.2(a) (page 55), the critical mode exhibited by the short columns is governed by local buckling, with high in-plane deformations of the cross-section. It presents an antisymmetric deformed shape with two half-waves along its length, each displaying a half-wavelength of roughly 20 cm. Note that the highest increase in the critical load is achieved by series S4* (9.3% higher compared to the reference series – Figure 4.22). Because the web is the governing wall of the cross-section (slenderest element) in local modes, the above-mentioned increase highlights the efficiency of the web reinforcement in columns that buckle locally. With the same exact amount of CF

reinforcement, series S3 presented the least relevant increase in terms of critical buckling load (only 3.7%). These results show that, as long as CF mats' delamination does not occur, unidirectional reinforcement is more recommended for the flanges, while bidirectional mats are more effective when used in the web (which is subjected to bending in the transverse direction due to in-plane deformation of cross-section).

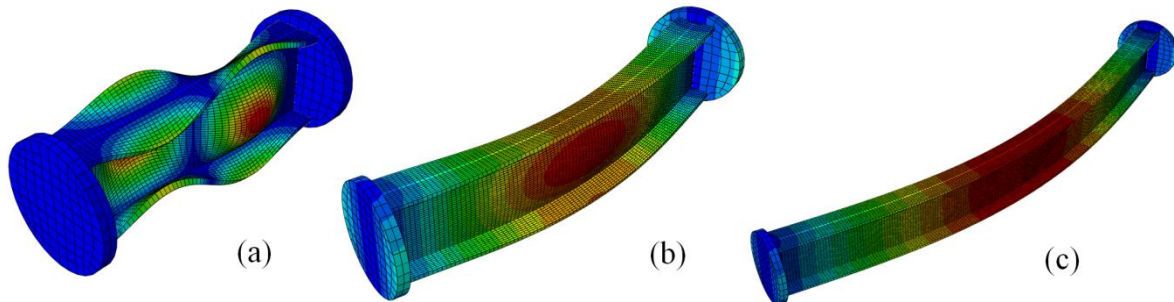


Figure 4.23: Deformed shape of the lowest buckling modes for (a) short, (b) intermediate, and (c) long columns.

In case of columns with intermediate lengths, the critical mode presents a mixed flexural-local buckling mode, combining a relevant contribution of minor-axis flexural buckling with a minor participation of local buckling (transverse bending of the web, more noticeable in mid-span sections). Regarding the advantages of using CF reinforcement, the results show that series S2 presented the highest increase in the critical load (19.1%) while series S4* proved to be the least effective (with an increase of only 4.9%). Series S3 presented a critical load 7.5% higher than that of the reference series. These results show that flange reinforcement (rather than the web reinforcements) is more beneficial for columns with intermediate lengths, because these are mostly affected by global buckling phenomena rather than local buckling. After comparing results obtained for series S2 and series S3 with the same amount of fibres, it also may be stated that unidirectional reinforcements were much more effective than the bidirectional ones. This evidence was expected due to the marginal contribution of local buckling to the critical mode.

Finally, the long columns buckle in a pure minor-axis flexural buckling mode. Regarding the advantages and drawbacks presented by each series, results shown herein confirm the statements already described for the columns with intermediate lengths (which are mostly governed by global modes). Series S2 was the most efficient, while series S4* presented the least increase in the critical load.

Taking into account these results, some relevant conclusions may be drawn already:

- Web reinforcement with bidirectional CF mats (represented by series S4*) should be designed for either short columns or columns of any length but laterally braced, for which local buckling modes are prevalent.

- Flange reinforcement with unidirectional CF mats (denoted by series S2) should be the adopted architecture for columns with moderate to long lengths, not laterally braced; from the comparison with the results obtained for series S3 and S4*, it may be concluded that the web reinforcement is not as effective as the flange reinforcement – note that this expected result is due to the position of web mats, much closer to the neutral axis if positioned in the web than in the flanges.
- A small amount of CF reinforcement in a bare GFRP pultruded profile may provide an increase of up to 20.6% in its critical load, depending on the column length and CF fibres' architecture.

4.5.2 Damaged vs. undamaged column behaviour

After completing the study on the elastic buckling behaviour of columns, two different nonlinear analyses were carried out to compare the results and accuracy of the different failure criteria. These analyses are designated as:

- Undamaged column analysis: this is a geometrically nonlinear analysis that uses either Tsai-Hill or Maximum Stress criteria to identify failure, but they do not influence the column response.
- Damaged column analysis: this is a genuinely (geometrically and physically) nonlinear analysis that not only adopts the Hashin criterion to identify failure but also considers its effect (material progressive failure) on the column response.

In this section, these analyses were only carried out for the reference series S0 and for short and intermediate columns (note that long columns did not exhibit any signs of damage in the tests). Regarding the other series and long columns, section 4.5.3 includes further results and discussion.

When performing a nonlinear analysis, there is the need to consider an initial geometrical imperfection of the structure so that the incremental-iterative technique used to solve the system of nonlinear equations is able to surpass the bifurcation point (buckling load) without numerical problems. Since it is complex to measure rigorously the imperfection pattern and amplitude of a structure by experimental means, it is often assumed that its imperfect shape corresponds to that of the critical buckling mode [91]. The imperfection amplitude might have a major effect on the load vs. deflection response and it might also affect the maximum load (strength) of the column.

Through the application of the Southwell plot method (section 4.3.3), it is possible to estimate the amplitude of the initial geometric imperfection and adopt its average value (intermediate and long columns) as input to nonlinear analyses. Since the modified Southwell plot method does not yield the imperfection amplitude but rather the curvature of the post-buckling path, the determination of the

amplitude consisted of a curve fitting process in which several values were tested and the best fit was adopted. The initial imperfection amplitudes adopted for each column length are presented in Table 4.9.

Table 4.9: Initial imperfection amplitudes for nonlinear analyses.

Column length	Imperfection amplitude
Short – 60 cm	0.05 mm
Intermediate – 100 cm	0.48 mm
Long – 200 cm	0.87 mm

Figure 4.24 plots the curves of load vs. lateral displacement for series S0 short (Figure 4.24(a)) and intermediate (Figure 4.24(b)) columns, obtained from both undamaged (dashed lines) and damaged (solid lines) column analyses. Additionally, Table 4.10 comprises the main results obtained in undamaged column analyses (initial failure loads using both Maximum Stress criterion, $P_{if,MS}$, and Tsai-Hill criterion, $P_{if,TH}$) and damaged column analyses (ultimate loads using the Hashin damage failure criteria, $P_{u,H}$). The ultimate loads obtained in experimental tests, $P_{u,Exp}$, are also presented in Table 4.10 and Figure 4.24 for comparison purposes. Figure 4.25 presents the percentage difference (Δ) between these loads ($P_{if,MS}$, $P_{if,TH}$, $P_{u,H}$) and the experimental ultimate load ($P_{u,Exp}$) for both short and intermediate columns.

Table 4.10: Initial and ultimate failure loads of short and intermediate columns using different numerical analyses (failure criteria) and experimental tests (series S0).

Criterion	Short columns	Δ	Intermediate columns	Δ
Experimental – $P_{u,Exp}$ (kN)	733.7	-	531.3	-
Max. Stress – $P_{if,MS}$ (kN)	668.8	-8.8%	472.9	-11.0%
Tsai-Hill – $P_{if,TH}$ (kN)	665.3	-9.3%	470.4	-11.5%
Hashin – $P_{u,H}$ (kN)	669.2	-8.8%	477.3	-10.2%

The numerical analyses provided conservative results, with a maximum difference of 11.5% with respect to the experimental ultimate load. For both column lengths, it may also be stated that there is no significant difference of results between the damaged and the undamaged column models in terms of ultimate and initial failure loads. Thus, if delamination is absent and interest is only focused on the prediction of ultimate load, it is recommended the use of either the Maximum Stress or the Tsai-Hill criteria rather than the Hashin criterion. The former models give a good estimate of maximum strength despite being much less complex than the latter. In fact, the undamaged columns analyses are simpler than damaged column analyses (using the Hashin criterion) because of two main reasons: (i) they are materially linear elastic (nonlinearity arises only from geometrically nonlinear effects), and (ii) they do not need the knowledge of the material fracture energy. The ABAQUS progressive damage model used in the framework of Hashin criterion (i) requires the input of fracture energies associated to four

damage modes (often difficult to determine by experimental means), and (ii) is numerically more demanding as the computational time is higher and severe convergence problems might arise due to unexpected change of equilibrium configurations (*e.g.*, sudden drops in equilibrium paths). Considering these facts and the accuracy of the numerical results obtained, it may be stated that the undamaged column analyses (using either the Maximum Stress or the Tsai-Hill criteria) are perfectly adequate for determining the ultimate load (maximum strength) of bare-GFRP columns subjected to concentric compression, for short and intermediate length columns.

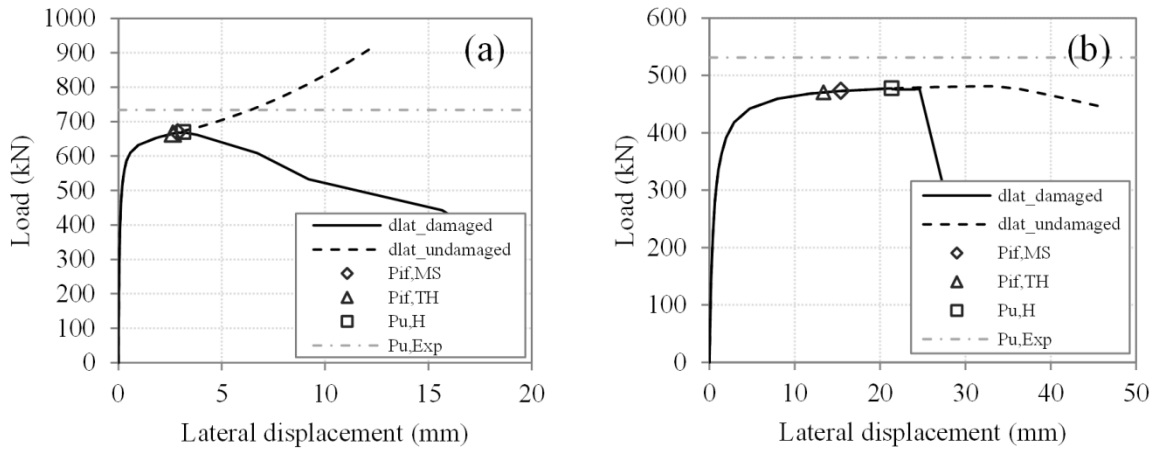


Figure 4.24: Load vs. lateral deflection curves obtained from the undamaged and damaged column analyses: (a) short columns and (b) intermediate columns (series S0).

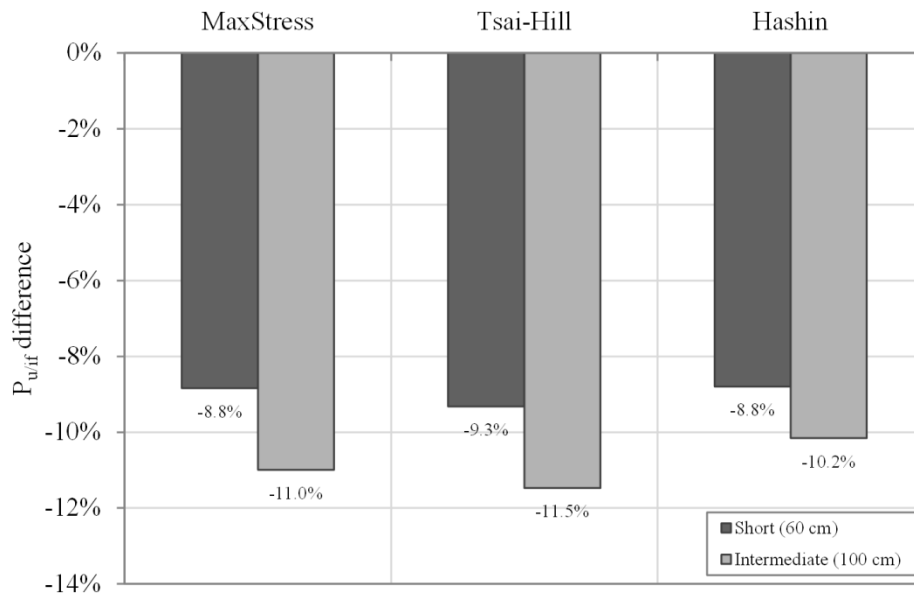


Figure 4.25: Percentage difference between the ultimate experimental loads and failure loads for short and intermediate columns using different failure criteria (series S0).

Note that the post-buckling path (P - δ) determined from the undamaged column analysis of the short column (see dashed line in Figure 4.24(a) for $P > 600$ kN) exhibits approximately a quadratic variation of load P with the lateral displacement δ , as described previously by Barbero and Trovillion [70].

In the case of the undamaged column analysis, the behaviour of intermediate columns is purely flexural for lateral displacements up to about 35 mm. At this stage, the load-displacement curve achieves a maximum (see solid curve in Figure 4.24(b)) and, for increasing displacements ($\delta > 35$ mm), a local deformation is slightly triggered (in-plane deformation of cross-section with low amplitude) and the load starts to decrease (only geometrically nonlinear effects come into play). Because the column behaviour is purely elastic and both individual buckling modes (flexural and local) are characterised by stable post-critical behaviour (*i.e.* the corresponding P - δ curves increase monotonically and do not display a peak), the peak of the P - δ solid curve depicted in Figure 4.24 (b) should be associated with interaction phenomena between both local and flexural buckling modes [26].

In the case of the damaged column analysis, the failure (peak of P - δ curve) occurs for a displacement ($\delta \approx 25$ mm) lower than 35 mm. Therefore, these columns with intermediate length are really affected by material degradation, as this precedes the occurrence of geometrically nonlinear effects. Effectively, this evidence was observed in experimental tests of intermediate columns (section 4.3), in which the load carrying capacity reduction was most likely due to the damage progression rather than buckling mode interaction.

4.5.3 Progressive failure behaviour of columns

This section provides the results of a numerical study on the progressive failure behaviour of pultruded FRP hybrid columns, which comprise (i) load vs. displacement curves, (ii) buckling loads and ultimate loads, (iii) stress vs. strain behaviour, and (iv) failure modes.

4.5.3.1 Load vs. displacement curves

In this sub-section, the results of numerical analyses (in terms of load vs. axial shortening curves, P - ΔL) are summarised and compared to experimental ones. The numerical P - ΔL curves were obtained from damaged column analyses, in which the Hashin failure criterion was associated with material progressive damage. Since all hybrid series have a qualitatively similar behaviour, the P - ΔL curves of reference series S0 are compared only to series S3 herein. Figure 4.26 and Figure 4.27 show the P - ΔL curves for short, intermediate and long columns of series S0 and S3, respectively, alongside the corresponding experimental curves (exhibited by the three specimens). The different dashed grey curves shown in each figure correspond to repeated tests. From the observation of these figures, it is

worth noting that, regardless of the column length (short, intermediate and long columns) and strengthening configuration (both reference and hybrid series), the numerical models simulated the experimental tests very accurately in terms of stiffness, loading path and ultimate load.

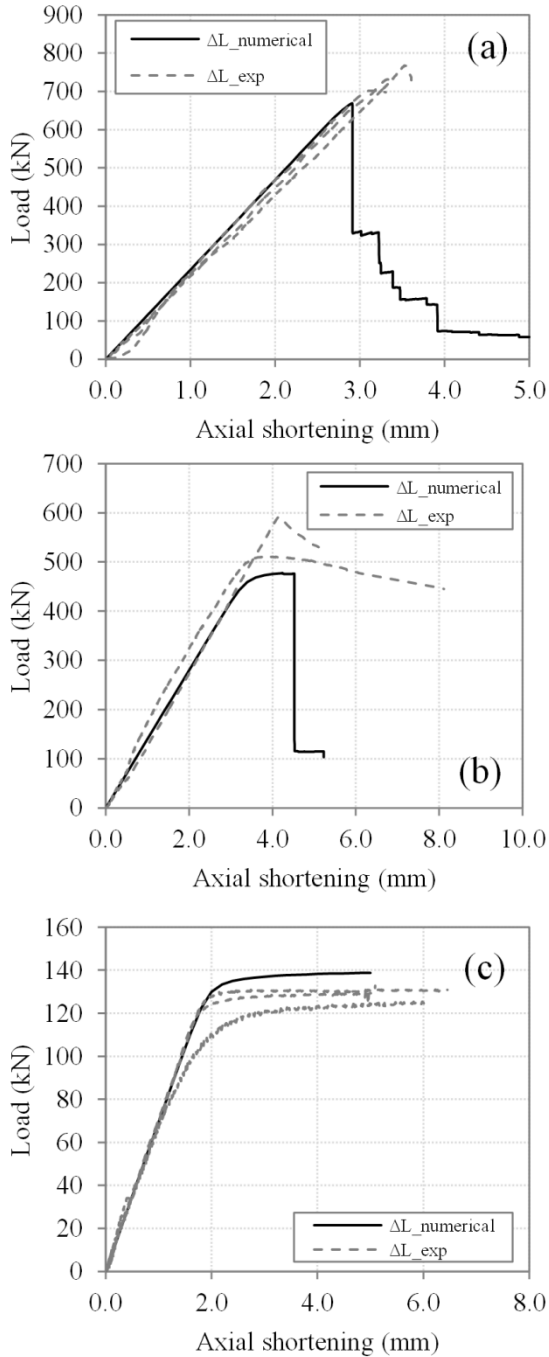


Figure 4.26: Load vs. axial shortening curves (numerical and experimental) of series S0 for (a) short, (b) intermediate and (c) long columns.

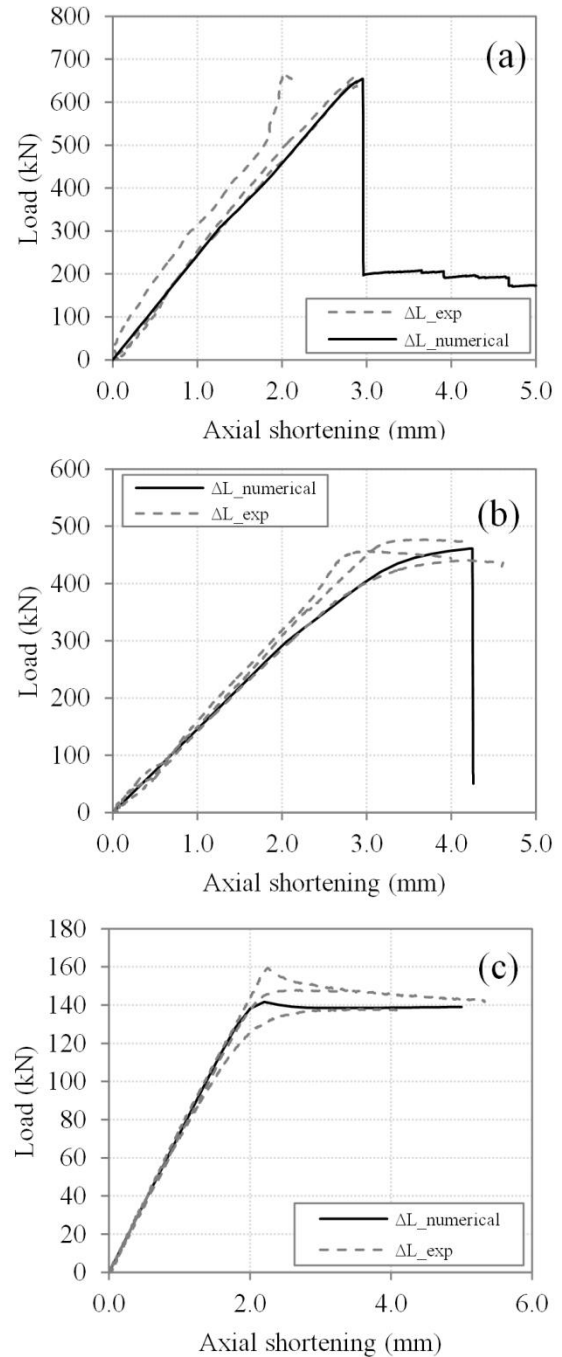


Figure 4.27: Load vs. axial shortening curves (numerical and experimental) of series S3 for (a) short, (b) intermediate and (c) long columns.

4.5.3.2 Critical and ultimate loads

In this sub-section, the results obtained from the nonlinear numerical analyses (in terms of loads) are summarised and compared to experimental ones. Table 4.11 shows the values of critical buckling loads (P_{bk}) and ultimate loads (P_u) for all column series (S0, S1, S2, S3 and S4*) as well as for all column lengths ($L = 60$ cm, $L = 100$ cm, $L = 200$ cm).

Table 4.11: Critical loads and ultimate loads obtained from numerical analyses and experimental tests (for comparison) for all column series and lengths

Length	Series	$P_{bk,exp}$ (kN)	$P_{bk,num}$ (kN)	$\Delta P_{bk,ref}$	$\Delta P_{bk,num-exp}$	$P_{u,exp}$ (kN)	$P_{u,num}$ (kN)	$\Delta P_{u,ref}$	$\Delta P_{u,num-exp}$
Short (60 cm)	S0	689.9	642.9	-	-6.8%	733.7	669.2	-	-8.8%
	S1	645.2	632.8	-1.6%	-1.9%	754.7	666.7	-0.37%	-11.7%
	S2	624.3	647.0	0.6%	3.6%	667.6	665.4	-0.57%	-0.3%
	S3	617.1	631.7	-1.8%	2.4%	660.2	654.3	-2.23%	-0.9%
	S4*	682.8	641.3	-0.3%	-6.1%	689.9	656.5	-1.90%	-4.8%
Intermediate (100 cm)	S0	547.3	487.1	-	-11.0%	531.3	477.3	-	-10.2%
	S1	529.6	470.2	-3.5%	-11.2%	511.4	462.4	-3.12%	-9.6%
	S2	531.5	466.4	-4.2%	-12.2%	517.4	463.9	-2.81%	-10.3%
	S3	476.6	470.4	-3.4%	-1.3%	457.9	461.3	-3.35%	0.7%
	S4*	502.5	485.0	-0.4%	-3.5%	486.3	474.6	-0.57%	-2.4%
Long (200 cm)	S0	133.4	141.2	-	5.8%	129.7	138.8	-	7.0%
	S1	153	157.9	11.8%	3.2%	150.2	151.2	8.93%	0.6%
	S2	149.6	168.5	19.3%	12.6%	144.8	162.3	16.93%	12.1%
	S3	146.4	149.1	5.6%	1.8%	148.4	141.7	2.09%	-4.5%
	S4*	155.4	141.5	0.2%	-8.9%	160.8	140.5	1.22%	-12.6%

In this table, both experimental and numerical values are presented for the critical and ultimate loads. It should be noted that the ultimate load values were determined from analyses in which the Hashin failure criterion was associated with material progressive damage, *i.e.* the damaged column analysis. Although not having collapsed (materially damaged), the ultimate load of long columns (both experimental and numerical) was defined as the maximum load achieved in the load vs. displacement data (horizontal plateau). The numerical critical loads ($P_{bk,num}$) shown in this section were computed by applying the Southwell plot method (or its modified version in the case of short columns) to the load vs. deflection data obtained in the nonlinear numerical analysis¹⁶. The percentage variation of the hybrid series' results with respect to the results of the reference series S0 is shown in Table 4.11 and depicted in Figure 4.28 (critical loads) and Figure 4.29 (ultimate loads).

¹⁶ Note that those values presented in section 4.5.1 were obtained directly from buckling (eigenvalue) analyses.

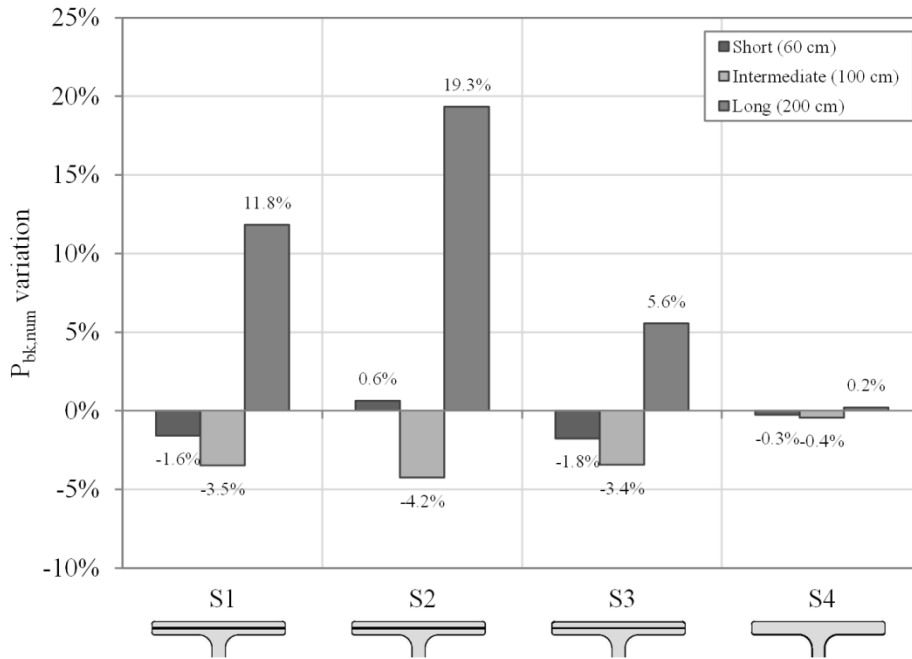


Figure 4.28: Percentage variation of critical loads (relative to reference S0) with column series and lengths (numerical analysis).

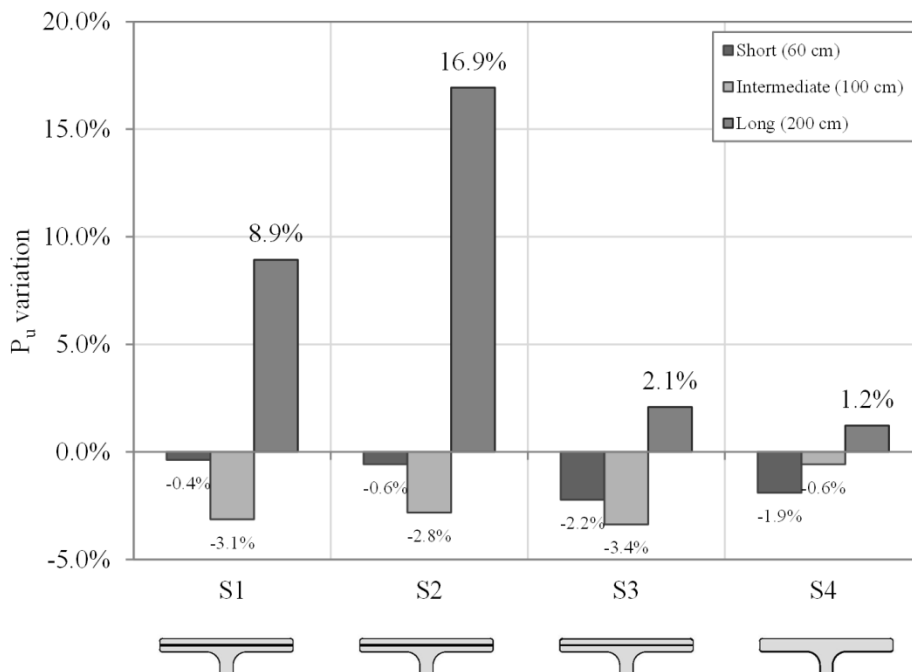


Figure 4.29: Percentage variation of ultimate loads (relative to reference S0) with column series and lengths (numerical analysis).

From the analysis of Table 4.11, Figure 4.28 and Figure 4.29 it is possible to conclude that the critical and ultimate loads of both short and intermediate hybrid columns were almost always lower than those of the reference profiles. This evidence is attributed to the delamination of the CF mats, which were absent in the reference S0 series. Only for long columns, the hybrid series showed to be more effective than the reference series. The replacement of the original GF mats by a small amount of CF

reinforcement (only 2.6% of the total cross-section area) provided a significant increase in terms of critical load, namely for series S2 (19.3%). Series S4* (with an increase of only 0.2%) showed to be the least effective series. These results could (to some extent) be anticipated because this series presented only bidirectional CF mats and the web reinforcement (more than 50% of the total) was much closer to the neutral axis than in the remaining series.

The results of the numerical analyses highlighted that both types of mats have a negative influence in the structural behaviour of short and intermediate FRP columns. In what concerns the short columns, only series' S2 critical load presented a residual increase (0.6%). All other hybrid short and intermediate columns displayed lower critical loads. In terms of ultimate loads of short and intermediate columns, all hybrid series presented lower values than the reference series S0. When comparing both types of mats, the results proved that the unidirectional CF mats are much more efficient than the bidirectional ones¹⁷.

When comparing the results obtained for long columns, series S2 exhibited an increase of 19.3%, much higher than the 5.6% increase obtained for series S3. When comparing the results obtained from experimental tests and numerical analyses (Table 4.11), differences ranging from 1.3% to 12.6% (critical loads) and from 0.3% to 12.6% (ultimate loads) were achieved. These results highlight the very reasonable agreement obtained between both studies, indicating that the developed numerical models are suitable for the simulation of the structural behaviour of FRP columns.

4.5.3.3 Stress vs. strain curves

In this sub-section, the results of numerical analyses (in terms of stress vs. axial strain curves, σ - ε) are presented and verified against experimental ones. As in preceding sub-sections, the numerical σ - ε curves were obtained from damaged column analyses. Figure 4.30 and Figure 4.31 show σ - ε curves obtained from the numerical analyses and experimental tests (for comparison) for all column lengths of series S0 and S3, respectively. The (average) stress corresponds to the applied load divided by the section area, whereas the strains refer to the mid-height section of the column. For the sake of clarity and better understanding of these figures, they only show the ascending branch of σ - ε curves – the sudden drops in stress (that actually occurred due to material failure) could be shown but they would rather lower the data readability.

In what concerns the validation of the numerical models, the σ - ε curves obtained numerically compared well to the corresponding experimental ones, in terms of initial elastic slope (related to column axial stiffness), curve trend and qualitative shape, as well as ultimate stress (related to critical

¹⁷ Note that the bidirectional mats were specially designed for column strengthening against local buckling phenomena, in the longitudinal and transverse directions. Once for these columns the strains developed trigger the mats' delamination prior to buckling, they are not efficient at all.

load). Despite the slight numerical/experimental differences observed for the short columns (most likely due to the “stiffer” test setup), both the stress vs. axial strain curves and the load vs. axial shortening showed that the developed numerical models are very accurate in simulating the compressive behaviour of hybrid FRP columns. Therefore, they might be used with confidence for the execution of parametric studies with other cross-section shapes and/or loading configurations.

4.5.3.4 Delamination and failure modes

Finally, this sub-section presents the results of numerical analyses related with (i) the delamination of the CF mats, and (ii) the column failure modes. Likewise, the failure modes were obtained from damaged column analyses. Figure 4.32 and Figure 4.33 show the patterns of delamination at (i) its onset and (ii) in the brink of failure. The Hashin failure mode corresponding to the delamination of the CF mats is the fibre compression in those layers. In these figures the red colour indicates a fully damaged (fully delaminated) element, $d = 1.0$, while the blue colour indicates the undamaged areas, $d = 0.0$.

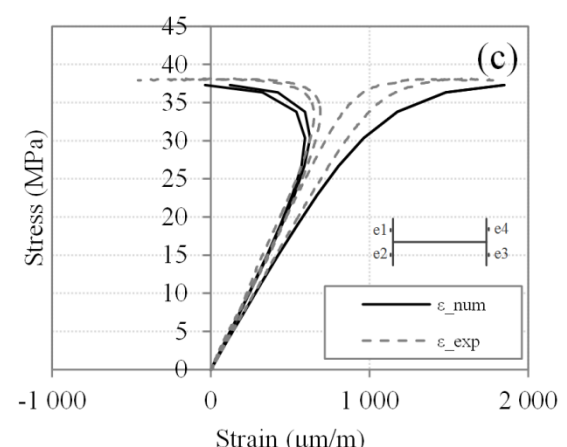
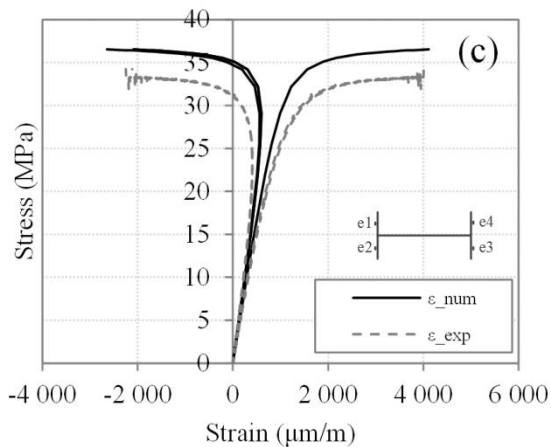
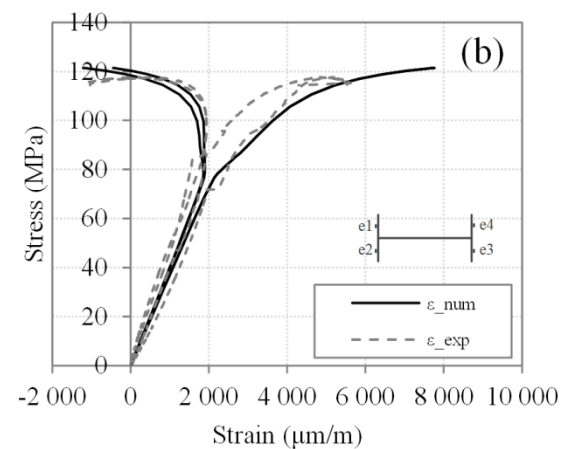
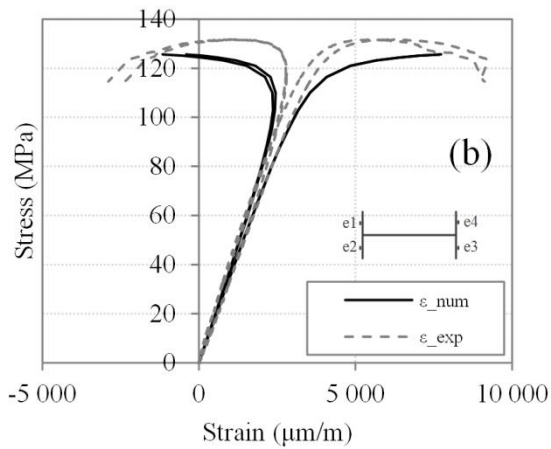
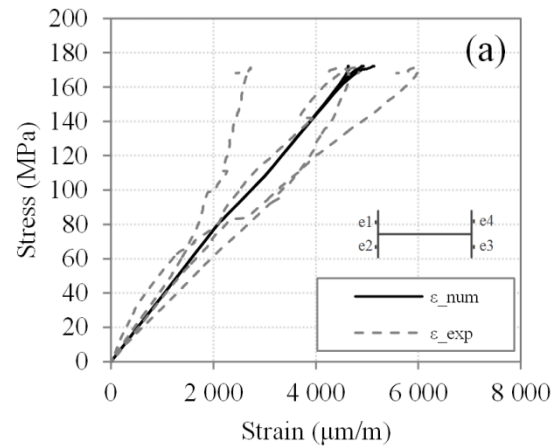
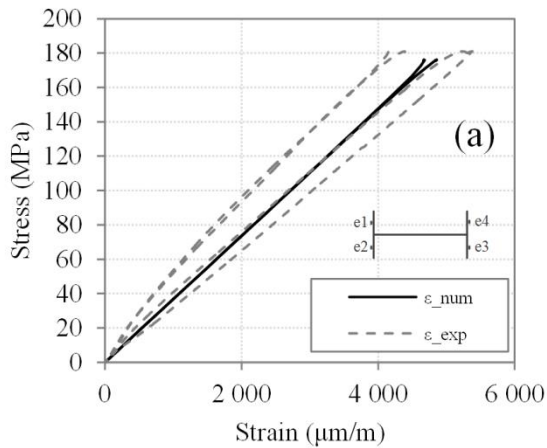


Figure 4.30: Stress vs. axial strain curves (numerical and experimental) of series S0 for (a) short, (b) intermediate and (c) long columns.

Figure 4.31: Stress vs. axial strain curves (numerical and experimental) of series S3 for (a) short, (b) intermediate and (c) long columns.

As expected, short columns seem to be the most affected by the delamination phenomenon, both due to the higher axial strains that they are subjected to and to the fact that the local buckling phenomenon does not introduce a significant eccentricity in the deformed shape. In Figure 4.32, it may be seen that the delamination is triggered all over the flange surface of short columns, being higher near the end sections. On the other hand, intermediate and long columns' delaminated areas are triggered in the

most compressed part of the flanges, due to the bending stress component arising from the initial imperfection shape. In the onset of collapse (Figure 4.33), the CF layers of the short columns were fully damaged (delaminated), while for intermediate columns they only delaminated in the areas corresponding to the most compressed parts of the flanges and close to the end sections.

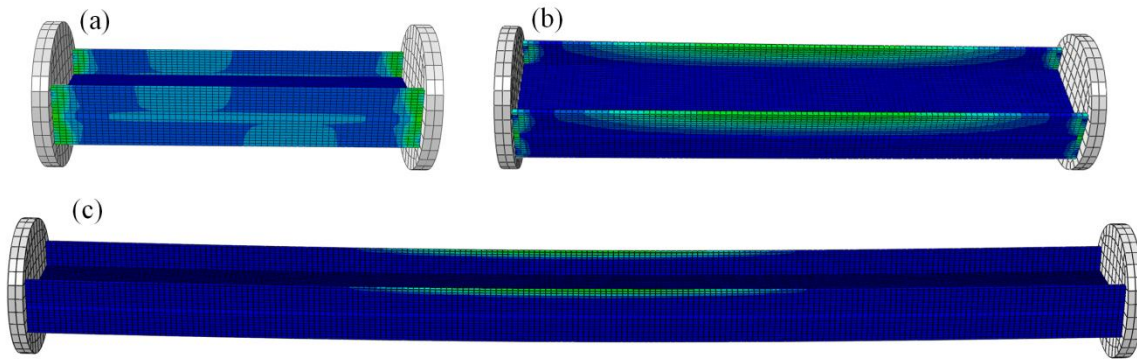


Figure 4.32: Pattern of delamination onset for (a) short, (b) intermediate and (c) long columns (series S3).

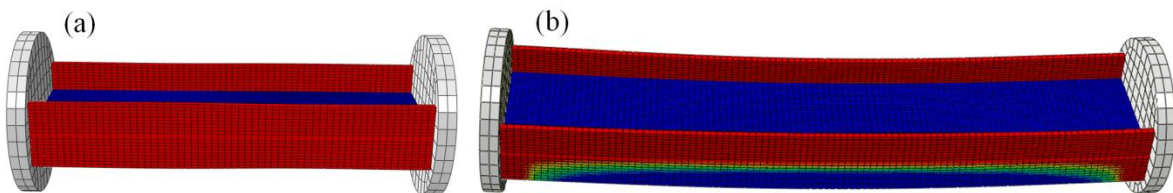


Figure 4.33: Delamination state in the onset of failure for (a) short and (b) intermediate columns (series S3).

Now let us turn our attention to the column failure (collapse) modes. Figure 4.34 illustrates the envelope of the damaged zones for the Hashin matrix tension and shear failure mode (which is the governing failure mode) at the onset of collapse for both short columns (Figure 4.34(a)) and intermediate columns (Figure 4.34(b)) of series S0 – in these figures the red colour indicates a fully damaged element, $d = 1.0$, while the blue colour indicates the undamaged areas, $d = 0.0$. Figure 4.35 is similar to Figure 4.34, but now for the case of post-failure mode. The long columns of the reference series S0 did not exhibit any damage zones for the maximum imposed shortening (5 mm), a fact that is also in agreement with the test results. Figure 4.36 shows the experimental observations in terms of failure modes.

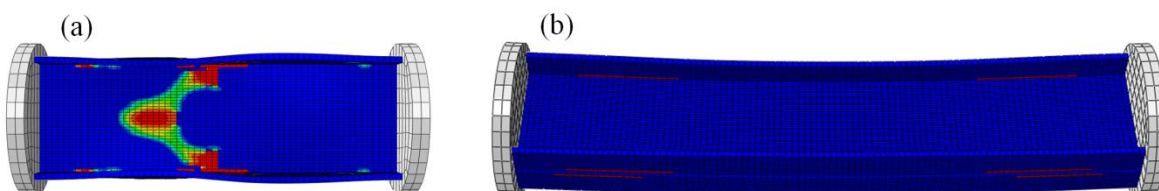


Figure 4.34: Pattern of damaged zones at the onset of failure of (a) short columns ($\Delta L = 2.91$ mm) and (b) intermediate columns ($\Delta L = 4.28$ mm) – reference series S0.

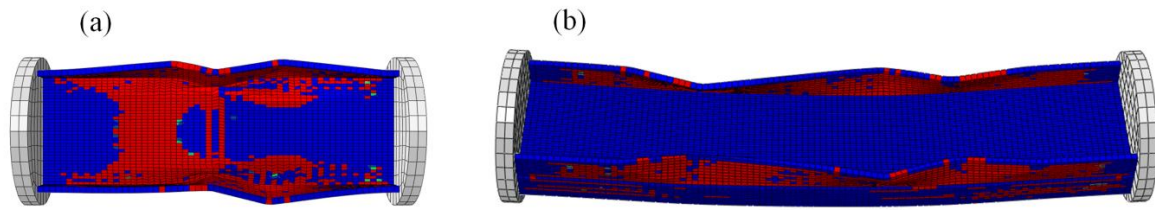


Figure 4.35: Pattern of damaged zones in failure mode of (a) short columns ($\Delta L = 5.0$ mm) and (b) intermediate columns ($\Delta L = 5.23$ mm) – reference series S0.

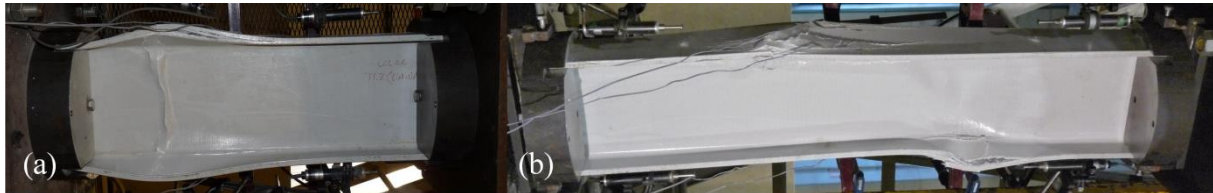


Figure 4.36: Experimental post-failure shape of (a) short and (b) intermediate columns.

For both short and intermediate lengths, the damaged zones concentrate in the web-flange junctions. Nevertheless, for short columns the web elements govern columns failure, while for intermediate columns the flange elements are more influential to failure. Figure 4.35 shows that, after failure, the damaged zones of the short columns comprise a large area in both flanges and web, while the damaged zones in intermediate columns are mainly restricted to the flanges. As seen in these figures, the numerical models have simulated the experimental observations very accurately.

4.6 ASSESSMENT OF DESIGN STANDARDS

In this section, three different analytical approaches for the design of FRP columns are presented and their predictions are compared to the numerical and experimental results presented herein and in sections 4.2 and 4.3. It is known that the ultimate load of columns under compression is influenced by a combination of material strength and buckling phenomena. The existing rules for the design of FRP composite columns consider the material strength and the buckling phenomena separately, never in combination: neither the material strength affects the buckling phenomena, nor the buckling phenomena influence the material strength. This is clearly shown in the design formulas presented next, which are related to the design provisions of two main standards: (i) the Italian *Guide for the Design and Construction of Structures made of FRP Pultruded Elements* [12], and (ii) the American (ASCE) *Pre-Standard for Load & Resistance Factor Design (LRFD) of Pultruded Fibre Reinforced Polymer (FRP) Structures* [11]. Additionally, the design approach suggested by Bank [2] is also thoroughly described.

Because FRP materials exhibit high mechanical strength but moderately low elastic properties, the buckling phenomena almost always govern the column ultimate behaviour, while the material strength is seldom the major influence on column ultimate behaviour. Although FRP columns could present a

considerable post-buckling strength, namely those possessing wide flanges¹⁸, most design approaches follow the assumption proposed by Bank [2] and consider that an FRP column always fails when its critical load is achieved. Therefore, the column ultimate load considered in FRP design codes is often the critical buckling load. In order to verify the suitability of this assumption and assess its impact on the accuracy of the main FRP design standards and guidelines for pultruded composites, the numerical results obtained herein (namely the critical loads) were compared to those provided by the Italian guidelines, the American pre-standard and Bank's design approach.

There are some noticeable differences in the application of these design methods. The Italian guidelines [12] follows a methodology similar to that of Eurocode 3 [92] for steel columns. The equations used in this design approach are listed next.

$$N_{c,Rd} = \min\{N_{c,Rd1}, N_{c,Rd2}\} \quad (27)$$

$$N_{c,Rd1} = A f_c \quad (28)$$

$$N_{c,Rd2} = \chi N_{l,Rd} = \chi \frac{A f_l}{\gamma_f} \quad (29)$$

$$f_l = \min\{f_l^f, f_l^w\} \quad (30)$$

$$f_l^f = 4 G_{LT} \left(\frac{t_f}{b_f} \right)^2 \quad (31)$$

$$f_l^w = k_c \frac{\pi^2 E_L t_w^2}{12 (1 - \nu_{LT} \nu_{TL}) d_w^2} \quad (32)$$

$$k_c = 2 \sqrt{\frac{E_T}{E_L}} + 4 \frac{G_{LT}}{E_L} \left(1 - \nu_{LT}^2 \frac{E_T}{E_L} \right) + 2 \nu_{LT} \frac{E_T}{E_L} \quad (33)$$

$$\chi = \frac{1}{c \lambda^2} \left(\Phi - \sqrt{\Phi^2 - c \lambda^2} \right) \quad (34)$$

$$\Phi = \frac{1 + \lambda^2}{2} \quad (35)$$

$$\lambda = \sqrt{\frac{N_{l,Rd}}{N_E}} \quad (36)$$

$$N_E = \frac{1}{\gamma_f} \frac{\pi^2 E I_{min}}{L_{bk}^2} \quad (37)$$

in which $N_{c,Rd}$ is ultimate load; $N_{c,Rd1}$ is compressive squash load (accounting for material strength); $N_{c,Rd2}$ is critical load (accounting for instability effects); A is cross-section area; f_c is longitudinal compressive strength; $N_{l,Rd}$ is local buckling load; f_l , is local buckling stress; χ is local buckling reduction factor; γ_f is safety factor; k_c is coefficient accounting for the web boundary conditions; Φ

¹⁸ As seen in section 4.5.2, the profile studied in this chapter possesses narrow flanges and presented only 1.3% of post-buckling strength.

is auxiliary coefficient; c is coefficient accounting for the local-global buckling interaction; λ is column slenderness; N_E is flexural (Euler) buckling load; I_{min} is moment of inertia about the minor axis.

The key issue is that this methodology replaces the “axial plastic load” of the steel column (N_{pl}) considered in Eurocode 3 by the elastic local buckling load of the composite column (N_l). This can be clearly seen in Eq. (29). This replacement makes some sense because both depend only on cross-section geometry and do not depend on the column length. However, there is a misunderstanding in the “equivalence” between N_{pl} and N_l , because the former depends on the material strength (steel yield stress) and the latter does not (the local critical load is purely elastic and does not depend on FRP strength). Unlike the Eurocode 3, the Italian guidelines methodology does not consider an imperfection factor, or considers $\alpha = 0$, a fact that is clearly seen in Eq. (34), which does not include a linear term in λ (column slenderness), because it adopts the Eurocode 3 formula with $\alpha = 0$. The Italian guidelines also include a coefficient c that takes into account the possible interaction between buckling modes (local-flexural interaction). This coefficient always takes a unit value ($c = 1$) in Eurocode 3. Despite the three above mentioned differences, the design procedures of the Italian guidelines for FRP columns and Eurocode 3 for steel columns are identical.

The elastic local buckling load (N_l) of the column requires the calculation of stress for flange buckling (f_l^f), considering the flange simply supported on one edge and free on the other, and the stress for web buckling (f_l^w), considering the web simply supported on both edges. The elastic flexural load, or the Euler buckling load (P_E), should also be determined. Then, a factor χ (always lower than unit) that depends on the column local-flexural slenderness λ should be applied to reduce the local buckling load and get the elastic compressive load carrying capacity ($N_{c,Rd2}$) of the column. The level of reduction provided by factor χ depends on the relevance of global flexural buckling with respect to local buckling: $\chi \rightarrow 1$ if local buckling is much more prevalent than flexural buckling, otherwise $\chi \rightarrow 0$. Thus, the coefficient c enables this interaction between flexural and local buckling modes.

As mentioned before, the material strength is not considered in the calculation of $N_{c,Rd2}$ but only in the determination of the column squash load $N_{c,Rd1}$, which depends on the cross-section area and ultimate compressive stress of the material in the axial direction of the column. Because (i) the buckling effects are not considered in the calculation of $N_{c,Rd1}$ and (ii) material strength is not considered in the calculation of $N_{c,Rd2}$, it should be stressed that there is no interaction between physically nonlinear effects and geometrically nonlinear effects in the calculation of the column ultimate load, which is the minimum of $N_{c,Rd1}$ and $N_{c,Rd2}$.

The American pre-standard [11] provides a simpler approach than the Italian guidelines based on the assumption that the interaction between local and global buckling modes is absent. Therefore, four

critical stresses (equations listed next) are determined: (i) web local buckling stress (F_{crw}); (ii) flange local buckling stress (F_{crf}); (iii) flexural (Euler) buckling stress about the weak x -axis (F_{crx}); and (iv) flexural (Euler) buckling stress about the strong y -axis (F_{cry}). The critical load is then considered as the lowest of these critical stresses multiplied by the column cross-section area. The American pre-standard also preconizes that the compressive squash load should be computed as the compressive strength multiplied by the gross cross-section area.

$$P_u = \min\{P_{cr}; P_{comp}\} \quad (38)$$

$$P_{comp} = F_L^{comp} A_g \quad (39)$$

$$P_{cr} = F_{cr} A_g = \min\{F_{crx}; F_{cry}; F_{crf}; F_{crw};\} A_g \quad (40)$$

$$F_{crx} = \frac{\pi^2 E_L}{\left(\frac{K_x L}{r_x}\right)^2} \quad (41)$$

$$F_{cry} = \frac{\pi^2 E_L}{\left(\frac{K_y L}{r_y}\right)^2} \quad (42)$$

$$F_{crf} = \frac{G_{LT}}{\left(\frac{b_f}{2t_f}\right)^2} \quad (43)$$

$$F_{crw} = \frac{\left(\frac{\pi^2}{6}\right) (\sqrt{E_{L,w} E_{T,w}} + \nu_{LT} E_{T,w} + 2 G_{LT})}{\left(\frac{d_w}{t_w}\right)^2} \quad (44)$$

in which P_u is ultimate load; P_{cr} is critical buckling load; P_{comp} is compressive squash load; F_L^{comp} is material compressive strength in the fibre direction; A_g is gross cross-section area; F_{cri} is critical buckling stress of member i (x – global about x axis; y – global about y axis); f is flange local; w is web local); $E_{i,p}$ is elastic modulus in direction i and plate p ; K_i is effective buckling length factor in direction i ; r_i is cross-section radius of gyration in direction i ; L is member length; G_{LT} is shear modulus; b_f is flange width; t_f is flange thickness; d_w is web depth; t_w is web thickness ν_{LT} is Poisson ratio.

The third design approach described herein was proposed by Bank [2], partly based on the work of Kollár [71]. This approach is slightly more complex than that followed by the American pre-standard because the elastic rotational restraint of the stockiest plate to the slenderest plate is considered at the web-flange junction(s). Its equations are listed next.

$$P_u = \min\{P_{cr}^{comp}; P_{cr}\} \quad (45)$$

$$P_{cr}^{comp} = \sigma_{L,c} A_z \quad (46)$$

$$P_{cr} = k_{int} P_l \quad (47)$$

$$k_{int} = k_\lambda - \sqrt{k_\lambda^2 - \frac{1}{c \lambda}} \quad (48)$$

$$k_\lambda = \frac{1 + \left(\frac{1}{\lambda}\right)^2}{2c} \quad (49)$$

$$\lambda = \sqrt{\frac{P_l}{N_E}} \quad (50)$$

$$P_l = \sigma_{w,eff} A \quad (51)$$

$$\sigma_{w,eff} = \frac{\pi^2}{t_w d_w^2} \left(2\sqrt{D_L D_T (1 + 4.139\xi)} + (D_{LT} + 2D_S)(2 + 0.62\xi^2) \right) \quad (52)$$

$$\xi = \frac{1}{1 + 10 \left(\frac{D_{T,w}}{k_{l-web} d_w} \right)} \quad (53)$$

$$k_{l-web} = 4 \frac{D_{T,f}}{b_f} \left[1 - \frac{\sigma_w E_{L,f}}{\sigma_f E_{L,w}} \right] \quad (54)$$

$$\sigma_f = \frac{\pi^2}{t_f \left(\frac{b_f}{2}\right)^2} \left[D_L \left(\frac{\frac{b_f}{2}}{a}\right)^2 + 12 \frac{D_S}{\pi^2} \right] \quad (55)$$

$$\sigma_w = \frac{2\pi^2}{t_w d_w^2} (\sqrt{D_L D_T} + D_{LT} + 2D_S) \quad (56)$$

in which P_u is ultimate load; P_{cr}^{comp} is compressive squash load; P_{cr} is critical buckling load due to interaction between global and local modes; $\sigma_{L,c}$ is longitudinal compressive strength; A_z is cross-section area; k_{int} is factor that accounts for local and global imperfections; P_l is local buckling critical load; λ is non-dimensional slenderness ratio; c is empirical curve fitting constant; N_E is Euler buckling load; $\sigma_{w,eff}$ is effective web critical stress (due to the elastic restriction at the edge); D_L , D_T , D_S and D_{LT} is longitudinal, transverse, shear and coupling plate rigidities; a is half-wave length; k_{l-web} is spring constant.

The plate that triggers the buckling of the column is first identified considering the critical stresses (σ_f, σ_w) and the longitudinal elastic moduli ($E_{L,f}, E_{L,w}$) of the flange and web (considering a heterogeneous profile). As discussed by Bank, the half-wave length (a) required for the calculation of σ_f , is often not available¹⁹. Next, the local buckling load (P_l) is determined using the buckling stress of the governing plate ($\sigma_{w,eff}$), which is usually the web in narrow flange profiles like those studied herein, and also the elastic restriction at the web-flange junction, through the parameter ξ . The interaction between local and global buckling modes is also taken into account: interaction exists for local-global slenderness values within the range $0.5 < \lambda < 1.5$, while it is negligible for λ values

¹⁹ Herein, $a = 200$ mm was considered (distance between inflection points of the buckled shape in short columns).

outside this range (pure local or pure global buckling modes prevail). The procedure for interactive buckling is similar to that prescribed in the Italian guidelines. The failure due to limit of longitudinal compressive stress is simply computed as the compressive strength (determined in coupon testing) multiplied by the cross-section area. The interaction between material failure and buckling is not considered.

Now, let us turn our attention to the results. First, the squash load of the columns studied herein (either $N_{c,Rd1}$ [12], P_u [11], or P_{cr}^{comp} [2]), which depends on cross-section area and material axial strength, is roughly 1778 kN. This value does not vary much between series, as the small differences found are only due to the delamination of CF mats in hybrid series. This squash load is much higher (roughly 2.7 times) than the maximum buckling load (669.2 kN) obtained for all the columns' series and lengths. This evidence substantiates the previously mentioned fact (also suggested by Bank) that elastic buckling load prevails over material strength when the calculation of column ultimate load is sought. Hereafter, the presented design results will focus only on buckling loads as the column ultimate loads²⁰. The values obtained by the application of the three design approaches are presented in Table 4.12 for all series (not only reference series S0 but also the hybrid series) and lengths. Figure 4.37 also shows the three design curves obtained for series S0, one for each approach, and includes rhomb and square points denoting experimental and numerical buckling loads, respectively.

Both Italian guidelines and American pre-standard provided far too conservative predictions of the ultimate load of short columns (with differences of up to 32% and 28% when compared to the experimental and numerical results, respectively). In fact, neglecting the rotational restraint of the web-flange (*i.e.* considering simply supported edges) provides an estimate of critical load of the web up to 24% lower than that given by considering the flange rotational restraint. For this reason, the approach suggested by Bank is surely the most accurate one for short columns (maximum differences of 13% and 7% with respect to the experimental and numerical results, respectively), although not always conservative.

Regarding the global (pure flexural) buckling behaviour, all three design approaches presented reasonable predictions of the ultimate load. The Italian guidelines showed to be the most accurate, with a maximum difference of 9% to the experimental results.

²⁰ Note that none of these design approaches address the delamination phenomenon. Thus, they could be less suitable for hybrid FRP members.

Table 4.12: Critical (ultimate) loads obtained from three different design approaches.

Length	Series	$P_{u,American}$ (kN)	$N_{c,Italian}$ (kN)	$P_{cr,Bank}$ (kN)
Short (60 cm)	S0	533.2	465.8	600.0
	S1	533.5	495.0	652.8
	S2	520.4	498.4	654.9
	S3	548.3	491.2	648.3
	S4*	540.7	488.4	622.4
Intermediate (200 cm)	S0	533.2	354.5	438.8
	S1	533.5	386.3	489.1
	S2	520.4	394.9	502.0
	S3	548.3	377.0	474.1
	S4*	540.7	370.2	454.9
Long (200 cm)	S0	152.1	135.7	152.1
	S1	174.2	153.6	174.2
	S2	184.2	161.1	184.2
	S3	164.3	146.0	164.3
	S4*	157.6	140.8	157.6

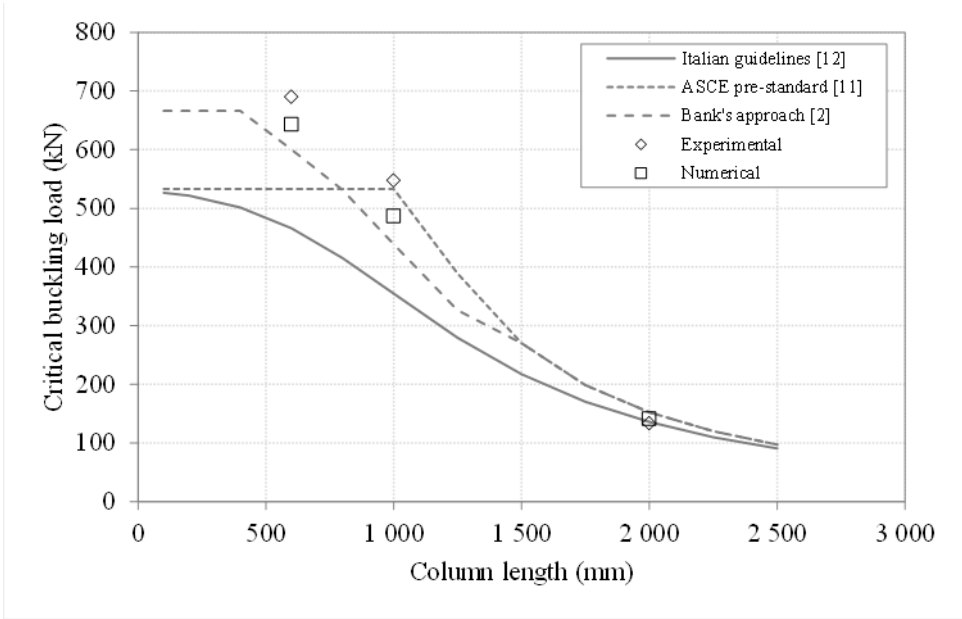


Figure 4.37: Column design curves from Italian guidelines [12], ASCE pre-standard [11] and Bank's approach [2], and comparison with experimental and numerical results (series S0).

In what concerns the intermediate length columns, the Italian guidelines showed to be far too conservative, while the approaches by Bank and the American pre-standard presented reasonably accurate predictions of the ultimate load. However, due to the fact that the latter does not consider the interaction between global and local buckling modes, its safety design factors might need a better

adjustment (note that the post-buckling behaviour in intermediate columns could be less stable due to local-flexural buckling interaction). The recommended values of the empirical coefficient c are 0.65 and 0.80 by the Italian guidelines and Bank, respectively.

4.7 CONCLUDING REMARKS

This chapter presented and discussed results obtained from an extensive experimental, numerical (finite element) and analytical studies campaign about the structural behaviour of hybrid FRP pultruded columns, with different lengths and incorporating different types and architectures of carbon fibre mats reinforcing glass-fibre reinforced polyester (GFRP) I-section profiles. The following main conclusions may be drawn:

1. Even though small amounts (2.6% of the cross-section area) of CF reinforcement were used, the hybridization of GFRP profiles was effective in stiffening the structural members, providing an increase in axial stiffness up to 17% exhibited in experimental tests.
2. In long columns, the above-mentioned stiffness increase enabled the hybrid columns to present higher experimental global buckling critical loads (10 to 17%) when compared to the reference GFRP profile.
3. In the experimental testing of both short and intermediate length hybrid columns, when the average axial stress across the I-section reached roughly 80 MPa, progressive delamination of the CF mats seems to have been triggered; consequently, the critical buckling load of those hybrid columns was lower (1 to 13%) than that of the reference series.
4. Delamination was more obvious in the axial stress *vs.* strain experimental curves of series S3. This fact may be explained by the saturation issues concerning the bidirectional CF mats reported by the manufacturer, or simply because series S3 was the only one in which the strain gauges were directly bonded to the CF mats.
5. The Hashin-based material progressive damage analysis used in the FE numerical models adequately simulated both the material failure and the delamination of carbon fibre mats.
6. For compression members (columns), the prediction of first failure load through the Tsai-Hill criterion agreed well with experimental and numerical (Hashin-based) ultimate loads. The good performance of Tsai-Hill criterion is related to the quasi-uniform stress state in the column: even in locally buckled columns, the stress redistribution arising from buckling deformation does not lead to very high stress concentration, *i.e.* the case in which Tsai-Hill criterion fails to achieve accurate ultimate load estimates (always too conservative).
7. Concerning the numerical ultimate loads, the results of progressive failure analyses presented a reasonably good agreement with the experimental data (maximum difference of 12.6%); the failure modes obtained in the numerical analyses were also consistent with those observed experimentally.

8. The three design approaches showed a reasonably good agreement to the experimental and numerical results in what regards moderately long and long columns; however, the Italian guidelines [12] and the American pre-standard [11] failed to provide accurate predictions of ultimate load for short columns (or even columns laterally braced).
9. For all column lengths, the approach suggested by Bank [2,71] proved to be the most accurate.

CHAPTER 5

STRUCTURAL BEHAVIOUR OF LATERALLY BRACED HYBRID FRP BEAMS

5.1 PRELIMINARY CONSIDERATIONS

The structural behaviour of GFRP pultruded members under bending has been widely investigated through experimental, analytical and numerical studies. It is known that GFRP pultruded beams may fail by global (lateral-torsional) buckling if bracing is absent. However, even if bracing exists, GFRP pultruded beams may collapse in local buckling modes, which are far less studied than lateral-torsional modes. In order to avoid (or at least delay) local buckling of GFRP beams, carbon fibre mats can be added to GFRP profiles to strengthen them. Unlike the GFRP beams, these hybrid FRP beams are still scarcely studied in regard to their local buckling behaviour. Alongside the study presented in Chapter 4 for hybrid C-GFRP pultruded columns, similar analyses were performed to address the flexural behaviour of these pultruded profiles.

The flexural response of GFRP pultruded members has been investigated through experimental, analytical and numerical studies. This section presents a brief literature review of the main studies performed in this field. Correia [9] and Nunes [8] performed experimental and numerical studies about the structural behaviour of a bare GFRP beam and a hybrid C-GFRP beam with unidirectional CF mats, respectively, with similar I-section. Despite the fact that the hybrid beam presented considerably higher initial bending stiffness than the all-GFRP beam, it failed prematurely due to the delamination of the CF mats located in the compressed flange, causing a cross-section reduction. Numerical FE models provided a reasonably good agreement with the experimental results both in terms of stiffness and ultimate load, but the progressive delamination and failure behaviour of the hybrid beam were not addressed. Since the delamination was very noticeable in the load vs. deflection curves of the hybrid beam, two different (simplified) numerical models were developed (one with and another without CF mats) and their curves were adjusted (joined) in the point for which delamination occurred.

Bank and Yin [24] developed FE models in the NIKE3D software to study the post-buckling behaviour of laterally braced wide-flange GFRP pultruded beams. The authors simulated the

progressive failure of the web-flange junction using a node-separation technique. The results obtained were later compared with experimental data. A good agreement was obtained in terms of buckling and ultimate loads, and the simulation of the progressive web-flange separation was also successful.

Hai *et al.* [47] carried out flexural tests on hybrid C-GFRP I-beams comprising different CF contents in the flanges. The bending stiffness consistently increased with the amount of CF, while the maximum load carrying capacity was obtained for an intermediate CF content (33%) (*i.e.*, for higher amounts of CF reinforcement the maximum load decreased). Unfortunately, no results were reported for a reference all-GFRP beam, which would allow for a more accurate and comprehensive evaluation of the advantages of introducing CF in bare GFRP profiles. Furthermore, the experimental tests were not numerically modelled in this work.

As already mentioned in section 4.1, Ragheb [45] performed a parametric numerical study on the behaviour of hybrid C-GFRP pultruded beams. Different fibre patterns, with varying CF amount, were designed aiming at maximizing the linear critical buckling load of I-section beams under four-point bending. Results indicated that the critical load is highly dependent on the CF reinforcement geometry and content. The optimal CF geometry (in terms of maximum increase of critical load) consisted of reinforcing the web-flange junction; at the same time, this was the most economical hybrid solution. Despite their relevance, the numerical results obtained in this study were only validated for the all-GFRP series – no experiments were performed regarding the hybrid cross-sections. Moreover, neither the delamination between the GF and CF layers nor the failure behaviour of the FRP beams were addressed.

This chapter aims at fulfilling some of the gaps pointed out in the brief review previously presented. A comprehensive experimental campaign and FE numerical simulations were carried out in order to study the serviceability and failure behaviour of laterally hybrid FRP pultruded beams, comprising different types and architectures of CF mats, and addressing the material progressive delamination and failure. Similarly to the study presented in Chapter 4, linear eigenvalue analyses and progressive damage analyses using the Hashin damage initiation criterion were implemented in ABAQUS in order to simulate the structural behaviour of the tested beams. Extensive mechanical characterisation tests provided the input data required for the numerical models. The experimental and numerical ultimate loads were then compared to analytical predictions provided by two different design approaches: (*i*) the Italian guidelines [12] and (*ii*) the American pre-standard [11]. The accuracy of each design approach is discussed.

5.2 EXPERIMENTAL STUDY

5.2.1 Objectives and experimental program

The main objectives of the experimental study were to evaluate the advantages and drawbacks of introducing CF mats in all-GFRP profiles subjected to bending, regarding their performance for both serviceability and ultimate limit states. To that purpose, a total of five laterally braced hybrid C-GFRP profiles were tested in four-point bending up to failure. These tests allowed assessing the influence of introducing CF in the stiffness, ultimate loads and failures modes of the FRP profiles. Alongside these full-scale tests, small-scale material characterisation tests were also performed to determine the elastic and strength properties of the composite laminates.

5.2.2 Experimental series and mechanical characterisation tests

As already mentioned all five hybrid FRP pultruded series (Figure 5.1) were designed based on previous research carried out by the authors. The pultruded profiles presented an I-section geometry ($200 \times 100 \times 10$ mm, web height \times flange width \times wall thickness) and were manufactured by *ALTO Perfis Pultrudidos, Lda*. The interested reader should refer to section 4.2.2 (page 51) for detailed information regarding the design and manufacturing of each hybrid series. The properties obtained in the small-scale coupon mechanical characterisation tests are listed in Table 5.1 and Table 5.2. Note that the properties listed in Table 5.1 refer to the homogenized GFRP and C-GFRP hybrid laminates.

Table 5.1: Elastic properties of GFRP and C-GFRP laminates.

Type of laminate	$E_{L,t}$ (GPa)	$E_{L,c}$ (GPa)	$E_{T,c}$ (GPa)	G_{LT} (GPa)	ν
GFRP	32.7	33.4	10.8	3.65	0.266
Uni. C-GFRP	40.8 ⁽¹⁾	-	-	-	-
Bidir. C-GFRP	35.9 ⁽²⁾	-	-	-	-

⁽¹⁾ From the laminate geometry and fibre architecture, the unidirectional CFRP longitudinal elastic modulus was computed as 193 GPa based on the classical lamination theory (rule of mixtures).

⁽²⁾ Using the same procedure, the bidirectional CFRP longitudinal elastic modulus was computed as 95.9 GPa.

Table 5.2: Strength properties of GFRP laminate and C-GFRP laminae.

Type of laminate/laminae	$\sigma_{L,t}$ (MPa)	$\sigma_{L,c}$ (MPa)	$\sigma_{T,c}$ (MPa)	τ_{LT} (MPa)	F^{sbs} (MPa)
GFRP laminate	365	468	110	30.6	27.6
Uni. C-GFRP laminae	1389 ⁽¹⁾	-	-	-	-
Bidir. C-GFRP laminae	837 ⁽¹⁾	-	-	-	-

⁽¹⁾ The longitudinal strength corresponds to the CFRP layers only and was computed by multiplying the CFRP material longitudinal elastic modulus by the ply failure strain.

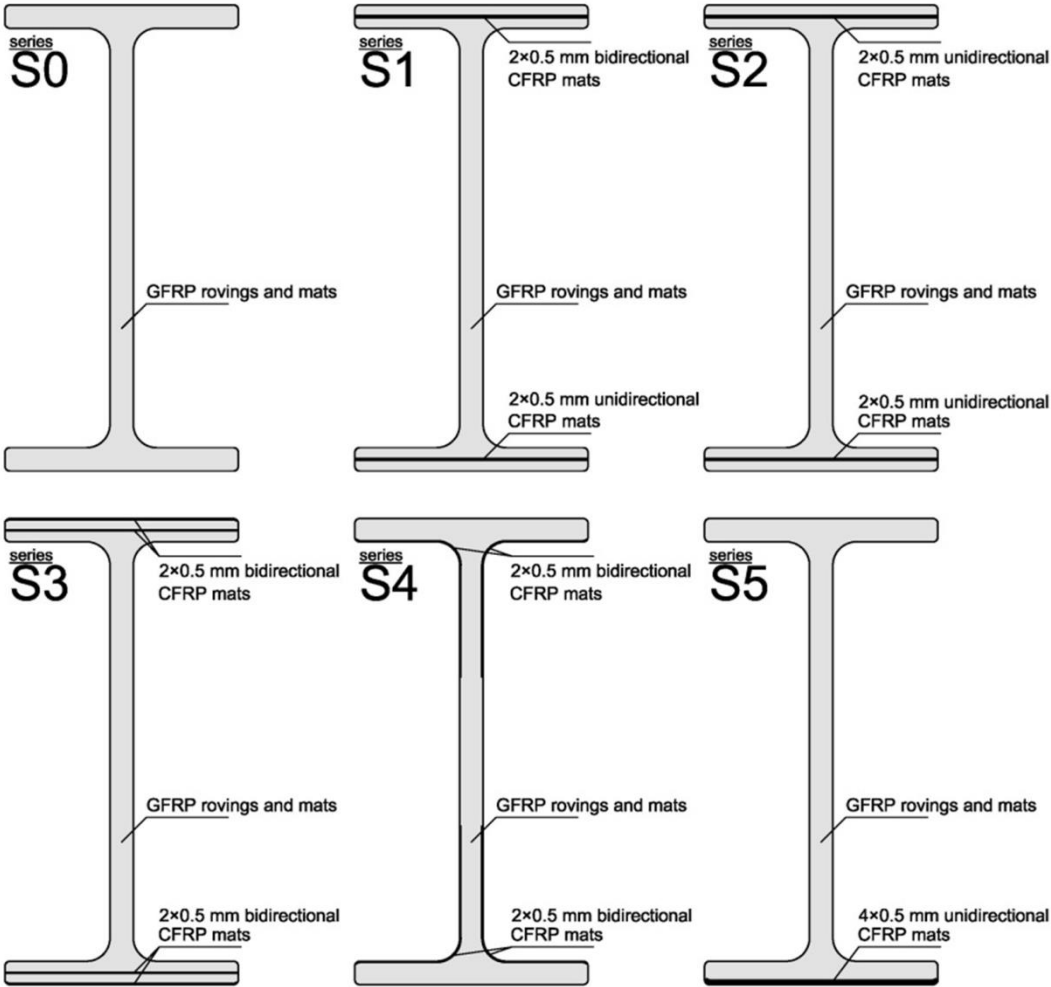


Figure 5.1: Reference GFRP (S0) and hybrid C-GFRP (S1 to S5) pultruded experimental series.

In this campaign, a total of 12 specimens (two replicate specimens per series) were laterally braced and tested under bending. Each specimen is uniquely labelled according to the following nomenclature: *series_specimen*. For instance, the first specimen of series S5 is identified as S5_1.

5.2.3 Flexural tests - setup, instrumentation and procedure

The test setup is schematically illustrated in Figure 5.2. The 4.20 m long FRP beams were tested in a simply supported configuration in a span of 4.00 m. The beams were tested in four-point bending, subjected to two point loads applied at thirds of the span (≈ 1.33 m).

The end supports were materialized by two sets of rollers-and-plates. The load was applied by means of an *Enerpac* hydraulic jack (capacity of 600 kN) and measured with a *Novatech* load cell (capacity of 100 kN). An IPE 180 steel beam was used to transfer the load from the jack to the loaded sections. The deflections under the loaded sections and under the mid-span section were monitored using respectively two TML-50 displacement transducers and one TML-500 displacement transducer. The

former displacement transducers were used only in the early loading stage aiming at checking the test setup's symmetry. They were then manually removed when the measuring piston nearly reached its stroke length²¹; subsequently, only the mid-span transducer was used to measure the overall beam deflection up to failure. Four strain gauges were bonded to the flanges' outer faces in sets of two, with an offset of 20 mm from the flange border. They were bonded to all tested specimens at a known section, offset 30 cm from the mid-span.

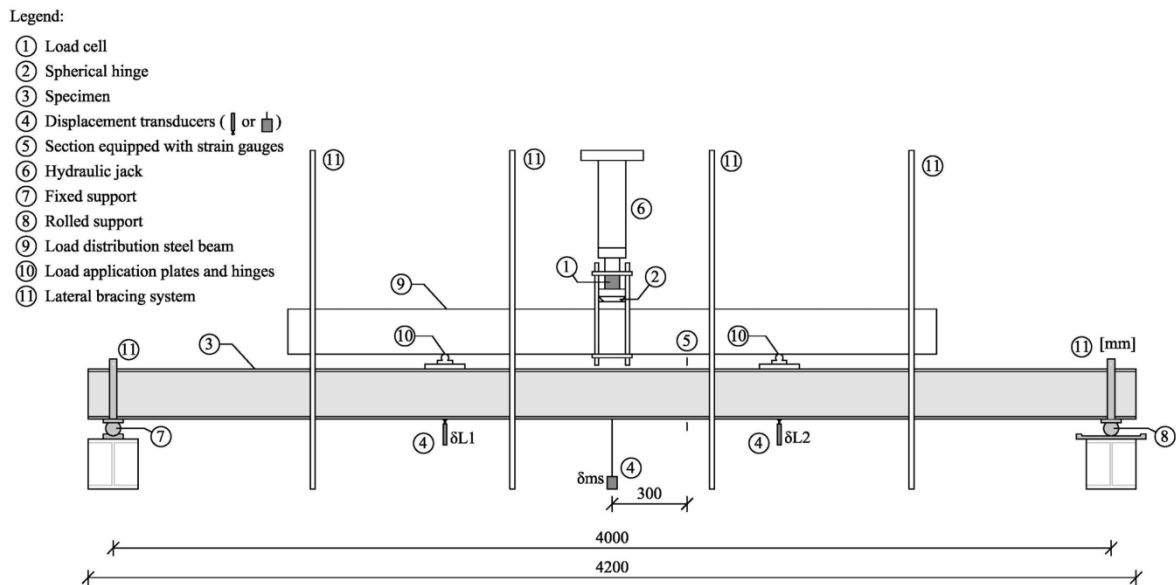


Figure 5.2: Setup used in four-point bending tests.

The lateral bracing system consisted of eight RHS $40 \times 20 \times 2$ (mm) and four steel SHS $25 \times 25 \times 1$ (mm) steel bars. The RHS bars were attached to the steel closed loading frame and were filled with timber in order to absorb more efficiently the impact energy released during the brittle failure of the FRP pultruded beams. The SHS bars were welded to the support plates and connected through an M8 bolt (Figure 5.3). To avoid any type of restriction to the vertical deformation of the FRP beams, the lateral bracing system was positioned keeping a free distance of about 1 mm to the flanges' edges and the inner surfaces of the bars were carefully greased.

Data were acquired at a rate of 50 Hz using an HBM *Spider8* data logger and registered in PC. Tests were conducted under load control at an average speed of 0.25 kN/s.

²¹ This procedure was adopted to protect the equipment from the brittle and high energy releasing failure that characterizes FRP pultruded flexural members.

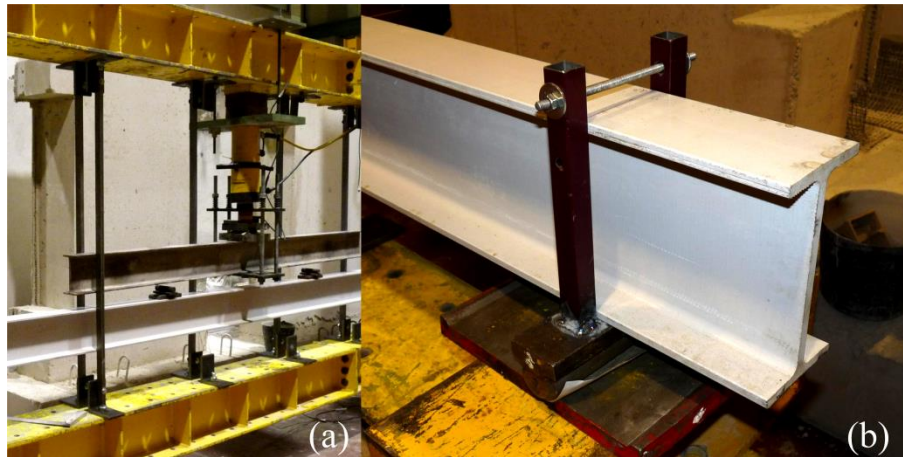


Figure 5.3: Lateral bracing system: (a) RHS bars attached to the framework and (b) SHS bars welded to the supports.

5.3 EXPERIMENTAL RESULTS

5.3.1 Load vs. deflection behaviour

Figure 5.4 depicts the load vs. mid-span deflection curves of representative specimens from all series (one from each series)²². It is worth mentioning that the deflections measured under the loaded sections were practically coincident for the same load level, thereby attesting the symmetry of the test setup.

The results obtained confirm that the introduction of CF fibres in bare GFRP profiles increases the flexural stiffness, at least for serviceability limit states, since all hybrid curves lay above the reference one, namely in their early stages (2.2% to 7.8% higher). One may also notice that in two of these representative specimens (S1 and S3) the flexural stiffness decreased throughout the test and, for loads closer to the ultimate load, the corresponding displacement became roughly similar to that of the reference profile. This seems to indicate that in these specimens delamination of the CF mats might have occurred. The only common aspect in these two series is the bidirectional CF mat positioned in the top flange (which, as already mentioned was more difficult to impregnate – section 4.2.2).

The load vs. deflection curves allowed determining the beams' bending stiffness²³ (K), ultimate load (P_u) and corresponding ultimate bending moment (M_u). The ultimate shear stresses ($\tau_{LT,u} = P_u/2A_v$, A_v being the shear area) were also determined. Table 5.3 presents a comparison of the results obtained for all series, including the stiffness and ultimate load ratios between the hybrid and the reference series. The relative differences in terms of ultimate load are also depicted in Figure 5.5.

²² The results obtained from one specimen (S4_1) were discarded due to a manufacturing defect; that beam specimen was unloaded before collapsing.

²³ The data considered in the trendline comprised mid-span deflections ranging from 10 mm to 25 mm.

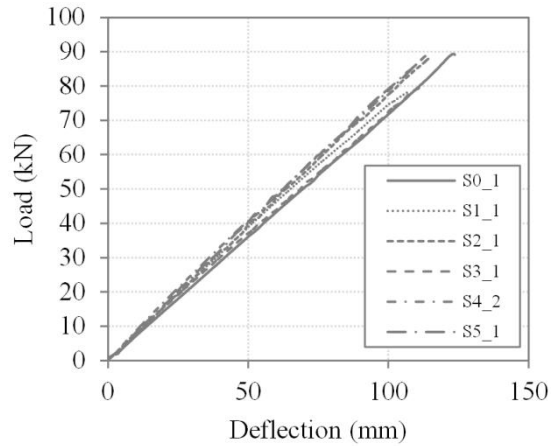


Figure 5.4: Load vs. mid-span deflection curves for representative specimens of all series.

Table 5.3: Average bending stiffness (K), ultimate load (P_u), ultimate bending moment (M_u), and ultimate shear stress ($\tau_{LT,u}$).

Series	K (kN/mm)	K/K^{S0} (-)	P_u (kN)	P_u/P_u^{S0} (-)	M_u (kN m)	$\tau_{LT,u}$ (MPa)
S0	0.770	-	87.8	-	58.4	24.5
S1	0.800	1.039	80.8	0.920	53.7	22.6
S2	0.788	1.023	87.9	1.001	58.4	24.6
S3	0.786	1.022	81.3	0.926	54.1	22.7
S4 ⁽¹⁾	0.830	1.078	88.8	1.011	59.0	24.8
S5	0.810	1.052	82.6	0.941	54.9	19.3

⁽¹⁾ Value corresponding to a single specimen.

There are a few relevant conclusions that may be drawn from this analysis. In average, the ultimate load of the hybrid profiles was 4% lower than that of the reference one and this seems to stem from the saturation issues faced with the bidirectional CF mats (reported by the manufacturer). Indeed, the relatively high fibre density of the CF mats may have turned their interfaces into “weak points”, more prone to delamination triggering. This issue was more acute in series S1 and S3 than in series S4, most likely because the position of the latter series’ CF mats is more favourable in terms of delamination, since they are located closer to the cross-section centroid (neutral axis).

The results obtained indicate that symmetrical unidirectional CF mats (series S2) are preferable for flexural beam applications; in fact, a small amount of CF reinforcement led to a significant bending stiffness increase and furthermore it did not compromise the beams’ ultimate strength.

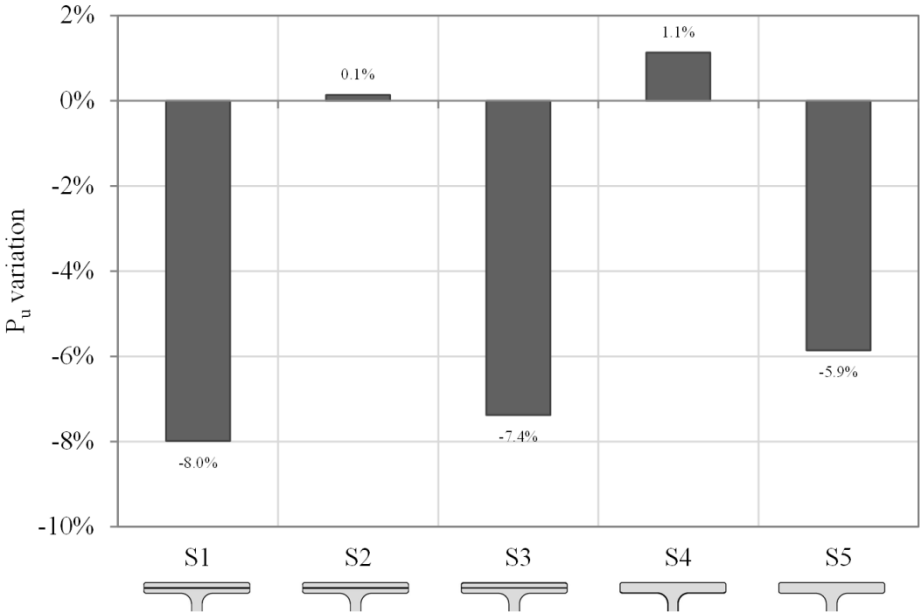


Figure 5.5: Relative difference between the average ultimate loads of the different hybrid series compared to reference series S0.

5.3.2 Load vs. strain behaviour

Now regarding the load vs. strain data, Figure 5.6 presents the curves measured at each strain gauge of one representative specimen from series S0 and series S3 for comparison purposes²⁴.

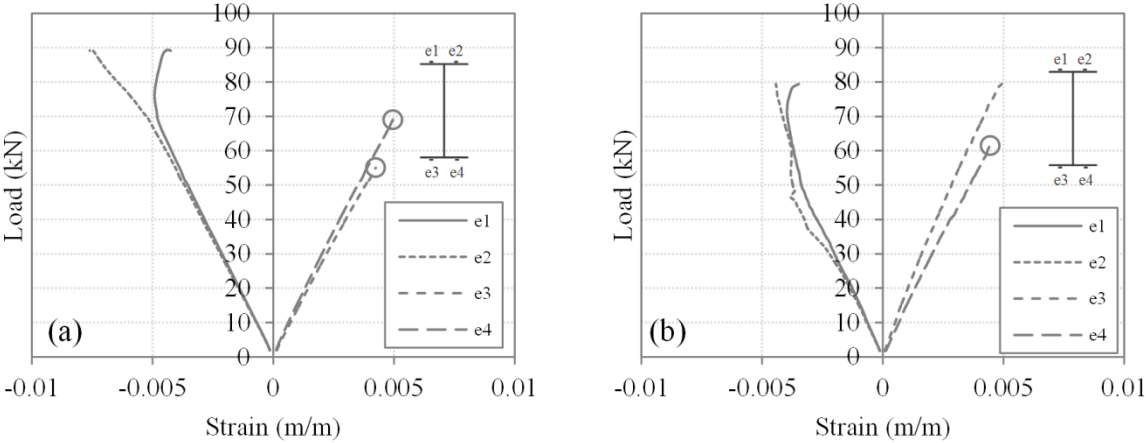


Figure 5.6: Load vs. strain curve of (a) specimen S0_1 and (b) specimen S3_1 (the circumferences (o) indicate the instant when strains stopped being measured).

²⁴ The bottom flange strains were not always measured up to failure. Indeed, due to the large deformations developed in the profile, the strain gauges installed in some specimens provided valid measurements only up to a certain load level. In these figures the circumferences (o) indicate the levels for which the strains stopped being measured.

As expected, all the profiles presented an initial linear elastic load path, which was kept up to a load level of roughly 80% of their ultimate load. Some specimens, like *S3_1* (Figure 5.6(b)), presented a slight twist eccentricity despite the efforts made in correctly positioning the beam specimens and the applied loads. In most specimens, the top flange strains started diverging in the final stage of the test, indicating some sort of buckling phenomenon (Figure 5.6(a)). From the load vs. strain curves, it is difficult to state whether the nature of the buckling phenomenon was either local or global²⁵. In series S3, the upper flange path showed a major perturbation in both specimens for axial strains around 0.002. Such perturbation was most likely due to the triggering of delamination of the bidirectional mats, also patent in the load vs. deflection data.

The modified Southwell plot method [70] could have been used to evaluate the local buckling load obtained from the experimental tests. However, it seems that material failure was triggered closely to the onset of local buckling and, therefore, it might have deteriorated the stiffness of the initial post-buckling path. This fact precludes the use of Southwell plot, which was developed for elastic (undamaged) buckling states. In order to illustrate such evidence, the top flange strain gradient ($\Delta\varepsilon = \varepsilon_1 - \varepsilon_2$, cf. Figure 5.2, page 105) was used as the perturbation parameter to determine the local buckling load using the modified Southwell plot method. This option was deemed adequate since the difference between the strains measured at each strain gauge is negligible up to the onset of buckling and then it rapidly increases. In order to illustrate the above mentioned evidence, the modified Southwell plot method was applied to beam *S0_1* (Figure 5.7) and a local buckling load of 72.9 kN was computed.

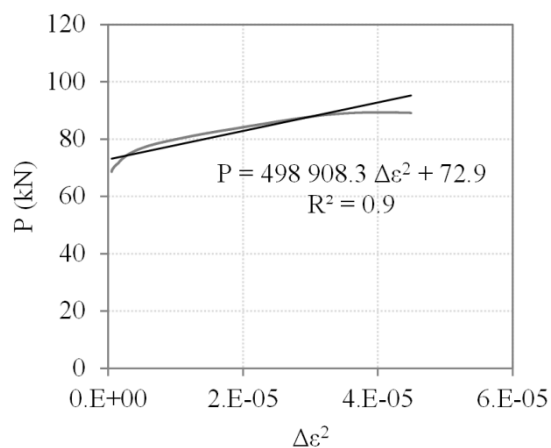


Figure 5.7: Load vs. squared strain gradient of specimen *S0_1*: application of modified Southwell plot method.

Effectively, this value is much lower than that obtained from the numerical analysis (119.0 kN, cf. Table 5.6) but only slightly lower than the ultimate load measured from experimental tests (87.8 kN,

²⁵ To some extent, this difficulty may have been caused by the limited stiffness provided by the lateral bracing system used in the test setup.

cf. Table 5.3, page 107). This result reflects a very limited local post-buckling stiffness, which is not a trademark of elastic local post-buckling. Most likely the result was influenced by pre-buckling material failure. Because the modified Southwell plot should be used for elastic (undamaged) structures, it will not be applied herein.

5.3.3 Failure modes

In this section, the failure mode configurations are presented and discussed. As already referred, a single specimen (S4_1), out of 12, was not considered in this analysis, as it presented a very unusual failure mode, which was not considered to be valid and was attributed to a flaw during manufacturing. Regarding the remaining tests, a single failure mode was observed, which was highly brittle and energy releasing. It comprised the rupture of the top web-top flange junction, the crushing of the top flange and the in-plane buckling of the web. These three events occurred almost simultaneously and thus it was impossible to visually determine each event separately. In some cases, the damaged zone included also the web-bottom flange junction. Regarding this failure mode, the only difference among the various beam specimens was the section in which failure occurred. In some specimens failure took place under one of the loaded sections, while in others it occurred in a section of the loaded span (Figure 5.8). Since the loaded sections were subjected to both longitudinal and shear stresses and those of the loaded span were subjected only to longitudinal stresses, in the absence of local buckling, *a priori* one expected failure to be governed by the former sections due to stress interaction. As it was mentioned before, this behavioural evidence might also be attributed to the occurrence of localized failure of the material prior to local buckling of the top (compression) flange. Further insight on this matter will be provided in sections 5.4 and 5.5 (numerical analyses).

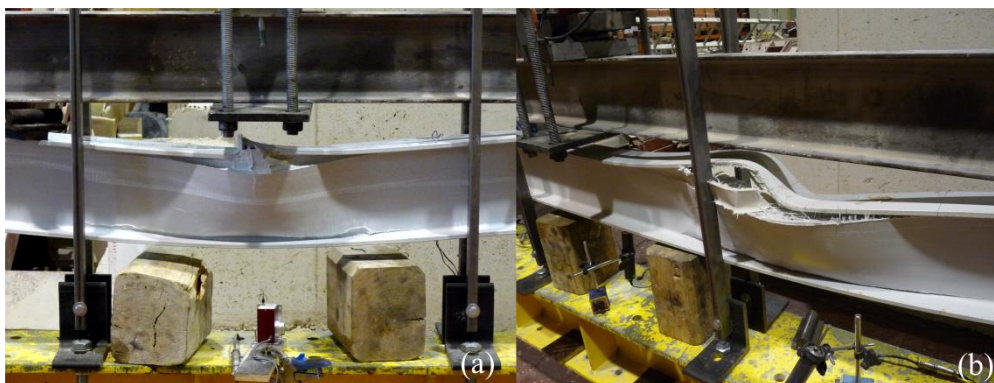


Figure 5.8: Failure modes: (a) at one section of the loaded span (specimen S0_1) and (b) at one loaded section (specimen S0_2).

5.4 DESCRIPTION OF THE NUMERICAL MODELS

The main objective of the numerical analyses presented herein was to simulate the structural behaviour of the hybrid FRP pultruded beams exhibited in the flexural tests described earlier in sections 5.2 and

5.3. First, the elastic critical buckling loads and the corresponding buckling modes were computed for all beam series (S0 to S5). Also, the first buckling mode (corresponding to the least critical load) was used as initial imperfection for the progressive damage analyses performed afterwards. Next, a progressive damage analysis was carried out in order to simulate the failure behaviour of the beams. The progressive failure of the material was implemented in ABAQUS using the Hashin-based damage analysis (thoroughly described in sections 4.4.2 and 4.4.3, page 74). The numerical results were compared to the experimental data, hence validating the FE models developed. One should note that experimental series S4 was the only one in which the introduction of the CF mats was not made by direct replacement of the original GF mats. Thus, this series presented more reinforcing material than the remaining ones. For an accurate and fair numerical comparison between the different series, a similar fibre content (partially replacing glass fibres) was considered in this series and thus it was designated as S4* in this section.

The finite element (FE) numerical models were developed using the software ABAQUS by Simulia [72]. Similarly to the columns' study, several independent parts were defined, namely: (i) the FRP pultruded beam, (ii) the lateral bracing system (RHS and SHS steel bars), and (iii) the supports and load plates, reproducing the dimensions used in the experimental campaign (Figure 5.9).

All steel elements were meshed using eight-node solid elements with reduced integration (C3D8R) and assigned isotropic elastic properties so that the equivalent flexural stiffness (EI_{eq}) was equal to their actual stiffness. To adequately simulate the experimental tests, the lateral edges of the steel bars were offset 1.0 mm from those of the pultruded profile. Such procedure allowed for the free deformation of the beam in the early loading stage and for the consideration of an initial imperfection according to the first buckling mode (which was considered to have amplitude of 0.5 mm). The I-section FRP profiles ($200 \times 100 \times 10$ mm) were meshed using eight-node continuum shell elements with reduced integration and three integration points across each layer's thickness (SC8R). The interested reader should refer to section 4.4.1 for more information regarding continuum shell elements.

The FRP beams were meshed uniformly with an element length-to-width ratio of 10:5 (mm) except for the web-flange junction, which was meshed with a ratio of 10:10 (mm). The pultruded I-sections thus presented a total of 74 elements and 150 nodes in their cross-section and a total of 31,080 elements and 63,150 nodes in the whole member. Preliminary studies on the convergence of FE mesh were performed (not shown here).

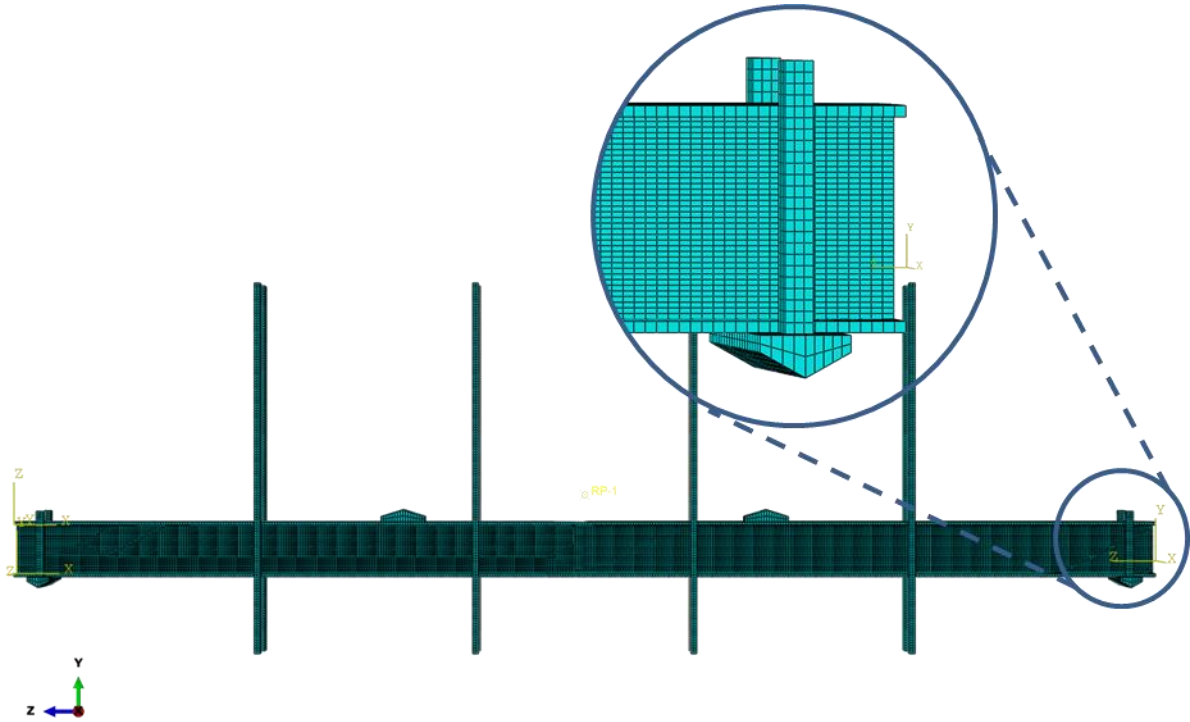


Figure 5.9: Finite element model and mesh.

According to the experimental series, three different types of materials were considered: (i) GFRP, (ii) unidirectional CFRP, and (iii) bidirectional CFRP. The elastic and strength properties considered for all composite materials were the same as the adopted in Chapter 4 (regarding the structural behaviour of hybrid columns) and are presented in Table 5.4 and Table 5.5, respectively, where E_i is the Young’s modulus in the i direction, ν_{ij} is the Poisson ratio between directions i and j , G_{ij} is the shear modulus in the ij plane, $S_{t,i}$ and $S_{c,i}$ are respectively the tensile and compressive strengths in the i direction, and S_{ij} is the shear strength in the ij plane.

Table 5.4: Elastic properties of the different composite materials.

Material	E_1 (MPa)	E_2 (MPa)	ν_{12}	G_{12} (MPa)	G_{13} (MPa)	G_{23} (MPa)
GFRP laminate	36633	10754	0.266	3648	3648	1601
Unidir. CFRP laminae	192853	10754	0.266	3648	3648	1601
Bidir. CFRP laminae	95920	95920	0.266	3648	3648	3648

The interfaces between the FRP beams and the supports/load plates were modelled using a surface-to-surface contact interaction with hard normal contact and a tangential friction coefficient of 0.5 (minimum possible to avoid convergence issues due to slipping). The interfaces between the FRP beams and the lateral bracing system were also modelled with hard normal contact but frictionless tangential behaviour.

Table 5.5: Strength properties of the different composite materials.

Material	$S_{t,1}$ (MPa)	$S_{c,1}$ (MPa)	$S_{t,2}$ (MPa)	$S_{c,2}$ (MPa)	S_{12} (MPa)	S_{23} (MPa)
GFRP laminate	365	468	85.8	110	30.6	30.6
Unidir. CFRP laminae	1389	569	85.8	110	30.6	30.6
Bidir. CFRP laminae	837	201	837	201	30.6	30.6

Load and boundary conditions were applied directly to the steel plates. Load was applied to both load plates in the same proportion in the negative way of the y axis by means of concentrated loads in the linear buckling analysis and imposed displacements in the nonlinear analysis. Regarding the support plates, restrictions were set in their reference edge (corresponding to the centre of rotation), allowing only for free rotation about x in both supports and displacement along z in the sliding support. The lateral bracing system was considered to be fully fixed in its attachment to the steel framework.

The Hashin damage initiation criterion used in this study is a fibre composite specific initial failure criterion that allows predicting the failure initiation of a given FRP member. The interested reader should refer to sections 4.4.2 and 4.4.3 for more information regarding the failure initiation criterion and the progressive damage evolution model used in ABAQUS.

The delamination between the CFRP and GFRP layers was modelled also using the Hashin damage criterion, namely considering the fibre compression mode of the CFRP layers. Thus, no actual separation was considered at the interface, but rather a decrease of stiffness in the CFRP layers as damage progresses. The fracture energies associated to the delamination (*i.e.*, G_{fc} of the CFRP layers) adopted herein are the same as those adopted for the numerical modelling of hybrid columns (section 4.4.3, page 75). The use of the viscous damage regularization coefficient is recommended to avoid convergence difficulties associated with softening analyses [72]. The value of 1.0×10^{-5} was used in the present study.

5.5 NUMERICAL RESULTS, VALIDATION AND DISCUSSION

The following sub-sections present the results obtained in the numerical study. First, the elastic buckling behaviour of the beams is evaluated and the buckling loads of all series are presented. Next, in order to assess the nonlinear behaviour and failure of laterally braced beams, the results of the progressive failure analyses are shown and discussed. The results obtained, namely the load-deflection and stress-strain curves, are compared to the corresponding experimental data presented earlier to validate the suitability of the numerical models.

5.5.1 Linear buckling behaviour

An eigenvalue linear buckling analysis was first performed aiming at determining each series' elastic buckling load. One should note that the eigenvalue analysis is physically linear and thus the delamination of the CF mats is not considered herein. Table 5.6 presents the results obtained for each series in terms of the global (unbraced) critical load ($P_{bk,g}$), corresponding to the lateral-torsional buckling phenomenon (*i.e.*, not accounting for the effect of the lateral bracing system), and the local (braced) buckling critical loads ($P_{bk,l}$). In both cases, the ratios between the hybrid and reference series are provided. The two main buckling modes (lateral torsional buckling and local buckling) are illustrated in Figure 5.10.

Table 5.6: Global ($P_{bk,g}$) and local ($P_{bk,l}$) buckling loads obtained from numerical analyses.

Series	$P_{bk,g}$ (kN)	$P_{bk,g}/P_{bk,g}^{S0}$	$P_{bk,l}$ (kN)	$P_{bk,l}/P_{bk,l}^{S0}$
S0	6.09	-	119	-
S1	6.37	1.046	116	0.975
S2	6.71	1.102	117	0.983
S3	6.34	1.041	122	1.025
S4*	6.49	1.066	143	1.202
S5	6.24	1.025	123	1.034

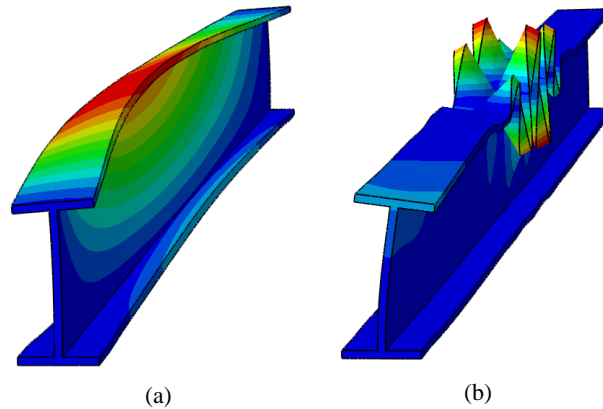


Figure 5.10: Deformed shapes of the main numerical buckling modes.

As expected, series S2 presents the highest lateral-torsional buckling load increase compared to series S0, since it also presents the stiffest CF reinforcement in the top flange. Regarding the local buckling of the top flange, series S4* was the most effective by far, confirming the study from Ragheb [45], who pointed out that the reinforcement of the web-flange junction in flexural members increases the local buckling critical load. Note also that the critical buckling load increases about 20 times due to the lateral braces.

It can be seen that the local buckling loads obtained from the numerical models are significantly higher than the ultimate loads measured in the tests (for instance, in series S0 the experimental ultimate load was 26% lower than its local buckling critical load). These results seem to indicate that the instability phenomenon observed in the experimental campaign were not triggered by the local buckling (instability of the top flange). Since the numerical ultimate loads (listed further in section 5.5.2) cope with the corresponding experimental results, being significantly lower than the local buckling loads, it may be concluded that local buckling phenomena did not cause the beam collapse, but another source instead.

5.5.2 Progressive failure behaviour

5.5.2.1 Load vs. displacement curves

Figure 5.11 and Figure 5.12 plot the numerical load vs. mid-span deflection curves obtained for series S0 and S3, respectively, for comparison purposes. The experimental curves obtained in each specimen are also presented. Figure 5.13 compares the load-displacement curves obtained for each series. Table 5.7 summarises the numerical bending stiffness (K_{num}), ultimate loads ($P_{u,num}$) and their experimental counterparts ($P_{u,exp}$); the stiffness and ultimate load ratios between the hybrid and reference series are also presented as well as the ratio between the experimental and numerical ultimate loads.

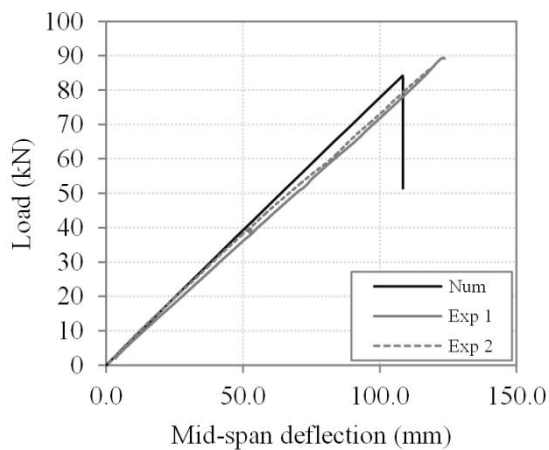


Figure 5.11: Numerical and experimental load vs. mid-span deflection curve for series S0.

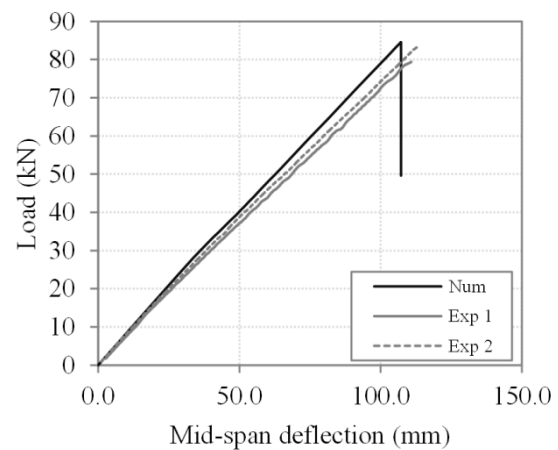


Figure 5.12: Numerical and experimental load vs. mid-span deflection curve for series S3.

Table 5.7: Numerical bending stiffness (K_{num}) and ultimate loads ($P_{u,num}$) and comparison with reference series (S0) and experimental data.

Series	K_{num} (kN/mm)	K_{num}/K_{num}^{S0} (-)	K_{num}/K_{exp} (-)	$P_{u,num}$ (kN)	$P_{u,num}/P_{u,num}^{S0}$ (-)	$P_{u,num}/P_{u,exp}$ (-)
S0	0.785	-	1.020	84.2	-	1.043
S1	0.857	1.091	1.071	84.9	1.008	0.952
S2	0.905	1.153	1.149	85.6	1.017	1.026
S3	0.814	1.037	1.035	84.6	1.004	0.961
S4*	0.797	1.015	0.960	97.4	1.157	0.911
S5	0.906	1.154	1.119	86.2	1.024	0.958

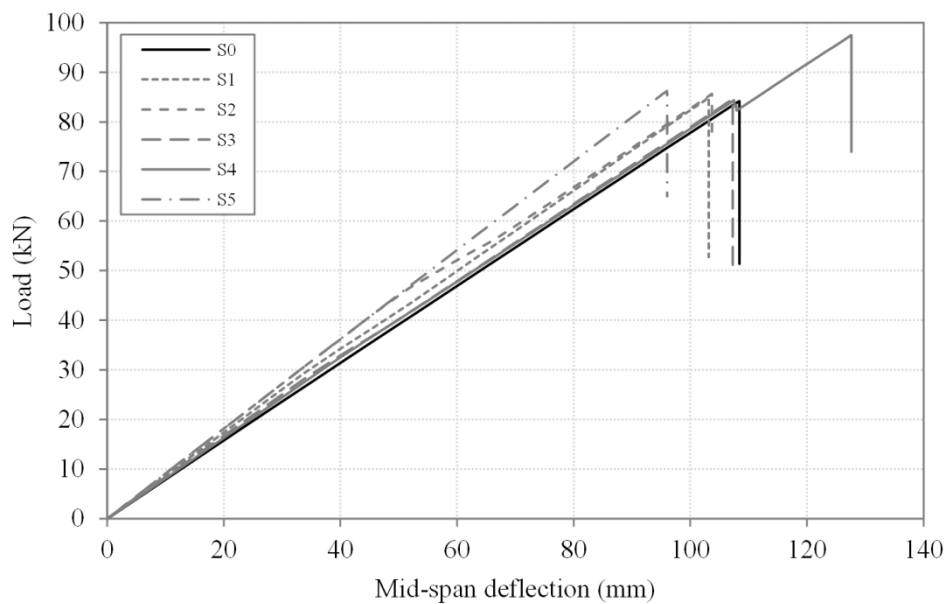


Figure 5.13: Numerical load vs. mid-span deflection curves comparison.

The load vs. deflection curves plotted in Figure 5.11 and Figure 5.12 show that the numerical models presented a slightly higher bending stiffness than that exhibited by the experimental specimens (average relative difference among all series of 7.2%). Such fact was consistent in all series except for series S4*, whose specimens presented a higher fibre volume than the remaining experimental series. That fact explains the higher bending stiffness of experimental series S4. Nonetheless, generally it is fair to claim that the numerical loading paths presented a very satisfactory agreement with the corresponding experimental curves. Moreover, the ultimate load predicted by the numerical models was very accurate, with maximum and average relative differences compared to the experimental data of only 8.9% and 4.8%, respectively.

It is worth highlighting that the CF reinforcement was only effective in terms of load carrying capacity in series S4*, providing an increase in the (numerical) ultimate load of 15.7% when compared to the

reference series. For the remaining series, the CF reinforcement provided only a residual increase of ultimate load (up to 2.4%). The fact that series S4* was the only one with CF reinforcement in the web, together with the local buckling load being considerably (and consistently) higher than the ultimate load (section 5.5.1), provides further evidence that material failure triggered the collapse mechanism of the beams, namely the exceeding of shear stresses. This assumption is supported by the upcoming analysis regarding the stress vs. strain behaviour and the failure modes (see sections 5.5.2.2 and 5.5.2.3).

Figure 5.13 provides interesting additional insights concerning the relation between the loading paths of series S1, S2 and S5. Series S5, in which the numerical results show no delamination up to failure, presents the highest bending stiffness up to failure. The curve of series S2, which presents the same amount and type of CF reinforcement, is coincident to that of series S5 up to roughly 47 kN, for which the delamination of the upper flange CF reinforcement is triggered in series S2. Then, the curve of series S2 gradually approaches the curve of series S1; this is in agreement with the fact that these profiles without the upper flange CF layers have exactly the same geometry.

5.5.2.2 Stress vs. strain curves

Figure 5.14 and Figure 5.15 present, respectively for series S0 and S3, the numerical stress vs. strain curves, with strains being computed in the very same locations where the strain gauges were installed. The experimental curves of a representative specimen of each series are also plotted in these figures.

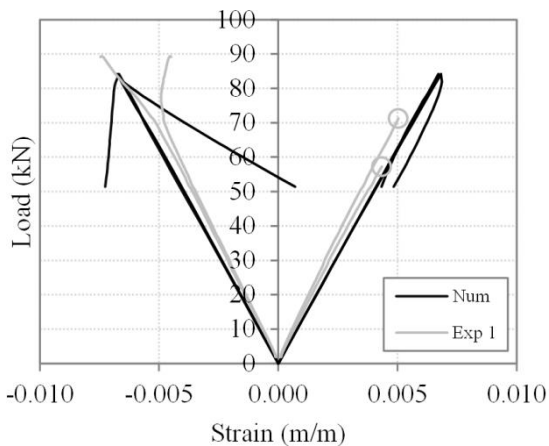


Figure 5.14: Numerical and experimental load vs. strain curves of series S0 (the circumferences (o) indicate the instant when strains stopped being measured).

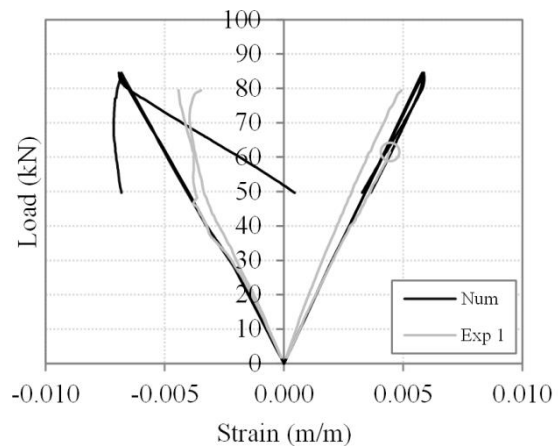


Figure 5.15: Numerical and experimental load vs. strain curves of series S3 (the circumferences (o) indicate the instant when strains stopped being measured).

In general, the numerical curves present a good agreement with the experimental ones, following roughly the same path. It can be seen that none of the numerical models simulated the strain gradient exhibited in the later stages of the experimental tests. The following two hypotheses may support such

fact: (i) despite the efforts in simulating the exact test setup, the stiffness of the lateral bracing system considered in the numerical models was probably higher than that of the experimental tests²⁶; and/or (ii) the introduction of very small eccentricities in the load applied in the tests (which were not considered in the numerical simulations) tended to magnify the strain gradient in the upper flange.

5.5.2.3 Delamination and failure modes

The failure modes exhibited in the numerical models were identical for all series, except for series S4*, which has presented a different failure mode. Failure and collapse were governed by shear stress concentrations under the loaded sections. Figure 5.16 to Figure 5.18 plot the shear stresses, the Hashin matrix compression index and the corresponding damage fields for series S0, in the brink of failure and after the collapse. In the last two figures the red colour indicates a fully damaged element, $d = 1.0$, while the blue colour indicates the undamaged areas, $d = 0.0$.

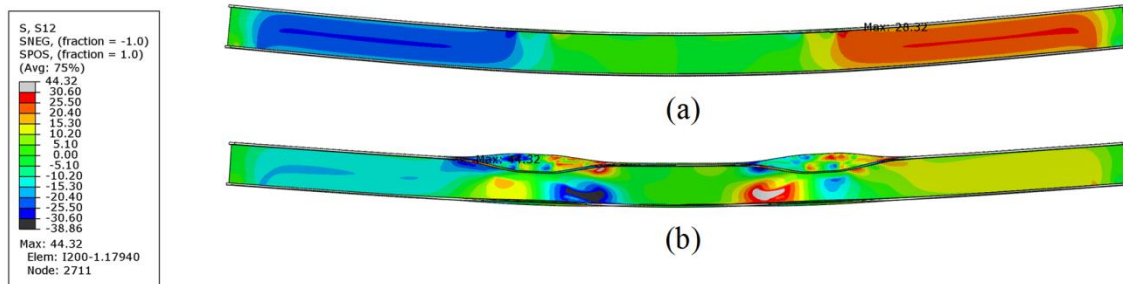


Figure 5.16: Shear stresses for series S0 (a) in the brink of failure and (b) after collapse (in MPa, according to colour scale).

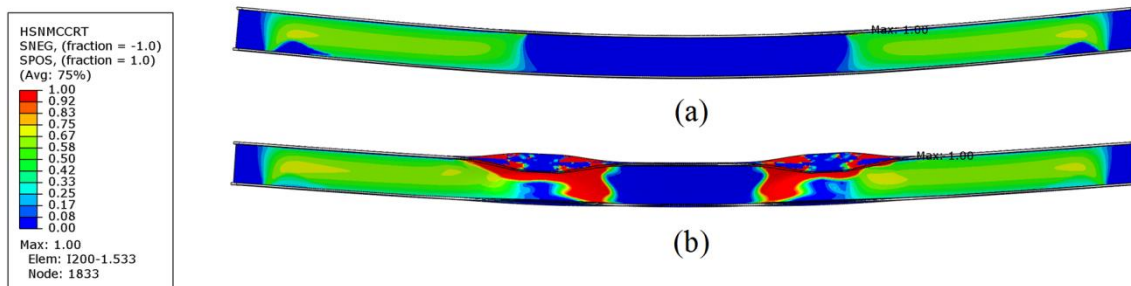


Figure 5.17: Hashin matrix compression index for series S0 (a) in the brink of failure and (b) after collapse.

²⁶ Indeed, in the numerical models, the end sections of the RHS bars were considered to be fully fixed in the steel framework, while in the experimental tests they presented finite rotation stiffness.

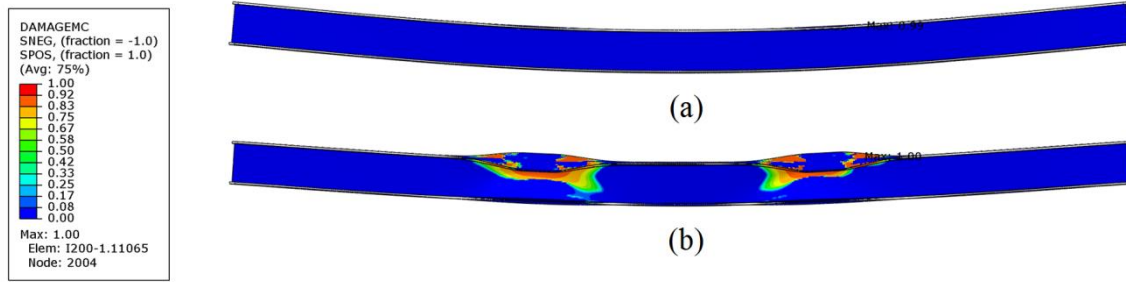


Figure 5.18: Matrix compression damage for series S0 (a) in the brink of failure and (b) after collapse.

Figure 5.16 shows that the shear stresses in the brink of failure are highly linear, with roughly constant values between the end supports and the nearest loaded section and null values in the loaded span. However, some shear stress concentrations arise under the loaded sections reaching their maximum in that particular position and prompting the failure initiation. After failure initiation, since some damaged zones under the loaded section present lower stiffness, the shear stress field becomes highly nonlinear. Some areas in the model attain higher shear stresses than the actual material shear strength. This is related to the damage regularization coefficient²⁷ and therefore the results obtained after collapse locally are not fully accurate, but rather an approximation.

Figure 5.17 illustrates the Hashin criterion index for the matrix compression mode, which takes the shear stresses into account. In the vast majority of the web area, in the brink of failure such index is somewhere between 0.50 and 0.75. However, due to the already referred shear stress concentrations under the loaded sections it reaches the maximum of 1.0 in the web-flange junction and spreads further as the collapse is triggered. When the failure index reaches 1.0 in a given finite element, the progressive damage of the material is triggered. It can be seen in Figure 5.18(b) the spread of the damaged areas corresponding to those elements in which the failure index has already achieved 1.0.

The beam from series S4* presented a slightly different failure mode. For a relatively low load level (31.2 kN \approx 0.32 P_u), fibre compressive damage was triggered on the compressed layers corresponding to the CF mats around the top web-flange junction (Figure 5.19(a)). For a load level of 48.9 kN (\approx 0.50 P_u), the CFRP layers presented damage of matrix in compression near the end supports, which correspond to the delamination of the CF mats in the transverse direction (Figure 5.19(b)). Finally, the web-flange junction failure was triggered for roughly the same load level as the remaining series (Figure 5.19(c)); however, unlike the latter, beam S4* still presented additional load carrying capacity (up to 97.4 kN) due to the presence of the CFRP layers²⁸. At this point, the web damage was triggered across its entire depth under one of the loaded sections and spread further in the direction of the nearest end support (Figure 5.19(d)).

²⁷ Note that without such viscous regularization, it would be virtually impossible to simulate the collapse mechanism due to convergence issues.

²⁸ Note that, since the Hashin failure modes are independent from each other, although the CF layers are fully damaged in the longitudinal direction, they still present stiffness in their transverse direction.

As discussed earlier, the web reinforcement with CF fibres (series S4*) was the only hybrid section which presented a significant increase in the numerical ultimate load (15.7%), compared to the reference series. However, this prediction does not cope with the experimental results (in which the increase in the ultimate load was barely residual); yet, it should be reminded that there are differences between the experimental (S4) and numerical (S4*) series.

As described in section 5.3.3, in the experiments, some of the FRP pultruded beams failed in a section located along the loaded span. This failure mode was not replicated in any of the developed numerical models, which always predicted failure localised under the loaded sections. Nonetheless, it should be highlighted that, although the Hashin-based analysis considers the material progressive damage by reducing the element stiffness, it does not allow the physical separation (crack) of the material. In the experimental tests, the dynamic effect associated to the brittle and sudden failure of the web-flange junction probably triggered the collapse of the beam. Most likely, this is a limitation of the current model which is based on implicit analysis (time-independent). In order to overcome these issues, the extended finite element method (XFEM) procedure could be used to include a physical separation (crack) of the material and explicit analysis (time-dependent) could also be used to consider the dynamic effects arising from sudden failure.

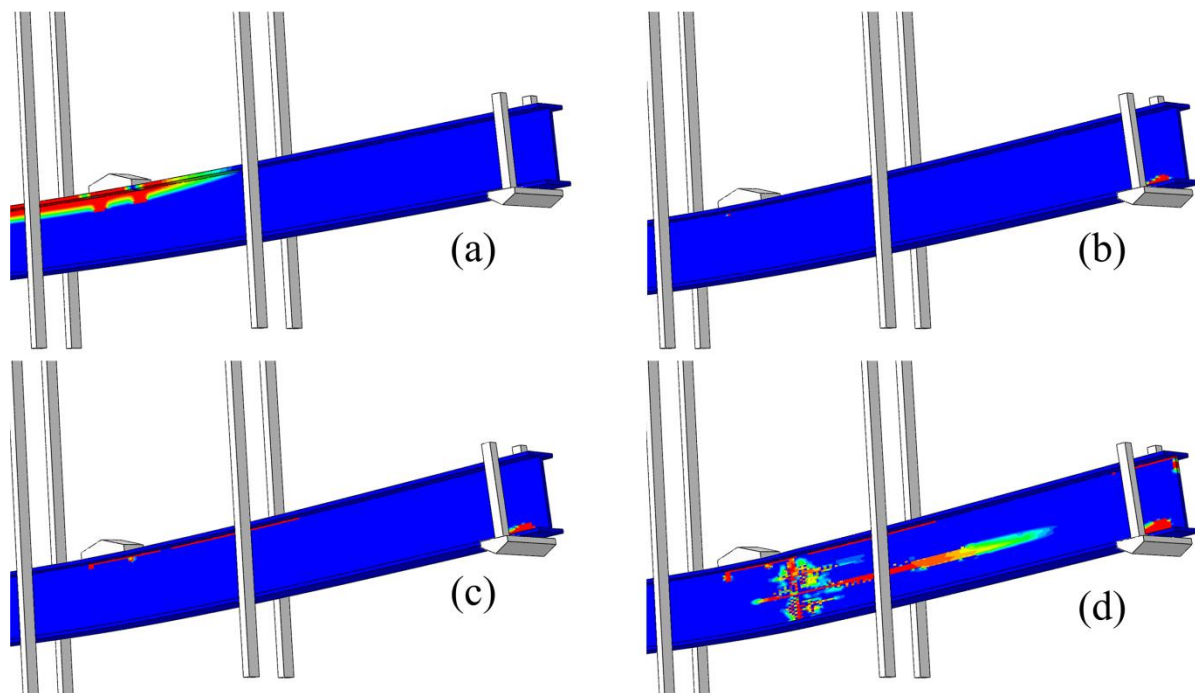


Figure 5.19: Numerical failure mode of series S4*: (a) longitudinal delamination of the CF mats ($F = 48.5$ kN); (b) transverse delamination of the CF mats ($F = 79.7$ kN); (c) web-flange junction failure at the GFRP layer ($F = 83.7$ kN); and (d) matrix compressive damage and shear envelope in the brink of failure (colour scale of the damage variable for all figures: blue – 0.0 – to red – 1.0).

5.6 ASSESSMENT OF DESIGN STANDARDS

The complex numerical modelling and simulations presented earlier are time consuming and not viable in engineering practice. Alternatively, the structural design generally resorts to analytical formulae provided in standards and guidelines. This section aims at investigating the accuracy of the main design standards and guidelines for pultruded FRP composites by comparing their predictions (ultimate loads) with the experimental and numerical data presented in the preceding sections. In this assessment, the two following documents were considered: (i) the Italian *Guide for the Design and Construction of Structures made of FRP Pultruded Elements* [12]; and (ii) the American pre-standard for *Load & Resistance Factor Design (LRFD) of Pultruded Fibre Reinforced Polymer (FRP) Structures* [11]²⁹.

Aiming at performing a sound comparison between the analytical, experimental and numerical ultimate loads, the safety factors used in both design approaches were set to 1.0. Although the numerical models have indicated that local buckling is triggered only after the collapse of the beam, the analytical predictions were computed according to the requirements of both standards concerning both buckling and material failure³⁰. The delamination of the CF mats was not considered.

The American pre-standard [11] does not consider the interaction between longitudinal and shear stresses. It basically preconizes the following set of equations,

$$M_{sd} \leq M_{Rd} \quad (57)$$

$$V_{sd} \leq V_{Rd} \quad (58)$$

in which M_{sd} and M_{Rd} are the design values of the maximum (acting) and ultimate (resisting) bending moment, respectively, and V_{sd} and V_{Rd} are the design values of the maximum and ultimate shear force, respectively. For the calculation of the design ultimate forces (M_{Rd} and the V_{Rd}), the following formulae apply,

$$M_{Rd} = \min(M_{Rd,1}, M_{Rd,2}) \quad (59)$$

$$M_{Rd,1} = \min(M_{Rd,1}^{comp}, M_{Rd,1}^{tens}) \rightarrow \begin{cases} M_{Rd,1}^{comp} = W S_{c,1} \\ M_{Rd,1}^{tens} = W S_{t,1} \end{cases} \quad (60)$$

²⁹ In terms of design philosophies, the American pre-standard is based on the Load and Resistance Factor Design (LRFD) approach, whereas the Italian guidelines follow the limit states approach, in line with the Eurocodes.

³⁰ Since the beams were laterally braced, only the local buckling critical loads were computed. No calculations addressed the lateral-torsional ultimate behaviour.

$$M_{Rd,2} = f_{cr} \frac{E_{L,f} I_f + E_{L,w} I_w}{y E_{L,f}} \quad (61)$$

$$f_{cr} = \frac{4t_f^2}{b_f^2} \left(\frac{7}{12} \sqrt{\frac{E_{L,f} E_{T,f}}{1 + 4.1\xi}} + G_{LT} \right) \quad (62)$$

$$\xi = \frac{E_{T,f} t_f^3}{b_f k_r 6}$$

$$k_r = \frac{E_{T,w} t_w^3}{6h} \left(1 - \left[\left(\frac{48t_f^2 h^2 E_{L,w}}{11.1\pi^2 t_w^2 b_f^2 E_{L,f}} \right) \left(\frac{G_{LT}}{1.25\sqrt{E_{L,w} E_{T,w}} + E_{T,w} \nu_{LT} + 2G_{LT}} \right) \right] \right) \quad (63)$$

$$V_{Rd} = A_v S_{12} \quad (64)$$

in which $M_{Rd,1}$ is the design bending moment due to material failure (superscripts *comp* and *tens* indicate failure due to exceeding compressive and tensile strengths, respectively), $M_{Rd,2}$ is the design bending moment due to local buckling of the compressed flange, I is the (web, flange) moment of inertia about the axis of bending, W is the section modulus, $S_{c,l}$ and $S_{t,l}$ are the longitudinal compressive and tensile strengths, respectively, f_{cr} is the critical stress, E is the Young's modulus, y is the distance from the neutral axis to the extreme fibre of the member, G_{LT} is the shear modulus, t is the plate thickness, b is the width, h is full height of the member (subscripts L , T , f and w indicate longitudinal, transverse, flange and web, respectively), k_r is the rotational stiffness, A_v is the shear area and S_{12} is the shear strength.

Despite using the same formulae for the definition of the design forces due to material failure, the Italian guidelines [12] preconize a slightly different approach for the determination of the critical moment due to local buckling of the compressed flange. Furthermore, they consider the interaction between bending and shear stresses. In this case, the following set of equations should be used,

$$M_{sd} \leq M_{Rd} \quad (65)$$

$$V_{sd} \leq V_{Rd} \quad (66)$$

$$\left(\frac{M_{sd}}{M_{Rd}} \right)^2 + \left(\frac{V_{sd}}{V_{Rd}} \right)^2 \leq 1 \quad (67)$$

$$M_{Rd} = \min(M_{Rd,1}, M_{Rd,2}) \quad (68)$$

$$M_{Rd,1} = \min(M_{Rd,1}^{comp}, M_{Rd,1}^{tens}) \rightarrow \begin{cases} M_{Rd,1}^{comp} = W S_{c,1} \\ M_{Rd,1}^{tens} = W S_{t,1} \end{cases} \quad (69)$$

$$M_{Rd,2} = f_{cr} W = \frac{f_{cr} I_h}{y} \quad (70)$$

$$f_{cr} = \frac{\sqrt{D_{11,f} D_{22,f}}}{t_f \left(\frac{b_f}{2}\right)^2} \left(K [15.1 \eta \sqrt{1 - \rho} + 6(1 - \rho)(1 - \eta)] + \frac{7(1 - K)}{\sqrt{1 + 4.12\zeta}} \right) \quad (71)$$

$$\zeta = \frac{D_{12,f}}{\frac{\tilde{k} b_f}{2}} \quad (72)$$

$$\tilde{k} = \frac{D_{22,w}}{b_w} \left(1 - \frac{t_f f_{cr,f}^{axial} \frac{1}{E_{L,f} t_f}}{t_f f_{cr,w}^{flex} \frac{1}{E_{L,w} t_w}} \right) \quad (73)$$

$$\rho = \frac{D_{12,f}}{2D_{66,f} + D_{12,f}} \quad (74)$$

$$\eta = \frac{1}{\sqrt{1 + (7.22 - 3.55\rho)\zeta}} \quad (75)$$

$$K = \frac{2D_{66,f} + D_{12,f}}{\sqrt{D_{11,f} D_{22,f}}} \quad (76)$$

$$V_{Rd} = A_v S_{12} \quad (77)$$

where I_h is the moment of inertia of the homogenized section about the axis of bending inertia, D is the flexural plate stiffness (subscripts $i = 1, 2, 6$ indicate the direction, f indicates flange and w indicates web) and \tilde{k} is the torsional stiffness given by the web.

Although the American pre-standard does not define the shear area, in practice this is often considered as the web area (for I- and WF-sections). Hence, the shear area was considered to be the same despite the analytical approach considered ($A_v = 2000 \text{ mm}^2$). Also one should highlight that the Italian

guidelines consider the lowest design bending moment in the interaction formula, whether it is due to material failure or buckling.

Table 5.8 presents the analytical results, namely the shear force for material failure (V_{Rd}), the bending moment for material failure (M_{RdI}), the bending moments for local buckling ($M_{Rd2,It}$ and $M_{Rd2,Am}$) and the maximum load that meets the criterion of Equation (67) ($P_{u,It}$), the minimum load that is yielded from Equations (57) and (58) ($P_{u,Am}$) and the ratios between the analytical predictions and the corresponding experimental and numerical results.

Table 5.8: Analytical predictions, experimental and numerical ultimate load results.

Series	V_{Rd} (kN) ⁽¹⁾	M_{RdI} (kNm)	Italian guidelines				American pre-standard			
			$M_{Rd2,It}$ (kNm)	$P_{u,It}$ (kN)	$P_{u,It} / P_{u,exp}$	$P_{u,It} / P_{u,num}$	$M_{Rd2,Am}$ (kNm)	$P_{u,Am}$ (kN)	$P_{u,Am} / P_{u,exp}$	$P_{u,Am} / P_{u,num}$
S0	61.2	83.7	57.8	70.8	0.807	0.841	65.4 ³¹	98.1	1.118	1.165
S1	61.2	104.1	72.2	81.1	1.004	0.955	66.3	99.4	1.230	1.171
S2	61.2	106.9	76.7	83.8	0.953	0.979	66.7	100.1	1.138	1.169
S3	61.2	96.9	68.0	78.3	0.963	0.926	65.9	98.8	1.215	1.168
S4*	61.2	93.7	65.7	76.7	0.864	0.788	65.9	98.9	1.113	1.015
S5	61.2	112.4	72.5	81.3	0.985	0.943	65.4	98.1	1.188	1.138
Average					0.929	0.905			1.167	1.138

⁽¹⁾ When considering the same shear area and the same shear modulus, the ultimate shear force is the same despite the series.

Regardless of the standard, the values of V_{Rd} and M_{RdI} for material failure are obtained from the same expressions. However, because of distinct material failure criteria, the maximum load P_m supported by the beam ($V_{Sd} = 2P_m$; $M_{Sd} = 3P_m/2$) up to material failure is different for American pre-standard and Italian guidelines. For the former, the shear force criterion (Eq. (58)) gives $P_m=122.4$ kN regardless of beam series. For the latter, the criterion of quadratic interaction between shear force and bending moment (Eq. (67)) leads to P_m values between 87.6 kN (S0) and 99.1 kN (S5). Either from American pre-standard or the Italian guidelines, it may be concluded that P_m values are always below (Italian guidelines) or close (American pre-standard) to the local buckling loads ($P_{bk,l}$) obtained numerically. This fact clearly shows that material failure occurred prior (or simultaneously) to local buckling in the experiments.

³¹ It is worth pointing out that design calculations for local buckling strength (M_{Rd2}) do not consider the mid-line dimensions of the cross-section, as it is usual in the design of thin-walled sections (e.g., cold-formed steel). For example, in case of series S0, considering h as the “mid-line width of the web” ($h=190$ mm) and not the “full height of the member” ($h=200$ mm), impacts on the calculation of f_{cr} (through k_r , I_w and y , all being cumulative. By doing this, the critical bending moment increases 11% for S0, from 65.4 kNm ($h=200$ mm) to 72.6 kNm ($h=190$ mm). This value ($M_{Rd2}=72.6$ kNm) leads to a local buckling load value ($P_{bk,l}=109$ kN) closer to the numerical one ($P_{bk,l}=119$ kN). This trend also takes place for the remaining series (S1 to S5).

If the bending moment for local buckling (M_{Rd2}) is also taken into account, the maximum bending moment (M_{Rd}) supported by the beams, as well as their ultimate loads (P_u), are always governed by local buckling regardless of the standard. The values of $M_{Rd2,It}$ and $M_{Rd2,Am}$ do not compare well with the results obtained from linear buckling numerical analyses. For instance, when referring to series S0, the local buckling load computed using the Italian guidelines and the American pre-standard is, respectively, 27.1% and 21.3% lower than that determined by the numerical eigenvalue analysis (119 kN). However, when using the American pre-standard approach and performing all calculations with respect to the plates' midline such difference is only 9.3% (see footnote #31).

Regarding the ultimate load values, the comparison between both analytical approaches shows that the P_u estimates provided by the American pre-standard were non-conservative. In fact, the average relative difference to the experimental results was +16.7% (+13.8% for the numerical estimates). In opposition, the analytical predictions computed using the Italian guidelines were conservative and slightly more accurate, with an average relative difference to experimental ultimate loads of only -7.1% (-9.5% compared to the numerical predictions).

Some issues stemming from the application of these design approaches are worth being commented. Regarding the American pre-standard, the non-conservative estimates of the ultimate load are attributed mostly to the non-consideration of the interaction between bending and shear stresses. While the use of mid-line dimensions to calculate $M_{Rd2,Am}$ would increase the accuracy of the local buckling moment estimates (compared with the numerical ones), it would also lead to even more unsafe design unless a M - V interaction criterion is used. In opposition, the current adoption of exterior (edge to edge) web dimensions leads to less unsafe predictions when using simple (separate V and M) criteria. On the other hand, the Italian guidelines considers the interaction between the shear force and the bending moment³² and proved to be slightly conservative. Two separate approaches should be considered when addressing (i) the local buckling phenomenon and (ii) the material failure due to exceeding stresses. The differences between both design approaches are still one of the major issues that should be solved in order to have more consensual design codes.

5.7 CONCLUDING REMARKS

This chapter presented an experimental, numerical and analytical study about the structural behaviour of hybrid FRP pultruded beams with different types and architectures of CF mats reinforcing GFRP I-section profiles. The following main conclusions may be drawn:

³² Even though ultimate shear force V_{Rd} and critical buckling moment M_{Rd2} are not related to the same phenomenon: the former associated to material failure while the latter to elastic buckling.

1. All hybrid series tested presented higher bending stiffness than the reference all-GFRP profile, therefore confirming the effectiveness of hybridization in improving the serviceability performance of pultruded beams.
2. The CF reinforcement was not able to increase the overall load carrying capacity of the FRP beams; despite the slight strength increase obtained in series S2 and S4, series S1, S3 (both with bidirectional CF mats in the upper flange) and S5 presented a worse performance than the reference series.
3. A single failure mode was observed in the tests, comprising the rupture of the web-top flange junction, under one of the loaded sections, or in a section of the loaded span.
4. The numerical models, which accurately reproduced the linear behaviour of the different beams, indicated that failure is governed by exceeding the in-plane shear strength and thus the CF reinforcement is ineffective in terms of ultimate behaviour.
5. The Hashin progressive failure analysis implemented in ABAQUS proved to be a very useful and accurate tool for the modelling of the delamination and progressive collapse of hybrid FRP pultruded flexural members.
6. Both American pre-standard and Italian guidelines were not accurate in estimating the failure load of the tested hybrid beams, providing non-conservative and slightly over-conservative predictions, respectively. Indeed, the American pre-standard does not consider the interaction between axial and shear stresses while the Italian guidelines (nonetheless slightly more accurate) include the local buckling moment into the (material failure) stress interaction equation.

CHAPTER 6

PROGRESSIVE FAILURE OF THE WEB-CRIPPLING PHENOMENON

6.1 PRELIMINARY CONSIDERATIONS

The low content of fibres in the direction transverse to the pultrusion axis leads to low stiffness and strength of the section walls in such direction and, therefore, turns FRP pultruded profiles prone to web crippling (either buckling, crushing, or both) when they are subjected to transverse concentrated loads. This phenomenon, nearly understood in case of steel structures, remains not well documented in case of GFRP structures. The information available in the literature and the design rules in existing standards are still very scarce [11,92,93]. Thus, it is necessary to adequately study the response of GFRP pultruded profiles subjected to such type of loading. In case of steel structures, there are four main web crippling loading configurations used to assess this phenomenon (see Figure 6.1):

- EOF (End One Flange) – the web fails in the end section of the beam due to the load application in one flange of that end section.
- IOF (Internal One Flange) – the web fails in an internal section of the beam due to the load application in one flange of that internal section.
- ETF (End Two Flange) – the web fails in the end section of the beam due to the load application in the two flanges of that end section.
- ITF (Internal Two Flange) – the web fails in an internal section of the beam due to the load application in the two flanges of that internal section.

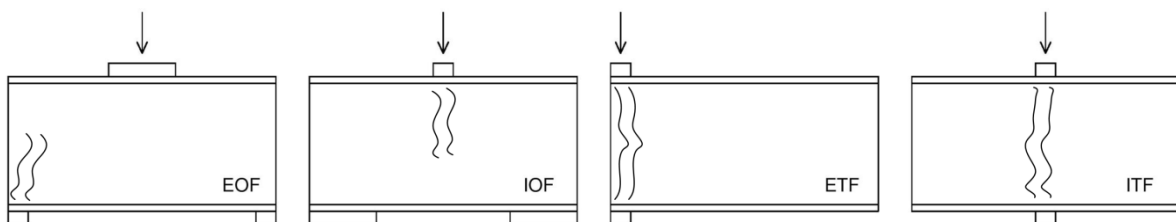


Figure 6.1: EOF, IOF, ETF and ITF load configurations for the study of the web-crippling phenomenon [14].

Borowicz and Bank [27,28] studied the web crippling phenomenon of I-section and wide-flange GFRP profiles under IOF loading. The obtained results indicated that such GFRP beams fail for shear loads ranging from 20% to 46% of the reported in-plane shear strength. The addition of bearing plates (with length ranging from 48.3 to 152.4 mm and thickness of 12.7 to 25.4 mm) to the loaded section increased the load capacity of the GFRP beams ranging from 35% to 83%, depending on the plate's length and thickness [27]. They further investigated the effect, on web-crippling strength [28], of adding several types of GFRP stiffeners to the profiles. All the reinforcement solutions were effective, but the reinforcement of the upper web-flange junction not only presented the highest increase in terms of ultimate load (of 59%) but also avoided the failure mode of the control beam – the development of a shear wedge failure under the loaded section – forcing failure to occur in the bottom web-flange junction near the end supports.

Wu and Bai [29] reported a study on the web-crippling behaviour of GFRP square hollow section pultruded profiles subjected to ETF and ITF load conditions, and also to “end bearing load” and “interior bearing load” (profiles continuously supported on solid ground). The initial failure of the tested specimens was triggered at the web-flange junction and was followed by web failure modes, due to shearing, buckling or crushing, depending on the web slenderness. As expected, specimens under ITF loading presented higher strength than those under ETF loading.

In addition to these studies, there are few available design codes and guidelines for FRP pultruded structures, namely the EuroComp design code [10] and the Italian guidelines [12]. However, none of these documents presents design formulae specifically addressing the web-crippling phenomenon. The recent ASCE Pre-Standard [11] includes design formulae for predicting the web-crippling strength, which are based on the research of Borowicz and Bank [27] and were only calibrated for IOF and EOF configurations.

More recently, Fernandes *et al.* [14,15] performed extensive experimental, numerical and analytical studies regarding the structural response of different GFRP I-section profiles under ETF and ITF loading (described in detail in the next section). The authors tested several specimens and developed geometrically nonlinear numerical models to predict the initial failure load of GFRP I-section profiles using the Tsai-Hill index. They found that the initial failure load predictions given from Tsai-Hill-based analyses were far too conservative when compared to the ultimate loads obtained in experimental tests. It was concluded that in order to obtain more accurate ultimate load estimates, a new failure criterion should be sought for web crippling analysis, which must include progressive damage of the composite material.

As already mentioned in Chapter 4 and Chapter 5 the most recent versions of ABAQUS [72] include a progressive damage analysis specifically developed for fibre reinforced composites, which combines

the Hashin damage initiation criteria [77,78] with a damage evolution model proposed by Camanho and Dávila [79]. Nonetheless, there is still a lack of information available for the practice-oriented engineer to implement such damage analyses. Most likely, the spread use of the Hashin-based progressive damage analysis has been hindered by the large amount of material data required for input. Despite this fact, some numerical investigations have been carried out [30,31]. The interested reader should refer to section 4.1 for more information on this subject.

The objectives of this chapter are two-fold: (i) to apply the Hashin progressive damage analysis to the study of web crippling phenomenon of GFRP pultruded profiles, and (ii) to obtain more reliable ultimate load estimates, using the experimental data given by Fernandes *et al.* [14,15].

In the next section, previous experiments carried out by Fernandes *et al.* [14,15] are summarised. The FE numerical model is presented afterwards, including the element types, failure criteria and damage model. Subsequently, the results of preliminary analyses (mesh size and viscous regularization) are shown and discussed. Then the model assessment is presented through the study of different loading configurations (ETF, ITF) and distinct bearing lengths and their impact on load *vs.* displacement curves, damage zones and failure modes. Finally, the model sensitivity to different parameters is analysed and the main conclusions drawn are listed.

6.2 SUMMARY OF PREVIOUS EXPERIMENTS

The results of previous experiments and numerical analyses carried out by Fernandes *et al.* [14,15] on web crippling of GFRP pultruded profiles are summarised herein. A total of four different cross-sections (I100, I120, I200 and I400) were studied for two loading configurations (ETF and ITF) and three different bearing lengths (15, 50 and 100 mm). The specimens' length was twice their web height. Three specimens per series were tested (cross-section, bearing length and load configuration). Loads were applied monotonically up to failure by means of an *Instron* universal testing machine under controlled displacement at a constant rate. In case of I400 cross-section, only one bearing length was tested (100 mm). The interested reader should refer to Fernandes *et al.* [14] for more detailed information on the test setup and instrumentation.

The numerical models proposed by Fernandes *et al.* [15] were developed within the framework of commercial software ABAQUS [72]. Shell elements with reduced integration (*S4R*) were used to simulate the GFRP profiles, while the bearing plates were modelled using continuum solid elements with reduced integration (*C3D8R*). The interface between the bearing plates and the I-sections was modelled using a surface-to-surface interaction with given normal and tangential behaviours. Geometrically nonlinear behaviour was assumed, while linear elastic material behaviour was adopted. The Tsai-Hill criterion was used to identify the initial failure loads, but no material damage model was

adopted. More details on the description of the numerical models can be found by Fernandes *et al.* [15].

Figure 6.2 (ETF) and Figure 6.3 (ITF) display the load vs. displacement curves obtained from experimental tests and numerical analyses of a representative specimen of each series – (a) I100, (b) I120, (c) I200 and (d) I400. In these figures, the circumferences (○) marked across the numerical curves correspond to the initial failure load, *i.e.* the load for which the Tsai-Hill index reaches $I_{F,TH} = 1.0$.

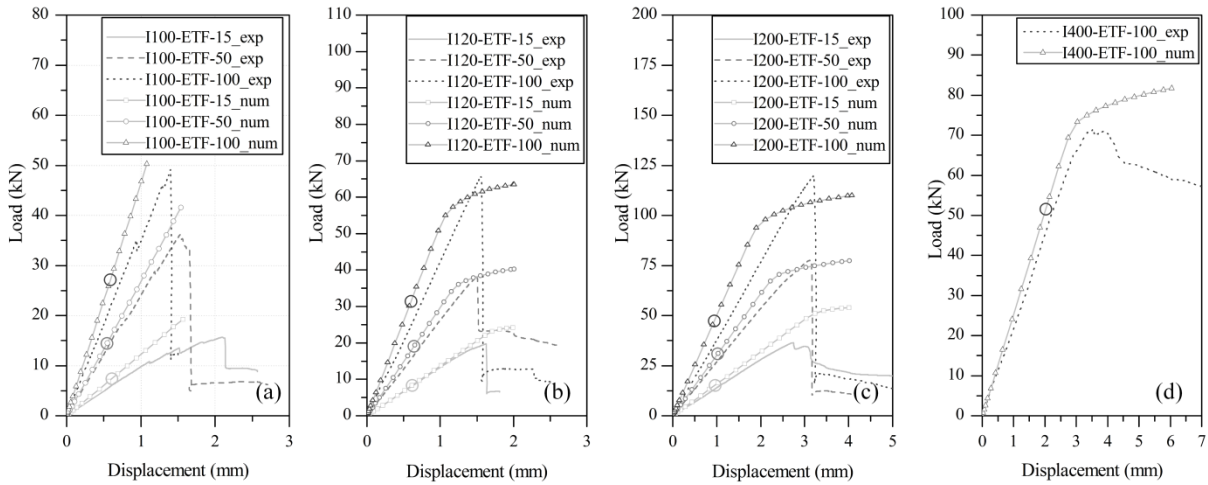


Figure 6.2: Experimental (E) and numerical (N) load-displacement curves for GFRP pultruded sections under ETF loading: (a) I100, (b) I120, (c) I200 and (d) I400 [15].

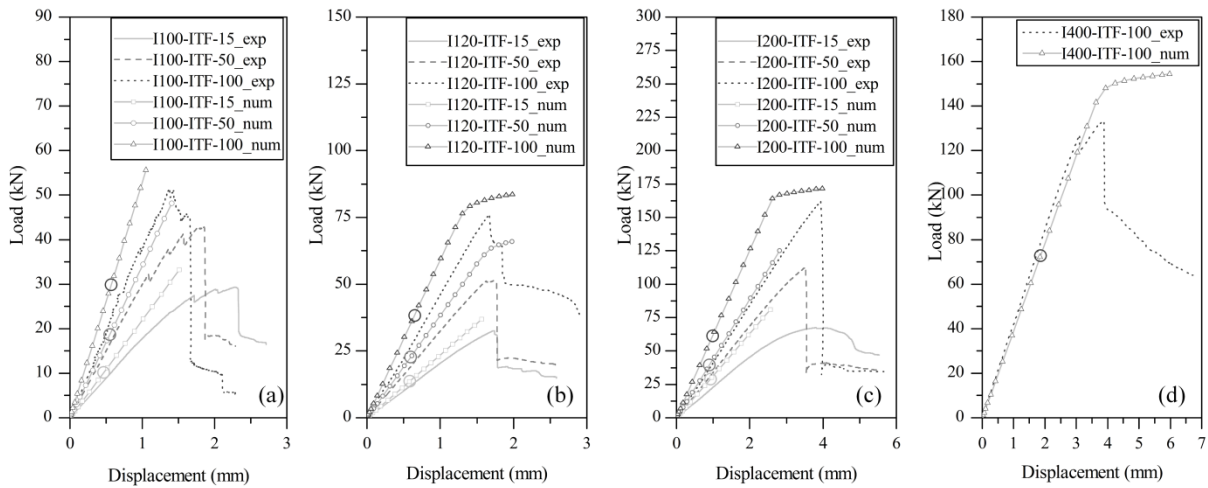


Figure 6.3: Experimental (E) and numerical (N) load-displacement curves for GFRP pultruded sections under ITF loading: (a) I100, (b) I120, (c) I200 and (d) I400 [15].

As it can be seen in these figures, the numerical estimates of the ultimate load (first failure load) using the Tsai-Hill criterion are too conservative when compared to the experimental loads. This is because

the stress state in GFRP profiles is highly concentrated in zones close to the applied loads and the failure of these very limited zones does not necessarily mean the collapse of the profile. In fact, the profiles possess structural redundancy and capacity to redistribute these localized stresses by spreading them to other neighbour (stiffer) zones, thus being able to support loads much higher than those of initial failure.

6.3 FINITE ELEMENT MODEL

In order to capture the stress redistribution capacity mentioned before and to assess the damage evolution of GFRP material in pultruded profiles under concentrated loads, let us perform a numerical study based on Hashin progressive damage model, instead of the Tsai-Hill criterion used by Fernandes *et al.* [14,15]. Because the aim of this chapter is to study the impact of several parameters on the numerical results and validate them through the comparison with experimental data, the scope of the analyses was limited to the I200 cross-section. Such profile consists of a narrow flange I-section, manufactured by *ALTO Perfis*, with the dimensions of $200 \times 100 \times 10$ mm (web height \times flange width \times plate thickness). The web-flange junctions and the flanges' edges are round and present radius of 10 and 2.0 mm, respectively.

The numerical approach based on continuum shell elements proposed in Chapter 4 and Chapter 5 respectively for hybrid columns and beams under concentric compression and beams under four-point bending, was adopted here because of its proven accuracy. In the following paragraphs, general aspects of the developed numerical models are described, namely the type of elements, material properties, applied loading, boundary conditions and surface interactions, the adopted failure initiation criterion and the damage evolution model.

As already mentioned the numerical models presented in this chapter were developed to resemble the experimental tests performed by Fernandes *et al.* [14]. Two different parts were modelled: (i) the I200 profile and (ii) the bearing plates. The pultruded section ($200 \times 100 \times 10$ mm – web height \times flange width \times plate thickness) with a length equal to twice the web height (400 mm) was meshed using continuum shell FEs with reduced integration (SC8R in ABAQUS FE library). Contrary to conventional shell FEs (such as S4, S4R or S8), in which the thickness is a section property, the thickness of continuum shell FEs is defined by the distance between nodes in the direction orthogonal to the element mid-plane. The adopted mechanical properties were those reported by Fernandes *et al.* [14] and are presented in Table 6.1.

Table 6.1: Elastic and strength properties adopted in the numerical models.

Plate	E_1 (GPa)	E_2 (GPa)	G_{12} (GPa)	G_{23} (GPa)	ν	$S_{1,t}$ (MPa)	$S_{1,c}$ (MPa)	$S_{2,t}$ (MPa)	$S_{2,c}$ (MPa)	S_{12} (MPa)	S_{23} (MPa)
Web	33.0	7.70	3.70	1.60	0.266	385	464	106	106	27.5	27.5
Flange	35.9	5.90	3.70	1.60	0.266	414	389	70.4	70.4	27.5	27.5

The bearing plates were modelled using eight-node continuum solid elements with reduced integration (C3D8R). They were considered as an isotropic material and were assigned to steel elastic properties ($E = 210$ GPa and $\nu = 0.3$). The bottom plate's displacements were restricted in all directions and the upper plate ones were set free only in the vertical direction (direction along the web height). The load was applied to the upper bearing plate by means of an imposed displacement in the vertical direction. The interface between both materials was simulated using a surface-to-surface contact interaction, with hard normal behaviour and a tangential friction coefficient of 0.4. Figure 6.4 depicts a representative example of the geometry and FE mesh of the developed numerical models (ITF_50).

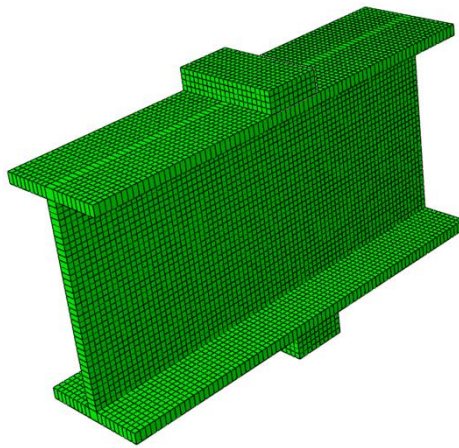


Figure 6.4: Whole meshed model.

The Hashin damage initiation criterion and the ABAQUS built-in damage evolution model were adopted for this study. Detailed information regarding each of these matters can be found in sections 4.4.2 and 4.4.3. The fracture energies adopted for each failure mode were the same as in the studies performed for columns and beams for the GFRP material and are presented in Table 6.2.

Table 6.2: Adopted values for fracture energies.

G_{ft} (N/mm)	G_{fc} (N/mm)	G_{mt} (N/mm)	G_{mc} (N/mm)
2.38	5.28	0.424	0.948

6.4 PRELIMINARY ANALYSES AND REFERENCE MODEL

In this section, preliminary calibrations of the numerical model are performed in order to select an adequate element size (mesh convergence analysis) and an acceptable viscous regularization coefficient (softening stage of the loading path).

The first step of this numerical study was the definition of the best FE mesh, *i.e.* the reference mesh. In order to evaluate the mesh accuracy, several linear buckling analyses with different element sizes were performed. The criterion for evaluating the mesh convergence was set as the percentage difference between the critical buckling load of the member with a given FE mesh and that of a more refined FE mesh. The stopping criterion for that ratio was considered to be 1.0%. A total of 4 meshes ($n=1, \dots, 4$) with different element sizes were analysed for models with both ETF and ITF configurations and displaying intermediate plate length (50 mm). Table 6.3 indicates the buckling loads obtained for each mesh ($P_{bk,n}$) and also the buckling load ratio between consecutive meshes ($P_{bk,n}/P_{bk,n-1}$).

Table 6.3: FE mesh convergence analysis.

Mesh	Element size (mm)	ETF		ITF	
		$P_{bk,n}$ (kN)	$P_{bk,n}/P_{bk,n-1}$	$P_{bk,n}$ (kN)	$P_{bk,n}/P_{bk,n-1}$
$n=1$	15.0	87.3	-	177.0	-
$n=2$	10.0	82.4	0.944	170.5	0.963
$n=3$	5.0	80.2	0.973	164.0	0.962
$n=4$	2.5	79.3	0.990	162.6	0.991

At a first glance, the insufficient number of finite elements to approximate to the member deformed shape could be the reason behind the difficulties in reaching numerical convergence. However, other two factors may contribute to this problem: (i) the highly nonlinear stress fields, and/or (ii) the use of reduced integration (mandatory when using continuum shell elements). The results obtained in the convergence analysis indicated that the element size of 5.0 mm is the optimal one for the accurate determination of the critical buckling load for both ETF and ITF configurations. Therefore, this mesh was adopted as reference for the forthcoming analyses.

Because numerical (convergence) difficulties arise in solving the system of nonlinear equations with softening included, the use of the damage stabilization option is recommended in ABAQUS User Manual [72]. It also vaguely states that, in order not to compromise the numerical results of the softening stage, a viscous regularization coefficient (η) should be used and its value should be small as possible (so that $t/\eta \rightarrow \infty$, in which t represents time).

Aiming at defining an adequate viscous regularization coefficient, several numerical analyses using three different meshes were performed: (i) reference mesh ($n = 3$); (ii) mesh F – with a fine

discretization ($n = 4$); and (iii) mesh C – with a coarse discretization ($n = 2$). If the ABAQUS damage stabilization option (*i.e.* considering that $\eta = 0$) is not used, the solution does not converge after the damage initiation has been reached. Thus, in these analyses several viscous regularization coefficients were tested, ranging from 1×10^{-7} to 1×10^{-3} , and the load-displacement curves obtained are presented in Figure 6.5. In these curves, the load (vertical axis) and the displacement (horizontal axis) correspond to the reaction force and the imposed displacement in the top bearing plate in the direction of the web height, respectively. Being very time consuming, these calibration models were only developed for the ETF configuration with an intermediate bearing plate length (50 mm).

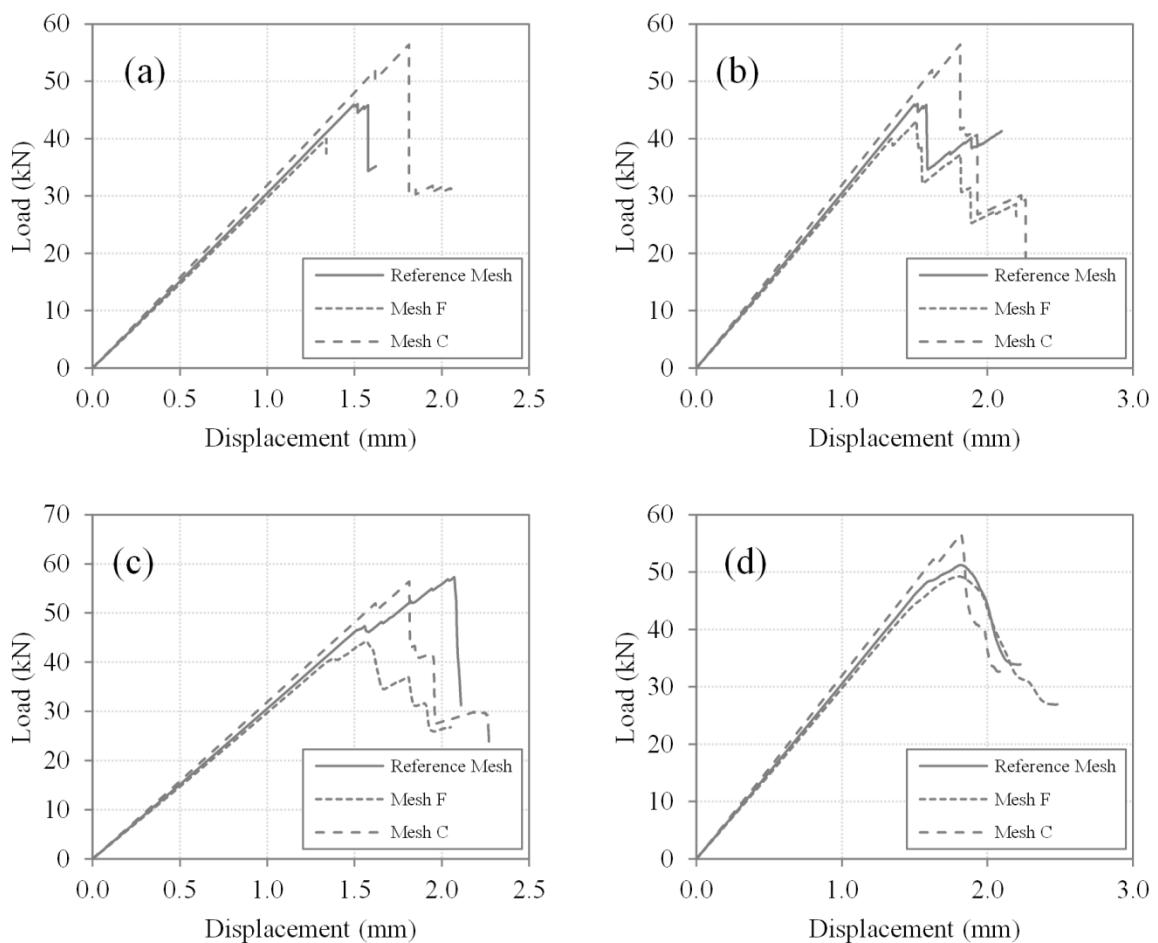


Figure 6.5: Load vs. displacement curves of the three tested meshes with different viscous regularization coefficients: (a) $\eta = 1 \times 10^{-7}$, (b) $\eta = 1 \times 10^{-5}$, (c) $\eta = 1 \times 10^{-4}$ and (d) $\eta = 1 \times 10^{-3}$.

The results presented in Figure 6.5 indicate that:

- Using the smallest viscous regularization coefficient ($\eta = 1 \times 10^{-7}$, Figure 6.5(a)), there is a strong mesh dependency, not in terms of the softening stage itself (which is roughly vertical for the three tested meshes), but rather in terms of ultimate load. The ultimate load obtained

for the reference mesh was 46.0 kN, while the results for meshes F and C were 13.2% lower and 22.5% higher, respectively.

- Regarding the largest coefficient tested ($\eta = 1 \times 10^{-3}$, Figure 6.5(d)), it is clear that the softening stage was clearly affected (showing a gradual load decrease) despite the lower differences in terms of ultimate loads; the reference mesh reached 51.2 kN, while the differences to the finer and larger meshes were respectively -3.8% and +10.5%.
- None of the remaining tested values of η can be assumed to be either correct or incorrect; both provide reasonable results, either approximating the response of the reference mesh to that of mesh F (Figure 6.5 (b)) or to that of mesh C (Figure 6.5(c)).

The authors have then decided to comply with the recommendations provided in the ABAQUS User Manual in using the minimum possible value and considered $\eta = 1 \times 10^{-5}$ in the analyses performed afterwards. Such value was also used by Coelho *et al.* [30] and in the numerical simulations presented in Chapter 4 and Chapter 5, all having obtained a good agreement between numerical and experimental results.

6.5 MODEL ASSESSMENT

After the performance of preliminary analyses and definition of the reference model (best mesh and viscous regularization coefficient), the model was then verified for the case of I200 pultruded profile in the ETF and ITF load configurations using a bearing plate of 15, 50 and 100 mm (six models). Figure 6.6 and Figure 6.7 plot the load vs. displacement curves obtained for configurations ETF and ITF, respectively.

The ultimate loads obtained from the progressive failure analyses ($P_{u,Hashin}$) are presented in Table 6.4 alongside the experimental results obtained by Fernandes *et al.* [14] ($P_{u,Exp}$) and the corresponding numerical results using the Tsai-Hill index as the initial failure criterion [15] ($P_{IF,TH}$). In this table, the numerical-to-experimental ultimate load ratios $P_{IF,TH}/P_{u,Exp}$ and $P_{u,Hashin}/P_{u,Exp}$ are also presented.

As expected, a higher bearing length leads to a higher loading stiffness and ultimate load. The latter is increased roughly 3.0 and 2.3 times for the ETF and ITF load configurations, respectively, when the bearing length is increased from 15 mm to 100 mm. On the other hand, the displacement at failure is approximately the same, despite the load configuration and bearing length (in average 1.59 mm and with a coefficient of variation of only 6.8%). Such fact indicates that the displacement (or transverse strain) under the applied load might provide a reliable monitoring criterion, which is roughly independent of the load configuration and bearing length. These results comply with the experimental data obtained by Fernandes *et al.* [14] (see Figure 6.2 and Figure 6.3) in which, at least for sections I120 and I200, the displacement at failure is about the same.

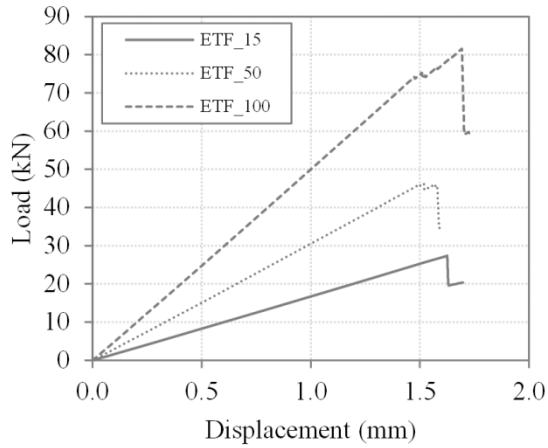


Figure 6.6: Load vs. displacement curves for the ETF configuration.

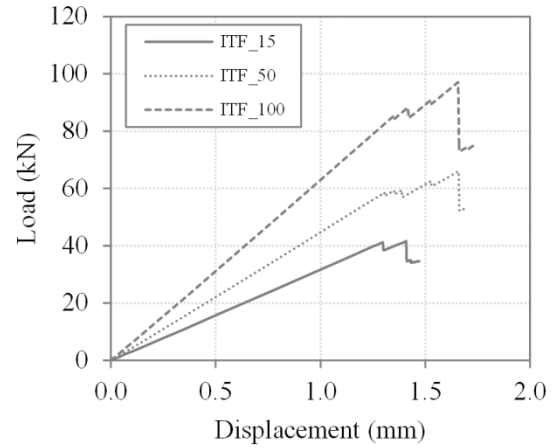


Figure 6.7: Load vs. displacement curves for the ITF configuration.

Table 6.4: Comparison between numerical and experimental [14,15] ultimate loads.

Conf.	L (mm)	$P_{IF,TH}$ (kN)	$P_{u,Hashin}$ (kN)	$P_{u,Exp}$ (kN)	$P_{IF,TH}/P_{u,Exp}$	$P_{u,Hashin}/P_{u,Exp}$
ETF	15	15.2	27.4	37.2	0.409	0.737
	50	30.9	46.1	78.2	0.395	0.590
	100	47.3	81.5	115.3	0.410	0.707
ITF	15	29.0	41.6	67.8	0.428	0.614
	50	39.4	65.9	109.1	0.361	0.604
	100	61.4	97.0	161.3	0.381	0.601

The linear elastic behaviour up to failure and the sudden drop in the load carrying capacity observed in the experimental campaign were accurately simulated using the ABAQUS built-in Hashin-based damage analysis.

In fact, the ultimate loads obtained using a Hashin-based progressive damage analysis were significantly higher than the initial failure loads predicted by the Tsai-Hill index without the consideration of stiffness degradation (+43.4% to +80.3%, depending on the bearing length and the load configuration). Despite this achievement, the ultimate loads predicted by the Hashin damage analysis were still very conservative when compared to the experimental results (26.3% to 41.0% lower).

In order to better understand the roots of damage in web crippling analysis, the patterns of transverse compressive stresses and shear stresses are presented next and discussed. The damaged zones of the governing Hashin failure criterion (matrix compression and shear) are also shown herein. Figure 6.8 to Figure 6.10 present, for the six tested models, the transverse compressive stress field, the shear stress field and the damaged areas at the onset of failure. In these figures the colour scales are: (i) in the compressive and shear stress fields, blue corresponds to $\sigma_{2,c} = 0$ MPa, while red corresponds to the

material's strengths (106 and 27.5 MPa, respectively); and (ii) in the matrix compression damage fields, blue corresponds to an undamaged element ($d_m = 0.0$), while red represents a fully damaged element ($d_m = 1.0$).

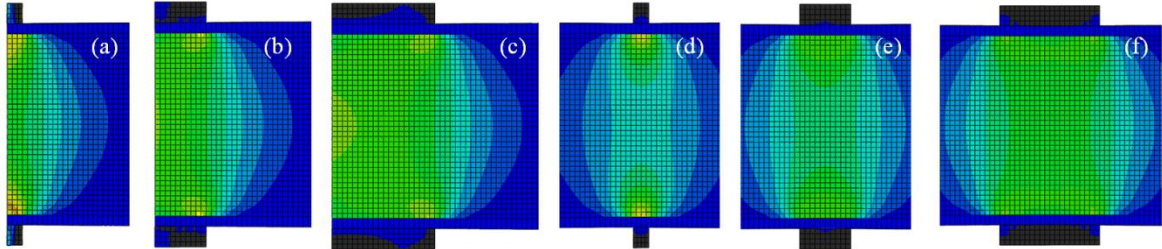


Figure 6.8: Transverse compressive stress fields at the onset of failure: (a) ETF_15, (b) ETF_50, (c) ETF_100, (d) ITF_15, (e) ITF_50 and (f) ITF_100.

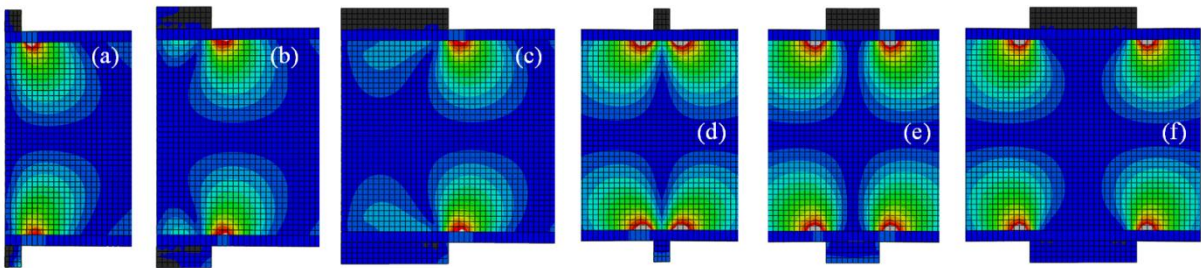


Figure 6.9: Shear stress fields at the onset of failure: (a) ETF_15, (b) ETF_50, (c) ETF_100, (d) ITF_15, (e) ITF_50 and (f) ITF_100.

As shown herein, the shear strength governs failure initiation regardless of the load configuration and bearing length. In fact, at the onset of failure, the transverse compressive stress is somewhere between 61 and 82 MPa (58% to 77% of the material strength). On the other hand, the shear stress reaches the corresponding strength in all models. Some of them even present an area in which the shear stress is slightly higher than the corresponding material strength (which is due to the viscous regularization of the material). Damaged areas are concentrated in certain finite elements of the web-flange junction close to the edges of the bearing plate.

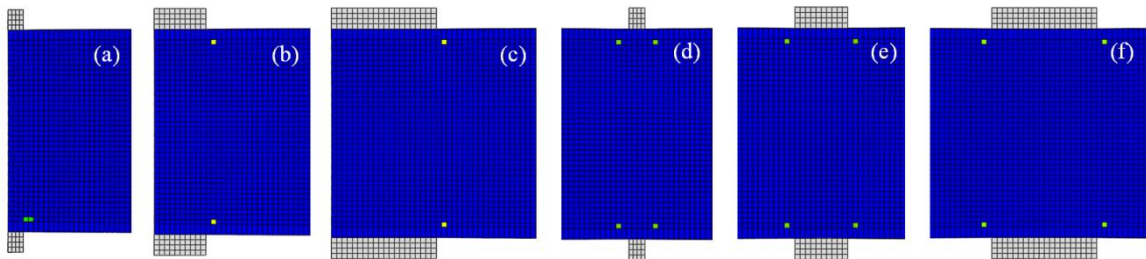


Figure 6.10: Matrix compression damaged areas at the onset of failure: (a) ETF_15, (b) ETF_50, (c) ETF_100, (d) ITF_15, (e) ITF_50 and (f) ITF_100.

Independently of the load configuration and bearing length, the global responses in terms of stress fields and damaged zones are roughly similar. Hence, only the results obtained for ITF_100 load configuration are presented next. Figure 6.11 and Figure 6.12 show the transverse compressive stress field, shear stress field, and matrix compression damage field respectively in (i) the brink of collapse and (ii) after collapsing.

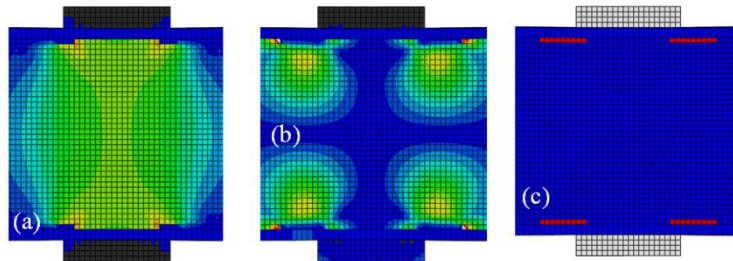


Figure 6.11: ITF_100 profile on the brink of collapsing: (a) compressive stress, (b) shear stress and (c) matrix compression damaged areas.

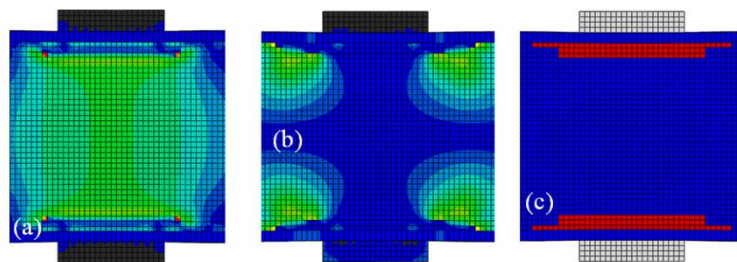


Figure 6.12: ITF_100 profile on the after collapsing: (a) compressive stress, (b) shear stress and (c) matrix compression damaged areas.

As failure progresses, the damaged areas spread further in the web-flange junction and the maximum shear and transverse compressive stresses shift in the direction of the midline. Damaged elements lose their stiffness and thus present roughly null stress states. ETF configuration allows for lower stress redistribution as the ratio between the initial failure load and the ultimate load is 1.00, 0.994 and 0.908 for bearing lengths of 15, 50 and 100 mm, respectively. For the same bearing lengths, the ITF results show slightly higher stress redistribution, as the same ratio assumes the values of 0.983, 0.888 and 0.878. As expected, longer bearing lengths allow for higher stress redistribution (up to a maximum of 12.2% in the ITF_100 load configuration).

When the load reaches its peak, the damaged areas are concentrated in a single layer of finite elements of each web-flange junction, near the edges of the loading plate (see Figure 6.11(c)). Beyond the ultimate load (collapse), the damaged areas spread further affecting several (two to four) layers of finite elements (*i.e.*, 10 to 20 mm) under the whole length of the plate (see Figure 6.12(c)). The progressive damage analyses (using Hashin-based criterion) allow the identification of the effective

stress fields and damaged zones, being much more comprehensive than purely elastic analyses that only identify zones in which the strength is overcome (using Tsai-Hill index).

6.6 MODEL SENSITIVITY

Previously, it was shown that the ultimate loads obtained using the Hashin damage analysis were significantly improved, in comparison with their Tsai-Hill failure counterparts. However, the results obtained for the I200 profile were still very conservative when comparing to the experimental ultimate loads (-41.0% to -39.6%). Thus, there is the need to study the influence of the different parameters on the ultimate loads and the way they affect the beam failure. Among several parameters, those more influential are: (i) the transverse compressive strength – $S_{2,c}$, (ii) the in-plane shear strength – S_{12} , (iii) the matrix compressive fracture energy – G_{mc} , and (iv) the modelling of web-flange rounded corner.

While the former two parameters were determined using standard experimental methods [14], the fracture energies were computed using non-standardized test methods and assumptions that may lack full reliability (*cf.* section 4.4). Therefore, the variation of strength parameters ($S_{2,c}$ and S_{12}) was bounded between -20% and +20% of their reference values, while the variation of fracture energy (G_{mc}), being limited to a minimum value³³ (which is -27% of the reference G_{mc}), was varied to a maximum of 50 times its reference value. These parametric studies were performed in two models (ETF and ITF) considering an intermediate bearing length (50 mm).

6.6.1 Strength parameters: transverse compression and in-plane shear

In order to achieve the aforementioned goal and to simplify the presentation of results, the ratio between the considered (varied) strength S and the reference (actual) strength S_r is denoted by parameter $a_S = S/S_r$ ($S_{2,cr} = 106$ MPa and $S_{12r} = 27.5$ MPa). To achieve the -20% and +20% strength variation, for both transverse compression and in-plane shear, the following values were considered: $a_S = 0.8, 0.9, 1.0, 1.1, 1.2$. Figure 6.13 to Figure 6.16 plot, for each strength parameter variation ($S_{2,c}$ or S_{12}) and load configuration (ITF or ETF), (i) the load vs. displacement curves (Figure 6.13(a) to Figure 6.16(a)) and (ii) their influence on the Hashin initial failure and ultimate loads (respectively $P_{IF,H}$ and P_u in Figure 6.13(b) to Figure 6.16(b)).

³³ Since ABAQUS computes the fracture energy as the area under the whole stress vs. strain curve, the minimum value of the G_{mc} was calculated, considering a vertical softening stage, as the area of the triangle in which the base is the strain at failure ($\varepsilon = S_{2,c}/E_2$) and the height is the transverse compressive strength $G_{mc,min} = (S_{2,c})^2/2E_2 = 0.730$ N/mm.

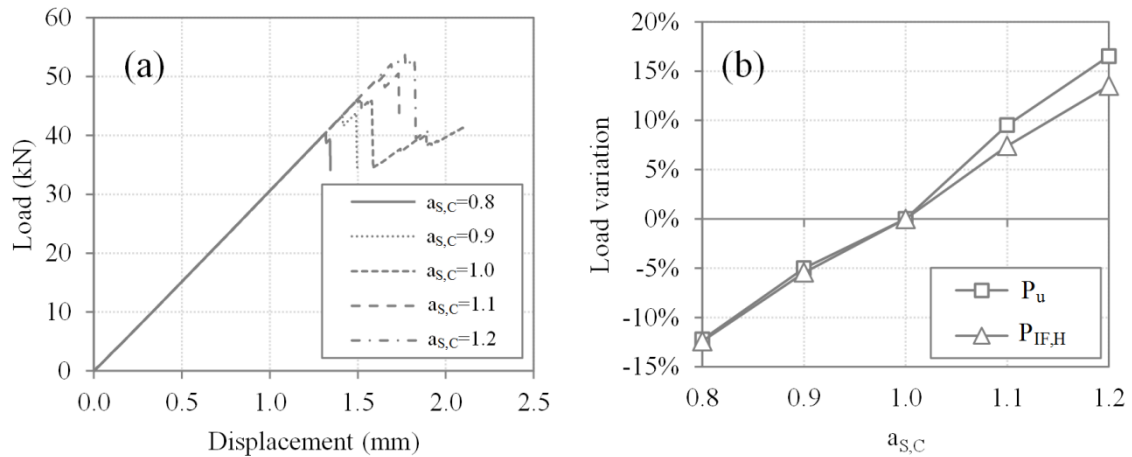


Figure 6.13: Influence of the variation of $S_{2,c}$ for series ETF_50: (a) load vs. displacement curves, and (b) initial failure load and ultimate load variation.

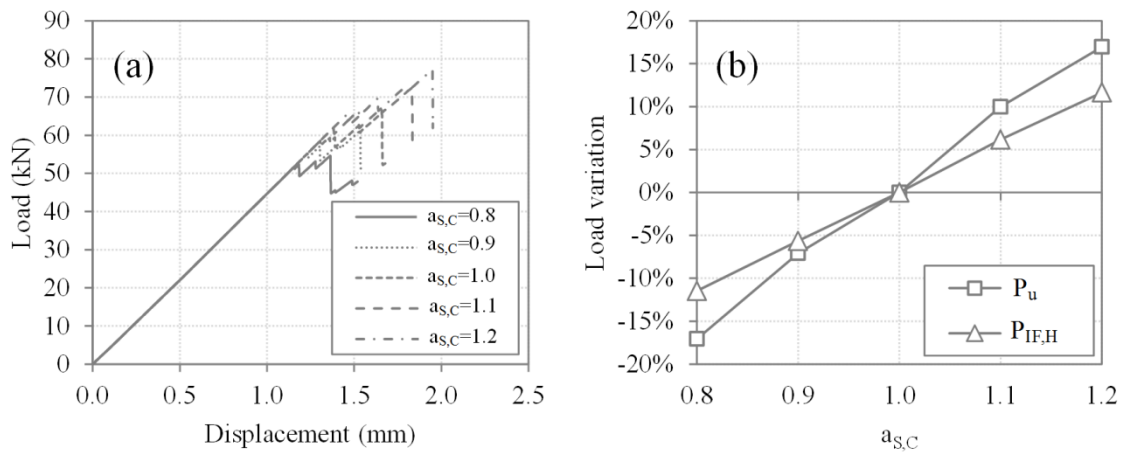


Figure 6.14: Influence of the variation of $S_{2,c}$ for series ITF_50: (a) load vs. displacement curves, and (b) initial failure load and ultimate load variation.

The results obtained indicate that despite the slight differences in terms of amplitude, the variation of both strength parameters led to approximately linear correlations between the variation of initial failure load (for both load configurations) and the corresponding parameter a . Nonetheless, the initial failure load seems to be more dependent on the variation of the in-plane shear strength, as a 20% variation of the S_{12} led to a variation in terms of the initial failure load in the same proportion (18% to 20%). On the other hand, a similar variation in the $S_{2,c}$ led to a smaller variation in terms of the initial failure load (11% to 14%). These results confirm the observations made in terms of stress fields and damaged zones, in which it was concluded that the shear strength is more influential to the initial failure behaviour than the transverse compressive strength.

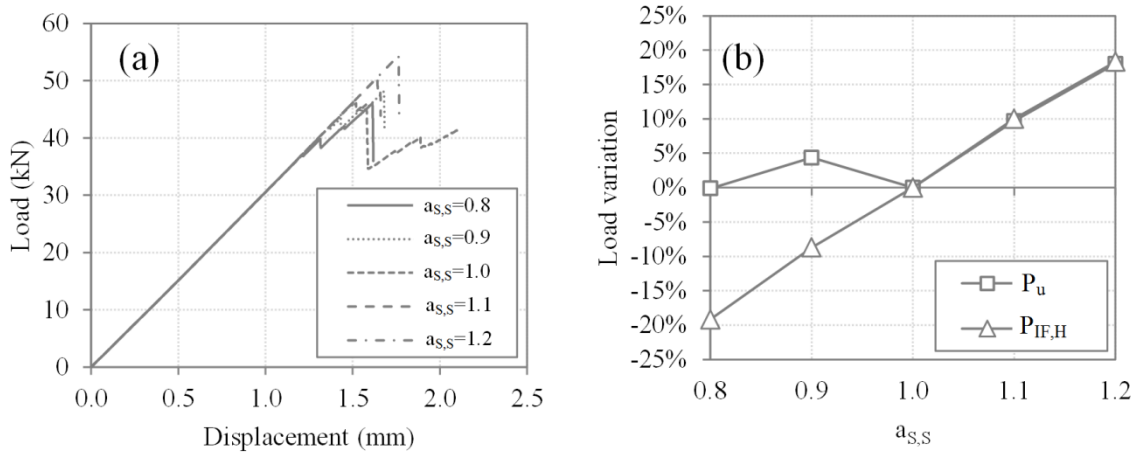


Figure 6.15: Influence of the variation of S_{12} for series ETF_50: (a) load vs. displacement curves, and (b) initial failure load and ultimate load variation.

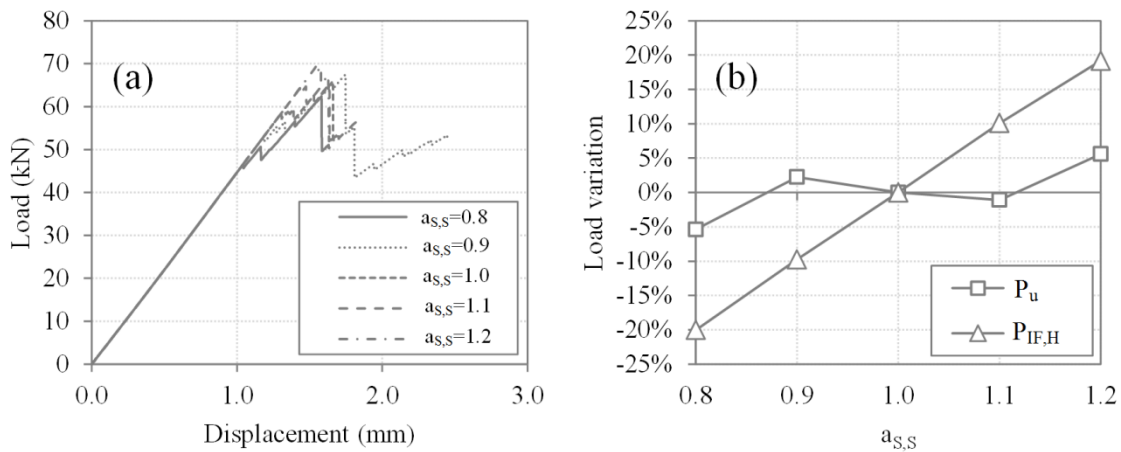


Figure 6.16: Influence of the variation of S_{12} for series ITF_50: (a) load vs. displacement curves, and (b) initial failure load and ultimate load variation.

On the other hand, it was concluded that $S_{2,c}$ affected the ultimate load more than S_{12} . As depicted in Figure 6.13(b) and Figure 6.14(b), the influence of the former parameter variation on the ultimate load is roughly linear and a 20% variation led to ultimate load variations between 12% and 17%.

The ultimate load results obtained by the variation of in-plane shear strength led to less obvious conclusions. In fact, for both ETF and ITF configurations, the load vs. displacement curves yielded from the variation of S_{12} exhibited a similar global response (Figure 6.15(a) and Figure 6.16(a)), in opposition to those obtained from the variation of $S_{2,c}$, in which the increase of the transverse compressive strength clearly led to the increase of the ultimate load. For the ETF configuration, lower values of S_{12} did not seem to have a major impact on the ultimate load results (10% drop of S_{12} led to 4% increase of P_u), while higher values of S_{12} led to a roughly equivalent increase in terms of the ultimate load. For the ITF configuration, the variation of such parameter by 20% led to ultimate load variations between -5% and +6%.

These results are of major importance and highlight the unsuitability of the physically linear models based on the Tsai-Hill criterion for the simulation of the web-crippling failure of GFRP I-section profiles. Using the Tsai-Hill models, Fernandes *et al.* [14,15] concluded that the in-plane shear stress governs web-crippling failure. While such conclusion might be accurate and reliable for failure initiation, the parametric analyses presented before show that in-plane shear stress does not govern the ultimate behaviour of web-crippling failure.

Although the S_{12} showed to be the parameter with higher influence on the initial failure load, the ultimate load showed to be more dependent on the variation of the $S_{2,c}$. The most relevant conclusion to be drawn herein is that both parameters affect (either moderately or highly) the progressive damage and failure behaviour of GFRP pultruded profiles under transverse compressive loads. Hence, they should always be accounted in the design calculations against web-crippling of GFRP pultruded profiles.

6.6.2 Fracture energy

Similarly to the parametric study regarding the strength parameters, the ratio between the considered (varied) fracture energy G_{mc} and the reference (actual) fracture energy G_r is denoted by parameter $a_G = G/G_r$ ($G_{mc,r} = 0.948$ N/mm). In this parametric study, the following values were considered: $a_G = 0.73, 1.0, 5.0, 10.0, 25.0, 50.0$. Figure 6.17(a) and Figure 6.18(a) depict the load *vs.* displacement curves for different values of parameter a while Figure 6.17(b) and Figure 6.18(b) show the variation of ultimate load³⁴ with a (the percentage is calculated with respect to P_u , for the reference case G_r). The obtained results showed that the global response of the GFRP profile was roughly the same using either the reference fracture energy or the minimum value (-27%) – note that the corresponding load *vs.* displacement curves overlapped for both ITF and ETF configurations.

When using higher G_{mc} values as input, higher ultimate loads were obtained. The ultimate behaviour was linear elastic up to failure for values between 0.73 and 10 times the reference matrix compression fracture energy. For higher G_{mc} values (25 or 50 times the reference value), the collapse was not as brittle as observed in the experimental campaign. Thus, these values might be overestimating the real matrix compression fracture energy. Moreover, as this parameter is increased, the damaged zones also tend to be less concentrated (localised), but rather distributed after collapse. For five and 10 times the reference value, the damaged areas were realistic and complied best with experimental observations (Figure 6.19(b)). When using G_{mc} values higher than these, the damaged zones comprised a large

³⁴It should be mentioned that low fracture energies require a very small time increment to avoid numerical problems. Therefore, the initial failure load is usually accurately determined, but these low fracture energies also lead to slow numerical convergence in the analysis after failure initiation, which render the models very time consuming. When increasing the fracture energy, the time-increment required for the converged solution is not as small and the analyses are less time consuming, but the identification of initial failure load is not accurate enough. For this reason, only the ultimate loads are presented and discussed in this section.

portion of the web, but the finite elements in these areas were only partially damaged (which did not correspond to the experimental observations – Figure 6.19 (c)).

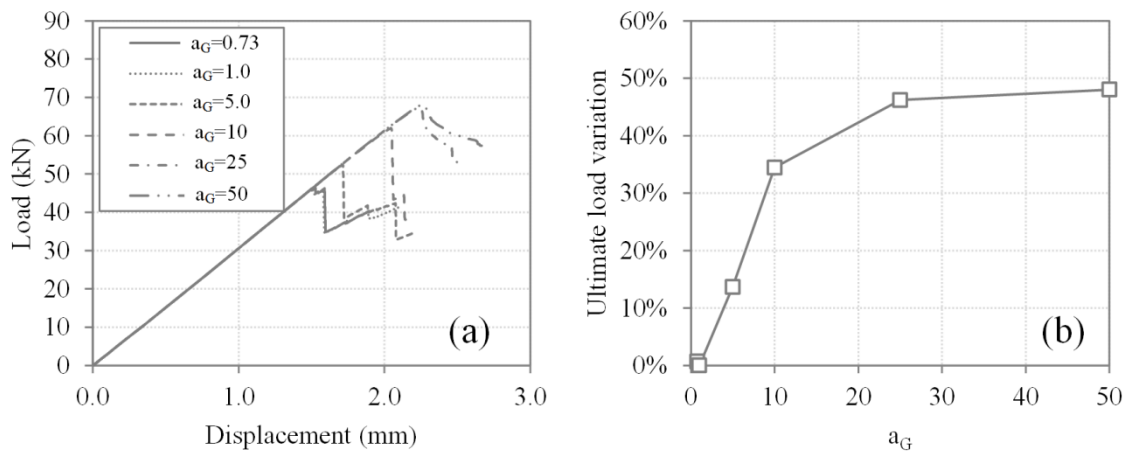


Figure 6.17: Influence of the variation of G_{mc} for series ETF_50: (a) load vs. displacement curves, and (b) ultimate load variation.

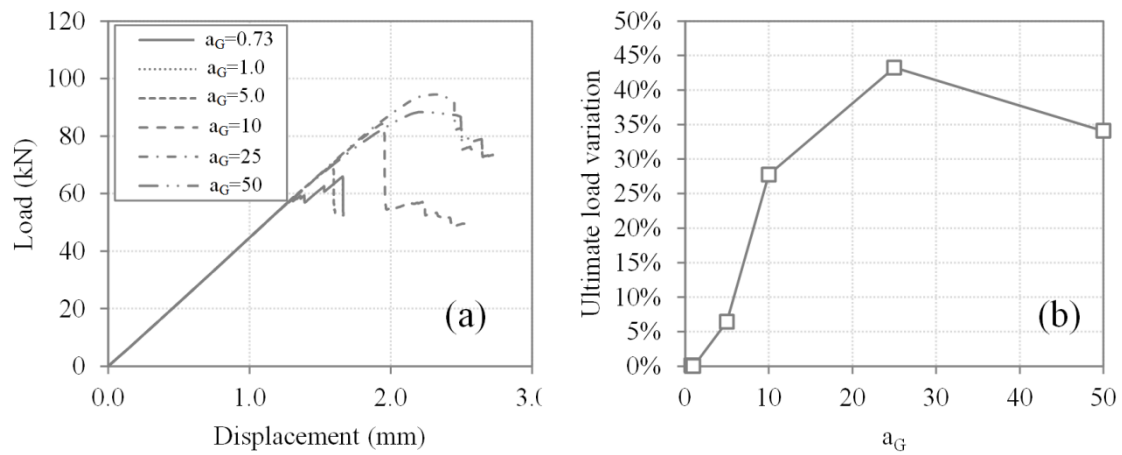


Figure 6.18: Influence of the variation of G_{mc} for series ITF_50: (a) load vs. displacement curves, and (b) ultimate load variation.

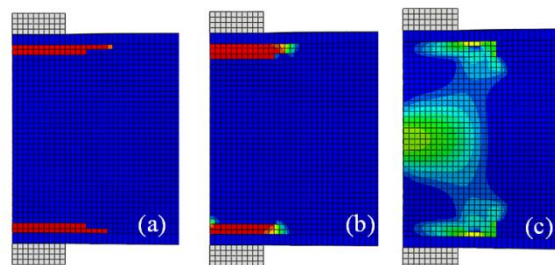


Figure 6.19: Matrix compression damaged zones for the ETF_50 using different G_{mc} values: (a) reference – 0.948 N/mm – (b) 10 times higher – 9.48 N/mm – and (c) 50 times higher – 47.4 N/mm.

The result obtained by Barbero *et al.* [31] for the fracture energy of an epoxy embedded laminate (11.5 N/mm) under matrix tensile failure mode is similar to that obtained by multiplying the reference G_{mc} by 10 times (9.48 N/mm). Despite the differences to Barbero's study (regarding materials and failure modes), both studies shown that a fracture energy of about 10 N/mm (10 times the reference value) seems to lead to more reliable results: a linear elastic behaviour similar to that observed in the experiments and a wider damage area. Also the ultimate load obtained by increasing the G_{mc} 10 times was closer to the corresponding experimental result (-20.8% instead of the initial -41.0% for the ETF configuration and -22.8% instead of -39.6% for the ITF configuration).

6.6.3 Web-flange rounded corner

Although still slightly conservative (in comparison with the experimental data), the numerical results obtained in the previous parametric studies are quite satisfactory. However, as pointed out by Bank [2], the web-flange junction is the weakest zone of GFRP profiles and thus it should be carefully modelled. In the previous analyses, the rounded corner of web-flange junction was disregarded as a sharp corner was considered. Aiming at studying the influence of considering the web-flange rounded corner, additional analyses were performed for ETF_50 and ITF_50 configurations using thicker continuum shell elements to approximately simulate the higher thickness of the web in the web-flange corner (according to the geometrical properties of the pultruded section – Figure 6.20). In these analyses, the reference G_{mc} multiplied by 10 (9.48 N/mm) was adopted. Figure 6.21 depicts the load vs. displacement curves of the models with and without modelling the web-flange rounded corner alongside the experimental load value. The ultimate loads obtained for the ETF and ITF configuration were 70.5 kN and 91.6 kN, respectively. These figures mean that a significant increase of ultimate load (13.9% for ETF and 8.8% for ITF) was achieved only by considering the slightly thicker elements in the web-flange junction.

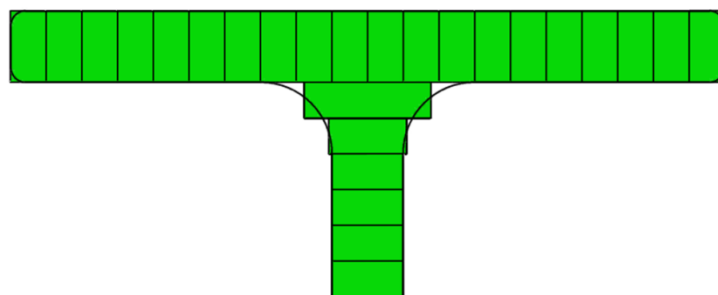


Figure 6.20: Approximated geometry of web-flange rounded corner using continuum shell elements.

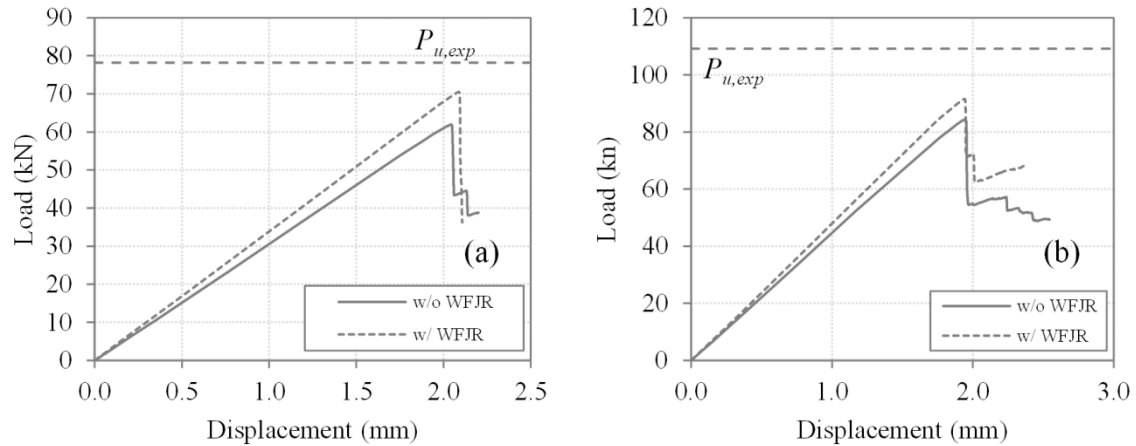


Figure 6.21: Load vs. displacement curves of the numerical models with (w/) and without (w/o) considering the web-flange junction radius (WFJR): (a) ETF_50 and (b) ITF_50.

Since the experimental small-scale coupon tests performed to determine the transverse compressive strength and the shear strength presented coefficients of variation of 26.9% and 12.4% respectively [14], it may be stated that the differences between the experimental and numerical results (9.8% and 16.0% for the ETF_50 and ITF_50 configurations, respectively) obtained through the proposed models are acceptable.

Aiming at achieving more reliable results when using the progressive damage analysis, efforts should be made in measuring accurate values of the intralaminar fracture energy for pultruded members, as well as in developing a reliable experimental test method to provide such values.

6.7 CONCLUDING REMARKS

In this chapter, numerical (finite element) models were developed and proposed to study the web-crippling phenomenon in a GFRP pultruded I-section. The models comprised the use of continuum shell elements and the implementation of Hashin-based progressive damage analysis. The numerical results were then compared to the experimental and numerical data obtained by Fernandes *et al.* [14,15]. Parametric studies were also performed to provide insights on the influence of strength and fracture energy parameters, as well as the modelling of the web-to-flange rounded corner, on the ultimate behaviour of GFRP pultruded I-section under concentrated transverse loads. The following main conclusions are drawn:

1. Despite having performed mesh convergence analyses and tested different viscous regularization coefficients, the models have highlighted the strong mesh dependency both in terms of ultimate (peak) load and the post-peak softening stage.
2. The Hashin-based progressive damage analysis showed to be adequate for the simulation of the web-crippling phenomenon, provided that the given input material data is also accurate

and complete. It led to much more reliable results (ultimate loads) than the physically linear analysis using the Tsai-Hill criterion.

3. The stiffness and the ultimate load increased (expectedly) for higher bearing lengths. For the same bearing length, the ultimate loads for web crippling of ITF configurations were (in average) 38% higher than those for ETF configurations.
4. The in-plane shear stresses and strength govern the failure initiation. For the peak load only a single layer of finite elements near the edges of the bearing plate was damaged (5 mm). After having collapsed, the damaged areas spread further and few layers under the bearing plate were affected (2-4 layers, corresponding to 10-20 mm height).
5. The transverse compressive stresses and strength govern the ultimate behaviour. Such evidence was more noticeable in case of the ITF configuration;
6. The fracture energy G_{mc} associated to the governing failure mode has a major impact on the overall response of the profile subjected to transverse concentrated loads. As the G_{mc} value was increased, higher ultimate loads and less vertical post-peak load paths were obtained. A value of 10 times the reference G_{mc} was found to lead to the most accurate results (both in terms of ultimate loads and damaged areas);
7. Efforts should be made in establishing an experimental test method for the accurate definition of the intralaminar fracture energy for pultruded profiles, as this parameter is crucial for the accurate simulation of damage mechanisms of GFRP pultruded I-section under concentrated loads.

CHAPTER 7

CONCLUSIONS AND FUTURE DEVELOPMENTS

7.1 CONCLUSIONS

Fibre reinforced polymer (FRP) pultruded profiles are being increasingly used as structural members in civil engineering applications. Their main advantages over traditional materials (such as steel and reinforced concrete) stem from their low self-weight, high strength and reduced maintenance requirements, which are valuable assets in a market with increasing demand for lighter, more durable and faster construction. However, some drawbacks are still hindering the widespread use of FRP pultruded structures, namely those comprising glass reinforcement (GFRP): the typical high deformability and susceptibility to buckling phenomena, the brittle failure modes, the poor behaviour under elevated temperatures and the lack of consensual design codes.

With the purpose of providing further insights about the structural behaviour of FRP pultruded profiles and aiming at the development of more consensual design approaches, this thesis presented results from experimental, numerical and analytical studies addressing three particular aspects: (i) the effect of small eccentricities about the major axis in compressed members, (ii) the influence of hybridization on the structural behaviour of columns and beams, and (iii) the progressive failure of beams subjected to concentrated transverse loads (web-crippling). Relevant conclusions were drawn from these studies, which are described in the next paragraphs.

The results obtained from the three studies mentioned above confirmed the linear elastic behaviour up to failure of the FRP material, which generally occurs in a sudden and brittle way. Regarding the compression members, the only ultimate limit state that provided some prior warning of failure was the global buckling of concentrically loaded columns (long and non-braced). However, one should note that the experimental testing of FRP columns was conducted under displacement control rather than load control. Hence, and since the load paths indicated that the load stabilizes for increasing applied displacements (very limited post-buckling strength arises in global buckling modes), for actual structures submitted to overloads, the collapse would also occur without prior warning signs in a

sudden manner. Regarding the collapse of beams and despite being also brittle, it is worth mentioning that the FRP beams all exhibited very significant deflections prior to failure and in spite of their linear response this should constitute a clear warning sign of structural malfunctioning.

The numerical models performed both in GBTUL and ABAQUS provided reasonably accurate results in terms of linear elastic buckling loads compared to the available experimental data. Regarding the nonlinear analyses carried out in ABAQUS and despite the type of element used (shell or continuum shell elements) one obtained a good fit to the experimental loading paths, both in terms of load *vs.* displacement behaviour and stress *vs.* strain behaviour. The buckling behaviour of compressive members was also well simulated according to the experimental results. The application of the ABAQUS built-in Hashin-based progressive damage analysis was successful in all the load configurations tested (axial compression, four-point bending and concentrated transverse loading). These analyses highlighted the importance of providing accurate input data for the numerical models, namely in load configurations that allow for a significant stress redistribution (web-crippling phenomenon). In these cases, parametric studies were also performed aiming at fully understanding the influence of strength and fracture energy parameters in the structural response of the simulated FRP member. The analysis of the stress fields in the numerical models indicated that shear stresses generally govern failure initiation, namely when local buckling modes are triggered.

More detailed conclusions about the three main topics investigated in this thesis are described in the following subsections.

7.1.1 Small eccentricity effects in columns

Regarding the study on the effect of eccentric loading about the major axis of GFRP pultruded I-section columns, the results obtained for non-braced and braced columns under concentric loading outlined the importance of designing adequate bracing systems in compressed GFRP members. In fact, for the adopted test setup the design loads increased up to 8 times just by providing adequate bracing and thus avoiding critical global buckling modes. When comparing the ultimate loads of concentrically and eccentrically loaded columns with lateral bracing, one concluded that small eccentricities within the section kern are of major importance as they affect both the loading stiffness (due to the second-order P - δ effects) and the ultimate load (which presented a roughly linear variation with the eccentricity level and decreased by 40% for the maximum level tested). Analytical estimates for the global and local buckling loads of non-braced and braced concentrically loaded columns obtained, using respectively Euler's and Kollár's [71] formulations, provided very good agreement with the experimental data (with relative differences lower than 6%). GBT analysis emphasised that the combination of local modes changes with the eccentricity. As the eccentricity is increased, the less compressed flange twists less than the most compressed flange and this effect is given by the

increasing participation of the anti-symmetric mode (mode 6) and decreasing participation of the symmetric mode (mode 5). One should also underline the fact that the GBT and the ABAQUS results presented a very good agreement (maximum relative difference of 8%) and thus GBTUL proved to be a strong and reliable tool for the quick determination of the elastic buckling loads of FRP members. As already mentioned, the nonlinear analysis performed with ABAQUS was very consistent with the experimental data both in terms of axial strains and axial shortening. Using the Tsai-Hill criterion, one determined the contribution of longitudinal and shear stresses to the overall failure index, concluding that shear stresses are always governing, regardless of the eccentricity level.

7.1.2 Hybridization effects in columns and beams

With respect to the study of the structural behaviour of hybrid C-GFRP pultruded compression members (columns) and flexural members (beams), one concluded that small amounts of CF reinforcement are effective in stiffening those structural members, providing an increase in the initial axial and bending stiffness up to 17% and 8%, respectively. However, the CF reinforcement was not effective up to failure – delamination of the CF mats occurred in both flanges in the case of short and intermediate columns and in the top flange in the case of beams. Although delamination probably occurred in all series (since stiffness reduction was measured throughout the test, consistent for all hybrid beams, short and intermediate columns), it was much more noticeable in series S3, which involved bidirectional mats in both flanges. Such fact may be explained by two possible hypotheses: either due to the fact that S3 was the only series in which the strain gauges were directly bonded to the CF mats or to the resin impregnation issues (reported by the manufacturer in the production stage) which caused delamination to be more denoted in that particular series. Since the strain levels in long columns were lower than in the remaining geometries, their stiffness was sustained up to the end of the test leading to 10 to 17% higher critical buckling loads, when compared to the reference GFRP profile. In both short and intermediate length hybrid columns the critical buckling load was 1% to 13% lower than that of the reference series. Regarding the ultimate behaviour of the hybrid beams, results were not as conclusive. Despite the slight ultimate load increase verified in series S2 and S4, series S1, S3 and S5 presented a worse performance than the all-GFRP reference series. The Hashin-based progressive damage analysis adequately simulated both the material failure and the delamination of the CF mats, thus being a useful and accurate tool for the modelling of the delamination and progressive collapse of hybrid FRP pultruded flexural members. The numerical ultimate load results presented a maximum difference of 13% in pultruded columns and 9% in pultruded beams. Nonetheless, at least for compressive members, the Tsai-Hill index presented a reasonably good approximation both to the experimental and the Hashin numerical ultimate load. The failure modes were also consistent with those observed in the experimental tests. Regarding the analytical approaches for the estimation of the design loads, Bank's approach [2] seemed to be the most suited

for compression members. Regarding flexural members, none of the design approaches assessed was fully accurate. In fact, the American pre-standard [11] does not consider the interaction between axial and shear stresses (and thus presented non-conservative results), while the Italian guidelines [12] include the critical local buckling bending moment into the material failure stress interaction equation (and thus presented overly conservative results). Although the occurrence of delamination prevented the maximum exploitation of the material potential, one may state that unidirectional reinforcement of the flanges is the optimal fibre configuration for beams and long columns, while for short and laterally braced columns (subjected to local buckling modes) the bidirectional reinforcement of the web is more effective.

7.1.3 Web-crippling effects in beams

Finally, regarding the numerical models proposed to study the web-crippling phenomenon, it was found that the progressive damage presents a strong mesh dependency associated to the post-peak of load-displacement curves (ultimate load and path of the post-peak softening stage). The Hashin-based progressive damage analysis showed to be adequate for the simulation of the web-crippling phenomenon. Despite its conservative results (compared to the experimental data), the ultimate loads obtained from Hashin-based analysis were much more reliable (and much less conservative) than those obtained from physically linear analysis using the Tsai-Hill criterion [15]. The parametric studies performed also allowed concluding that (i) the shear stresses and strength govern the failure initiation while (ii) the ultimate loads (peak load) are more dependent on the transverse compressive stresses and strength. The fracture energy associated to the governing failure modes also presented a major impact on the ultimate behaviour of the simulated GFRP pultruded members. The initially adopted reference fracture energy (nearly 1.0 N/mm), based on the area under the stress vs. strain curves of uniaxial stress state small scale specimens, showed to be inaccurate. By increasing that parameter 10 times, much more reliable ultimate loads were obtained, *i.e.* more consistent with those obtained experimentally by Fernandes *et al.* [14]. Such value (about 10 N/mm) is also coherent with other studies reported in the literature review [31].

7.2 FUTURE DEVELOPMENTS

Having summarised the most relevant conclusions drawn in the framework of this thesis, current research needs and recommendations for future developments are highlighted in the following paragraphs.

The Hashin-based progressive failure analysis available in the most recent versions of the commercial software ABAQUS proved to be a very useful tool for modelling the collapse of FRP composites. Despite being much more complex and demanding (both in terms of time and computational

resources), it showed to present an adequate alternative to classic physically linear finite element numerical models (using failure initiation criteria without stiffness degradation). Its inherent advantages are obvious. It allows simulating the progressive failure of the material and thus, for load configurations with high stress concentrations (namely when using more refined meshes), it has proved to be much more reliable than other failure criteria such as the maximum stress or the Tsai-Hill. Nonetheless, one concluded that when using inaccurate input data (namely in terms of fracture energies) the numerical response can deviate significantly from the experimental observations, particularly if stress redistributions are allowed. Hence, one considers that one of the top priorities for future research addressing the simulation of the progressive collapse of FRP members (particularly using the Hashin criterion) is the development of test methods able to accurately define the intralaminar fracture energies (of the four failure modes) for pultruded profiles.

Also regarding the numerical simulation of the material progressive damage, the use of explicit instead of implicit analysis should be addressed. While for the loading stage of the tests in FRP members, the load application rate is very low and thus it can be accurately simulated by an implicit quasi-static analysis, for the softening stage the phenomenon is brittle and high energy releasing, presenting sudden load drops and thus corresponding to a dynamic phenomenon.

Another issue that needs further insights is the study of the delamination of the CF mats and how to delay it or even to totally avoid it. Possible approaches might be the use of a different resin as embedding matrix (*e.g.* vinylester) or adopting a different manufacturing procedure. Regarding hand-layup laminates, stitching has proved to be effective in delaying the delamination of laminae with different types of fibres [94]. Efforts should be made in finding a similar approach to pultruded structures and studying different fibre architectures in order to achieve more solid conclusions. Multi-objective optimisation tools [95] should also be implemented to define the architecture of such hybrid reinforcement, taking into account not only the structural performance of FRP pultruded profiles but also their cost.

Regarding the analytical approaches for compression and flexural members, one expects that the better understanding of the behaviour of these structural members (presented and discussed throughout this thesis) contribute for future reviews of the Italian and American guidelines (which are still provisional) for the design of pultruded profiles.

Additionally, other types of local buckling strengthening systems or reinforcement should be studied as they may increase the ultimate loads significantly. From the studies presented herein it was clear that the web-flange junction plays a major role in the local buckling phenomenon and thus efforts should be made in stiffening and strengthening that particular region in order to increase the overall load carrying capacity.

Regarding the web-crippling phenomenon, numerical models for different load and boundary configurations (IOF and EOF) should be developed and validated according to experimental data. Also, cross-sections other than the I200 should be addressed.

REFERENCES

- [1] J.R. Correia, Glass Fibre Reinforced Polymer (GFRP) Pultruded Profiles. Application of GFRP-Concrete Hybrid Beams in Construction, MSc Dissertation in Construction, Instituto Superior Técnico, 2004 (in Portuguese).
- [2] L.C. Bank, Composites for Construction: Structural Design with FRP Materials, John Wiley & Sons, 2006.
- [3] J.R. Correia, “Fibre-reinforced polymer (FRP) composites”, in Materials for Construction and Civil Engineering (Editors: M.C. Gonçalves, F. Margarido), Materials for Construction and Civil Engineering: Science, Processing, and Design, Springer, Dordrecht, 2015.
- [4] M.M. Correia, F. Nunes, J.R. Correia, N. Silvestre, Buckling behavior and failure of hybrid fiber-reinforced polymer pultruded short columns, *J. Compos. Constr.* 17 (2013) 463–475.
- [5] J.R. Correia, Y. Bai, T. Keller, A review of the fire behaviour of pultruded GFRP structural profiles for civil engineering applications, *Compos. Struct.* 127 (2015) 267–287.
- [6] J.R. Correia, M.M. Gomes, J.M. Pires, F.A. Branco, Mechanical behaviour of pultruded glass fibre reinforced polymer composites at elevated temperature: Experiments and model assessment, *Compos. Struct.* 98 (2013) 303–313.
- [7] J.R. Correia, “Pultrusion of advanced composites”, in Advanced Fibre-Reinforced Polymer (FRP) Composites for Structural Applications (Editor: J. Bai), Woodhead Publishing Limited, 2013.
- [8] F.F. Nunes, Structural Behavior of GFRP Pultruded Profiles Reinforced with CFRP Sheets: Experimental Characterisation and Numerical Modeling, MSc Dissertation in Civil Engineering, Instituto Superior Técnico, 2012 (in Portuguese).
- [9] M.M. Correia, Structural Behavior of Pultruded GFRP Profiles: Experimental Study and Numerical Modeling, MSc Dissertation in Civil Engineering, Instituto Superior Técnico, 2012 (in Portuguese).
- [10] J. Clarke (ed.), Structural Design of Polymer Composites – Eurocomp Design Code and Handbook, E & FN Spon, London, 1996.
- [11] ASCE, American Society of Civil Engineers (ASCE). Pre-Standard for Load & Resistance Factor Design (LRFD) of Pultruded Fiber Reinforced Polymer (FRP) Structures. Submitted by the American Composites Manufacturers Association (ACMA) to ASCE, (2010).
- [12] CNR, Guide for the Design and Construction of Structures made of FRP Pultruded Elements, (2008).
- [13] ASCE, Structural Plastics Design Manual, No 63, American Society of Civil Engineers, Reston, VA, 2002.

- [14] L.A. Fernandes, J. Gonilha, J.R. Correia, N. Silvestre, F. Nunes, Web-crippling of GFRP pultruded profiles. Part 1: Experimental study, *Compos. Struct.* 120 (2015) 565–577.
- [15] L.A. Fernandes, F. Nunes, N. Silvestre, J.R. Correia, J. Gonilha, Web-crippling of GFRP pultruded profiles. Part 2: Numerical analysis and design, *Compos. Struct.* 120 (2015) 578–590.
- [16] E.J. Barbero, M. Turk, Experimental investigation of beam-column behavior of pultruded structural shapes, *J. Reinf. Plast. Compos.* 19 (2000) 249–265.
- [17] J.T. Mottram, N.D. Brown, D. Anderson, Buckling characteristics of pultruded glass fibre reinforced plastic columns under moment gradient, *Thin-Walled Struct.* 41 (2003) 619–638.
- [18] S. Timoshenko, *Theory of Elasticity*, 2nd ed., McGraw-Hill, London, 1970.
- [19] E. Barbero, J. Tomblin, Euler buckling of thin-walled composite columns, *Thin-Walled Struct.* 17 (1993) 237–258.
- [20] J. Tomblin, E. Barbero, Local buckling experiments on FRP columns, *Thin-Walled Struct.* 18 (1994) 97–116.
- [21] E. Barbero, J. Tomblin, A phenomenological design equation for FRP columns with interaction between local and global buckling, *Thin-Walled Struct.* 18 (1994) 117–131.
- [22] E.J. Barbero, E.K. Dede, S. Jones, Experimental verification of buckling-mode interaction in intermediate-length composite columns, *Int. J. Solids Struct.* 37 (2000) 3919–3934.
- [23] J.T. Mottram, Determination of critical load for flange buckling in concentrically loaded pultruded columns, *Compos. Part B Eng.* 35 (2004) 35–47.
- [24] L.C. Bank, J. Yin, Failure of web-flange junction in postbuckled pultruded I-beams, *J. Compos. Constr.* 3 (1999) 177–184.
- [25] J.R. Correia, F.A. Branco, N.M.F. Silva, D. Camotim, N. Silvestre, First-order, buckling and post-buckling behaviour of GFRP pultruded beams. Part 1: Experimental study, *Comput. Struct.* 89 (2011) 2065–2078.
- [26] N.M.F. Silva, D. Camotim, N. Silvestre, J.R. Correia, F.A. Branco, First-order, buckling and post-buckling behaviour of GFRP pultruded beams. Part 2: Numerical simulation, *Comput. Struct.* 89 (2011) 2065–2078.
- [27] D.T. Borowicz, L.C. Bank, Behavior of pultruded fiber-reinforced polymer beams subjected to concentrated loads in the plane of the web, *J. Compos. Constr.* 15 (2011) 229–238.
- [28] D.T. Borowicz, L.C. Bank, Effect of web reinforcement on the behavior of pultruded fiber-reinforced polymer beams subjected to concentrated loads, *Constr. Build. Mater.* 47 (2013) 347–357.
- [29] C. Wu, Y. Bai, Web crippling behaviour of pultruded glass fibre reinforced polymer sections, *Compos. Struct.* 108 (2014) 789–800.

- [30] A.M.G. Coelho, J.T. Mottram, K.A. Harries, Finite element guidelines for simulation of fibre-tension dominated failures in composite materials validated by case studies, *Compos. Struct.* 126 (2015) 299–313.
- [31] E.J. Barbero, F. A. Cosso, R. Roman, T.L. Weadon, Determination of material parameters for Abaqus progressive damage analysis of E-glass epoxy laminates, *Compos. Part B Eng.* 46 (2013) 211–220.
- [32] J.R. Correia, *GFRP Pultruded Profiles in Civil Engineering: Hybrid Solutions, Bonded Connections and Fire Behaviour*, PhD Thesis in Civil Engineering, Instituto Superior Técnico, Technical University of Lisbon, 2008.
- [33] Strongwell Corporation, Strongwell Corporation, (2016). <http://www.strongwell.com/> (accessed January 1, 2016).
- [34] C.T. Sun, R.S. Vaidya, Prediction of composite properties from a representative volume element, *Compos. Sci. Technol.* 56 (1996) 171–179.
- [35] TWI, Cranfield University, ADVISE, ISOJET, EXEL Composites, IAI, PUL-AERO, (2016). <http://www.pul-aero.eu/>.
- [36] Nuplex Corporate, Nuplex Corporate, (2016). <http://www.nuplex.com/Corporate/>.
- [37] T. Keller, Recent all-composite and hybrid fibre-reinforced polymer bridges and buildings, *Prog. Struct. Eng. Mater.* 3 (2001) 132–140.
- [38] C.E. Bakis, L.C. Bank, V.L. Brown, E. Cosenza, et al., Fiber-reinforced polymer composites for construction – State-of-the-art review, *J. Compos. Constr.* 6 (2002) 73–87.
- [39] Fiberline Composites, Fiberline Composites, (2014). <http://www.fiberline.com/>.
- [40] ALTO Perfis Lda, , (2016). <http://www.alto.pt/>.
- [41] Zoltek Corporate, Zoltek Corporate, (2016). www.zoltek.com (accessed January 1, 2016).
- [42] S&P Reinforcement, (2016). <http://www.sp-reinforcement.com.br/> (accessed January 1, 2016).
- [43] A.R. Bunsell, B. Harris, Hybrid carbon and glass fibre composites, *Composites.* 5 (1974) 157–164.
- [44] Y. Swolfs, L. Gorbatikh, I. Verpoest, Fibre hybridisation in polymer composites: A review, *Compos. Part A Appl. Sci. Manuf.* 67 (2014) 181–200.
- [45] W.F. Ragheb, Hybridization effectiveness in improving local buckling capacity of pultruded I-beams, *Mech. Adv. Mater. Struct.* 17 (2010) 448–457.
- [46] Creative Pultrusions, (2016). <http://www.creativepultrusions.com/index.cfm/products-solutions/custom-pultrusions/> (accessed February 27, 2016).
- [47] N.D. Hai, H. Mutsuyoshi, S. Asamoto, T. Matsui, Structural behavior of hybrid FRP composite I-beam, *Constr. Build. Mater.* 24 (2010) 956–969.

- [48] C. Waldron, Determination of the design parameters for the Route 601 Bridge: A bridge containing the strongwell 36 in. hybrid composite double web beam, (2001).
- [49] J. Gonilha, GFRP-Concrete Hybrid Structural Systems. Application to the Development of a Footbridge Prototype, PhD Thesis in Civil Engineering, Instituto Superior Técnico, University of Lisbon, 2014.
- [50] J.A. Gonilha, J.R. Correia, F.A. Branco, Creep response of GFRP–concrete hybrid structures: Application to a footbridge prototype, *Compos. Part B Eng.* 53 (2013) 193–206.
- [51] J.A. Gonilha, J.R. Correia, F.A. Branco, Dynamic response under pedestrian load of a GFRP–SFRSCC hybrid footbridge prototype: Experimental tests and numerical simulation, *Compos. Struct.* 95 (2013) 453–463.
- [52] J.A. Gonilha, J.R. Correia, F.A. Branco, E. Caetano, Á. Cunha, Modal identification of a GFRP-concrete hybrid footbridge prototype: Experimental tests and analytical and numerical simulations, *Compos. Struct.* 106 (2013) 724–733.
- [53] J.A. Gonilha, J. Barros, J.R. Correia, J. Sena-Cruz, F.A. Branco, L.F. Ramos, et al., Static, dynamic and creep behaviour of a full-scale GFRP-SFRSCC hybrid footbridge, *Compos. Struct.* 118 (2014) 496–509.
- [54] M. Sá, Analysis of Pultruded GFRP Multicellular Deck Panels – Application to Pedestrian Bridges, PhD Thesis in Civil Engineering, Instituto Superior Técnico, 2014 (in Portuguese).
- [55] M.F. Sá, A.M. Gomes, J.R. Correia, N. Silvestre, Creep behavior of pultruded GFRP elements – Part 1: Literature review and experimental study, *Compos. Struct.* 93 (2011) 2450–2459.
- [56] M.F. Sá, A.M. Gomes, J.R. Correia, N. Silvestre, Creep behavior of pultruded GFRP elements – Part 2: Analytical study, *Compos. Struct.* 93 (2011) 2409–2418.
- [57] M. Sá, A. Gomes, J.R. Correia, N. Silvestre, Experimental Evaluation of the performance of pultruded deck panels for footbridge applications, *CICE 2012 – The 6th International Conference on FRP Composites in Civil Engineering*, Rome, Italy (2012).
- [58] T. Morgado, J.R. Correia, A. Moreira, F.A. Branco, C. Tiago, Experimental study on the fire resistance of GFRP pultruded tubular columns, *Compos. Part B Eng.* 69 (2015) 201–211.
- [59] M. Garrido, J.R. Correia, F.A. Branco, T. Keller, Creep behaviour of sandwich panels with rigid polyurethane foam core and glass-fibre reinforced polymer faces: Experimental tests and analytical modelling, *J. Compos. Mater.* 48 (2013) 2237–2249.
- [60] J.M. Sousa, J.R. Correia, S. Cabral-Fonseca, Durability of Glass Fibre Reinforced Polymer Pultruded Profiles: Comparison Between QUV Accelerated Exposure and Natural Weathering in a Mediterranean Climate, *Exp. Tech.* (in press, doi: 10.1111/ext.12055).
- [61] J.M. Sousa, J.R. Correia, S. Cabral-Fonseca, A.C. Diogo, Effects of thermal cycles on the mechanical response of pultruded GFRP profiles used in civil engineering applications, *Compos. Struct.* 116 (2014) 720–731.
- [62] M.C.S. Ribeiro, A. Fiúza, A.C.M. Castro, F.J.G. Silva, J.P. Meixedo, M.L. Dinis, et al., Sustainability improvement of a composite materials’ industry through recycling and re-

- engineering process approaches, 6th International Conference on Mechanics and Materials in Design, Ponta Delgada, Azores, Portugal (2015) 1–9.
- [63] G.J. Turvey, Y. Zhang, A computational and experimental analysis of the buckling, postbuckling and initial failure of pultruded GRP columns, *Comput. Struct.* 84 (2006) 1527–1537.
- [64] T.T. Nguyen, T.M. Chan, J.T. Mottram, Influence of boundary conditions and geometric imperfections on lateral–torsional buckling resistance of a pultruded {FRP} I-beam by {FEA}, *Compos. Struct.* 100 (2013) 233–242.
- [65] A. Zureick, D. Scott, Short-term behavior and design of fiber-reinforced polymeric slender members under axial compression, *J. Compos. Constr.* 1 (1997) 140–149.
- [66] F. Engesser, *Die Knickfestigkeit gerader Stäbe*, (1891) (in German)
- [67] Z.A. Hashem, R.L. Yuan, Short vs. long column behavior of pultruded glass-fiber reinforced polymer composites, *Constr. Build. Mater.* 15 (2001) 369–378.
- [68] E.J. Barbero, E.K. Dede, S. Jones, Experimental verification of buckling-mode interaction in intermediate-length composite columns, *Int. J. Solids Struct.* 37 (2000) 3919–3934.
- [69] R. V. Southwell, On the analysis of experimental observations in problems of elastic stability, *Proc. R. Soc. A Math. Phys. Eng. Sci.* 135 (1932) 601–616.
- [70] E.J. Barbero, J. Trovillion, Prediction and measurement of the post-critical behavior of fiber-reinforced composite columns, *Compos. Sci. Technol.* 58 (1998) 1335–1341.
- [71] L.P. Kollár, Buckling of unidirectionally loaded composite plates with one free and one rotationally restrained unloaded edge, *J. Struct. Eng.* 128 (2002) 1202–1211.
- [72] Simulia, *Abaqus 6.11 User's Manuals*, (2011).
- [73] R. Bebiano, P. Pina, N. Silvestre, D. Camotim, *GBTUL 1.0 – GBT theoretical background*, (2008).
- [74] R. Bebiano, P. Pina, N. Silvestre, D. Camotim, *GBTUL 1.0 – buckling and vibration analysis of thin-walled members*, (n.d.).
- [75] N. Silvestre, D. Camotim, Local-plate and distortional postbuckling behavior of cold-formed steel lipped channel columns with intermediate stiffeners, *J. Struct. Eng.* 132 (2006) 529–540.
- [76] R.M. Jones, *Mechanics of Composite Materials*, Second Ed., Taylor & Francis, Philadelphia, 1998.
- [77] Z. Hashin, A. Rotem, A fatigue failure criterion for fiber reinforced materials, *J. Compos. Mater.* 7 (1973) 448–464.
- [78] Z. Hashin, Failure criteria for unidirectional fiber composites, *J. Appl. Mech.* 47 (1980) 329–334.
- [79] P.P. Camanho, C.G. Davila, Mixed-mode decohesion finite elements for the simulation of delamination in composite materials, *NASA Report TM-2002-211737* (2002).

- [80] N.F. Knight, User-Defined Material Model for Progressive Failure Analysis, Nasa C/R-2006-214526. (2006).
- [81] J.A. Gonilha, J.R. Correia, F.A. Branco, Structural behaviour of a GFRP-concrete hybrid footbridge prototype: Experimental tests and numerical and analytical simulations, *Eng. Struct.* 60 (2014) 11–22.
- [82] CEN, ISO 527-1 Plastics - Determination of Tensile Properties - Part 1: General Principles, (1997).
- [83] CEN, ISO 527-4 Plastics - Determination of Tensile Properties - Part 4: Test Conditions for Isotropic and Orthotropic Fibre-Reinforced Plastic Composites, (1997).
- [84] ASTM, ASTM D 695-02 Standard Test Method for Compressive Properties of Rigid Plastics, (2002).
- [85] J.M. Hodgkinson, *Mechanical Testing of Advanced Fibre Composites*, CRC Press, Boca Raton, 2000.
- [86] ASTM, ASTM D2344 / D2344M Standard Test Method for Short-Beam Strength of Polymer Matrix Composite Materials and Their Laminates, (2006).
- [87] S. Tsai, Strength Theories of Filamentary Structures, in: R.T. Schwartz, H.T. Schwartz (Eds.), *Fundam. Asp. Fiber Reinf. Plast. Compos.*, Wiley, New York, 1968: pp. 3–11.
- [88] Z. Bazant, B. Oh, Crack band theory of concrete, *Mater. Struct.* 16 (1983) 155–177.
- [89] F. Li, D. Xingwen, Mesh-dependence of material with softening behavior, *Chinese J. Aeronaut.* 23 (2010) 46–53.
- [90] C. Veyhl, I. V. Belova, G.E. Murch, A. Öchsner, T. Fiedler, On the mesh dependence of nonlinear mechanical finite element analysis, *Finite Elem. Anal. Des.* 46 (2010) 371–378.
- [91] A. Reis, D. Camotim, *Estabilidade e Dimensionamento de Estruturas*, Orion, 2012 (in Portuguese).
- [92] CEN, Eurocode 3: Design of Steel Structures, (2010).
- [93] AISI, North American Specification for the Design of Cold-Formed Steel Structural Members, (2007).
- [94] R. Velmurugan, S. Solaimurugan, Improvements in mode I interlaminar fracture toughness and in-plane mechanical properties of stitched glass/polyester composites, *Compos. Sci. Technol.* 67 (2007) 61–69.
- [95] A.L. Custódio, J.F.A. Madeira, A.I.F. Vaz, L.N. Vicente, Direct multisearch for multiobjective optimisation, *SIAM J. Optim.* 21 (2011) 1109–1140.
- [96] L.A. Fernandes, *Structural Behaviour of GFRP Beams Subjected to Concentrated Loads: Experimental Tests, Numerical Modeling and Analytical Study*, MSc Dissertation in Civil Engineering, Instituto Superior Técnico, 2014 (in Portuguese).

- [97] V. Dhand, G. Mittal, K.Y. Rhee, S.-J. Park, D. Hui, A short review on basalt fiber reinforced polymer composites, *Compos. Part B Eng.* 73 (2015) 166–180.
- [98] A. Greco, A. Maffezzoli, G. Casciaro, F. Caretto, Mechanical properties of basalt fibers and their adhesion to polypropylene matrices, *Compos. Part B Eng.* 67 (2014) 233–238.